



GRUPPO NAZIONALE DI GEOFISICA  
DELLA TERRA SOLIDA



# Atti del 34<sup>o</sup> Convegno Nazionale

Trieste, 17-19 novembre 2015  
Palazzo dei Congressi  
della Stazione Marittima

**Tema 3: Geofisica applicata**



ISTITUTO NAZIONALE DI  
OCEANOGRAFIA E DI  
GEOFISICA SPERIMENTALE



—15<sup>o</sup> Convegno Nazionale



GRUPPO NAZIONALE DI GEOFISICA DELLA TERRA SOLIDA



# 34° convegno nazionale

**Trieste**  
17-19 novembre 2015  
Stazione Marittima

**ATTI**

**Tema 3: Geofisica Applicata**



ISTITUTO NAZIONALE DI  
OCEANOGRAFIA E DI  
GEOFISICA SPERIMENTALE

In collaborazione con



## 34° Convegno Nazionale Atti - Tema 3: Geofisica Applicata

---

### Comitato organizzatore

D. Slejko  
D. Albarello  
A. Argnani  
F. Bianco  
G. Caielli  
G. Cassiani  
A. Del Ben  
D. Di Bucci  
M. Dolce  
E. Eva  
G. Florio  
P. Galli  
L. Martelli  
P. Mazzucchelli  
G. Naso  
R. Nicolich  
F. Pacor  
R. Petrini  
L. Sambuelli

A cura di: D. Slejko, A. Riggio,  
A. Rebez, G. Caielli, G. Cassiani,  
G. Florio, P. Mazzucchelli,  
R. Nicolich, L. Sambuelli

Con la collaborazione di:  
M. Bobbio e P. Giurco

Copertina: M. Sedmach

Impaginazione e stampa:  
Luglioprint, Trieste

Finito di stampare nel mese di novembre 2015

ISBN: 978-88-940442-7-0 questo volume  
ISBN: 978-88-940442-4-9 collezione completa

*Ancora a Trieste. Perché l’OGS è di casa, perché la città ospita un palazzo dei congressi bello e adeguato alle necessità, ma anche, o soprattutto, perché Trieste è risultata gradita nel passato ai partecipanti.*

*Come ben si sa il Gruppo Nazionale di Geofisica della Terra Solida (GNGTS) ufficialmente non esiste dal 2000, anno in cui il Consiglio Nazionale delle Ricerche (CNR) ha deciso di chiudere i suoi Organi. Da allora il GNGTS esiste nella misura in cui i ricercatori hanno creduto, e credono, che esista: si potrebbe dire che il GNGTS è la materializzazione del desiderio dei ricercatori di incontrarsi una volta all’anno e raccontarsi cosa hanno fatto e soprattutto cosa stanno sviluppando. Niente “messa cantata”, dunque, ma snella presentazione dei “lavori in corso”. Nelle intenzioni di chi coordina il GNGTS, per dar spazio soprattutto ai giovani di “presentarsi in società” e fare il “battesimo del fuoco”. Recentemente la partecipazione dei giovani sembra un po’ diminuita, probabilmente perché sempre meno giovani trovano posto negli atenei e negli istituti di ricerca e anche perché i fondi sono sempre più risicati e pure trasferite vicine gravano sui bilanci. Oppure, come qualcuno mi ha segnalato recentemente, perché il convegno si è spostato anche su temi di carattere normativo e applicativo coinvolgendo professionisti ed amministratori e perdendo, forse, un po’ della sua verginità scientifica.*

*Il GNGTS, dicevo, non esiste ufficialmente e, dopo esser sopravvissuto 15 anni in questa “terra di mezzo” è giunta l’ora di strutturarla. Per questo è in fase di realizzazione un accordo fra enti per garantire in futuro l’esistenza di questa realtà, finché se ne sentirà l’utilità.*

*L’ubicazione relativamente decentrata di Trieste e il ripetersi per la quinta volta del convegno in questa sede non dovrebbero favorire l’affluenza dei ricercatori, considerando anche i fondi sempre limitati destinati alla ricerca che condizionano da anni la partecipazione, specialmente dei più giovani. I presupposti per una buona riuscita del convegno, comunque, ci sono, visto l’alto numero di note ricevute per la presentazione e il numero di pre-iscritti che un mese prima del convegno sfiora le 200 unità.*

*La strutturazione del convegno su 3 temi, proposta negli ultimi anni, è stata mantenuta:*

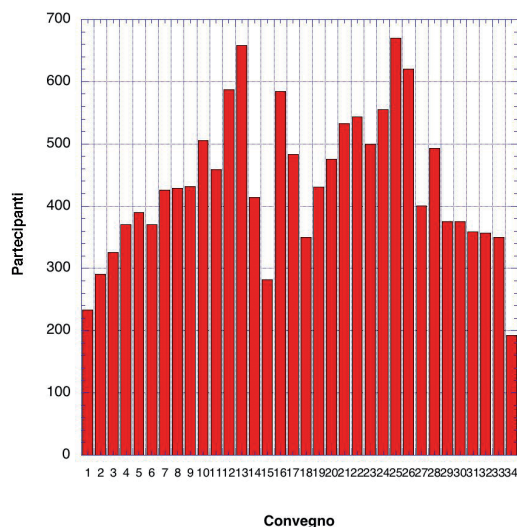


Fig. 1 – Numero di partecipanti ai convegni GNGTS. Il primo convegno si è tenuto nel 1981 e, in seguito, ha avuto cadenza annuale con l’eccezione del 1982. Il numero dei partecipanti all’ultimo convegno è aggiornato ad un mese prima dell’inizio del convegno stesso.

*ci sembra rispecchi le principali discipline geofisiche e risulta di semplice organizzazione. Pertanto anche quest’anno le presentazioni sono state suddivise nei tre temi generali: Geodinamica, Caratterizzazione Sismica del Territorio e Geofisica Applicata, che sintetizzano i grandi filoni lungo i quali si articola la ricerca geofisica italiana. Ogni tema, poi, si sviluppa in tre sessioni specifiche con apertura sia alla componente geologica che a quella ingegneristica. È doveroso segnalare l’interesse che l’argomento sismologico riveste da alcuni anni e che si manifesta in maniera decisa con l’elevato numero di relative presentazioni che spaziano dall’individuazione di faglie potenzialmente attive e lo studio di particolari terremoti alle stime di pericolosità sismica e di risposta locale per giungere alle ricadute in termini normativi atti a salvaguardare la sicurezza di persone e cose nel caso di terremoto.*

*Anche quest’anno è stata fatta la scelta di raccogliere note estese (ma non troppo) a*

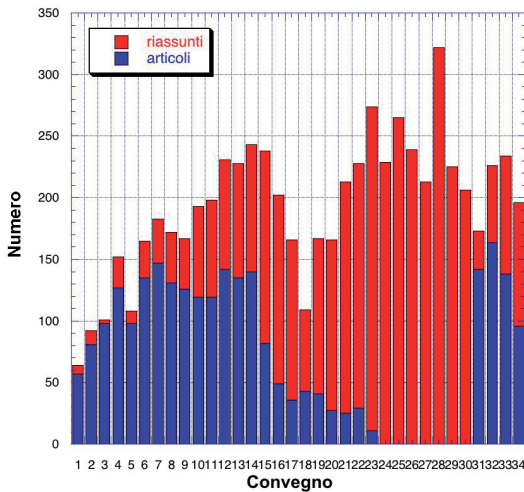


Fig. 2 – Numero di note presentate nei convegni NGGTS. Fino al 2004 è stato pubblicato il volume (dal 1997 sotto forma di CD-Rom) degli atti del convegno contenente in forma estesa le note presentate (barre rosse). In seguito, si è deciso di pubblicare soltanto il volume dei riassunti estesi (barre blu).

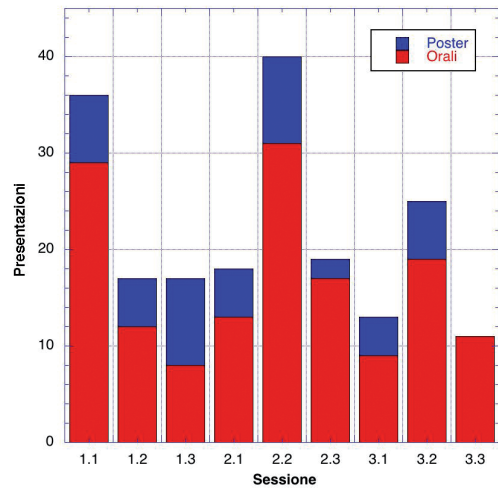


Fig. 3 – Numero di note presentate nelle varie sessioni del 34° convegno. Vengono indicate le comunicazioni orali con il colore rosso e quelle in forma di poster con il colore blu.

*formare gli atti del convegno. Ricordiamo che questa scelta è stata dettata dalla necessità di produrre un volume utilizzabile per la valutazione ufficiale dell'attività scientifica dei ricercatori e degli enti. Il presente volume raccoglie ben 96 note, delle 195 che verranno presentate al convegno. Si tratta di una percentuale (49%) decisamente più bassa di quella degli anni passati, che deve far riflettere. La produzione di atti di rilevanza scientifica ha determinato la necessità di avviare un processo di referaggio di tutti i testi. I convenor se ne sono fatti carico e, pertanto, risultano responsabili della qualità del materiale presentato. La notevole mole di materiale da stampare ha fatto confermare la scelta di suddividere gli atti in tre volumi, ciascuno dei quali raccoglie le note relative ad uno dei tre temi. Molte note (64) sono in lingua inglese: ciò permette una diffusione del presente volume anche all'estero. Delle 196 note in programma, ben 149 sono destinate alla presentazione orale.*

Anche quest'anno alcune sessioni del convegno NGGTS (quelle di Geofisica Applicata) sono state organizzate in collaborazione con la Sezione Italiana EAGE-SEG, che realizza così il suo 15° Convegno Nazionale.

Una segnalazione degna di nota va all'Associazione Geofisica Licio Cernobori, che ha scelto anche quest'anno il convegno NGGTS quale sede per l'attribuzione del premio in memoria di un caro collega ed amico prematuramente scomparso anni or sono.

Un ringraziamento particolare va ai convenor (Dario Albarello, Andrea Argnani, Francesca Bianco, Grazia Caielli, Giorgio Cassiani, Anna Del Ben, Daniela Di Bucci, Mauro Dolce, Elena Eva, Giovanni Florio, Paolo Galli, Luca Martelli, Paolo Mazzucchelli, Giuseppe Naso, Rinaldo Nicolich, Francesca Pacor, Riccardo Petrini e Luigi Sambuelli), che hanno proposto e organizzato le varie sessioni e hanno curato il referaggio dei testi, ed alla Segreteria Organizzativa (Anna Riggio, Alessandro Rebez, Paolo Giurco e Muzio Bobbio), che ha raccolto e preparato tutto il materiale qui stampato. Desideriamo ringraziare, infine e soprattutto, il Presidente dell'OGS, che ha accolto ancora una volta con entusiasmo e con generosità l'idea di finanziare il convegno NGGTS, nonostante le difficoltà economiche con cui tutti gli enti di ricerca devono scontrarsi, e Codevintec Italiana S.r.l. e Misure Meccaniche S.r.l., nostri sponsor di questo convegno.

Dario Slejko



*"...cerco qualcosa: un briciolo di conoscenza in questo nostro piccolo grande pianeta. E in me stesso..." L. C. 1989.*

## PREMIO DELL'ASSOCIAZIONE PER LA GEOFISICA "LICIO CERNOBORI" - 2015

L'Associazione per la Geofisica Licio Cernobori - AGLC, nata il 30 ottobre del 2000 per ricordare Licio Cernobori, geofisico prematuramente scomparso, ed il suo entusiasmo contagioso, ha come fine la promozione degli studi geofisici, e soprattutto la formazione scientifica e la crescita dei più giovani.

Tale fine è stato perseguito attraverso l'elargizione di un premio di studio presso l'Università di Trieste, aperto anche a laureandi/laureati in Geofisica Applicata di altre università o strutture scientifiche coinvolte in progetti comuni con l'Ateneo di Trieste. Si ricordano i vincitori degli anni passati Giulio Paoli (2001), Sara Cisilin (2002), Marica Calabrese (2003), Manfredi Scozzi (2004), Ivan Gladich (2006), Manuela Zuliani (2006), Andrejka Starec (2008), Sara Ferrante (2009).

Oltre all'attività didattica/divulgativa che i componenti dell'Associazione svolgono in diverse occasioni, sono stati finanziati negli anni diversi convegni, scuole, progetti, iniziative, in Italia e all'estero:

- Copie degli Atti del Convegno TRANSALP (Trieste, febbraio 2003) per le biblioteche universitarie;
- Agevolazioni per gli studenti al Congresso: STRUCTURES IN THE CONTINENTAL CRUST AND GEOTHERMAL RESOURCES (Siena, 24-27 September 2003);
- Sovvenzione di uno studente, Alberto Gaudio dell'università di Urbino, per la Scuola di Processing dati sismici marini (Trieste, ottobre 2004);
- Agevolazioni per studenti del terzo mondo alla partecipazione del Workshop IRIS-Orfeus "Understanding and managing information from seismological networks" (Palmanova (UD) 28 febbraio – 6 marzo 2005);
- Finanziamento di € 400 Euro ad Andrejka Starec (2006), allora studentessa, per garantirle un altro mese presso il TNO (Paesi Bassi) a conclusione della sua borsa e consentirle la conclusione della tesi sullo stoccaggio geologico della CO<sub>2</sub>, con la guida di Pascal Winthagen e del chiar.mo Prof. Rinaldo Nicolich dell'Università di Trieste.
- Finanziamento annuale di € 400 per la partecipazione di un insegnante ai seminari GIFT per gli insegnanti delle scuole elementari e secondarie nell'ambito del convegno dell'European Geosciences Union - Geophysical Information for Teachers (GIFT): Giovanni Banchelli (2007), Pier Paolo Caputo (2008), Giovanni Agliadoro (2009), Francesco Gobbo (2010), Giulia Realdon (2011), Eva Godini (2012), Maria Barbera (2013).

Nell'occasione del decennale (2010) si è istituito un premio per i giovani relatori al Congresso annuale GNGTS, ripetuto nel 2011. Nel 2010 il premio di 2000,00 € è andato alla dottoressa Marina Pastori, per il lavoro "*Crustal fracturing field and presence of fluid as revealed by seismic anisotropy: case-histories from seismogenic areas in the Apennines*", selezionato tra 40 lavori e 8 finalisti, nel 2011 al dott. Edoardo Peronace, per il lavoro "*Shallow geophysical imaging of the mt. Marzano fault zone; a kaleidoscopic view through ERT, GPR and HVSR analyses*", selezionato tra 38 lavori e 13 finalisti.

Dal 2012 il premio è stato suddiviso tre premi di 700,00 €, uno per ciascuno dei Temi del convegno: *Geodinamica, Caratterizzazione sismica del territorio e Geofisica applicata*. I vincitori sono stati: Lorenzo Bonini, per il lavoro: "*Comprendere la gerarchia delle faglie attive per migliorare la caratterizzazione sismica del territorio: l'esempio del terremoto di L'Aquila del 2009 (Mw 6.3)*", Rocco Ditommaso, per il lavoro "*Risposta sismica delle strutture: dalla non stazionarietà alla non linearità apparente*", Gianluca Fiandaca, per il lavoro "*Time domain induced polarization: 2D inversion for spectral information*", selezionati tra 31 lavori presentati.

Nel 2013 i vincitori sono stati: Giuseppe Pezzo, per il lavoro "*Fault activity measurements from InSAR space geodesy: the fundamental role of geological constraints for correct data interpretation and analytical fault modeling*", Giovanni Rinaldin, per il lavoro "*Effectiveness of the N2 Method for the seismic analysis of structures with different hysteretic behaviour*" e Daniele Sampietro, per il lavoro "*Il modello GEMMA: realizzazione, validazione e distribuzione*", selezionati su 28 candidati.

Nel 2014 i vincitori sono stati: Daniele Cheloni, per il lavoro "*Interseismic coupling along the southern front of the Eastern Alps and implications for seismic hazard assessment in N-E Italy*", Chiara Bedon, per il lavoro "*Structural monitoring and seismic analysis of a base-isolated bridge in Dogna*" e Jacopo Boaga per il lavoro "*L-shaped array refractions microtremors (LeMi)*", selezionati su 18 candidati.

Quest'anno i lavori presentati sono 11. Purtroppo si è registrato un generale calo nelle domande, in particolare per il tema 1 che per il tema 2, sulle cui cause ci stiamo interrogando ed invitiamo tutta la comunità scientifica a riflettere ed a suggerire possibili rimedi e strategie. I riassunti e le presentazioni preliminari sono attualmente all'esame delle tre commissioni, che stanno lavorando per scegliere i vincitori, che verranno annunciati e premiati nel corso dell'Assemblea del Convegno (18 novembre 2015).

Per altre informazioni, per diventare socio e contribuire a continuare e migliorare le iniziative dell'Associazione per la Geofisica Licio Cernobori –AGLC, scrivere a [cernobor@units.it](mailto:cernobor@units.it).

---

**Roberto Cassinis (31/10/1921-22/8/2015)**


---



Lo scorso agosto è mancato Roberto Cassinis, classe 1921, insigne scienziato della Geofisica italiana. La sua carriera è stata contrassegnata dalla partecipazione ad importanti progetti e decisioni che hanno trasformato la Geofisica, soprattutto quella di prospezione, attribuendole lustro anche a livello internazionale.

Roberto, professore di Geofisica Mineraria all'Università di Palermo (1964-1968), poi ordinario di Fisica Terrestre all'Università degli Studi di Milano (dal 1968 al pensionamento, nel 1997), è stato direttore dell'Istituto di Geofisica della Litosfera del C.N.R. e direttore della Scuola Internazionale di

Geofisica di Erice. Ha effettuato numerose campagne di prospezione geofisica finalizzate sia alla ricerca di giacimenti di idrocarburi, sia di giacimenti di minerali solidi. Ha anche svolto studi geofisici per accertare la fattibilità di grandi opere civili, fra cui il ponte sullo Stretto di Messina. È stato autore di numerose pubblicazioni scientifiche, libri e dispense su cui molti studenti e colleghi hanno avuto modo di imparare ed apprezzare le tecniche di studio dell'interno del nostro pianeta.

Anche dopo il pensionamento si è occupato, in maniera discreta come nel suo carattere, del tutorato di giovani laureandi o laureati che si avvicinavano al mondo del lavoro. Ha altresì continuato a collaborare alla stesura di pubblicazioni scientifiche con colleghi a cui raccontava dei "bei tempi" in cui i progetti erano degni di tale nome e di quante difficoltà vi fossero nel trattare ingenti quantità di dati con i limitati mezzi informatici dell'epoca. Uno dei suoi grandi rammarichi era proprio la convinzione che "se fosse nato dopo", come diceva lui, gli stessi dati avrebbero rappresentato una fonte inesauribile di informazioni grazie alla possibilità di acquisirli e sfruttarli in maniera adeguata. Per questo usava ogni mezzo a sua disposizione, dalla disponibilità a collaborare in progetti fino alla condivisione di testi ed informazioni personali, per conservare la memoria di quei *database* e divulgarli per consentire anche ad altri di poterne usufruire.

Sulla scorta di una carriera brillante, sarebbe dunque semplice descrivere lo scienziato Roberto Cassinis elencando i titoli, le conquiste di carriera e le responsabilità scientifiche per inquadrarne la capacità, l'importanza ed il ruolo di rilievo nel suo campo di studio. Ma chi lo ha conosciuto sa anche che era un uomo molto aperto, affatto presuntuoso, sempre disponibile alla discussione, un fine osservatore della società in generale e non solo di quella scientifica, un grande appassionato della Scienza, una persona sempre alla ricerca di risposte nello stile proprio di un vero ricercatore. Ed è così che lo vogliamo ricordare, quando a più di ottanta anni, ancora lucidissimo, apriva con cura il suo computer e snocciolava dati e teorie chiedendo scusa di averci dovuto meditare un po' su, giustificando con l'età avanzata l'onestà intellettuale di chi vuole capire prima di esporre una idea; accettando critiche e commenti come chi sa che la Scienza è confronto; insomma come uno della "vecchia scuola", quella in cui le persone contavano più delle cariche o delle pubblicazioni.

**Claudio Eva e Stefano Solarino**

---

**Fabio Meloni (18/11/1957-29/8/2015)**

---



Quest'estate, sul mare d'agosto, ancora più tragica e inaspettata ci ha raggiunto la notizia che Fabio se n'era andato. Inaspettata perché chi a conoscenza della sua malattia ne era stato da lui stesso rassicurato sugli sviluppi e sulle prospettive.

Fabio era nato a Sant'Angelo Romano nel 1957, laureandosi alla Sapienza di Roma nel 1983 con uno "Studio di macrosismica e sismotettonica nell'alto Lazio e nell'Abruzzo settentrionale". E gli studi sulla sismicità storica sono sempre rimasti il suo maggiore interesse scientifico e una passione che ha perseguito anche quando, entrato in Regione Lazio, di tutt'altre incombenze ha dovuto occuparsi.

I suoi primi lavori su questo argomento datano dalla metà degli anni Ottanta fino a tutti gli anni Novanta quando, con l'ENEA e l'ISMES prima e col CNR-GNDT poi, ha compiuto numerose ricerche sulla sismicità storica non solo del Lazio, ma di numerose parti d'Italia, ivi comprese quelle sugli indizi delle liquefazioni avvenute in occasione dei terremoti storici, producendo decine e decine di rapporti tecnici. Già a partire dal 1985 Fabio ha presentato in anteprima le sue ricerche proprio qui, al NGGTS, che lo ha visto partecipare per oltre 25 anni, sino al Convegno del 2011.

Dopo essere stato responsabile della segreteria tecnica del GNDT fino a tutto il 1998, Fabio transitò in Regione Lazio, nell'ex Ufficio Geologico, dove i colleghi lo ricordano per la sua impostazione rigorosamente scientifica anche nei confronti del disbrigo delle pratiche di carattere più amministrativo o burocratico.

Di fatto, Fabio ha sempre nutrito una forte curiosità scientifica verso tutte le materie relative alle Scienze della Terra, appassionandosi negli ultimi anni anche al fenomeno dei sinkhole nel Lazio che lo ha visto estensore di un catalogo regionale unificato degli stessi. Il medesimo rigore e approfondimento lo metteva in tutti i lavori in cui si cimentava, anche quelli relativi alla libera professione che aveva praticato nella sua zona di residenza agli inizi della sua carriera. Da questo punto di vista viveva con entusiasmo il suo lavoro, affrontando con tenacia, con grande capacità di analisi, ma anche con una proverbiale serenità e sicurezza tutti gli imprevisti e le novità che gli si prospettavano, contagiando e rassicurando chi gli stava accanto. I colleghi della Regione Lazio lo ricordano immerso nelle sue carte fino a tardi, quando le guardie giurate lo invitavano a tornarsene a casa. Ricordiamo Fabio per la sua innata disponibilità e correttezza verso tutti noi, per la sua flemma, la calma con la quale non riusciva a mandarci in bestia nemmeno quando invece di concludere, rimetteva in discussione tutto il lavoro fatto fino a quel momento.

**Paolo Galli e Antonio Rossi**

# Indice

<b>Lectio Magistralis</b> .....	XI
IL TERREMOTO DEL FRIULI: CONSIDERAZIONI SU UN EVENTO SINGOLARE	
M. Ruscetti .....	XIII
<b>Tema 3 - Geofisica applicata</b> .....	1
<b>sessione 3.1 - Geofisica applicata profonda</b> .....	3
UNA SEZIONE SISMICA REGIONALE SUL MARGINE CONTINENTALE DELLA CAMPANIA (GOLFO DI NAPOLI-GOLFO DI SALERNO)	
G. Aiello .....	5
SEISMIC RESERVOIR CHARACTERIZATION IN OFFSHORE NILE DELTA. PART I: COMPARING DIFFERENT METHODS TO DERIVE A RELIABLE ROCK-PHYSICS MODEL	
M. Aleari, F. Ciabbari, F. Peruzzo, A. Mazzotti .....	11
SEISMIC RESERVOIR CHARACTERIZATION IN OFFSHORE NILE DELTA. PART II: PROBABILISTIC PETROPHYSICAL-SEISMIC INVERSION	
M. Aleari, F. Ciabbari, B. Garcea, A. Mazzotti .....	20
IGNEOUS BODIES CHARACTERIZATION BY MEANS OF SEISMIC REFLECTION ATTRIBUTES AND WAVELET TRANSFORM	
E. Gianturco, A. Tognarelli, S. Rocchi, L. Pandolfi .....	28
SEISMIC ANALYSIS OF A BSR IN THE DOVE BASIN (SOUTH SCOTIA SEA)	
A. Mocnik, D. Civile, A. Del Ben, R. Geletti .....	33
<b>sessione 3.2 - Geofisica applicata superficiale</b> .....	41
STUDY OF A RECONSTRUCTED RIVER EMBANKMENT THROUGH A COMBINATION OF NON-INVASIVE GEOPHYSICAL METHODOLOGIES	
L. Busato, J. Boaga, L. Peruzzo, G. Asta, S. Cola, P. Simonini, G. Cassiani .....	43
CONTRIBUTION OF THE CLUSTER ANALYSIS OF HVSR DATA FOR NEAR SURFACE GEOLOGICAL RECONSTRUCTION	
P. Capizzi, R. Martorana, A. D'Alessandro, D. Luzio .....	50
SEISMIC MEASUREMENTS IN UNSTABLE SEA CLIFF AREAS	
R. Iannucci, S. D'Amico, D. Farrugia, P. Galea, S. Martino, A. Paciello .....	56
MARINE GEOPHYSICAL AND GEOLOGICAL INVESTIGATIONS IN SUPPORT TO THE CONSTRUCTION OF NEW HARBOUR INFRASTRUCTURES: THE TRIESTE MARINE TERMINAL EXTENSION	
C.A. Masoli, L. Petronio, E. Gordini, M. Deponte, D. Cotterle, R. Romeo, G. Böhm, A. Barbagallo, R. Belletti, S. Maffione, F. Meneghini .....	63
GEOPHYSICAL INVESTIGATIONS IN A DISMISSED INDUSTRIAL SITE: EX-ESSO (TRIESTE, ITALY)	
R. Romeo, L. Petronio, A. Affatato, A. Barbagallo, R. Belletti, G. Boehm, J. Boaga, G. Cassiani, P. Paganini, M.T. Perri, D. Sorigo, M. Rossi .....	70
A 5-KM LONG WATERBORNE CVES SURVEY ON THE PO RIVER IN THE TOWN OF TURIN: PRELIMINARY RESULTS	
L. Sambuelli, C. Comina, A. Fiorucci, P. Dabove, I. Pascal, C. Colombero .....	76

DIRECT INTERPRETATION OF SURFACE WAVES FOR 2-D AND 3-D SUBSURFACE IMAGING  
 S. Bignardi, N. Abu Zeid, G. Santarato ..... 82

INTEGRATED GEOPHYSICAL PROSPECTING IN THE ARCHAEOLOGICAL SITE OF BADIA  
 M.T. Giannotta, G. Leucci, L. De Giorgi, R. Persico, M. Leo Imperiale, G. Muci ..... 88

RILIEVI GEOFISICI IN SITI DI INTERESSE ARCHEOLOGICO IN AGRO DI BAUCINA (PA)  
 G. Leucci, A. Cubito, L. De Giorgi, S. Pappalardo, T. Giaccone, C. Greco ..... 93

INFLUENCE OF DIFFERENT ARRAY DATASETS ON RELIABILITY OF ELECTRICAL RESISTIVITY TOMOGRAPHY  
 R. Martorana, P. Capizzi, A. D’Alessandro, D. Luzio ..... 98

GROUND PENETRATING RADAR APPLICATIONS FOR ROADS AND AIRPORT PAVEMENTS INVESTIGATIONS  
 A. Mocnik, M. Dossi, E. Forte, R. Zambrini, A. Zamariolo, M. Pipan ..... 106

NON-INVASIVE PROSPECTING IN THE OLD TOWN CENTRE OF MESAGNE (BRINDISI, SOUTHERN ITALY)  
 G. Leucci, L. De Giorgi, L. Matera, R. Persico ..... 112

**sessione 3.3 - Modelling e aspetti teorici ..... 119**

SINGLE-PASS SURFACE RELATED 3D MULTIPLE ESTIMATION FOR OBS DATA  
 WITH DATA DRIVEN + BATHYMETRY APPROACH  
 M. Codazzi, P. Mazzucchelli ..... 121

AUTOMATIC  $V_{RMS}$  BUILDER  
 S. Costagliola, P. Mazzucchelli ..... 126

LESS IS MORE: FROM VAN DER ROHE TO THE 4-CHANNEL SYSTEM  
 FOR THE EFFICIENT AND HOLISTIC ACQUISITION OF SURFACE WAVES: AN URBAN CASE STUDY  
 G. Dal Moro, S.R. Moustafa, N. Al-Arifi ..... 134

APPLICATION OF ATTRIBUTE-BASED AUTOMATED PICKING TO GPR AND SEISMIC SURVEYS  
 M. Dossi, E. Forte, M. Pipan ..... 141

3D MAGNETOTELLURIC RESPONSE IN PRESENCE OF RESISTIVITY DISPERSION:  
 SNAKE RIVER PLAIN (IDAHO) EXAMPLE  
 R. Esposito, A. Troiano, M.G. Di Giuseppe, D. Patella, C. Troise, G. De Natale, R.M. Castelo Branco ..... 147

OPTIMAL PARAMETERS FOR FINITE DIFFERENCE MODELING OF 2D SEISMIC WAVE EQUATION  
 B. Galuzzi, E. Stucchi, E. Zampieri ..... 153

APPLICATION OF THE RECONFIGURABILITY OF THE INTEGRATION TIME  
 IN STEPPED FREQUENCY GPR SYSTEMS: FIRST EXAMPLES IN THE FIELD  
 R. Persico, D. Dei, F. Parrini, L. Matera, S. D’Amico, A. Micallef, P. Galea ..... 159

A NEW INVERSION METHOD OF VERTICAL GRAVITY AND MAGNETIC SOUNDINGS  
 A. Vitale, D. Di Massa, M. Fedi, G. Florio ..... 166

GN/GTS 2015



# Lectio Magistralis



## IL TERREMOTO DEL FRIULI: CONSIDERAZIONI SU UN EVENTO SINGOLARE

M. Riuscetti

Nei quasi 40 anni che sono passati dal 6 maggio 1976 sono molti gli eventi celebrativi che si sono succeduti in varie sedi istituzionali e scientifiche. Sono stati fondati musei, allestite mostre, pubblicati libri, organizzati congressi e scritti numerosi articoli.

Inevitabilmente la funzione commemorativa ha assunto peso sempre più prevalente rispetto alla funzione di contributo alla conoscenza che, invece, è fondamentale per insegnare a diminuire l'impatto sociale ed economico che avranno i futuri terremoti.

A ciò si aggiunga che anche le criticità e gli errori che pur ci furono sono stati sottaciuti perché non venisse offuscato l'esito complessivamente positivo della ricostruzione.

La singolarità che cercherò, sia pur brevemente, di delineare risiede nel fatto che il terremoto del Friuli si inserisce, ed in parte provoca, con il successivo terremoto dell'Irpinia-Basilicata di cui ricorre tra pochi giorni il trentaseiesimo anniversario, in un clima di notevoli cambiamenti e progressi sia scientifici che legislativi ed organizzativi come mai era accaduto in precedenza, salvo poi costringerci a constatare la loro labilità ed il lento ed apparente ritorno a condizioni che molto ricordano sotto vari aspetti le condizioni precedenti.

Ricordare i quasi 1.000 morti e la distruzione totale o parziale di 86.000 edifici, fabbriche, chiese è doveroso così come è comprensibile l'enfasi sui risultati della ricostruzione che, unica nella storia della Repubblica, può essere accostata a quella del secondo dopoguerra (anche se, a mio parere, la meravigliosa ricostruzione della Sicilia orientale dopo il terremoto del 1693 è qualcosa di insuperato e forse insuperabile). Ciò avverrà anche nell'anno che sta per iniziare con numerose iniziative già annunciate ed altre che sicuramente seguiranno. In questa sede è più appropriato ed utile dare enfasi alla funzione conoscitiva di cui dicevo poc' anzi.

Cerchiamo allora di collocare il terremoto del 1976 con particolare riguardo agli aspetti sismologici *lato sensu*.

Va innanzitutto rilevato che l'evento, come tutti gli altri che lo precedettero nel secolo scorso, avvenne in una zona "non sismica". La prassi normativa vigente dal 1909 (anno della prima legge in materia) si limitava a prescrivere l'osservanza della regolamentazione alle "aree colpite da terremoto" di fatto dopo il 1909. Tale prassi continuò per decenni (fino al 1962), nonostante le norme venissero spesso riviste, migliorate ed adeguate al progredire delle conoscenze e delle tecniche costruttive (come, ad esempio, il cemento armato).

Ciò consentì che si continuasse ad ignorare il pericolo sismico per circa 70 anni in regioni come la Sicilia orientale, colpita nel 1693 da quello che forse può essere considerato il più forte terremoto nella storia dell'Europa continentale. Anche se le conseguenze possono sembrare poco rilevanti data che la normativa sismica, in un Paese intensamente antropizzato da secoli, si sarebbe dovuta applicare solamente alle nuove costruzioni, si pensi invece alla gran mole di costruito e ricostruito dopo la seconda guerra mondiale. Venne sprecata dunque una grande (e speriamo irripetibile) occasione di mettere in sicurezza una gran parte, soprattutto, delle maggiori città italiane.

Le Scienze della Terra, per quanto riguarda gli aspetti sismologici, erano agli inizi degli anni '70 in uno stato di notevole arretratezza. La Sismologia, ad esempio, veniva insegnata in pochissime università. La quasi totalità dei geologi si rifacevano alle poche informazioni fornite come parte dei corsi di Fisica Terrestre e, dove esistevano, di quelli di Geofisica Applicata. Non dimentichiamo che la maggior parte delle cattedre di Geologia erano occupate da laureati in Scienze Naturali, Chimica e financo Farmacia.

Si accettava, senza che ne venisse grande scandalo, che il titolare di una cattedra geofisica di Palermo dichiarasse che il terremoto del Bélice (1968) fosse dovuto alla grande quantità di magnetite, contenuta nelle rocce profonde della Sicilia occidentale, il cui campo magnetico era stato perturbato dall'intensa attività solare di quel gennaio. Per inciso egli era lo stesso autore di un testo, adottato per il suo corso, in cui tra le rocce ad alta suscettività magnetica erano

segnalate le ghiaie magnetiche (sic!) che altro non erano che la pirrotite che in tedesco si chiama Magnetkies, parola composta, appunto da Magnet e Kies (ghiaia).

Il grosso della dotazione strumentale dell'Istituto Nazionale di Geofisica (la Vulcanologia sarà aggiunta in seguito) era costituito da 14 Wiechert con orologi a pendolo su cui era basata la rete nazionale integrata in maniera non organica da osservatori di varia natura e gestione spesso affidata alla buona volontà di religiosi secondo una tradizione ottocentesca. Erano presenti reti sismiche locali moderne a Napoli e Genova e stazioni sismiche di buona qualità a Trieste, L'Aquila, Messina. Alcune erano dedicate alla vulcanologia (Napoli), altre facevano parte della rete americana per il controllo delle esplosioni nucleari sotterranee dell'Unione Sovietica (Trieste e L'Aquila).

Lo stato generale del sistema risultava evidente nella "guerra degli epicentri" (la definizione è di Massimiliano Stucchi) che si scatenava dopo ogni terremoto forte abbastanza da essere registrato in più punti del territorio nazionale. Ricordo, per inciso, che tra gli epicentri proposti nella notte del 6-7 maggio 1976 per la scossa delle 21:00 era anche il Golfo di Genova!

Nella prima metà degli anni '70, però, qualcosa aveva iniziato a perturbare l'immobilità del sistema che governava le Scienze della Terra: in sede internazionale era stato lanciato il Progetto Internazionale Geodinamica come conseguenza della nascita della rivoluzionaria teoria della Tettonica a zolle. Ad esso aveva aderito l'Italia in cui il C.N.R. aveva deciso di riorganizzare la ricerca pubblica con lo strumento dei progetti finalizzati. Il progetto finalizzato venne così definito: *"Il Progetto Finalizzato è un insieme coordinato di attività di ricerca, sviluppo e dimostrazione di prototipi relativi a prodotti, processi e servizi, di durata definita, volto all'acquisizione di conoscenze e innovazioni, trasferibili al sistema produttivo, al tessuto economico sociale e al contesto politico-giuridico del Paese, relative a tematiche considerate prioritarie nel quadro della programmazione economica nazionale"*. La risposta che tentò di dare il sistema fu quella di mascherare ciò che si era sempre fatto ignorando di fatto gli scopi dei progetti finalizzati. Venne varato un ponderoso piano di ricerche organizzate su grandi sezioni crostali (le geotraverse). Tutto venne spazzato via in una tempestosa assemblea a Roma, al C.N.R., dove molti ricercatori dopo veementi critiche (che a dire al vero trovarono deboli risposta nei baroni increduli di fronte a tanta mancanza di rispetto) chiesero ed ottennero di riscrivere il progetto finalizzandolo alla costruzione di un quadro organizzativo e di conoscenze volta alla riduzione dei rischi sismico e vulcanico.

Lascio alla penna di Paolo Rumiz (La Repubblica, 1999) la descrizione di ciò che fu il Progetto Finalizzato Geodinamica: *"Non c'è scienziato che non parli con nostalgia di quegli anni. Si mobilitano risorse, scendono in campo geologi, ingegneri, storici. Cadono steccati, baronie. L'interazione di cervelli dà frutto, il patrimonio edilizio del Paese comincia a essere monitorato. La protezione civile si mette agli ordini della scienza. L'Italia diventa avanguardia, compie un balzo di venti' anni"*.

Forse c'è un po' di sopravvalutazione ma certamente fu chiaramente indicata la volontà di rendere immediata la ricaduta sociale della ricerca tradizionalmente perseguita attraverso l'istituto delle consulenze professionali mediante i quali lo Stato centrale e le sue ramificazioni territoriali compravano i risultati di ricerche da essi in precedenza finanziate; ciò in nome di una capziosa difesa del diritto alla proprietà intellettuale.

Tra i fatti di sistema grandemente positivo fu, a mio avviso, l'approccio multidisciplinare ed in particolare quello tra le discipline praticate dai "geocosi" (come Giuseppe Grandori scherzosamente definiva gli scienziati della Terra) e gli ingegneri.

Si partiva da una situazione (in un *excursus* breve come questo alcune semplificazioni sono inevitabili) in cui ad esempio le indagini macrosismiche venivano generalmente effettuate da geologi che difficilmente erano in possesso del necessario sapere in materia di Scienza e Tecnica delle costruzioni (e d'altra parte, quando gli autori erano gli ingegneri, i danni erano considerati come variabile indipendente dalle condizioni geo-morfologiche dei siti) e per l'Ingegneria (non solo in Italia) il terremoto era compiutamente rappresentato, a fini pratici,

da un'accelerazione orizzontale di picco e relativa frequenza: fisica della sorgente e differenze tra *near-* e *far-field* erano bellamente ignorate. Se le azioni rilevate sembrano incompatibili con questo semplicistico modello, la reazione era (e purtroppo lo è ancora) quella di proporre l'aumento dei valori di accelerazioni orizzontali di progetto. Si vuole ignorare che nelle aree epicentrali le accelerazioni verticali possono superare ampiamente il valore di  $g$  come è noto a chiunque abbia letto trattati, anche antichi, di sismologia elementare.

Si cercò, inoltre, di gestire il progetto nel modo più democratico possibile in un mondo ad esso tradizionalmente e pervicacemente impervio (esemplare, a questo proposito il nome del primo presidente del C.N.R.: il Maresciallo d'Italia Pietro Badoglio). Continui e continuamente stimolati erano i confronti ed i congressi anche in corso d'opera nei quali si discutevano i risultati, si decidevano, quando necessario le correzioni di rotta anche al di là di quanto previsto nei progetti iniziali riducendo al minimo le riunioni monodisciplinari al fine di ottenere un'effettiva integrazione a partire anche dallo stesso linguaggio, si decidevano gli indirizzi delle attività future.

I risultati diretti ed indiretti, con un'attenta ottimizzazione delle poche risorse disponibili, furono importanti sia a livello scientifico che organizzativo ed esattamente nello spirito e nella lettera di quanto previsto nella definizione di Progetto Finalizzato più sopra ricordata.

Tra i primi sono la definizione su tutto il territorio nazionale della pericolosità sismica (una mappa del genere in California veniva definita mappa di rischio!) con grande attenzione al rapporto costi/benefici ed integrando i dati del catalogo sismico, rapidamente redatto, con le informazioni di carattere sismotettonico e neotettonico provenienti dai relativi sottoprogetti; il miglioramento della normativa tecnica; la costruzione di strumenti di comunicazione moderni per la diffusione delle conoscenze ritenute elemento fondamentale per un'efficace politica di difesa dai terremoti.

Tra i secondi: l'importante e riconosciuto contributo alla definitiva approvazione della legge in materia di protezione civile che ha un impianto originale rispetto a quelle di altre legislazioni europee dando ampio spazio alle azioni di prevenzione oltre a quelle di gestione delle emergenze; la gemmazione dei gruppi nazionali per la difesa dai terremoti e per il rischio vulcanico; l'impulso alla creazione di una rete sismica nazionale supportata da un Istituto Nazionale di Geofisica e Vulcanologia adeguatamente finanziato e dotato di personale; l'istituzione della Commissione Grandi Rischi a supporto scientifico dell'organizzazione civile di cui fa parte integrante, intesa, almeno inizialmente, come interfaccia con la comunità scientifica di ricerca attiva nei settori relativi ai grandi rischi.

Un importante riconoscimento della qualità del lavoro svolto ci fu all'assemblea generale dell'IUGG di Canberra, dove la relazione italiana venne a lungo applaudita e, fatto inusuale, fu riconosciuta con comunicazione scritta dalla presidenza dell'associazione.

Affermare che allora si misero le basi per un duraturo consolidamento di metodi, filosofia e strutture sarebbe eccessivo. La catastrofe de L'Aquila credo abbia minato le convinzioni anche dei più ottimisti ma di essa non voglio parlare se non per rilevare il singolare destino di una città sede dei due più importanti processi imperniati sui rapporti tra scienza e società (terremoto e Vajont) e sulla natura ed utilità della previsione.

Oggi si è tornati improvvidamente alla vecchia separatezza disciplinare, la normativa è, a mio avviso, eccessivamente severa ma i provvedimenti importanti per migliorare la sicurezza della gran parte del patrimonio edilizio pubblico e privato mancano o sono timidi, saltuari e male indirizzati; la ricerca risente della crisi finanziaria delle università e della drastica e per alcuni versi stolta riduzione del rimpiazzo del personale in quiescenza o emigrato, l'autolesionista prevalenza del finanziamento della ricerca applicata (si badi bene: applicata, non finalizzata) che riduce le possibilità di avere autentica innovazione a favore di quella tecnologica che può essere utile sul breve termine soprattutto per i committenti che sono sollevati da oneri che sarebbero loro ma che nel tempo produrrà una difficilmente recuperabile capacità di tenere il passo con Paesi maggiormente consapevoli dell'importanza strategica di ricerca e formazione

di alto livello, i servizi tecnici statali continuano ad essere nello stato denunciato quasi 40 anni fa nella nota relazione Barberi-Grandori al Senato (Barberi e Grandori, 1980), le Regioni tra le strette finanziarie e le molte ed irrisolte questioni concernenti i poteri trasferiti, concorrenti, negati non sono in grado di risolvere problemi accumulati in decenni.

Infine un rapido cenno alla regione nel cui territorio ci troviamo. Nel 1976 era ancora vivo il ricordo della catastrofe del Vajont (1963) che l'aveva colpita sia pur marginalmente. Era inoltre ben presente alla classe dirigente ciò che stava avvenendo nel Bélice. Per questi motivi si richiesero allo Stato provvedimenti inediti che, insieme con la grande solidarietà nazionale ed internazionale che garantì un continuo e largamente sufficiente flusso di finanziamenti, portarono a completare la ricostruzione in un decennio. Fatto mai avvenuto prima e mai ripetuto dopo esclusa, forse, la ricostruzione dopo la seconda guerra mondiale. Va detto che uno dei fattori decisivi del successo fu la possibilità di dotarsi rapidamente di leggi *ad hoc* derivante dal regime speciale della Regione Friuli Venezia Giulia (Ruscetti, 1996).

La legge regionale sulla Protezione Civile del 1986 fu largamente ispirata dal Progetto Finalizzato Geodinamica che in Friuli ebbe il suo battesimo del fuoco e ad essa si rifà anche la successiva legge nazionale finalmente uscita dalle pluriennali secche parlamentari. Essa ancor oggi dimostra la sua validità anche se alcuni aspetti innovativi e fondamentali sono stati progressivamente trascurati.

Proprio in virtù della legge del 1986 la Direzione Regionale della Protezione Civile si assunse il compito di sostenere finanziariamente, senza incertezze, il progetto di ricerca degli enti regionali consorziati (Università ed O.G.S.) per la realizzazione della Mappa Regionale del Rischio Sismico. Successivamente diede il contributo per la realizzazione del progetto ASSESS, sempre della stessa compagine, per determinare in maniera speditiva il quadro della vulnerabilità degli edifici scolastici richiesto dal Governo in conseguenza del disastro di San Giuliano.

Per tre anni, inoltre, contribuì alla realizzazione di un ciclo di aggiornamento professionale in tema di *Seismic Risk Management* ben noto a molti dei partecipanti al congresso che vi hanno insegnato. Ad esso hanno partecipato appartenenti agli ordini professionali degli ingegneri e dei geologi nonché tecnici della Regione

Queste ricerche e quelle da esse direttamente derivate per i provvedimenti di emergenza diventati patrimonio del Corpo Nazionale dei Vigili del Fuoco e per la ricognizione dei danni hanno avuto larga eco in ambito UNESCO che li ha proposti per l'utilizzo in molti Stati (Nepal, Laos, Indonesia).

Va detto che esse non hanno avuto altrettanto riconoscimento nella nostra regione dove l'apprezzabile sostegno alla ricerca che per molti anni era continuato pur nel frequente succedersi degli assessori alla Protezione Civile si è malamente interrotto con la sostituzione del vertice tecnico della Direzione Regionale.

Evidentemente, ancora una volta, con il passare del tempo l'attenzione ai problemi delle catastrofi si attenua e si azzera. Eppure la Mappa del Rischio Sismico, che giace nei cassetti degli uffici regionali, dice prima o poi ci ritroveremo ad affrontare un'emergenza simile a quella del 1976 in qualche altra parte della regione e dovremo piangere per non aver approfittato del trascorso periodo di calma per migliorare le difese e diminuire gli impatti negativi su uomini e cose.

Chi ha avuto ed ha il potere di intervenire avrà magari la possibilità di trarre vanto dal successo della prossima ricostruzione invece di essere chiamato a rispondere per non aver operato come doveva e poteva per evitare la catastrofe. Forse è questo l'insegnamento più amaro che ci lascia la storia dei 40 anni.

## Bibliografia

Barberi F. e Grandori G.; 1980: *Difendersi dai terremoti – La lezione dell'Irpinia*. CNR – Progetto Finalizzato Geodinamica, Roma.

Ruscetti M.; 1996: *Il terremoto del Friuli: scenario di una ricostruzione improbabile in Italia*. In: Bonfanti P. (a cura di), Friuli 1976-1996. Contributo sul modello di ricostruzione, Forum, Udine, pp. 49-60.

Rumiz P.; 2009: *I miracoli di S. Emidio*. La Repubblica del 26/8/2009, Roma.

GNCTS 2015



## Tema 3

### Geofisica Applicata



## **sessione 3.1**

### **Geofisica applicata profonda**

**Convenor: G. Caielli e R. Nicolich**

**co-organizzata con Sezione Italiana Eage-Seg**

---



## UNA SEZIONE SISMICA REGIONALE SUL MARGINE CONTINENTALE DELLA CAMPANIA (GOLFO DI NAPOLI-GOLFO DI SALERNO)

G. Aiello

Istituto per l'Ambiente Marino Costiero (IAMC), Consiglio Nazionale delle Ricerche (CNR), Sede di Napoli, Italia

**Introduzione.** E' presentata una sezione sismica regionale sul margine continentale della Campania. I nuovi dati sulla struttura geologica del Golfo di Napoli sono proposti utilizzando una sezione composta da più linee sismiche acquisite lungo l'allineamento Ischia-Capri-Volturno (Aiello *et al.*, 2011). Le principali morfo-strutture riconosciute su scala regionale in base ai dati sismo-stratigrafici profondi precedentemente analizzati sono: il *Banco di Fuori*, un alto morfo-strutturale composto da carbonati meso-cenozoici geneticamente correlabili alla "Piattaforma Campano-Lucana" Auct. (D'Argenio *et al.*, 1973); il *Canyon Dohrn*, che separa il settore orientale del Golfo di Napoli, dove affiorano sequenze sismiche sedimentarie, da quello occidentale, dove prevalgono unità sismiche vulcaniche (Fusi *et al.*, 1991; Mirabile *et al.*, 2000; Milia, 2000; Aiello *et al.*, 2005; Di Fiore *et al.*, 2011); l'*alto strutturale di Capri*, un alto sedimentario collegato al sollevamento tettonico regionale dei carbonati meso-cenozoici lungo l'allineamento strutturale Isola di Capri-Penisola Sorrentina (Barattolo e Pugliese, 1987); il *Canyon Magnaghi*, che erode una spessa unità sismica di natura vulcanica localizzata a sud dell'Isola di Procida (Chiocci *et al.*, 1998; Aiello *et al.*, 2010; ISPRA, 2011; Aiello and Marsella, 2015); il *Bacino di Capri*, un bacino profondo localizzato a sud del Golfo di Napoli, caratterizzato da una coltre sedimentaria di età pleistocenico-olocenica, che ricopre un basamento acustico meso-cenozoico di natura carbonatica; il *Bacino di Salerno*, un semi-graben riempito da tre unità sismiche rappresentate da depositi marini quaternari (Aiello *et al.*, 2009) che ricoprono un'unità sismica caotica geneticamente collegata al "Flysch del Cilento" Auct. (Bonardi *et al.*, 1992; Aiello and Marsella, 2013); il *Bacino del Volturno*, riempito da quattro sequenze sismiche deposte in ambiente marino, costiero e deltizio, caratterizzate da frequenti intercalazioni di livelli vulcanoclastici (Aiello *et al.*, 2011), che ricoprono unità sismiche più profonde, geneticamente correlabili con i flysch miocenici dell'Appennino centrale ("Flysch di Frosinone" Auct.; Aiello *et al.*, 2000) e con i carbonati meso-cenozoici delle unità tettoniche affioranti nell'area in studio (Bigi *et al.*, 1992).

Il profilo sismico presentato, denominato Sister 9\_1, attraversa l'offshore dell'Isola di Capri, l'alto morfo-strutturale del Banco di Fuori, il canyon Dohrn ed il Bacino di Salerno da nord-ovest verso sud-est. Mentre i tre primi lineamenti geologici appartengono al dominio morfologico e sedimentario del Golfo di Napoli, l'ultimo dominio morfologico e geologico appartiene al Golfo di Salerno, di cui rappresenta il collettore sedimentario principale.

Mentre una grande quantità di rilievi sismici strettamente spaziali sulla piattaforma continentale del Golfo di Napoli è stata acquisita ed illustrata in studi precedenti di carattere geofisico e geologico sui Golfi di Napoli e Salerno, questi nuovi dati sismici forniscono un quadro geologico sui principali bacini sedimentari e gli alti morfo-strutturali tra questi interposti ad una scala dell'intera piattaforma esterna, scarpata e piana batiale sud-tirrenica. Alcuni lineamenti morfo-strutturali identificati non erano stati descritti in dettaglio da studi precedenti. Tra questi si annoverano l'alto vulcanico dell'Isola di Ischia, l'alto sedimentario dell'Isola di Capri ed i Bacini di Capri e di Salerno, la cui stratigrafia sismica ed assetto morfo-strutturale sono relativamente poco noti. Lo studio in oggetto è stato facilitato dall'uso di criteri di correlazione terra-mare, che hanno consentito una migliore comprensione geologica delle strutture sismiche studiate.

Il Mar Tirreno rappresenta un'area estensionale localizzata in un contesto geodinamico di collisione tra le zolle continentali europea ed africana. La distensione è iniziata circa 10 milioni di anni fa, portando alla formazione di crosta oceanica durante il Pliocene (Patacca e Scandone, 1989). Tre margini continentali, cioè il margine sardo, il margine nord-siciliano ed il margine dell'Italia meridionale delimitano la piana batiale sud-tirrenica. L'area

è caratterizzata da sismicità e vulcanismo attivo ed ha subito forti movimenti orizzontali e verticali. Una zona di Benioff ristretta e profonda, che si estende dallo Ionio al Tirreno meridionale, corrisponde a un piano di subduzione della litosfera del Mediterraneo orientale (Sartori, 2003) che migra verso est. A partire dall'Oligocene e fino a tempi recenti, i processi di subduzione hanno generato i bacini di retro-arco tirrenici, come pure il cuneo di accrezione dell'**Appennino meridionale**.

La distensione nel Mar Tirreno è iniziata nel Miocene superiore e ha controllato i processi di formazione di crosta oceanica in corrispondenza dei Bacini del Vavilov e del Marsili durante il Plio-Quaternario (Kastens *et al.*, 1988). La comparsa tardiva del vulcanismo di arco rispetto alla durata dei processi estensionali nel sistema tirrenico-ionico è stata spiegata come una conseguenza degli stadi iniziali della litosfera continentale assottigliata (Ritsema, 1979; Malinverno and Ryan, 1986; Sartori, 2003). **L'età e l'andamento dei processi estensionali sono stati riassunti da studi precedenti (Sartori and Capozzi, 1998).** Un episodio di distensione retro-arco di età compresa tra il Tortoniano ed il Pliocene, in corrispondenza della formazione del margine sardo e del Bacino del Vavilov, ha indicato una migrazione dell'arco da ovest verso est. Un episodio pleistocenico, in corrispondenza della formazione del Bacino del Marsili, ha indicato una migrazione dell'arco da NW verso SE.

In questa ricostruzione geodinamica, il piano di Benioff non mantiene caratteri di omogeneità, dato che la sua porzione profonda consiste di litosfera continentale assottigliata, che ha formato la base della **"Piattaforma Campano-Lucana" dell'Appennino meridionale**. Tale ipotesi può spiegare la messa in posto tardiva del vulcanismo di arco, di età compresa tra 1.5 e 2 milioni di anni, rispetto all'inizio della distensione di retro-arco nel Tirreno, di età compresa tra 8 e 9 milioni di anni, assumendo che non ci sono archi relitti all'interno del sistema geodinamico in oggetto.

**Inquadramento geologico.** Il Golfo di Napoli giace nel settore meridionale di una depressione strutturale, la Piana Campana (D'Argenio *et al.*, 1973), localizzata tra il settore orientale del Mar Tirreno e la catena appenninica meridionale. Essa è stata prodotta dalla distensione di retro-arco, che ha accompagnato l'accrezione nord-est vergente dell'orogene appenninico durante il *roll-back* della zolla in subduzione (Malinverno e Ryan, 1986; Faccenna *et al.*, 1996).

Il settore occidentale del Golfo di Napoli è circondato dal distretto vulcanico dei Campi Flegrei, dove il vulcanismo è stato attivo almeno negli ultimi 50 milioni di anni (Rosi e Sbrana, 1987). La morfologia attuale del Golfo si riferisce ad eventi che si sono verificati dopo la messa in posto dell'Ignimbrite Campana (CI), un ampio flusso piroclastico eruttato 37.000 anni fa, quando l'area è stata soggetta ad un'intensa calderizzazione (Barberi *et al.*, 1978). Nel settore orientale del Golfo, i processi sedimentari collegati alla piana costiera del Sarno-Sebeto hanno controllato la deposizione di sedimenti marini e costieri durante il Pleistocene superiore e l'Olocene, spesso interstratificate con depositi vulcanici collegati al Somma-Vesuvio (Milia *et al.*, 1998; Aiello *et al.*, 2001).

Durante il Quaternario superiore i processi vulcanici e sedimentari hanno fortemente interagito nel controllare l'assetto stratigrafico del margine continentale della Campania. Nel Golfo di Napoli i vulcani sottomarini sono allineati lungo un lineamento morfo-strutturale che segue il canyon Dohrn, che divide il Golfo di Napoli in due domini: un dominio sedimentario ad est, caratterizzato da unità sismiche sedimentarie, ed un dominio vulcanico ad ovest, caratterizzato da unità vulcaniche e sub-vulcaniche (Fusi *et al.*, 1991). I complessi vulcanici sepolti, geneticamente collegati alle eruzioni del Somma-Vesuvio, dei Campi Flegrei e di Ischia e Procida sono stati identificati nel sottosuolo del Golfo di Napoli (Aiello *et al.*, 2005; Aiello and Marsella, 2015).

Una sezione crostale sul margine continentale della Campania (Milia *et al.*, 2003) ha mostrato un sistema di faglie asimmetrico caratterizzato da un livello di scollamento profondo da 10 a 12 chilometri e da quattro semi-graben riempiti con spessi depositi quaternari clastici e

vulcanici (Vulturno, Lago Patria, Campi Flegrei e Golfo di Napoli). Questa sezione è calibrata dai dati di pozzi esplorativi profondi.

Dati geologici di superficie e di affioramento hanno rivelato la presenza di faglie dirette con andamento NE-SW, E-W e NW-SE, che hanno controllato l'individuazione del margine continentale e la sua evoluzione tettonica (Milia *et al.*, 2003). Un evento estensionale più antico che si è verificato lungo faglie dirette con andamento NW-SE ed è stato seguito da un evento estensionale principale collegato all'attività di sistemi di faglie con andamento NE-SW. Quest'ultimo sistema, la cui attività ha un'età compresa tra 700 e 400 kyr, ha controllato la formazione di semigraben riempiti da spessi depositi quaternari. Sul margine continentale gli effetti della trascorrenza hanno incluso la rotazione di blocchi demarcati da faglie, che delimitano fosse tettoniche in subsidenza ed una leggera compressione tra blocchi e zone sollevate.

La natura e la struttura della crosta dal margine continentale fino alla piana batiale in corrispondenza del Bacino del Vavilov sono state investigate con prospezioni sismiche (Sartori *et al.*, 2004). Questo basamento, scarsamente riflettente in corrispondenza della Dorsale Gortani, dove sono stati perforati basalti MORB (sito ODP 655; Beccaluva *et al.*, 1990), diventa più riflettente verso il margine campano, dove è composto da due unità principali. Sulla base delle perforazioni sul sito ODP 651, queste unità sono interpretate come un mantello superiore serpentizzato, ricoperto in discordanza da lave a cuscino. Una natura continentale della crosta attraverso il margine continentale può essere comunque ipotizzata, come rivelato dalle anomalie magnetiche regionali, che sono localizzate in corrispondenza di corpi vulcanici.

**Metodologie e dati.** Un rilievo sismico marino di alta risoluzione è stato eseguito dal CNR-IAMC di Napoli nel mese di giugno 1999 con lo scopo di acquisire dati sismici profondi sul margine continentale del Tirreno meridionale e nella piana batiale tirrenica. I dati sono stati acquisiti usando Airgun come sorgenti sismiche, un cavo a 48 canali, un sistema di registrazione digitale.

Il profilo sismico Sister 9\_1 è stato registrato utilizzando specifici parametri di acquisizione rappresentati: dalla sorgente (N.2 Airgun, G/I Gun SI/Sodera), dalla lunghezza delle registrazioni (5 s), dall'intervallo di campionamento, dall'intervallo di scoppio (25 metri) e dall'intervallo fra gli idrofoni (12.5 metri).

I software utilizzati per il processing sismico sono il "Promax 2D" (Landmark LTD) e il "Seismic Unix" (Colorado School of Mines). Il flusso completo di elaborazione è di seguito brevemente riassunto. I dati sono stati elaborati per produrre sezioni *stack*, pronte ad essere interpretate. Alla rimozione e riduzione del rumore incoerente e delle multiple, ha contribuito ad un'accurata analisi di velocità e l'applicazione di una deconvoluzione predittiva. Queste tecniche hanno consentito di ottenere dati sismici di elevata qualità, in aree dove la presenza di livelli piroclastici e di corpi vulcanici ha prodotto un'elevata dispersione dell'energia acustica.

L'analisi di Fourier è stata eseguita per identificare il contenuto in frequenza del segnale dopo l'applicazione di un filtro passa-banda. Questo ha consentito di riconoscere l'intervallo di frequenza nel quale il segnale utile è presente. L'applicazione del recupero del guadagno (*gain*) è consistita nella compensazione del segnale per le perdite dovute all'assorbimento, allo *scattering* ed al decadimento delle ampiezze ed è stata eseguita con l'Automatic Gain Control (AGC). Sono state svolte analisi di velocità per le correzioni dinamiche. L'analisi è stata ripetuta dopo aver applicato altri processi di elaborazione tentando di produrre miglioramenti significativi.

Lo *stacking* ha consentito d'incrementare il rapporto segnale/disturbo, riducendo il rumore casuale mentre il segnale coerente è aumentato in ampiezza di un fattore equivalente alla copertura.

La procedura di attenuazione delle multiple ha incluso sia lo *stacking* sia la deconvoluzione. La differenza di *move-out* tra le riflessioni primarie e le multiple è stata discriminata definendo una funzione di velocità corretta per le riflessioni primarie (Yilmaz, 1988).

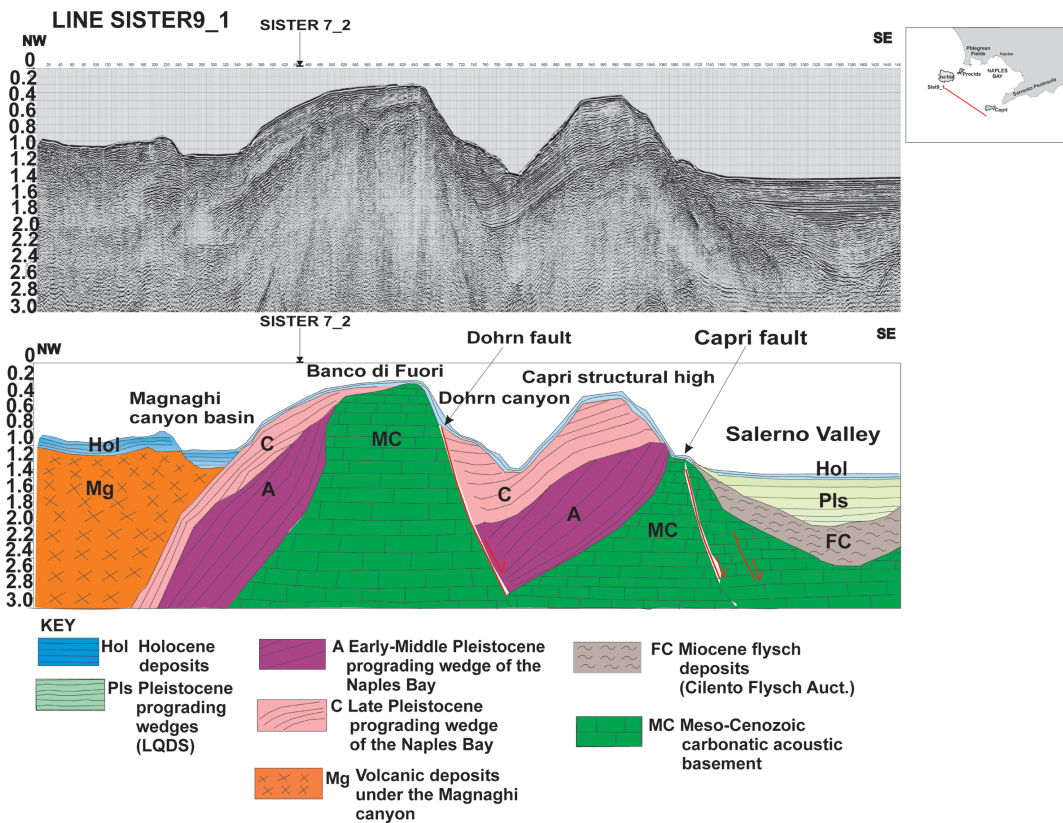


Fig. 1 – Profilo sismico regionale Sister 9\_1 e corrispondente interpretazione geologica. MC: basamento acustico. Carbonati meso-cenozoici affioranti nell’offshore della Penisola Sorrentina e dell’Isola di Capri. FC: basamento acustico. Depositi cenozoici silicoclastici collegati al “Flysch del Cilento” Auct., sottostanti il riempimento sedimentario della Valle di Salerno. A: cuneo progradante relitto del Pleistocene inferiore, che rappresenta l’unità sismica inferiore nell’architettura stratigrafica del Golfo di Napoli, caratterizzato da clinoformenti progradanti obliqui. B: cuneo progradante del Pleistocene superiore, che rappresenta l’unità sismica superiore nell’architettura stratigrafica del Golfo di Napoli, caratterizzato da clinoformenti a basso angolo da sigmoidali ad obliqui, alimentato dalla foce del paleo-Sarno. Mg: unità sismica vulcanica del Pleistocene superiore caratterizzata da una facies sismica trasparente e che costituisce l’ossatura dell’architettura stratigrafica dell’offshore di Ischia sotto il canyon Magnaghi. Pls: unità sismica pleistocenica che rappresenta l’unità superiore del riempimento sedimentario della Valle di Salerno, composto da sedimenti marini. Hol: cuneo olocenico di stazionamento alto del livello marino.

La deconvoluzione predittiva è stata eseguita per ridurre l’ampiezza dei segnali multipli, consentendo sia il recupero delle alte frequenze sia la ricostruzione della forma d’onda. Essa è consistita nella convoluzione del sismogramma con un filtro inverso (filtro di Wiener) ed ha migliorato la risoluzione e il carattere dei riflettori, favorendo le potenzialità interpretative.

**Interpretazione geologica del profilo sismico Sister 9\_1 e costruzione della sezione sismica regionale sul margine continentale della Campania.** Il profilo sismico Sister 9\_1 segue un andamento NE-SW e si estende per una lunghezza di circa 38 chilometri dall’offshore meridionale dell’Isola di Ischia all’offshore sud-occidentale dell’Isola di Capri, fino al Bacino di Salerno. La sezione sismica è stata interpretata riconoscendo diverse unità sismostratigrafiche che hanno consentito di costruire una sezione geologica regionale sul margine continentale della Campania, dal Golfo di Napoli al Golfo di Salerno (Fig. 1).

La sezione ha attraversato un piccolo bacino sedimentario adiacente al canyon Magnaghi (Golfo di Napoli), qui denominato Bacino del Canyon Magnaghi. Il profilo ha inoltre

attraversato la morfo-struttura regionale del Banco di Fuori e ha raggiunto il canyon Dohrn, per poi proseguire nel Bacino di Salerno. Le unità sismiche identificate sul profilo presentano caratteri sinsedimentari e si sono quindi deposte contemporaneamente ad intensi processi di deformazione tettonica che hanno interessato i Golfi di Napoli e Salerno durante il Pleistocene inferiore e medio. Questo è in accordo con l'assetto geologico regionale dei golfi oggetto di studio e delle retrostanti aree emerse, interessate da intense deformazioni tettoniche di carattere estensionale durante il Pleistocene inferiore e medio. Processi di crescita interessano le sequenze sismiche identificate. La linea interseca due lineamenti tettonici principali dei Golfi di Napoli e Salerno: la faglia del canyon Dohrn, faglia anti-appenninica principale del Golfo di Napoli, e la faglia Capri-Sorrento, che delimita il Bacino di Salerno ed appare interessata da forti rigetti verticali, dell'ordine di alcune migliaia di metri.

Nell'offshore di Ischia una facies sismica acusticamente trasparente, corrispondente a depositi vulcanici e vulcano clastici, è stata indicata come l'unità **Mg** (Fig. 1). Procedendo verso SE, una depressione adiacente al canyon Magnaghi è contraddistinta da riflettori paralleli e continui, interpretati come sedimenti marini olocenici (Hol in Fig. 1).

La scarpata meridionale del Banco di Fuori è ribassata da una faglia diretta con andamento NE-SW, che rappresenta la faglia del canyon Dohrn, l'importante lineamento anti-appenninico del Golfo di Napoli. La morfo-struttura del Banco di Fuori è caratterizzata da una scarsa penetrazione del segnale sismico. Si tratta dell'unità **carbonatica profonda (MC in Fig. 1)**. La faglia del canyon Dohrn presenta un rigetto verticale di circa 1.8 s. La faglia ribassa la sommità dell'unità **carbonatica profonda MC da 0.8 s (TWT) nel blocco rialzato (Banco di Fuori) a circa 2.8 s (TWT) nel blocco ribassato (Canyon Dohrn)**. Tali misure sono state effettuate a partire dalla sezione geologica regionale rappresentata in Fig. 1.

Due spesse unità sismiche che ricoprono il fianco nord-occidentale del Banco di Fuori sono state identificate sulla sezione geologica (Fig. 1) e sono interpretate come due cunei progradanti pleistocenici relitti. Un sottile strato di depositi olocenici ricopre tutta l'area.

L'alto strutturale dell'Isola di Capri mostra riflettori continui e paralleli inclinati verso nord-ovest (Fig. 1). Tale sequenza è stata interpretata come l'unità **B**. Essa ricopre l'unità **A**, cuneo progradante del Pleistocene inferiore-medio, che ricopre l'unità **carbonatica profonda** di età meso-cenozoica. I carbonati meso-cenozoici affiorano estesamente nell'alto strutturale composto da Penisola Sorrentina-Isola di Capri (Barattolo e Pugliese, 1987; Perrone, 1988).

Verso il Bacino di Salerno il corpo sismico è dislocato da una struttura con andamento NNW-SSE, localmente nota come la faglia Capri-Sorrento, faglia maestra che si è attivata durante il Pleistocene inferiore. Questa faglia assume importanza rilevante di carattere regionale, in quanto separa il Golfo di Napoli dal Golfo di Salerno. Apparentemente, questo lineamento non mostra alcuna relazione con la camera magmatica che alimenta i Campi Flegrei (Aiello *et al.*, 2009).

La faglia regionale Capri-Sorrento appare sulla sezione sismica Golfo di Napoli-Golfo di Salerno come una gradinata di faglie dirette. Ciò è suggerito dai *pattern* strutturali delle faglie che ribassano l'unità **carbonatica profonda meso-cenozoica (Fig. 1)**.

Il riempimento sedimentario del Bacino di Salerno consiste, procedendo dalla sommità verso la base della colonna stratigrafica, di tre unità sismiche principali, che ricoprono in discordanza il substrato carbonatico. L'unità superiore (unità **Hol**; Fig. 1) è caratterizzata da riflettori sismici continui e paralleli ed è ricollegabile ai depositi marini olocenici che ricoprono un'unità stratigraficamente più bassa, associata ai depositi del Pleistocene inferiore medio (unità **Pls**; Fig. 1). L'unità sottostante mostra riflettori discontinui di ampiezza elevata. La facies acustica caotica, tipica dei depositi flyschoidi, unitamente con le evidenze degli affioramenti a terra, suggeriscono l'interpretazione di depositi silicoclastici miocenici ("Flysch del Cilento" *Auct.*; Unità **FC**; Fig. 1).

L'unità sismica più profonda (Unità **MC**; Fig. 1), acusticamente trasparente per una scarsa penetrazione del segnale sismico è interpretata come carbonati meso-cenozoici, che

rappresentano il corpo principale dell'architettura stratigrafica del Golfo di Napoli. L'unità carbonatica appare fortemente dislocata e ribassata da importanti faglie dirette di carattere regionale (faglia del canyon Dohrn e faglia Capri-Sorrento; Fig. 1). Questa rappresenta una delle unità sismiche più importanti riconosciute nell'intero settore nord-orientale del Golfo di Napoli, dal Banco di Fuori all'alto sedimentario di Capri e fino al Bacino di Salerno (Fig. 1).

### Bibliografia

- Aiello G. and Marsella E.; 2013: *The contribution of marine geology to the knowledge of marine coastal environment off the Campania region (Southern Italy): the geological map n. 502 "Agropoli" (southern Campania)*. Marine Geophysical Researches, 34, 89-113.
- Aiello G. and Marsella E.; 2015: *Interactions between Late Quaternary volcanic and sedimentary processes in the Naples Bay, southern Tyrrhenian sea*. Italian Journal of Geosciences (Bollettino della Società Geologica Italiana), 134 (1), doi: 10.3301/IJG.2014.56.
- Aiello G., Marsella E. and Sacchi M.; 2000: *Quaternary structural evolution of Terracina and Gaeta basins (Eastern Tyrrhenian margin, Italy)*. Rendiconti Lincei, 11, 41-58.
- Aiello G., Budillon F., Cristofalo G., de Alteriis G., De Lauro M., Ferraro L., Marsella E., Pelosi N., Sacchi M. and Tonielli R.; 2001: *Marine geology and morpho-bathymetry in the Bay of Naples*. In: Faranda F.M., Guglielmo L., Spezie G. (Eds.) Structures and Processes of the Mediterranean Ecosystems, pp. 1-8, Springer-Verlag Italy.
- Aiello G., Angelino A., D'Argenio B., Marsella E., Pelosi N., Ruggieri S. and Siniscalchi A.; 2005: *Buried volcanic structures in the Gulf of Naples (Southern Tyrrhenian sea, Italy) resulting from high resolution magnetic survey and seismic profiling*. Annals of Geophysics, 48 (6), 1-15.
- Aiello G., Marsella E., Di Fiore V. and D'Isanto C.; 2009: *Stratigraphic and structural styles of half-graben offshore basins in Southern Italy: multichannel seismic and Multibeam morpho-bathymetry evidences on the Salerno Valley*. Quaderni di Geofisica, 77, 1-33.
- Aiello G., Putignano M.L., D'Argenio B. and Conforti A.; 2010: *Progetto di realizzazione di cartografia geologica secondo le modalità CARG. Foglio geologico n. 465 "Procida". Tavoleta I NW scala 1:25.000. Tavoleta II SW scala 1: 25.000. Tavoleta III SE scala 1:25.000. Tavoleta IV NE scala 1:25.000*. Stampato presso l'Istituto per l'Ambiente Marino Costiero, Consiglio Nazionale delle Ricerche, Sede di Napoli, 119 pp.
- Aiello G., Marsella E., Cicchella A.G. and Di Fiore V.; 2011: *New insights on morpho-structures and seismic stratigraphy along the Campania continental margin (Southern Italy) based on deep multichannel seismic profiles*. Rendiconti Lincei, 22, 349-373.
- Barattolo F. and Pugliese A.; 1987: *Il Mesozoico dell'Isola di Capri*. Quaderni dell'Accademia Pontaniana, 8, 1-36.
- Barberi F., Innocenti F., Lirer L., Munno R., Pescatore T. and Santacroce R.; 1978: *The Campanian Ignimbrite: a major prehistoric eruption in the Neapolitan area (Italy)*. Bull. Volcanol., 41 (1), 1-22.
- Beccaluva L., Bonatti E., Dupuy C. et al.; 1990: *Geochemistry and mineralogy of volcanic rocks from the ODP sites 650, 651, 655 and 654 in the Tyrrhenian sea*. Proc. ODP Results, 107, 49-74.
- Bigi G. et al.; 1992: *Structural Model of Italy*. Maps and Explanatory Notes.
- Bonardi G., Amore F.O., Ciampo G., De Capoa P., Miconnet P. and Perrone V.; 1992: *Il Complesso Liguride Auct.: stato delle conoscenze e problemi aperti sull'evoluzione pre-appenninica ed i suoi rapporti con l'Arco Calabro*. Memorie della Società Geologica Italiana, 41, 17-35.
- Chiocci F.L., Tommasi P., Aiello G., Baraza J., Bosman A., Cristofalo G., Ercilla G., Estrada F., Farran M., Martorelli E., Ortolani U., Sarli R., Senatore M.R., Tonielli R., Jacobs C.L., Wallace R.F., Matthews D. and Rouse I.; 1998: *Submarine debris avalanches off the southern flank of Ischia volcanic island, Gulf of Naples*. Proc. 2nd Intern. Symp. "Hard Soils and Soft Rocks", 12-14 Ottobre 1998.
- D'Argenio B., Pescatore T. and Scandone P.; 1973: *Schema geologico dell'Appennino meridionale (Campania e Lucania)*. Atti del Convegno "Moderne Vedute sulla Geologia dell'Appennino", Accademia Nazionale dei Lincei, Quad. 183, 49-72. Ge
- Di Fiore V., Aiello G. and D'Argenio B.; 2011: *Gravity instabilities in the Dohrn canyon (Naples Bay, Southern Tyrrhenian sea). Potential wave and run-up (tsunami) reconstruction from a fossil submarine landslide*. Geologica Carpathica, 62 (1), 55-71.
- Faccenna C., Mattei M., Funicello R. and Jolivet L.; 1996: *Styles of back-arc extension in the Central Mediterranean*. Terra Nova, 9, 126-130.
- Fusi N., Mirabile L., Camerlenghi A. and Ranieri G.; 1991: *Marine geophysical survey of the Gulf of Naples (Italy): relationships between submarine volcanic activity and sedimentation*. Memorie della Società Geologica Italiana, 47, 95-114.
- Kastens K.A., Mascle J., and Others, O.D.P.; 1988: *Leg 107 in the Tyrrhenian Sea: insights into passive margin and back-arc basin evolution*. Geol. Soc. Amer. Bull. 100, 1140-1156.
- ISPRA; 2011: *Carta geologica scala 1:10.000 – Isola di Procida. Regione Campania, Settore Difesa Suolo, Systemcart, Roma, Italia*.

- Maliverno A. and Ryan W.B.F.; 1986: *Extension in the Tyrrhenian sea and shortening in the Apennines as a result of arc migration driven by sinking of the lithosphere*. Tectonics, 5, 227-245.
- Milia A.; 2000: *The Dohrn canyon: a response to the eustatic fall and tectonic uplift of the outer shelf along the Eastern Tyrrhenian sea margin, Italy*. Geomarine Letters, 20 (2), 101-108.
- Milia A., Mirabile L., Torrente M.M. and Dvorak J.J.; 1998: *Volcanism offshore of Vesuvius volcano (Italy): implications for hazard evaluation*. Bull. Volcanol., 59, 404-413.
- Milia A., Torrente M.M., Russo M. and Zuppetta A.; 2003: *Tectonics and crustal structure of the Campania continental margin: relationships with volcanism*. Mineralogy and Petrology, 79, 33-47.
- Mirabile L., De Marinis E. and Frattini M.; 2000: *The Phlegrean fields beneath the sea: the underwater volcanic district of Naples, Italy*. Boll. di Geof. Teor. e Appl., 41 (2), 159-186.
- Patacca E. and Scandone P.; 1989: *Post-Tortonian mountain building in the Apennines. The role of passive sinking of a relic lithospheric slab*. In: Boriani A., Bonafede M., Piccardo G.P., Vai G.B. (Eds.) *The lithosphere in Italy*. Atti Accademia Nazionale dei Lincei, Advanced Earth Science Research, 157-176.
- Perrone V.; 1988: *Carta geologica della Penisola Sorrentina*. Atti 74 Cong Soc Geol Ital B, 336-340
- Ritsema A.R.; 1979: *Active or passive subduction at the Calabrian Arc*. In: Van Der Linden W.J.M. (Ed.), Fixism, mobilism or relativism: Van Bemmelen's search for harmony. Geol. Mijnbouw, 58, 127-134.
- Rosi M. and Sbrana A.; 1987: *Phlegrean Fields*. Quaderni De La Ricerca Scientifica, CNR, Roma, vol. 9, 168 pp.
- Sartori R.; 2003: *The Tyrrhenian back-arc basin and subduction of the Ionian lithosphere*. Episodes, 26 (3), 217-221.
- Sartori R. and Capozzi R.; 1998: *Patterns of Neogene to Rift related subsidence in the Tyrrhenian domain*. In: Cloetigh S., Ranalli G., Ricci C.A. (Eds.), Sedimentary Basins: Models and Constraints. Proceeding International School Earth and Planetary Sciences, CNR, Siena, pp. 147-158.
- Sartori R., Torelli L., Zitellini N., Carrara G., Magaldi M. and Mussoni P.; 2004: *Crustal features along a W-E Tyrrhenian transect from Sardinia to Campania margins (Central Mediterranean)*. Tectonophysics, 383, 171-192.
- Yilmaz O.; 1988: *Seismic data processing*. Soc. Expl. Geophys., Tulsa.

## SEISMIC RESERVOIR CHARACTERIZATION IN OFFSHORE NILE DELTA. PART I: COMPARING DIFFERENT METHODS TO DERIVE A RELIABLE ROCK-PHYSICS MODEL

M. Aleardi<sup>1</sup>, F. Ciabbarri<sup>2</sup>, F. Peruzzo<sup>2</sup>, A. Mazzotti<sup>1</sup>

<sup>1</sup> Earth Sciences Department, University of Pisa, Italy

<sup>2</sup> EDISON, Milano, Italy

**Introduction.** Seismic-reflection data are used in reservoir characterization not only for obtaining a geometric description of the main subsurface structures but also for estimating properties like lithologies and fluid contents of the target levels of interest. To this end, a rock-physics model (RPM) is incorporated into a seismic inversion scheme, such as amplitude versus angle (AVA) inversion (Grana and Della Rossa, 2010) or full-waveform inversion (Bacharach, 2006), to directly derive petrophysical rock properties from pre-stack seismic data. The outcomes of petrophysical-seismic inversion provide reservoir property maps to reservoir engineers for field appraisal, selection of optimal well location, and production enhancement (Bosh *et al.*, 2010). A rock-physics model is a generic transformation ( $f_{RPM}$ ):

$$[V_p, V_s, \text{Density}] = f_{RPM}(\phi, S_w, Sh, z) \quad (1)$$

The RPM relates the rock properties (which typically are porosity -  $\phi$  -, water saturation -  $S_w$  -, shale content -  $Sh$  -) and depth ( $z$ ) to the pressure conditions, to elastic attributes (such as P-wave and S-wave velocities -  $V_p$ ,  $V_s$  - and density). A rock-physics model can be based on theoretical equations (Avseth *et al.*, 2005), or on empirical set of equations derived from available information (e.g. well-log or core measurements) for the specific case of interest

(Mazzotti and Zamboni, 2003). In the last case, we considered either a linear or a non-linear model (Eberhart-Phillips *et al.*, 1989). In the non-linear approach, many methods can be used to derive such rock-physics model. Neural networks (Saggaf *et al.*, 2003) and stochastic optimizations (Aleari, 2015) have received great attention. **Anyway, independently from the method used, there is no doubt that the quality and the reliability of available well-log data and/or core measurements play an essential role in defining a solid RPM.**

The aim of this work is to derive a reliable RPM used in conjunction with an AVA inversion for the characterization of a clastic reservoir located in offshore Nile delta. We have employed both theoretical and empirical approaches to derive the RPM. For what concerns the empirical approaches we used both a linear and two non-linear methods to define different rock-physics models. We obtained the linear model by applying a multilinear stepwise regression, whereas neural networks and genetic algorithms are used to derive non-linear transformations from petrophysical to elastic properties. The main difference among neural networks and genetic algorithms is that the former is a gradient-based method while the latter is a global, stochastic, optimization method.

We start by introducing the different methods used to derive the theoretical and the empirical rock-physics models. Then, the detailed analysis of RPMs resulting from theoretical and empirical approaches let us to outline the benefits and the limits of each method. Moreover, in the empirical approaches we focus our attention on discussing the differences between linear and non-linear methods for the specific case under examination and on analyzing the drawbacks that characterize the neural network technique. The simplicity and the reliability of the empirical rock-physics model derived by applying multilinear stepwise regression and the optimal prediction capability of the theoretical rock-physics model enable us to consider these two RPMs in the petrophysical AVA inversion that is discussed in the companion paper titled “*Seismic reservoir characterization in offshore Nile Delta. Part II: Probabilistic petrophysical-seismic inversion*”.

**A brief introduction to the methods used for deriving the rock-physics models.** In this chapter, we briefly describe the empirical and the theoretical methods used to derive the rock-physics models. We start with the multilinear stepwise regression followed by the neural network approach, and by the optimization of the genetic algorithm used in the empirical approach. Thereafter, we will introduce the theoretical approach based on rock-physics models.

*Multilinear stepwise regression (SR).* Stepwise regression is a semi-automated process of deriving a linear equation by successively adding or removing variables in the regression procedure based solely on the *t*-statistics of their estimated coefficients (Draper and Smith, 1985). Three main approaches can be used in this regression method: forward selection, backward elimination and bidirectional elimination. The first approach starts with no variable in the model and proceeds forward (adding one variable at a time). The second approach starts with all potential variables in the model and proceeds backward (removing one variable at a time). In this study, we applied the third method, which is a combination of the approaches described above and is essentially a forward selection procedure but allows the elimination of a selected variable at each optimisation stage.

*Neural Network optimization (NN).* A neural network is a mathematical algorithm inspired by an animal’s central nervous system and trained to solve problems that would normally require human intervention (Haykin, 1999). In particular, a supervised neural network corresponds to a problem in which a set of input data and their corresponding outputs are available; in this way, the network can attempt to infer a relation between the input and the output. In this work, we apply a multilayer feed-forward neural network in which the petrophysical rock properties define the input, whereas the elastic attributes are the output of the net. The architecture of the network we used consists of one input layer, one output layer, and one hidden layer. In this work, the hidden layer consists of 25 neurons, whereas the input has as many nodes as the petrophysical properties of interest. The nodes in each layer are characterized by a sigmoid

transfer function. The weights associated with each node are computed such that the value at the output layer is equal to the training value in the least-squares sense. The NN optimization is essentially a steepest descent algorithm iteratively adjusting initial random weights using a technique called back-propagation (Haykin, 1999). For a review of neural networks and their geophysical applications, see van der Baan and Jutten (2000).

*Genetic algorithms (GA) optimization.* Genetic algorithms are a stochastic optimization method based on the mechanics of natural selection and evolution according to the Darwinian principle of “survival of the fittest” (Holland, 1975). In a GA optimization procedure a population of randomly generated individuals, which represent candidate solutions to an optimization problem, is evolved toward better solutions applying three main genetic operators, which are selection, cross-over and mutation. For more details see Mitchell (1996). In this work, we apply a GA optimization in which a population of 100 individuals evolves into 50 iterations. In this GA optimization, the equations describing the RPM are:

$$EP = k + \sum_{n=1}^N a_n PP_n^{b_n} \quad (2)$$

where:  $EP$  represents a generic elastic property (e.g. P-wave velocity, density...),  $PP$  is a generic petrophysical property (e.g. porosity, water saturation...) and  $N$  is the number of petrophysical properties considered in the regression process. The weight of each input variable is given by the coefficient  $a$ , the exponent  $b$  is used to reproduce the effects of variations in the petrophysical properties on the elastic property under consideration, whereas  $k$  is the intercept of the final equation. The coefficients ( $k; a_1, a_2, \dots, a_N; b_1, b_2, \dots, b_N$ ) are contained in each individual that is evolved during the GA optimization in which the  $L_2$  norm between observed and predicted elastic properties defines the error function to be minimized. Note that Eq. 2 represents a generalization of classical depth trends (Banchs *et al.*, 2001).

*Theoretical rock-physics model (TRPM).* With theoretical rock-physics model we refer to one or more theoretical equations that establish a relationship between elastic attributes and petrophysical rock properties. To this end, several models exist (e.g. granular media models and inclusion models). The reader can find an extensive discussion of TRPM in Avseth *et al.* (2005) and Mavko *et al.* (2009). In this work, following Avseth *et al.* (2005), we use the Hertz-Mindlin theory to define the shale and sand dry elastic properties at critical porosity and hydrostatic pressure. To simulate the compaction effect we used the Hashin-Strikmann lower bound, whereas the Gassmann equation defines the saturated elastic properties. Taking into account the depth interval considered in this study, characterized by a mechanical compaction regime, we assume a shale totally formed by smectite mineral and a not-cemented sand totally formed by quartz grains. The shale and sand critical porosities are fixed to 70% and 40%, respectively.

**Results.** In this chapter, we analyze and comment the RPMs resulting from theoretical (TRPM) approach and from linear (SR) and non-linear (NN and GA) empirical approaches. The well-log data used to estimate the RPMs pertain to four exploration wells drilled through the reservoir zone (sand) and the encasing non-reservoir rocks (shale). The petrophysical ( $Sh$ ,  $Sw$ ,  $\phi$ ) and elastic ( $Vp$ ,  $Vs$ , *density*) properties, that we consider, are all derived from appropriate formation evaluation analysis of actual well-log measurements and have been subjected to an accurate outlier removing procedure.

We know that non-linear relations often relate petrophysical properties and elastic characteristics. For example, non-linear relations link the shale content to  $Vp$  and  $Vs$  and the water saturation to  $Vp$  if considered in their full range from 0% to 100% (see Avseth *et al.*, 2005 for more details). However, in order to investigate the capability of a linear method in deriving a reliable rock-physics model, in this specific case, we consider the entire shale content and water saturation ranges (from 0% to 100%). Differently, the depth interval is limited to the target sands and the encasing shales and ranges from 2400 to 3000 m, approximately.

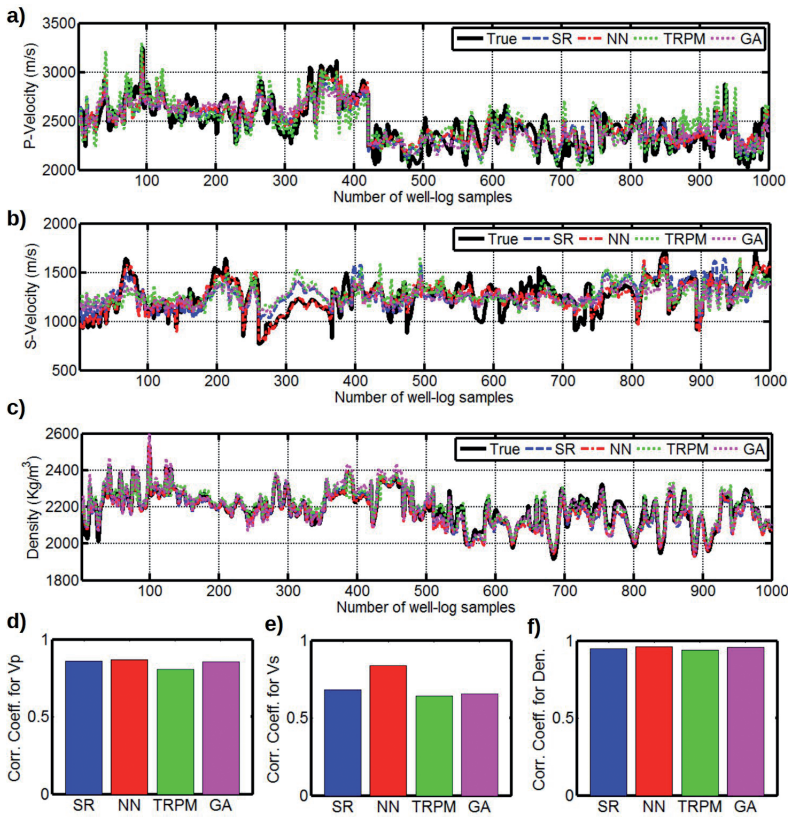


Fig. 1 – Comparison between the true and the predicted elastic properties.  $V_p$ ,  $V_s$  and density are represented in (a), (b) and (c), respectively. The correlation coefficients computed for each approach are shown in (d), (e) and (f) for  $V_p$ ,  $V_s$  and density, respectively.

A first assessment of the estimated RPMs can be done by comparing the true elastic properties, derived from well-log recordings, with those predicted by including the actual petrophysical data in the RPMs. The Fig. 1 shows this comparison together with the resulting correlation coefficients. First, we note that independently from the method applied (SR, NN, GA or TRPM) the quality of the prediction decreases passing from density (Fig. 1c) to  $V_p$  (Fig. 1a) and to  $V_s$  (Fig. 1b). Indeed, as it is well known, the relation linking the density to the petrophysical properties is simpler than the relations linking these properties to  $V_p$  and  $V_s$  (Aveseth *et al.* 2005). The higher correlation coefficient obtained for  $V_p$  (Fig. 1d) with respect to  $V_s$  (Fig. 1e) can be explained with the lower performance of the logging tools in measuring the S-velocity, and then the lower reliability of the  $V_s$  measurements with respect to the  $V_p$  and the density ones. For the density, the four methods return very similar results. Differently, for  $V_p$  and, particularly, for  $V_s$  the NN method yields final estimates with the highest correlation coefficients, whereas slightly lower correlation coefficient are obtained by the SR, GA and the TRPM methods. The slightly higher correlation coefficients obtained by the empirical methods with respect to the TRPM can be easily explained taking into account that the empirical approaches are data-driven procedures, and thus derive the final  $f_{RPM}$  on the basis of the actual petrophysical and elastic properties. Conversely, the TRPM is based on theoretical equations with general validity. Among the empirical approaches, NN produces a slightly better match than SR and GA, whereas the non-linear GA method and the multilinear SR algorithm return very similar predictions. The main advantage of the SR and GA methods over the NN approach

is that they directly provide equations (relating the petrophysical to the elastic properties) with an easily interpretable rock-physical meaning. Conversely, the NN result is a sort of “*black box*”.

In this work, the SR approach returns the following equations:

$$Vp[m/s] = 1732.3 + 0.542z + 1.647Sw - 28.742\phi - 9.056Sh \quad (3a)$$

$$Vs[m/s] = 1198.2 + 0.514z - 2.951Sw - 36.072\phi - 11.241Sh \quad (3b)$$

$$Density[Kg/m^3] = 2362.4 + 0.073z + 1.257Sw - 17.351\phi - 3.746Sh \quad (3c)$$

whereas with GA we obtain:

$$Vp[m/s] = 1685.5 + 0.623z^{0.94} + 1.831Sw^{1.16} - 30.142\phi^{0.87} - 8.547Sh^{1.04} \quad (4a)$$

$$Vs[m/s] = 1231.4 + 0.473z^{0.99} - 2.479Sw^{1.05} - 34.492\phi^{1.13} - 13.276Sh^{0.86} \quad (4b)$$

$$Density[Kg/m^3] = 2482.1 + 0.105z^{0.83} + 1.22Sw^{0.96} - 17.936\phi^{1.06} - 3.364Sh^{1.17} \quad (4c)$$

where: the depth ( $z$ ) is expressed in meters and  $Sw$ ,  $\phi$  and  $Sh$  in percentage. We note that the intercepts and the coefficients in Eqs. 3 and 4 are very similar. In addition, the exponents in Eq. 4 are very close to one. These characteristics enable us to conclude that, in the specific case under examination, the relations linking the petrophysical to the elastic properties are close to be linear. This is confirmed by the very similar predictions returned by GA and SR (as previously evidenced in commenting Fig. 1). The possibility of describing the RPM by means of the linear equations will simplify the uncertainty propagation in the probabilistic petrophysical-seismic inversion discussed in the aforementioned companion paper. From Eqs. 3 and 4 we note that, as expected,  $Vp$ ,  $Vs$  and density increase as the depth increases (the  $z$  parameter has always a positive coefficient), and decreases as the porosity increases (the  $\phi$  parameter has always a negative coefficient). Hydrocarbons are usually characterized by low bulk modulus and density and this fact explains the  $Vp$  and density increases as the water saturation increases (in Eqs. 3a, 3c and 4a, 4c, the  $Sw$  parameter has a positive coefficient). Conversely, the shear modulus is not affected by the saturating fluid and this fact, together with the density decrease produced by the increase of hydrocarbon saturation, explains the  $Vs$  increase as the water saturation decreases (in Eqs. 3b and 4b, the  $Sw$  parameter has a negative coefficient). The negative coefficients associated to the shale content can be related to the specific depth interval considered in this work (2400-3000 m), characterized by a mechanical compaction regime. As discussed in Avseth *et al.* (2005) in this depth interval the P-wave and S-wave velocities and the density of shales are usually lower than those of sands. Focusing our attention on the coefficients associated to the petrophysical variables we conclude that the porosity plays the major role in determining the elastic properties, followed by the shale content and the water saturation. Therefore, in the following seismic-petrophysical inversion, we expect that the porosity and, secondarily, the shale content will be the best determined parameters, whereas water saturation will be poorly resolvable (see the companion paper).

In Fig. 2 we have represented the so called rock-physics template (RPT) (Avseth *et al.*, 2005). The RPT is a cross-plot that shows the influence of each petrophysical property on the elastic attributes (in this work we consider the P-impedance ( $Ip$ ) and S-impedance ( $Is$ )). Fig. 2a shows the RPT derived from the actual well-log data and the associated petrophysical properties. The well-known hydrocarbon trend is also represented. As expected, we observe a decrease of  $Ip$  and an increase of  $Is$  as the water saturation decreases and a decrease of both  $Ip$  and  $Is$  with the increasing of porosity and with the increasing of shale content. These general trends are well matched by the RPTs derived from the empirical (Figs. 2b, 2c and 2e) and the theoretical (Fig. 2c) RPMs. As previously discussed, the RPTs estimated by GA and SR are very similar, and even in this case the NN method yields a better match with the actual RPT

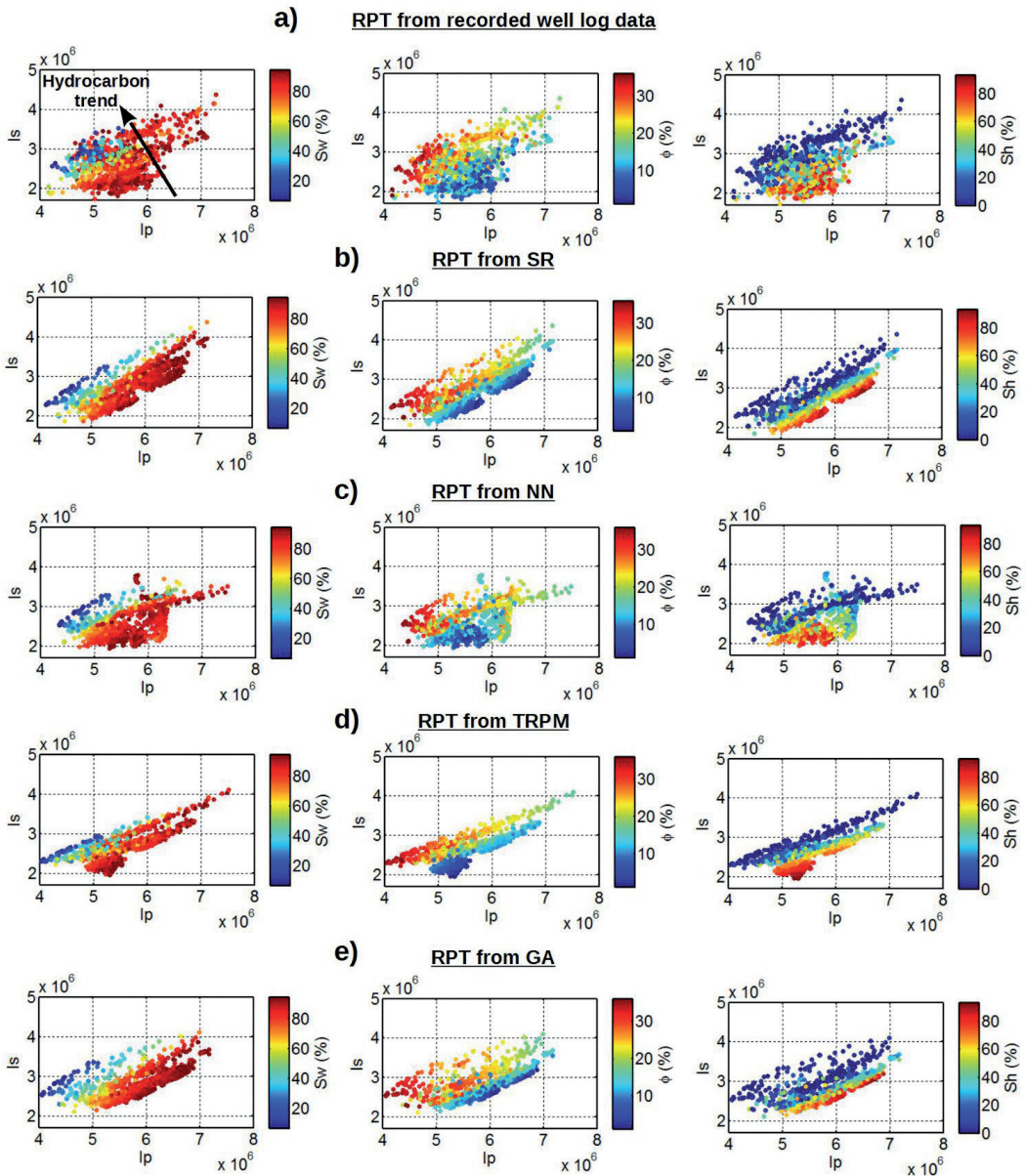


Fig. 2 – Rock-physic templates showing the influence of each petrophysical parameter on the P-impedance (Ip) and S-impedance (Is). Water saturation (Sw), porosity ( $\phi$ ) and shale content (Sh) are represented from left to right. Part (a) refers to the actual well-log data, whereas parts (b), (c), (d) and (e) refer to the elastic properties predicted by the SR, NN, TRPM and GA methods, respectively. In part a) the hydrocarbon trend is indicated by the black arrow.

computed from the actual well-log data. A slightly lower match characterizes the SR and the GA estimates and, particularly, the TRPM results.

The actual benefits and drawbacks of each method can be seen in Fig. 3. In Figs. 3a, 3b, 3c and 3d we show a graphical representation of the rock-physics models previously derived. SR, NN, TRPM and GA outcomes are depicted from Figs. 3a to 3d, respectively. For the lack of space, we restrict our attention to the  $V_s$  parameter and to the porosity-shaliness plane only. The great similarity between the SR and the GA results can be observed by comparing Figs.

**Visualizing the Predicted Relations**

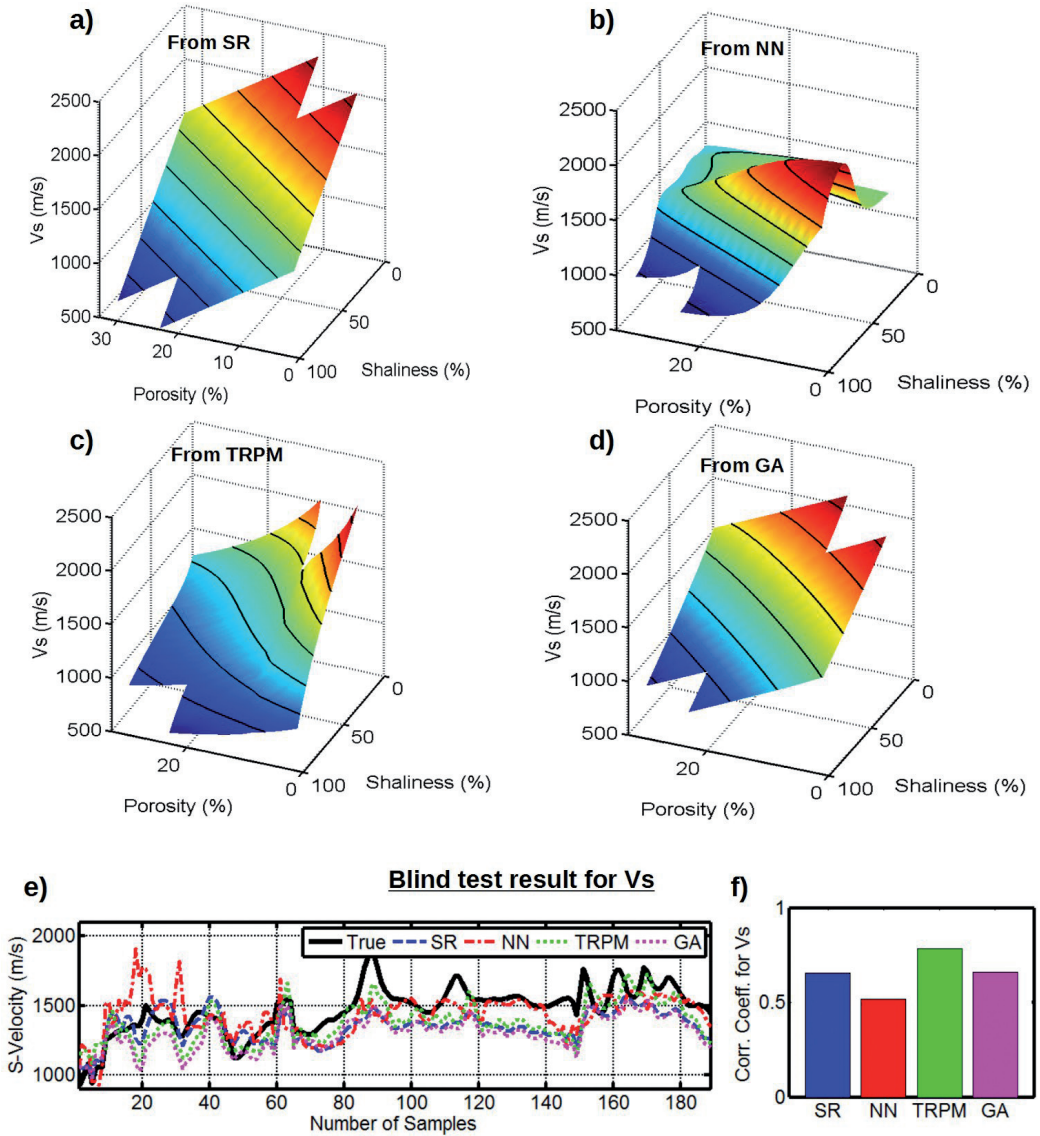


Fig. 3 – Graphical representations of the rock-physics models derived by step-wise regression (SR), Neural Network (NN), theoretical rock physics model (TRPM) and genetic algorithms (GA) are, respectively, shown in (a), (b), (c) and (d). These surfaces represent the  $V_s$  variations as a function of the shale content and the porosity, keeping fixed the depth and the water saturation to 2700 m and to 50%, respectively. (e) and (f) Results of the blind test and the corresponding correlation coefficients. See the text for additional comments.

3a and 3d. In addition, we note a fair similarity between the rock-physics models derived by the empirical SR and GA methods and the one resulting from the TRPM. All these three RPMs predict similar  $V_s$  increases with the decreasing of shale content and similar  $V_s$  increases as the porosity decreases. Conversely, the rock-physics model obtained by the NN method is substantially different from the other ones: it shows an un-physical  $V_s$  decrease for a shale content less than 40-50%, approximately. We interpret this fact as an overfitting problem that usually affects the NN method (see van der Bann and Jutten, 2000). In particular, in the

context of a NN optimization, an excessively complex network generates overfitting. Generally, overfitting occurs when a model describes random error or noise instead of the underlying relationship. A model that has been overfitted will generally have poor predictive performance. In the specific case, the overfitting associated with the NN method is visible by comparing Figs. 2a and 2c. In these figures, we note that the RPT derived from the NN approach tends to reproduce the scatter visible in the RPT derived from the recorded logs. Such scattered trend is clearly related to residual noise contamination in the well-log data or inaccurate measurements and it has no physical meaning. As a clarifying demonstration of the overfitting problem, we perform a blind test in which the petrophysical relations expressed by the four RPMs are used to predict the elastic properties in a nearby well that was not used in the estimation process of the RPMs (Fig. 3e). This well was drilled in the same target area and through geological formations with similar characteristics. This test is also aimed at quantifying the prediction capability of each rock-physics model. For the lack of space, we show the results of the blind test obtained for the S-velocity only that is the more difficult parameter to predict as demonstrated in Fig. 1. In Fig. 3e we note that, thanks to its general validity, the TRPM approach gives the best fit with the actual data. Conversely, the empirical, data-driven, approaches show lower correlation coefficients than TRPM. In particular, the NN approach is characterized by the lowest correlation coefficient (Fig. 3f), thus confirming that the overfitting problem is often associated with a sub-optimal prediction capability. Moreover, the blind test allows us to discuss a fundamental difference between the empirical and the theoretical approaches, that explains the lower correlation coefficients that characterize all the empirical RPMs with respect to the theoretical one (Fig. 3f). Even if the input set of elastic and petrophysical properties, used in defining the rock-physics model, belong to wells drilled through geological formations with similar characteristics, the empirical, data-driven, approaches return slightly different models depending on the set of input data considered in the prediction procedure. This fact can be ascribed to errors and uncertainties that affects the measured elastic properties and to errors and approximations made in the formation evaluation analysis to derive the petrophysical properties. Differently, the TRPM result, being based on theoretical equations, is totally independent from errors and uncertainties in well-log measurements.

**Conclusions.** We have analyzed the rock-physics models (RPMs) obtained by applying both theoretical and empirical approaches. The fair match between the measured and predicted elastic properties and between the actual and the predicted RPTs demonstrates the potential of all the considered methods to yield final equations that are capable of estimating the elastic properties from a set of input petrophysical properties. A very high correlation coefficients characterize the density estimates, whereas lower correlation coefficients characterize the predicted seismic velocities. This fact evidences that the relation that links density to the petrophysical parameters is simpler than the relations existing between the petrophysical parameters and  $V_p$  and  $V_s$ . In addition, the lower correlation coefficient observed for the  $V_s$  estimates might be due to the lower performance of the logging tools in measuring the S-velocity.

We have shown that the non-linear GA and the linear SR methods return very similar equations, demonstrating that the relations linking the input petrophysical properties to the elastic attributes are, in this specific case, close to be linear. This fact makes the application of an empirical non-linear method useless for the case under examination. However, in more complex geological settings the linear approach may not be enough to ensure a good match between measured and predicted properties. In these cases non-linear methods should be applied. Among the non-linear methods we tested, an important limitation of the NN over the GA method is the overfitting problem. Another drawback of the NN method, not analyzed here, is related to its local nature. In a NN optimization, the weights associated with each neuron are usually randomly initialized and are subsequently adjusted using a gradient-based strategy. This demonstrates the importance of a good initial model to prevent convergence towards a local minimum in the case of a complex multimimima error function. Conversely, GA method (or

other global search algorithms) circumvents this drawback by performing a wide and efficient exploration of the entire model space in a single inversion. Moreover, the main advantage of GA and SR over NN is that they directly provide simple equations characterized by easily interpretable rock-physical meanings.

The blind test demonstrated that the high correlation coefficients associated to the NN approach are likely related to the well-known overfitting problem. The blind test also demonstrated that the TRPM approach, thanks to its general validity, often ensures a higher prediction capability than the empirical, data-driven, approaches. This high prediction capability and the general validity are the main advantages of theoretical rock physics models with respect to the empirical methods. The prediction capability of theoretical rock physics models has been demonstrated worldwide and it is discussed in several papers (e.g. Avseth *et al.* 2005). However, such prediction capability is high in case of sedimentary basins formed by alternating shales-sand sequences subjected to hydrostatic pressure and mechanical compaction regime. In more complex geologic scenarios (fractured rocks, non-clastic rocks, overpressured rocks and chemical compaction regimes), the theoretical rock-physics models become very complex and their prediction capability decreases. In these cases, empirical, data-driven, approaches could be the only chance to obtain a reliable rock-physics model applicable for reservoir characterization.

The previous considerations enable us to consider the rock-physics models derived by the SR and by the TRPM approaches in the following petrophysical-seismic inversion discussed in the companion paper “*Seismic reservoir characterization in offshore Nile Delta. Part II: Probabilistic petrophysical-seismic inversion*”.

**Acknowledgments.** The authors wish to thank EDISON E&P for making the well log data available and for the permission to publish this work.

## References

- Aleardi, M.; 2015: *Seismic velocity estimation from well log data with genetic algorithms in comparison to neural networks and multilinear approaches*. Journal of Applied Geophysics, 117, 13-22.
- Avseth, P., Mukerji, T. and Mavko, G.; 2005: *Quantitative seismic interpretation: Applying rock physics tools to reduce interpretation risk*. Cambridge University Press.
- Bachrach, R.; 2006: *Joint estimation of porosity and saturation using stochastic rock-physics modeling*. Geophysics, 71(5), O53-O63.
- Banchs, R., Jiménez, J. and Del Pino, E.; 2001: *Nonlinear estimation of missing logs from existing well log data*. 2001 SEG Annual Meeting. Society of Exploration Geophysicists, pp. 598–600.
- Bosch, M., Mukerji, T. and Gonzalez, E.F.; 2010: *Seismic inversion for reservoir properties combining statistical rock physics and geostatistics: A review*. Geophysics, 75(5), 75A165-75A176.
- Draper, N.R. and Smith, H.; 1985: *Applied Regression Analysis*. 2nd ed. JohnWiley & Sons Inc.
- Eberhart-Phillips, D., Han, D. H. and Zoback, M.D.; 1989: *Empirical relationships among seismic velocity, effective pressure, porosity, and clay content in sandstone*. Geophysics, 54(1), 82-89.
- Grana, D. and Della Rossa, E.; 2010: *Probabilistic petrophysical-properties estimation integrating statistical rock physics with seismic inversion*. Geophysics, 75(3), O21-O37.
- Haykin, S.; 1999: *Self-organizing maps. Neural Networks—A Comprehensive Foundation*. Prentice-Hall.
- Holland, J.H.; 1975: *Adaptation in Natural and Artificial Systems*. University of Michigan Press.
- Mazzotti, A. and Zamboni, E.; 2003; *Petrophysical inversion of AVA data*. Geophysical Prospecting, 51(6), 517-530.
- Mavko, G., Mukerji, T. and Dvorkin, J.; 2009: *The rock physics handbook: Tools for seismic analysis of porous media*. Cambridge university press.
- Mitchell, M.; 1996: *An Introduction to Genetic Algorithms*. MIT Press.
- Saggaf, M., Toksöz N., and Mustafa H.M.; 2003: *Estimation of reservoir properties from seismic data by smooth neural networks*. Geophysics, 68, 1969–1983.
- Van der Baan M., and Jutten, C.; 2000: *Neural networks in geophysical applications*. Geophysics 65 (4), 1032–1047.

## SEISMIC RESERVOIR CHARACTERIZATION IN OFFSHORE NILE DELTA. PART II: PROBABILISTIC PETROPHYSICAL-SEISMIC INVERSION

M. Aleardi<sup>1</sup>, F. Ciabbari<sup>2</sup>, B. Garcea<sup>2</sup>, A. Mazzotti<sup>1</sup>

<sup>1</sup> Earth Sciences Department, University of Pisa, Italy

<sup>2</sup> EDISON, Milano, Italy

**Introduction.** Reservoir characterization plays an essential role in integrated exploration and reservoir studies, as it provides an optimal understanding of the reservoir internal architecture and properties. In reservoir characterization studies seismic reflection data are often used to derive petrophysical rock properties (water saturation, porosity, shale content) from elastic parameters (seismic velocities, rock density or impedances). The rock-physics model is the link between elastic properties and such petrophysical parameters and it can be based on theoretical rock-physics equations or on empirical set of equations derived from available information (well-log or core data) and valid for the specific case of interest.

The inverse problem of estimating petrophysical properties from seismic reflection data is multidimensional, ill posed and strongly affected by noise and measurement errors. Therefore, the statistical approach to seismic reservoir characterization has become the most popular approach. It is able to take into account the uncertainties associated with the simplified rock-physics model, the error in the seismic data, and the natural variability of the petrophysical properties in the subsurface. The goal of this approach is to predict the probability of petrophysical variables when seismic velocities or impedances and density are assigned, and to capture the heterogeneity and complexity of the rocks and the uncertainty associated with the rock-physics model. For many examples of applications of this approach to reservoir characterization studies constrained by seismic and well-log data, see for example Avseth *et al.* (2005).

In this paper, we apply a two-step procedure to seismic reservoir characterization. The first step is a Bayesian linearized amplitude versus angle inversion (AVA) in which, on the line of Buland and Omre (2003) and Chiappa and Mazzotti (2009), we derive the elastic properties of the subsurface and their associated uncertainties assuming Gaussian-distributed errors and Gaussian-distributed elastic characteristics. The second step is a petrophysical inversion that uses the outcomes of AVA inversion, the previously defined rock-physics model, their associated uncertainties and the prior distribution of the petrophysical variables, to derive the probability distributions of the petrophysical properties in the target zone. The derivation and the calibration of different rock-physics models is the topic of the companion paper titled “*Seismic reservoir characterization in offshore Nile Delta. Part I: Comparing different methods to derive a reliable rock-physics model*”. In that paper the empirical, linear, rock-physics model derived with a multilinear stepwise regression (named SR in the companion paper) and the theoretical rock-physics model (named TRPM in the companion paper) demonstrated to be the most reliable in predicting the elastic characteristics from the petrophysical properties. Then, the two rock-physics models are applied in the petrophysical inversion described here. In the context of petrophysical inversion, the main difference of applying a linear or a non-linear rock-physics model lies in the fact that the former allows the joint distribution of petrophysical and elastic properties to be analytically computed, while the latter requires a Monte Carlo simulation to derive such joint distribution.

We start with a brief theoretical description of the method and with a synthetic example based on actual well-log measurements. This test aims to demonstrate the applicability of the inversion method and to illustrate and compare the different results obtained by considering the empirical and the theoretical rock-physics models. Moreover, this synthetic test allows us to check the applicability and the reliability of the two rock-physics models in the specific case under examination. Then, a field case inversion is discussed. This inversion is performed for a single CMP location where well-control is available to validate the results.

**The method.** In the following discussion we will use  $m$  to indicate the elastic properties, typically P and S-impedance ( $I_p$  and  $I_s$ , respectively) and density,  $R$  to indicate the petrophysical properties, such as water saturation ( $Sw$ ), porosity ( $\phi$ ) and shaliness ( $Sh$ ), whereas  $d_{obs}$  indicates the observed seismic data (typically the measured AVA responses). The method we use is a two-step procedure: a Bayesian linearized AVA inversion followed by a probabilistic petrophysical inversion. This petrophysical inversion makes use of the a-priori distribution of the petrophysical properties  $p(R)$  derived on the basis of well-log data, of the previously defined rock-physics model and of the results of AVA inversion to derive the probabilistic distribution of the petrophysical properties in the subsurface.

The first step of the petrophysical-seismic inversion is the Bayesian AVA inversion that jointly estimates the posterior distributions of the elastic properties in the subsurface by making use of a reformulation of the linear approximation of the Zoeppritz equation derived by Aki and Richards (1980). In particular, we parameterize the inversion in terms of P and S-impedance ( $I_p$  and  $I_s$ , respectively) and density. In terms of impedances, the P-wave reflection coefficient  $R_{pp}$  as a function of the reflection angle ( $\theta$ ) can be written as follows:

$$R_{pp}(\theta) = \frac{1}{2 \cos^2(\theta)} \frac{\Delta I_p}{I_p} - 4 \frac{\bar{I}_s^2}{I_p^2} \sin^2(\theta) \frac{\Delta I_s}{I_s} + \left( \frac{1}{2} - \frac{1}{2 \cos^2(\theta)} + 2 \frac{\bar{I}_s^2}{I_p^2} \sin^2(\theta) \right) \frac{\Delta \rho}{\rho} \quad (1)$$

where  $\bar{I}_p$ ,  $\bar{I}_s$  and  $\bar{\rho}$  are, respectively, the averages of impedances and density at the reflecting interface, whereas  $\Delta I_p$ ,  $\Delta I_s$  and  $\Delta \rho$  are the corresponding contrasts. However, density estimates are not used in the petrophysical inversion since they are obviously correlated with the impedances ones and because the linear AVA inversion cannot retrieve reliable information about density with realistic noise levels (Buland and Omre, 2003). Following Stolt and Weglein (1985), the single-interface reflection coefficient in Eq. 1 can be easily extended to a time-continuous reflectivity function. The elastic properties estimated by Bayesian AVA inversion are delivered according to the following posterior probability distribution:

$$p(m | d_{obs}) = G(\mu_{m|dobs}, \Sigma_{m|dobs}) \quad (2)$$

where:  $G$  indicates the Gaussian distribution where the posterior expectation and the covariance are equal to  $\mu_{m|dobs}$  and  $\Sigma_{m|dobs}$ , respectively. The a-priori distributions and the vertical correlation of the elastic properties, needed to derive the posterior distribution in Eq. 2, can be determined from available well-log data. For full details about the Bayesian linearized AVA inversion see Buland and Omre (2003).

For what concerns the petrophysical inversion, we apply the method proposed by Grana and Della Rossa (2010) and briefly summarized in the following. Considering all variables as random vectors, we can write the rock-physics model ( $f_{RPM}$ ) as:

$$m = f_{RPM}(R) + \varepsilon \quad (3)$$

where:  $\varepsilon$  is the random error that describes the accuracy of the rock-physics model and can be determined by comparing the available well-log data with the predicted data. For the prior distribution of the petrophysical properties  $p(R)$  we assume a multivariate Gaussian mixture (GM) that is a linear combination of Gaussian distributions:

$$p(R) = \sum_{k=1}^{Nc} a_k G(\mu_R^k, \Sigma_R^k) \quad (4)$$

where:  $Nc$  indicate the number of components of the mixture and  $a_k$  are the weights associated with each component (with  $\sum_{k=1}^{Nc} a_k = 1$ ). Generally, each component is a specific litho-fluid class previously determined from available log data and from the geological knowledge of the investigated area. In this work, we consider three litho-fluid classes that are gas-sand, brine-sand and shale. The technique we adopt, to estimate the parameters of the Gaussian components

and the weights of the mixture, is the expectation maximization algorithm (Hastie *et al.*, 2005). This Gaussian mixture model allows us to describe the multimodality and the correlation that often characterize the distribution of the petrophysical properties in the subsurface.

If we assume that  $\varepsilon$  is Gaussian with zero mean and covariance  $\Sigma\varepsilon$ , the conditional probability  $p(m|R)$  can be expressed as:

$$p(m | R) = G(f_{RPM}(R) + \varepsilon, \Sigma_\varepsilon) \tag{5}$$

where:  $\Sigma\varepsilon$  can be estimated by comparing actual and predicted well-log data and is assumed independent from  $R$  and only related to  $\varepsilon$ . Note that this formulation allows us to account for uncertainties associated with the rock-physics model predictions that are expressed by  $\varepsilon$  and  $\Sigma\varepsilon$ .

The joint distribution of the elastic and the petrophysical properties is again a Gaussian mixture:

$$p(m, R) = \sum_{k=1}^{Nc} b_k G(\mu_{(m,R)}^k, \Sigma_{(m,R)}^k) \tag{6}$$

If the rock-physics model  $f_{RPM}$  is linear, this joint distribution can be derived analytically from the prior distribution  $p(R)$ . Conversely, if  $f_{RPM}$  is not linear the joint distribution  $p(m,R)$  can be obtained from a semi-analytical approach that makes use of Monte Carlo samples. This last approach applies the expectation maximization algorithm to Monte Carlo samples to compute the characteristics of the joint distribution (see Grana and Della Rossa, 2010, for full details). Since the joint distribution is a Gaussian mixture, the conditional distribution  $p(R|m)$  is again a Gaussian mixture and can be written as follows:

$$p(R | m) = \sum_{k=1}^{Nc} c_k G(\mu_{R|m}^k, \Sigma_{R|m}^k) \tag{7}$$

in which  $\mu_{R|m}^k$  and  $\Sigma_{R|m}^k$  are analytically computed from the joint distribution  $p(m,R)$ , from the prior model  $p(R)$  and from the results ( $m$ ) of Bayesian AVA inversion:

$$\mu_{R|m}^k = \mu_R^k + \Sigma_{R,m}^k (\Sigma_{m,m}^k)^{-1} (m - \mu_m^k) \tag{8}$$

and

$$\Sigma_{R|m}^k = \Sigma_{R,R}^k - \Sigma_{R,m}^k (\Sigma_{m,m}^k)^{-1} \Sigma_{m,R}^k \tag{9}$$

The weights  $c_k$  in the conditional GM distribution  $p(R|m)$  can be computed as follows:

$$c_k(m) = \frac{b_k G(\mu_{R|m}^k, \Sigma_{R|m}^k)}{\sum_{l=1}^{Nc} b_l G(\mu_{R|m}^l, \Sigma_{R|m}^l)} \tag{10}$$

To compute the final conditional probability  $p(R|d_{obs})$ , which expresses the probability of petrophysical variables conditioned by seismic data, we need to propagate the uncertainties that characterize the results of the Bayesian AVA inversion into the conditional probability  $p(R|m)$ . To this end the Chapman-Kolmogorov equation can be used (Papoulis, 1984):

$$p(R | d_{obs}) = \int P(R | m) P(m | d_{obs}) dm \tag{11}$$

This conditional probability is the final result of the petrophysical inversion conditioned by seismic data.

**Results.** To define the number of components of the a-priori Gaussian mixture distribution of the petrophysical properties ( $p(R)$ ; Eq. 4) we consider three different litho-fluid facies that are shale, brine sand and gas sands. These facies are defined on the basis of available well-log data and geological knowledge of the investigated area. This trivariate Gaussian mixture allows us to account for correlations observed between petrophysical variables in each litho-fluid class. The parameters that define this GM distribution were obtained applying the

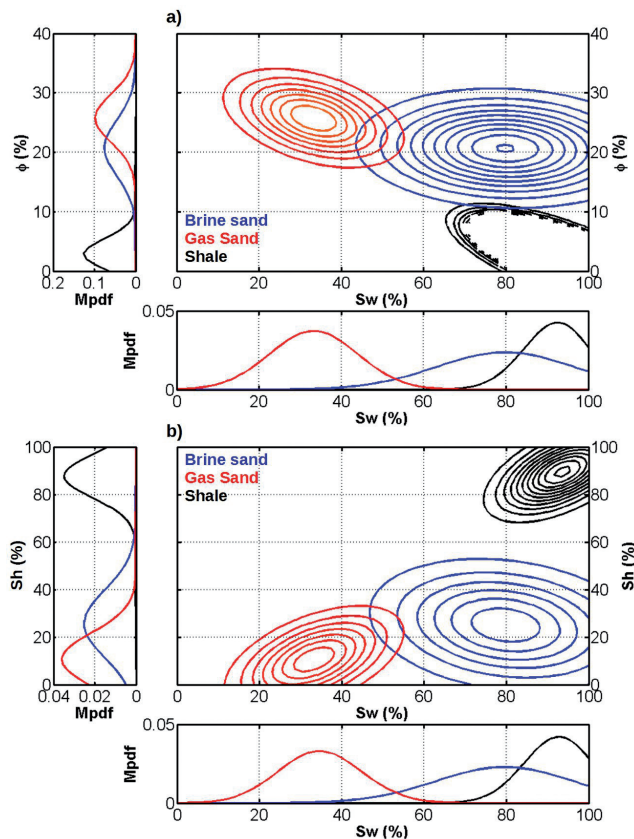


Fig. 1 – Prior probability distribution of the petrophysical variables ( $\phi$ ,  $Sw$  and  $Sh$ ) computed taking into account three different litho-fluid classes: brine-sand, gas-sand and shale. The prior is distributed according to a Gaussian mixture model that allows us to take into account the multimodality and the correlation that usually characterize the distribution of the petrophysical properties in the subsurface (see Eq. 4). a) Prior distribution projected onto the  $Sw$ - $\phi$  plane and the associated marginal distributions (Mpdf) computed along the  $Sw$  and  $\phi$  directions. b) Same as (a) but considering the  $Sw$ - $Sh$  plane.

expectation maximization algorithm. Fig. 1 represents the prior Gaussian mixture distribution of water saturation, porosity and shaliness for the three facies. In Fig. 1a we represent the prior distribution projected onto the  $Sw$ - $\phi$  plane, together with the associated two marginal prior distributions (Mpdf) computed along the  $Sw$  and  $\phi$  directions. As expected, the shale correspond to high  $Sw$  values and low porosity, whereas both brine sands and gas sands are characterized by higher porosity, with the gas sands at lower water saturation values than brine sands. Fig. 1b shows the prior distribution of the petrophysical properties projected onto the  $Sw$ - $Sh$  plane. Similarly to Fig. 1a, the marginal distributions are also represented. As expected, the shales are characterized by higher shaliness values with respect to brine sands and gas sands.

To test the applicability of the petrophysical-seismic inversion and to check the reliability of the two considered rock-physics models, we show a synthetic inversion in which actual well-log measurements, pertaining to a well drilled in the target area, have been used to compute the synthetic seismic data. The synthetic data have been computed by means of a 1D convolutional forward modeling and using a 50 Hz Ricker wavelet as the source signature. Fig. 2a shows the synthetic CMP gather in which the offset has been converted to incident angles, whereas Figs. 2b, and 2c illustrate the results of the Bayesian AVA inversion. The green arrows in Fig. 2a at 2.46 s indicate the target gas-sand interval. The decrease of  $I_p$  and density and the increase of  $I_s$  that characterize this gas-sand interval generate the typical class III AVA anomaly (Castagna and Swann, 1997) clearly visible in the synthetic seismogram. In Fig. 3a the blue curves depict the actual well-log data resampled at the seismic sample interval, the red curves illustrate the maximum a-posteriori (MAP) solution, and the gray curves are Monte Carlo realizations computed from the posterior distribution  $p(m/d_{obs})$  (see Eq. 2). Each Monte Carlo realization represents a possible solution. As expected, the uncertainties increase passing from  $I_p$ , to  $I_s$  and

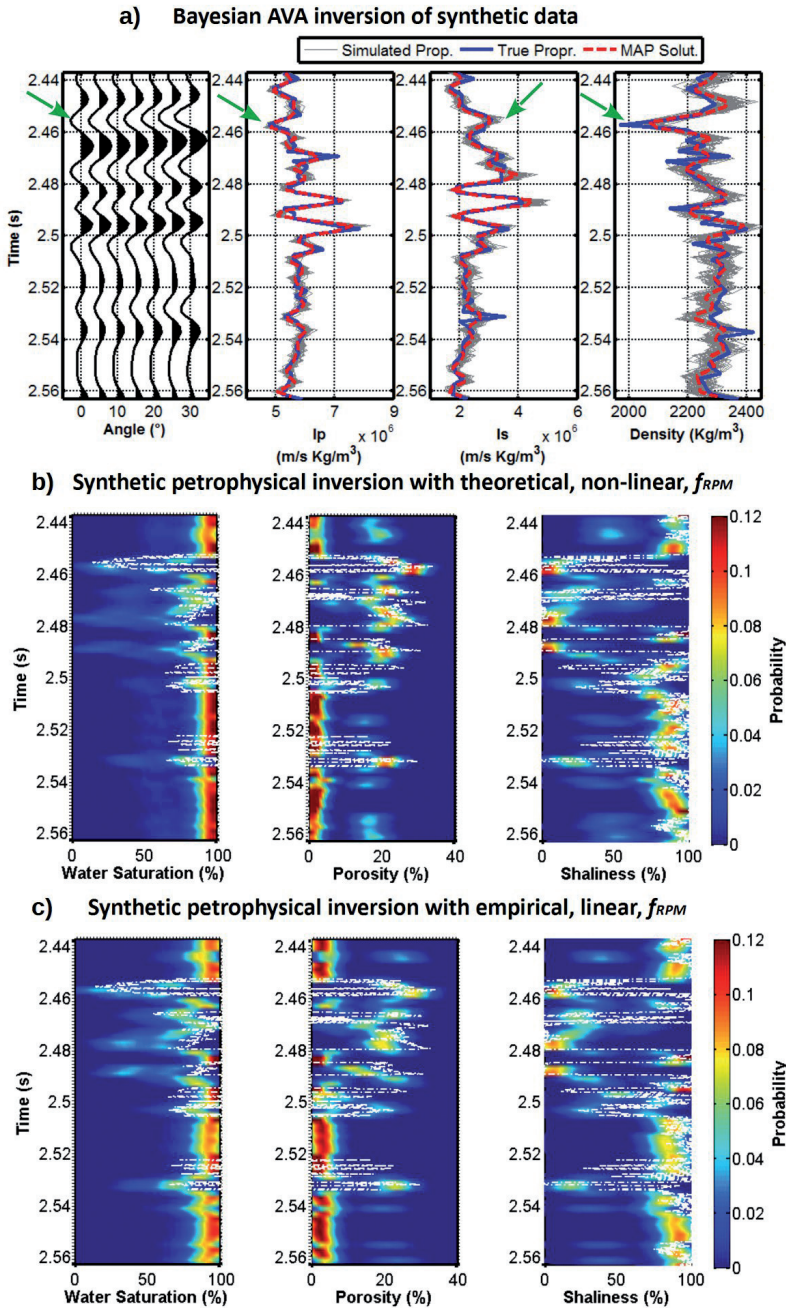


Fig. 2 – Results of the synthetic inversion based on actual well-log measurements. a) The synthetic CMP, P-impedance, S-impedance and density are represented from left to right. For impedances and density the x-axes are represented with the same scale to better illustrate the increase of uncertainty that occurs passing from the  $I_p$ , to the  $I_s$  and to the density estimates. In blue are represented the true elastic properties, in red the maximum a posteriori (MAP) solution, whereas the grey curves show Monte Carlo samples from the posterior probability distribution. The green arrows indicate the target gas-sand that generates a class III AVA anomaly in the synthetic seismogram. b) and c) Results of the petrophysical inversion that is the posterior conditional probability  $p(R|d_{obs})$  (see Eq. 11). The water saturation, porosity and shaliness are represented from left to right, respectively. b) Results obtained applying the theoretical, non-linear, rock-physics model. c) Results obtained with the empirical, linear, rock-physics model.

to density. However, we note that, although with a different resolution, the predicted elastic properties close match the true ones.

Now we move to describe the results of the petrophysical inversion obtained by applying both the linear, empirical, rock-physics model and the non-linear, theoretical, rock-physics model. The final, multimodal, Gaussian mixture distributions  $p(R|d_{obs})$ , derived for both the petrophysical inversions are represented in Figs. 2b and 2c. Fig. 2b shows the outcomes of the petrophysical inversion in which the theoretical, non-linear, rock-physics model (TPRM in the companion paper) has been considered, whereas Fig. 2c shows the results obtained when the empirical, linear, model (SR in the companion paper) has been used. In both cases we note that, as expected, the water saturation is poorly resolvable in the range 0-95% due to its minor influence in the  $I_p$  and  $I_s$  values (although the main gas sand interval at 2.46 s has been correctly predicted), whereas the shaliness and, particularly, the porosity are well resolved. Comparing the predicted petrophysical properties with the true ones (shown by the dotted white lines), we note that, within the resolution of the seismic data, both the theoretical and the empirical rock-physics models are able to correctly predict the porosity and the shaliness values. In particular, both petrophysical inversions have been able to predict the many porosity and shaliness variations that occur between 2.45 and 2.50 s, where a finely layered sand-shale sequence occurs. As expected, a lower match between each predicted and true value and a higher uncertainty characterize the water saturation estimates. For the water saturation, we also note that the theoretical rock-physics model seems to produce a better fit with the true water saturation values with respect to the empirical rock-physics model. This fact can be ascribed to the difficulty of a linear rock-physics model to take into account the non-linearity that characterizes the influence of the water saturation on the P and S impedances.

In conclusion, both the outcomes of the empirical, linear, and the theoretical, non-linear, rock-physics models show a fair match with the actual well-log measurements. This confirms the reliability and the applicability of the two rock-physics models in the petrophysical inversion. However, with respect to the analytical rock-physics model the theoretical model is more computer demanding as it requires a Monte Carlo simulation to compute the joint probability distribution  $p(m,R)$ . This peculiarity must be taken into account when the petrophysical inversion is performed on multiple CMP gathers.

The discussion about the field data inversion is limited to a single CMP location where a well-control is available. This CMP is the nearest to the well that has already been considered in the synthetic inversion. The seismic data have been processed paying particular attention at preserving the true amplitude of the reflections. However, due to the strong attenuation of high frequencies produced by several gas clouds occurring in the shallow layers, these seismic data are very poor in high frequencies. Consequently, the dominant frequency, at the depth of the target level, is around 15-18 Hz.

Fig. 3a illustrates the results of the Bayesian AVA inversion for the considered CMP gather. In the observed seismic data, despite the very low resolution, a clear class III AVA anomaly is visible at the target level (around 2.46 s). In blue are illustrated the true elastic properties resampled at the seismic sampling interval, the green lines show the true properties up-scaled to the seismic frequency band, the red curves represent the MAP solutions, while the gray lines are Monte Carlo realizations derived from the posterior distribution. As observed in the previous synthetic example the uncertainties increase passing from the impedances to the density estimates. However, the true up-scaled elastic properties (green lines) show a fair match with the estimated ones (red lines) and, more importantly, they lie inside the range defined by the Monte Carlo realizations.

Figs. 3b and 3c show the conditional probability distributions of the petrophysical properties predicted by using the theoretical, non-linear, and the empirical, linear, rock-physics models, respectively. At the low resolution of the seismic data, the differences in the results obtained with the two rock-physics models are negligible. Differently, from the previous synthetic test,

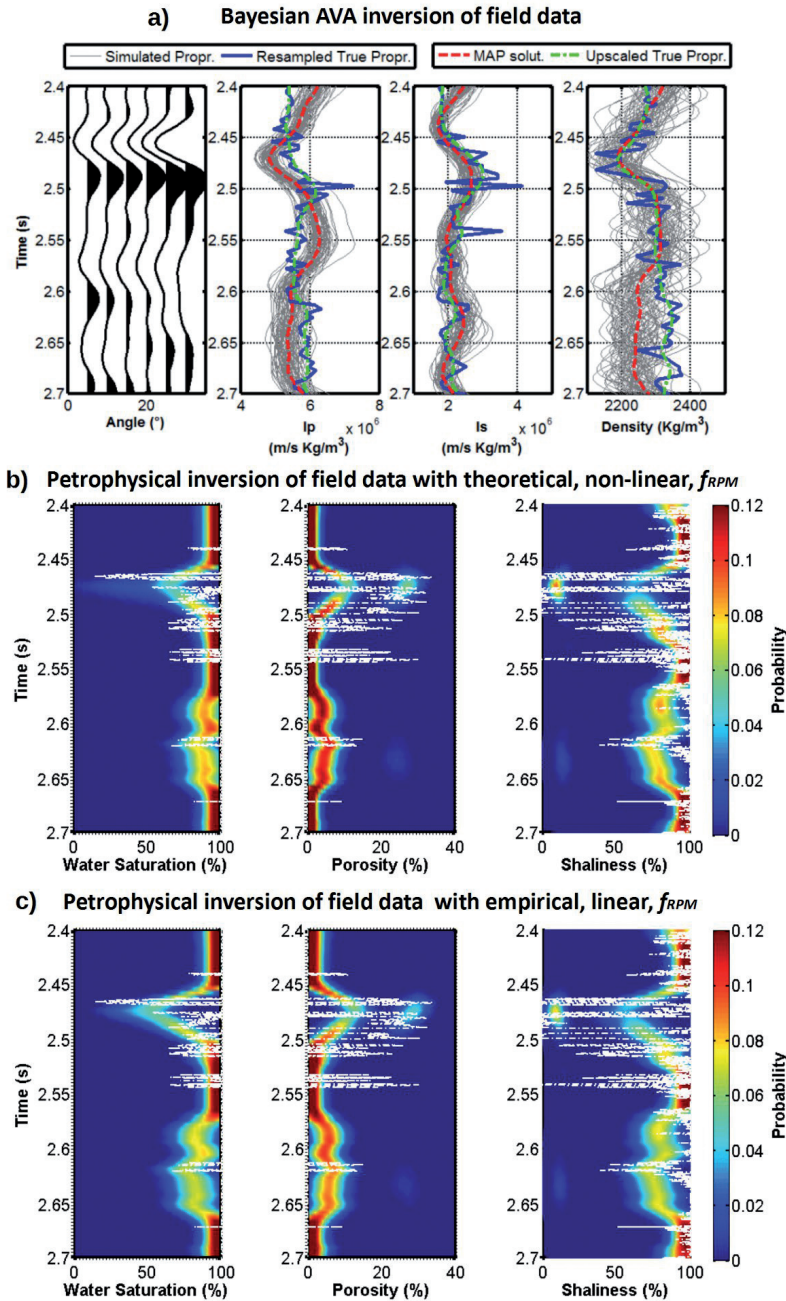


Fig. 3 – Results of the inversion of field data performed on the CMP location nearest to the well already considered in the synthetic inversion. a) The synthetic CMP, P-impedance, S-impedance and density are represented from left to right, respectively. For impedances and density the x-axes are represented with the same scale to better illustrate the increase of uncertainty that occurs passing from the  $I_p$ , to the  $I_s$  and to the density estimates. In blue are represented the true elastic properties resampled at the seismic sampling interval, in red the MAP solution, in green the true properties up-scaled to the seismic bandwidth, whereas the grey curves show Monte Carlo realizations from the posterior probability distribution. b) and c) Results of the petrophysical inversion that is the posterior conditional probability  $p(R|d_{obs})$  (see Eq. 11). The water saturation, porosity and shaliness are represented from left to right, respectively. b) Results obtained applying the theoretical, non-linear, rock-physics model. c) Results obtained with the empirical, linear, rock-physics model.

the low resolution of the seismic data makes a detailed characterization of the petrophysical properties in the subsurface impossible. However, despite the low-resolution issue, the petrophysical inversion has been able to predict the increase of porosity and the decrease of shaliness that occur between 2.45 and 2.50 s where the alternating shale-sand sequence occurs, but, differently from the synthetic inversion, this finely layered shale-sand sequence is resolved as a unique layer.

**Conclusions.** We presented a two-step probabilistic petrophysical inversion applied to reservoir characterization in offshore Nile delta. The first step of this procedure is a Bayesian linearized AVA inversion that returns the posterior probability distributions of the elastic properties ( $I_p$ ,  $I_s$  and density) in the subsurface. The second step is a probabilistic petrophysical inversion that makes use of the results of the previous AVA inversion, of the prior distribution of the petrophysical variables, and of a suitable rock-physics model to determine the posterior distribution of the petrophysical properties in the subsurface. This method propagates the uncertainties from seismic to petrophysical properties, including the effect of seismic noise error, the degree of approximation of the rock-physics model and the uncertainties that affect the estimated elastic properties. The Gaussian mixture model approach allows us to take into account the multimodality and the correlation that usually characterize the distribution of the petrophysical properties in the subsurface. The petrophysical inversion was performed making use of two different rock-physics models: a linear model (named SR in the companion paper) derived empirically by means of a stepwise regression from the available log data, and a non-linear model based on theoretical equations (named TRPM in the companion paper). Both rock-physics models returned very similar results, thus confirming their reliability and their applicability in the specific case under examination. The unique difference lies in the fact that the theoretical rock-physics model is more computer demanding as it requires a Monte Carlo simulation to compute the joint probability distribution  $p(m,R)$ . This peculiarity must be taken into account when applying the petrophysical inversion on multiple CMP locations.

The inversion of synthetic and field data confirmed the applicability of the proposed methodology. Shaliness and, particularly, porosity are the best resolved parameters. Conversely, water saturation in the range 0%-95% is poorly resolvable due to its minor influence on the  $I_p$  and  $I_s$  values. The field data inversion was performed on a single CMP location where well-control was available to validate the results. The main limit of the seismic data is the very narrow frequency bandwidth that makes them unsuitable for detailed reservoir characterization studies.

The results of the Bayesian linearized AVA inversion have been also used to perform a probabilistic litho-fluid facies classification that makes use of Markov-chain models. For the lack of space, the outcomes of this classification procedure have not been discussed here.

**Acknowledgments.** The authors wish to thank EDISON for making the seismic and the well log data available and for the permission to publish this work.

## References

- Aki, K. and Richards, P.G.; 1980: *Quantitative Seismology: Theory and Methods*. WH Freeman & Co.
- Avseth, P., Mukerji, T. and Mavko, G.; 2005: *Quantitative seismic interpretation: Applying rock physics tools to reduce interpretation risk*. Cambridge university press.
- Buland, A. and Omre, H.; 2003: *Bayesian linearized AVO inversion*. *Geophysics*, 68(1), 185-198.
- Castagna, J.P. and Swan, H.W.; 1997: *Principles of AVO crossplotting*. *The leading edge*, 16(4), 337-344.
- Chiappa, F. and Mazzotti, A.; 2009: *Estimation of petrophysical parameters by linearized inversion of angle domain pre-stack data*. *Geophysical Prospecting*, 57(3), 413-426.
- Grana, D. and Della Rossa, E.; 2010: *Probabilistic petrophysical-properties estimation integrating statistical rock physics with seismic inversion*. *Geophysics*, 75(3), O21-O37.
- Hastie, T., Tibshirani, R., Friedman, J. and Franklin, J.; 2005: *The elements of statistical learning: data mining, inference and prediction*. *The Mathematical Intelligencer*, 27(2), 83-85.
- Papoulis, A.; 1984: *Probability, random variables and stochastic processes*. McGraw-Hill.
- Stolt, R. H. and Weglein, A. B.; 1985: *Migration and inversion of seismic data*. *Geophysics*, 50(12), 2458-2472.

## IGNEOUS BODIES CHARACTERIZATION BY MEANS OF SEISMIC REFLECTION ATTRIBUTES AND WAVELET TRANSFORM

E. Gianturco, A. Tognarelli, S. Rocchi, L. Pandolfi

Earth Sciences Department, University of Pisa, Italy

**Introduction.** The aim of this work is the detection and characterization of several igneous bodies observed in a series of 2D reflection seismic sections. The seismic survey has been acquired offshore Senegal and western African margin, SW of Dakar.

The identification, description and characterization of the igneous bodies is carried out by means of the complex seismic attributes. The considered attributes are the Reflection Strength and its first and second derivative, the Instantaneous Frequency, the Instantaneous Phase, the Cosine of the Instantaneous Phase and the Sweetness. Moreover, in order to improve the visualization of the entire seismic dataset, the Continuous Wavelet Transform (CWT) is applied to the data. The CWT helps to better discriminate the geometrical features and the morphologies of the igneous bodies.

The seismic attributes analysis and the CWT allow the identification of the amplitude anomalies related to the igneous bodies, the description of the different seismic facies and the understanding of mutual relationship and behavior. Furthermore, this process consents the evaluation of the geometrical properties of the intrusive bodies such as thickness, lateral extent, emplacement depth. It also allows the delineation of the structural deformations that affected the overburden due to the igneous intrusion.

Finally, the variation in the attribute response let us to recognize in each seismic profile three seismofacies and to classify the intrusive bodies based on their age, shape and level of emplacement.

**Seismic reflection data.** This study is carried out interpreting eighteen seismic lines extracted from a 3D data volume. In particular, the entire dataset is composed by eleven in-lines and seven cross-lines. In Fig.1 the map of the survey with the position of the seismic lines here analyzed; in Tab.1 the most important acquisition and recording parameters are reported. All the sections are time migrated with zero phase conversion applied.

A *line by line* description of each amplitude anomaly is carried out. The seismic lines are characterized on the basis of their amplitude, phase and frequency by means of the complex seismic attributes (Taner *et al.*, 1979; White, 1991; Satyavani *et al.*, 2008; Barnes, 2001; Yushun, 2011; Subrahmanyam and Rao, 2008) Reflection Strength and derivatives, Instantaneous Phase, Instantaneous Frequency and Sweetness.

Tab. 1 - Acquisition and recording parameters.

Type of energy source	Air Guns
Number of source	2 groups
Source depth	5.5 m (+/- 1m)
Shot point interval	25 m
Number of streamers	10
Streamer length	6000 m
Number of traces	480 / streamer
Trace interval	12.5 m
Nearest seismic offset	360 m
Streamer depth	7 m +/- 1 m
Number of channels	10x480 + 37 auxiliary channels used
Record length	8100 ms
Sample interval	2 ms

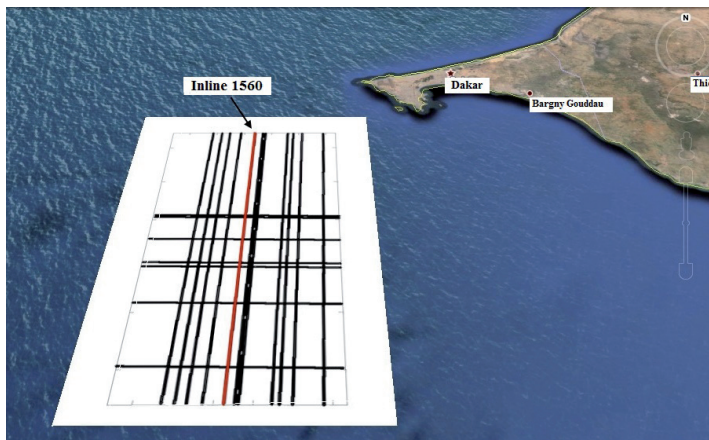


Fig. 1 – Map of the survey. In black are the positions of the analysed seismic sections. The inline 1560 is highlighted in red. The width of the map is 30 km along the E-W direction and 60 km in the N-S direction.

The Reflection Strength attribute permits to visualize the data taking into account the seismic reflectivity and, in particular, it highlights the strong impedance contrasts related to lithological changes and thus allows to discriminate the limits between sequences and to localize the amplitude anomalies from the igneous bodies.

Therefore, according to the observed amplitude response, each seismic section is divided into three different seismofacies (Fig. 2). The seismofacies A is located in the upper part of the sections and is characterized by alternating reflectors with medium to high Reflection Strength response. The seismofacies B (below A) is constituted by a package of reflectors that have the maximum amplitude values, alternated by thin reflectors with medium amplitude values. The seismofacies C, located in the lower part of the sections, presents discontinuous reflectors

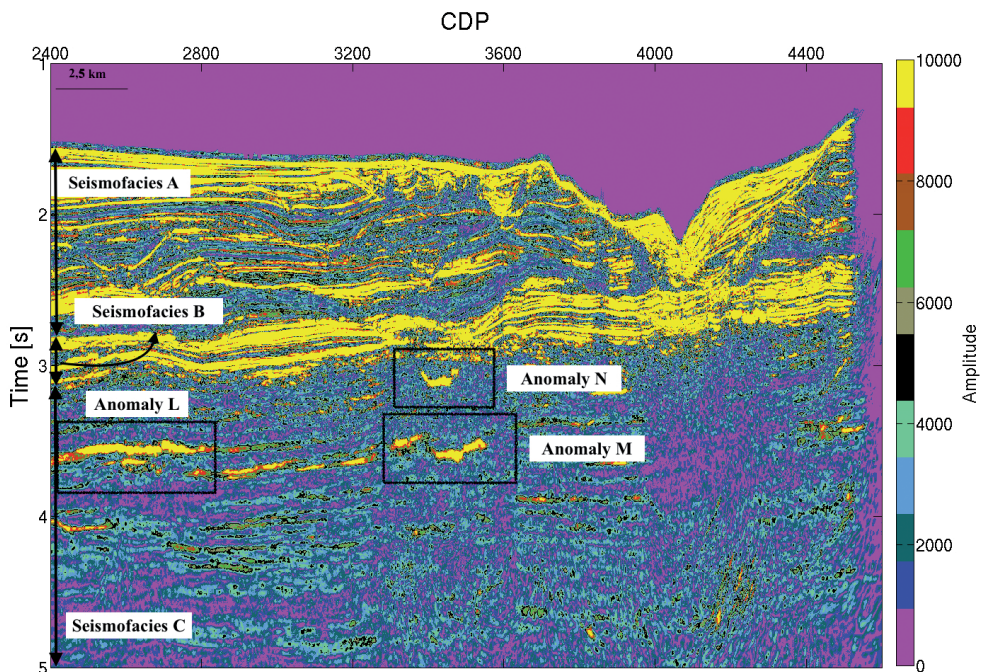


Fig. 2 – Reflection Strength of the inline 1560. The limits between the seismofacies A, B, C and the localized amplitude anomalies L, M and N, related to the igneous bodies, are highlighted. The strong impedance contrasts between the anomalies and the host-seismofacies C are evident.

with amplitude values much smaller than those of seismofacies A and B. In Fig. 2 is shown an example of the result obtained through the application of the Reflection Strength attribute for the inline1560 and the limits between the seismofacies A, B and C and the amplitude anomalies L, M and N are highlighted.

The Instantaneous Phase attribute is applied in order to emphasize the lateral continuity of strong as well as weak events, to estimate the geometrical properties of the amplitude anomalies and to highlight the discontinuities, such as discontinuities.

The Instantaneous Frequency attribute is useful to discriminate the different range of frequency that characterized the data. In particular, the three seismofacies exhibit distinct Instantaneous Frequencies trends: the seismofacies A and B are characterized by medium to high frequency reflectors, while the seismofacies C shows a low frequency content. Furthermore, the amplitude anomalies highlighted by the Reflection Strength attribute correspond to low Instantaneous Frequency anomalies.

The Sweetness attribute is calculated by the combination of Instantaneous Frequency and Reflection Strength (Hart, 2008; Riedel, 2010; Yushun, 2011) and it is useful to better distinguish the events characterized by high values of acoustic impedance. This attribute clearly highlights the limits of the three seismofacies as well as the anomalies. The seismofacies A presents dominant Sweetness values around zero and, within it, few reflectors with higher Sweetness values are observed. The seismofacies B is made up of packages of laterally continuous reflectors with medium-high Sweetness values. Below, the seismofacies C is characterized by the presence of less continuous reflections, compared with the seismofacies A and B. They exhibit quite high Sweetness values and are enclosed in a background that presents Sweetness values comprised between 0 and 1000.

Therefore, the detection of the anomalies related to the igneous bodies is performed through the application of the seismic attributes. In particular, the Reflection Strength and the Sweetness attributes permit to isolate the high amplitude value anomalies from the low reflective seismofacies C. The Instantaneous Phase allows the identification of some sills within the seismofacies B masked by chaotic reflections. These igneous bodies present antiformal junctions, T- and F-shaped morphologies and saucer-shaped geometries. The Instantaneous Frequency permits to characterize the sills as bodies with a frequency range of 25-30 Hz. The amplitude anomalies within the seismofacies C show values between 10 and 25 Hz, while the anomalies in the seismofacies A show values up to 40 Hz. Regarding to those within the seismofacies B, they are not resolved due to the chaotic facies with too high frequencies.

**The Continuous Wavelet Transform (CWT).** In order to improve the geometry interpretation, the Continuous Wavelet Transform (CWT) is applied (Debauchies, 1988; Mallat, 1989; Zhang *et al.*, 2006). The CWT provides a method for displaying and analysing signals as a function of time and scale. The scale and the frequency are related to an inverse relationship of proportionality, which means that the higher the scale the lower the frequency. Therefore, the wavelet transform allows to decompose the seismic data into a time versus scale (frequency band) domain and subsequently, if needed, to reconstruct them in the scales of interest. The analysis of the reconstructed common scale volumes permits to obtain a representation of the frequency information, which is contained in a seismic section.

In particular, the CWT is defined as follows (Debauchies, 1988; Zhang *et al.*, 2006):

It can be considered the cross-correlation between the seismic trace and the dilated and scaled versions of an user defined wavelet. The mother wavelet is the analysis wavelet function,  $a$  is the location parameter of the wavelet, so that  $(t-a)$  defines the shift of the wavelet along the trace, and  $b$  is the scaling (dilation) parameter.

By shifting and scaling the mother wavelet, the Wavelet Transform is able to capture information of short duration (high frequency) or information of long duration (low frequency), at the same time.

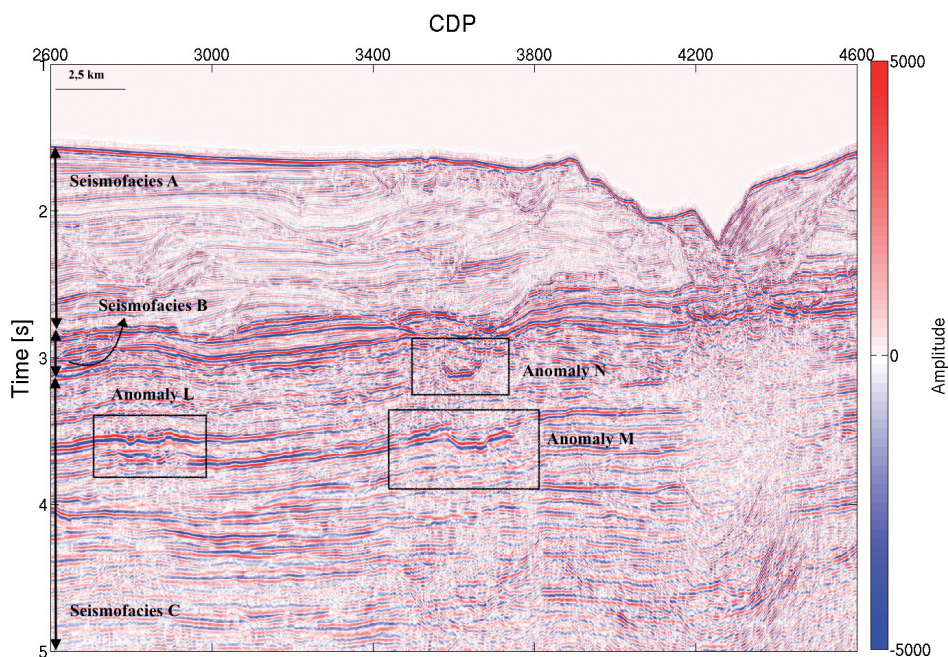


Fig. 3 – Reconstruction of the inline1560 through the sum of the coefficients of the chosen db2 scales. The limits between the seismofacies A, B, C and the localized amplitude anomalies L, M and N, related to the igneous bodies, are highlighted.

Finally, the CWT can be interpreted as a bank of band pass filters process, but it is more flexible than other time–frequency transform such as the Short Time Fourier Transform (STFT). Unlike the STFT, that uses a window with fixed width, the mother wavelet is dilated and translated in such a way to be designed to balance the resolution between time domain and frequency domain. Furthermore, the CWT is particularly useful to locate and identify signals with exotic spectral characteristics (Sadowsky, 1996).

As well as for the seismic attributes, a *line by line* CWT analysis is carried out.

The CWT is tested using three different mother wavelets: the Haar wavelet, the order 2 Daubechies wavelet (db2) and the Morlet wavelet (morl).

Although the best result was expected by the application of the Morlet wavelet, that is the commonly used wavelet, if the transform is aimed at improving the quality of the seismic section (Sadowsky, 1996), the db2 is adopted. As an example, the reconstruction of the inline 1560 through the sum of the coefficients of the chosen db2 scales is shown in Fig. 3.

The analysis shows that the anomalies related to the igneous bodies can be approximated in a frequency range from 20 up to 30 Hz. This is in agreement with the Instantaneous Frequency response. Furthermore, the application of the CWT is useful to discriminate the igneous bodies within the seismofacies B that are masked due to the presence of a chaotic facies.

**Conclusions.** The Senegal Basin is characterized by the presence of discordant low frequency high amplitude reflection anomalies that are interpreted as Miocene intrusive bodies (Rocchi *et al.*, 2007). This interpretation is supported by the data obtained from the on-shore survey of the Senegal area. The main result of this survey is the identification of magmatic activity ranges from Oligocene to Quaternary.

From the *line by line* analysis of the eighteen seismic lines results that the detected nineteen sills can be classified on the basis of their age, levels of emplacement and geometries. In particular, most of the sills develop within the seismofacies C at the first level of emplacement

(TWT >3.5 s). These anomalies show a flat inner saucer geometry, often bounded by an inclined sheet that crosscuts upwards the seismofacies C, and deform the overburden reflectors in a gently symmetrical antiformal fold.

The amplitude anomalies, which develop in the second level of emplacement ( $3.5 \text{ s} < \text{TWT} < 2.7 \text{ s}$ ), show a concave-upwards saucer-shaped morphology and are characterized by the formation of two inclined sheets, often one steeper than the other. Moreover, some of these bodies show T- and F-shaped or antiformal morphology. At the third level ( $\text{TWT} < 2.7 \text{ s}$ ), only two sills, developed within the seismofacies A, crosscut the seismo-stratigraphic reflectors, obliterate the underlying seismofacies B and deform the overlying reflectors as a structural dome.

Furthermore, by applying the seismic attributes, it is possible to better distinguish the sills based on the strong Reflection Strength and Sweetness response, which allow to isolate the seismic anomalies from the low amplitude background. Likewise, the Instantaneous Phase consents to distinguish, particularly within the seismofacies B, the seismic bodies characterized by a composite shape and masked in a chaotic facies. The Instantaneous Frequency is useful to differentiate the igneous bodies on the basis of the frequency values, always lower than the host-rock.

According to the seismic attributes, the results obtained by the application of the CWT permit to classify the anomalies as bodies with a frequency range of 25-30 Hz. Moreover, this tool permits to characterize the bodies based on their geometrical features and it is fundamental to compute thickness, lateral extent, emplacement depth, diameter-to-depth ratio and related-fold amplitude of the sills. Furthermore, from the obtained measurements it is possible to understand the relations between thickness and emplacement depth, to compare thickness and the related-fold amplitude and to compute the relationship between these parameters.

This work can supply new inputs improving the knowledge of the stratigraphy, of the geological setting and of the evolution of the investigated area. The achieved characterization of the igneous bodies can be of crucial importance for the hydrocarbon exploration. The presence of igneous intrusions in a petroleum system could cause important effects on the maturation of the source rocks, on the creation of structural and stratigraphic traps and, finally, could affect the oil migration pathway (Holford *et al.*, 2012; Thomson, 2007; Thomson *et al.*, 2008; Svensen *et al.*, 2006).

## References

- Barnes, A. E.; 2001: *Seismic attributes in your facies*. CSEG Recorder, 41-47.
- Debauchies, I.; 1988: *Orthonormal bases of Compactly supported wavelets*. Communication on Pure and Applied Mathematics, **41**, 909-996.
- Hart, B.S.; 2008: *Channel detection in 3-D seismic data using sweetness*. AAPG Bulletin, **92**, 6, 733-742.
- Holford, S.P., Schofield, N., MacDonald, J.D., Duddy, I.R. and Green, P.F.; 2012: *Seismic analysis of igneous systems in sedimentary basins and their impacts on hydrocarbon prospectivity: examples from the southern Australian margin*. APPEA Journal, 229-252.
- Mallat, S.G.; 1989: *A Theory for Multiresolution Signal Decomposition: The Wavelet Representation*. IEEE transactions on pattern analysis and machine intelligence, **2**, 7, 674-693.
- Riedel, M., Collett, T.S., Kumar, P., Sathe, A.V. and Cook, A.; 2010: *Seismic imaging of a fractured gas hydrate system in the KrishnaeGodavari Basin offshore India*. Marine and Petroleum Geology, **27**, 1476-1493.
- Rocchi, S., Mazzotti, A., Marroni, M., Pandolfi, L., Costantini, P., Bertozzi, G., Di Biase, D., Federici, F. and Lô, P.G.; 2007: *Detection of Miocene saucer-shaped sills (offshore Senegal) via integrated interpretation of seismic, magnetic and gravity data*. Terra Nova, **19**, 232-239.
- Sadowsky John; 1996: *Investigation of Signal Characteristics Using the Continuous Wavelet Transform*. Johns Hopkins APL Technical Digest, **17**, 3, 258-269.
- Satyavani, N., Kalachand S., Malcolm L. and Kumar, B. J. P.; 2008: *Seismic attribute study for gas hydrates in the Andaman Offshore India*. Mar Geophys Res, **29**, 167-175.
- Svensen, H., Jamtveit, B., Planke, S. and Chevallier, L.; 2006: *Structure and evolution of hydrothermal vent complexes in the Karoo Basin, South Africa*. Journal of the Geological Society, London, **163**, 671-682.
- Subrahmanyam, D. and Rao, P.H.; 2008: *Seismic Attributes- A Review*. 7<sup>th</sup> International Conference & Exposition on Petroleum Geophysics; Hyderabad, India.

- Taner, M. T., Koehler, F. and Sheriff, R. E.; 1979: *Complex seismic trace analysis*. Geophysics, **44**, 6, 1041-1063.
- Thomson, K.; 2007: *Determining magma flow in sills, dykes and laccoliths and their implications for sill emplacement mechanisms*. Bull. Volc., **70**, 183-201.
- Thomson, K. and Schofield, N.; 2008: *Lithological and structural controls on the emplacement and morphology of sills in sedimentary basins*. Thomson, K., Petford, N. (Eds.), Structure and Emplacement of High-Level Magmatic Systems. Geological Society, London, Special Publication, **302**, 31-44.
- White, R.E.; 1991: *Properties of instantaneous seismic attributes*. Geophysics: The leading edge of exploration, 26-32.
- Yushun, D., Zhaoquan, P., Lingbang, Z. and Mingbo B.; 2011: *Carbonate reservoir and gas-bearing property detection using sweetness*. SEG San Antonio 2011 Annual Meeting, 1197-1201.
- Zhang, L., Gao, R.X. and Lee, K.B.; 2006: *Spindle Health Diagnosis Based on Analytic Wavelet Enveloping*. IEEE Transactions On Instrumentation And Measurement, **55**, 5, 1850-1858.

## SEISMIC ANALYSIS OF A BSR IN THE DOVE BASIN (SOUTH SCOTIA SEA)

A. Mocnik<sup>1</sup>, D. Civile<sup>2</sup>, A. Del Ben<sup>1</sup>, R. Geletti<sup>2</sup>

<sup>1</sup> Dipartimento di Matematica e Geoscienze, University of Trieste, Italy

<sup>2</sup> OGS, Trieste, Italy

**Introduction.** In this paper we report the results from the seismic analysis of the part of the seismic profile IT95-167 that crosses a main part of the Falkland Plateau (Del Ben and Mallardi, 2004), the Dove Basin, located in the south Scotia Sea, with a N-S direction (Fig. 1). This analysis shows the presence of a high amplitude reflector that cuts the folded reflections related to the sedimentary infilling of the Dove Basin and mimics the shape of the seafloor. This Bottom Simulating Reflector (BSR) lays at about 750 ms. TWT below the seafloor, which is at a depth of more than 4200 m.

The Dove Basin is an oceanic basin bordered by the Pirie and Bruce Banks, respectively to its west and east margins, and by the continental slope of the South Scotia Ridge, to the south. It shows a roughly sigmoidal shape with an abyssal plain characterized by an average depth of about 3500 m. A prominent NNE-SSW elongated ridge (Dove Ridge), about 50 km long, is positioned in the central part of the basin and it is considered as an extinct spreading centre (Eagles *et al.*, 2005; Galindo-Zaldívar, 2014).

The seismic facies and the geometrical setting of the anomalous reflector identified suggested us to explore the origin of this BSR. Somoza *et al.* (2014) highlighted the presence of BSRs at three different levels in the Scan Basin located immediately to the east of the Bruce Bank. The authors interpreted the two deeper BSRs as fossil diagenetic fronts caused by elevated geothermal gradients respectively during the early and the middle Miocene; while the shallowest BSR would be originated by the presence of gas hydrates.

The presence of the seismic anomaly observed in the Dove Basin could be related to: 1) presence of Opal-A/Opal-CT transformation associated to a fossil diagenetic front; or 2) presence of a gas hydrate BSR in the Dove Basin. This second hypothesis should suggest the presence of abiogenic gas, derived by the serpentinization of basaltic rocks (Rajan *et al.*, 2012), which compose the oceanic basement of the Dove Basin.

- 1) Fossil diagenetic fronts are due to several varieties of silica minerals: amorphous quartz (opal-A), cryptocrystalline quartz (opal-CT/-C) and microcrystalline quartz (chalcedony, quartzine, etc). At low temperatures opal-A is generally precipitated inorganically or biogenically from natural aqueous solutions. During diagenesis siliceous deposits undergo mineralogical changes from opal-A to opal-CT/-C to microcrystalline quartz (Flörke *et al.*, 1982). This results in a density increase across the interface between the two forms of opal, producing a strong reflection with a positive polarity. This reflection follows

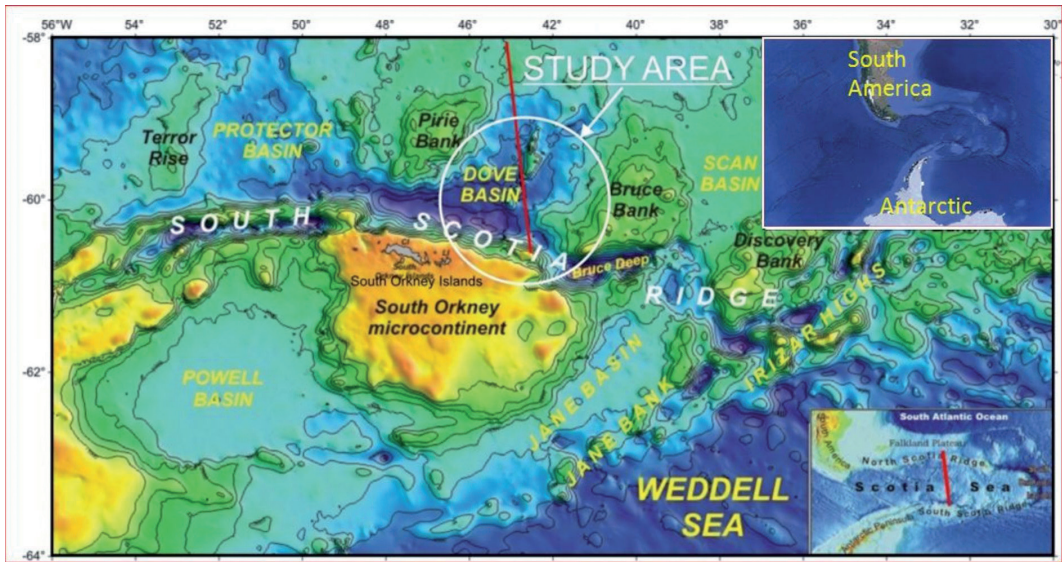


Fig. 1 – Physiographic map of the southern margin of the Scotia Sea, with the indication of the principal banks and basins. The study area is in the white circle.

an isothermal surface, mimicking and crosscutting the reflectors of the stratigraphic succession.

- 2) The gas-hydrate BSR displays high seismic amplitude with reverse polarity often accompanied by lowered frequency (low-frequency shadow) due to attenuation by free gas (Vanneste *et al.*, 2002). On a global scale, abiogenic or abiogenic  $\text{CH}_4$  is produced in much smaller amounts respect biogenic  $\text{CH}_4$ , and is generally not recognized in economically exploitable reservoirs. In many geological environments, biotic and abiogenic gases are mixed, and in many cases it is not easy to distinguish them. From scientific literature, magmatic process and gas-water-rock reactions trigger the production of abiogenic  $\text{CH}_4$  (Etiope and Sherwood Lollar, 2013). The most widely abiogenic  $\text{CH}_4$  generation mechanism in natural settings is the serpentinization of ultramafic rocks.

The two options presented are both compatible with the few available data on the geothermal gradient in the south Scotia Sea (yield values of  $86.89 \text{ mW/m}^2$  at 2918 m water depth in the Scan Basin, Barker *et al.*, 2013).

During the year 2013, a sub-project has been presented and funded by the PNRA to explore these alternative possibilities in the context of the project VALFLU.

**Geological setting.** The Scotia Sea region is mainly of oceanic crustal structure and origin. It is bounded by the Drake Passage to the west and by the Scotia Arc on three sides. The Scotia Arc consists of the North and South Scotia Ridges, which are an assemblage of islands, submarine fragments of continental crust and deep basins, and of the South Sandwich island arc to the east. Oceanic magnetic anomalies suggest an Oligocene–Early Miocene age for the first sedimentary unit covering the basement of the Scotia Sea (MalDONADO *et al.*, 2006). Lindeque *et al.* (2013) highlighted a diachronic opening in the Scotia Sea (17.3–12.0 Myr): the oldest part would be near the Antarctic Peninsula, while toward northwest it becomes younger. The Dove Basin is a small NNE-SSW oriented sigmoidal depression located in the South Scotia Ridge. It is positioned between  $60.5$  and  $58.5^\circ \text{ S}$ , and between  $45$  and  $40^\circ \text{ W}$ , about 200 km long and 150 km wide. A NNE-SSW elongated ridge (Dove Ridge), about 50 km long, occupies the central part of the basin, where MORB-type tholeiitic basalt rocks have been recovered. In the basin depocenter, the sedimentary succession overlying the oceanic basement reaches more than 1.5-s TWT.

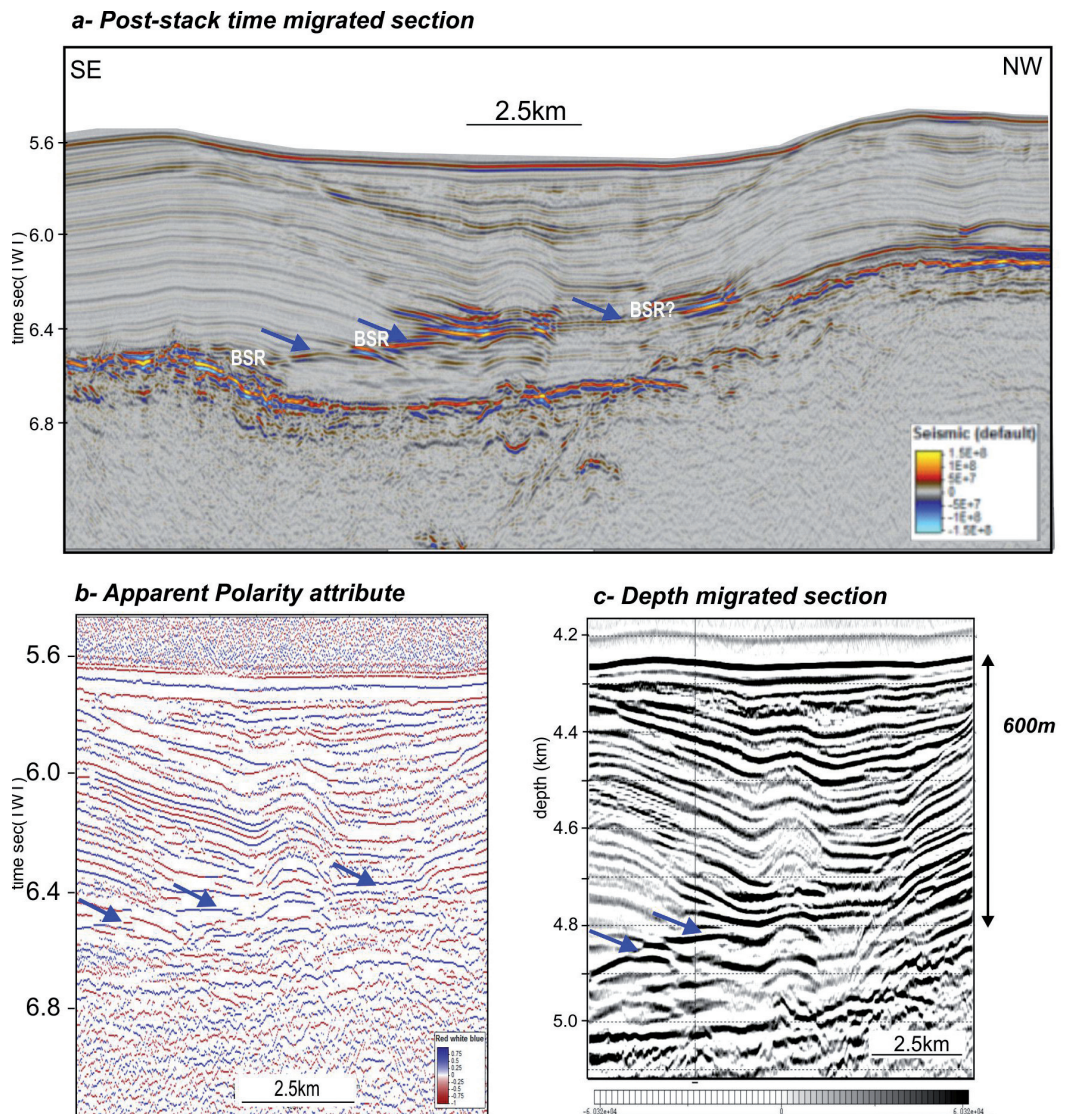


Fig. 2 – a) Portion of post-stack time migrated seismic profile 195-167 from SP1600 to SP2070; the blue arrows depict the extension of the observed BSR; b) application of Apparent Polarity seismic attribute obtained by Petrel software; the blue arrows indicate the position of BSR, which evidences a positive polarity; c) pre stack depth migrated section that let to reconstruct the real geometry of the layers and the depth of the BSR at about 600 m below the sea bottom.

Eagles *et al.* (2005) proposed an Eocene age (between 34.7 and 41 Myr) for the development of the Dove Basin, based on magnetic anomaly models and on the depth of the oceanic basement. Barker *et al.* (2013) suggested an age between 42 and 43 Myr for the oceanic crust, on the base of heat flow data. Galindo-Zaldivar *et al.* (2014) proposed, considering petrological, geochemical and geophysical data, integrated by absolute dating of dredge samples, that the Dove Basin was a back-arc basin developed from the Late Oligocene to the Early Miocene with a final volcanic episode at around 18 Myr.

**Analysis of seismic data.** *Seismic Data description.* The multichannel seismic reflection profile used in this work is the portion of the line IT95-167 crossing the Dove Basin in the south Scotia Sea. The data were collected by the Italian National Program for Antarctic Research

(PNRA) during the project SCOTIA (March 1995). The MCS data were acquired using an airgun source (combined chamber capacity of 80 l) and 120-channel seismic streamer with maximum offset of 3000 m. The recording parameters are: shot spacing 50 m, group interval spacing 25 m, CMP spacing 12.5 m and fold 30%. The total recording length is 15-s TWT and sample interval 4 ms; in this work, we considered the time window of 8-s TWT depth.

Along the analyzed seismic profile, the presence of a high amplitude reflector, which is almost parallel to the sea floor and cuts the reflections related to the sedimentary succession overlying the basement, is recognized at a depth of about 6.75-s TWT. It extends over about 600 CMP, covering a length of almost 7 km (Fig. 2a). These characteristics allow to define the recognized reflector as a BSR.

A BSR can be ascribed to:

- 1) a density increase across the interface between the two forms of opal, producing a strong reflection with a positive polarity;
- 2) the base of the stability zone (pressure and temperature conditions) of gas hydrates. Above a BSR, a solid phase of methane combined with water is present within a clastic matrix and this horizon produces an increment of the P-wave velocity. Below the BSR, free gas is present in the porous space of the rocks causing a drop of P-wave velocity. For this reason, the interface between the two gas phases is generally highlighted by a strong impedance contrast and high amplitude reflectors with negative polarity.

To analyze peculiar seismic features along the reflector, we re-processed the seismic profile focusing on the velocity analysis, depth migration and seismic attribute analysis.

*Re-processing and pre-stack depth migration.* We re-processed the portion of seismic profile using Focus (Paradigm) software, focusing on the velocity analysis of the acoustic wave across the interface; the first results of this analysis doesn't evidence clear velocity inversions along the entire length of the considered reflector.

A preliminary seismic attribute analysis of this reflector has been carried on to highlight the amplitude-phase and frequency characteristics.

The main objective of the use of attributes is to provide detailed information to the interpreter on structural, stratigraphic and lithological parameters of the seismic prospect. The attributes extraction allows to detect more easily some features that might not be directly observed on the original data and which are typically expressed by the attribute "amplitude". The benefit is to obtain the measured attributes at the same scale as the original seismic data.

A general definition of seismic attribute has been given by Chopra and Marfurt (2005). In the most general sense, they consider as seismic attributes all the quantities derived from a seismic data, including interval velocity, inversion of acoustic impedance, pore pressure prediction, reflectors termination and Amplitude Variation with Offset (AVO). This approach is useful in hydrocarbon exploration, because it contributes to improve the reservoir analysis and some attributes can be used as specific Direct Hydrocarbon Indicators.

Instantaneous amplitude, phase, cosine of phase and frequency attributes are the most effective to highlight the features of the observed BSR and could give a qualitative approach for a first ascription to one of the different hypothesis.

We analyzed the Apparent Polarity attribute to recognize possible phase inversion of acoustic wave at the base of BSR, due to solid/gas conversion below the Gas Hydrates Stability Zone (GHSZ). This attribute (Fig. 2b) shows in red-blue-red the phase behavior of the sea-bottom; the BSR shows the same passage of phase. Together with the velocity analysis, this represents a further result that reduces the possibility of a gas hydrate BSR.

Using Geodepth (Paradigm) software, we performed a further velocity analysis in order to convert root mean square values into interval velocity values using Dix equations. This led to create Common Depth Gather and to obtain a depth migrated sections (Fig. 2c).

This processing phase allowed to reconstruct the real geometry of the reflectors and to measure the thickness of the sedimentary sequence above the BSR. The water depth is at about

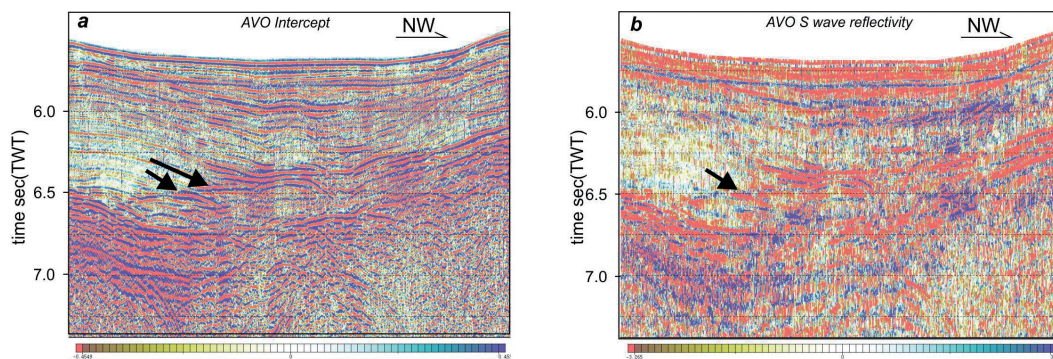


Fig. 3 – Application of AVO seismic attributes using Focus software (Paradigm) after true amplitude recovery by spherical divergence and generation of common angle gathers. In a), the result of AVO Intercept/P wave reflectivity at zero offset enhances the acoustic impedance in correspondence of the BSR, characterized by positive values; in b), the result of S wave reflectivity that shows a weak reflection in correspondence of the black arrow, denotes change of density across the interface.

4270 m and the thickness of sediments above the BSR ranges from 500-600 m. This value seems to be higher respect the common depth of the GHSZ.

*AVO seismic attributes analysis.* By the analysis of the P and S wave reflectivity, of the velocity values variation and of the components of the seismic data (amplitude, phase and frequency), we can obtain the information that allow to ascribe or not this seismic features to the presence of gas.

Nowadays, the AVO analysis has become a commercial tool for the oil industry; in particular, it lets geophysicists to better locate and classify gas or oil reservoirs, reducing the possibility of unproductive drills. The AVO techniques could be considered a good discriminator even in the case of gas-hydrate.

The offset-dependent reflectivity has its basis in the theoretical relationships between reflection coefficient, angle of incidence and variation of the compressional P wave velocity, shear S wave velocity and density across an interface; these contrasts are in turn dependent on rock properties variations. In presence of gas, brine-saturated and water-saturated unconsolidated sediments, these parameters have distinctive relationships; thus, using AVO analysis, bright spots caused by gas accumulation can be distinguished by mislead anomalous amplitude reflectors that could be caused by coal, cineritic or other low impedance units.

The AVO analysis is based on the observation and interpretation of the curves describing the variation of the Incident reflectivity with the angle of incidence (Castagna and Swan, 1997). Different AVO attributes have been extracted to apply multivariate analysis: the two most important are the zero offset reflectivity, defined Intercept, and the AVO Gradient, based on Shuey's approximation.

In presence of gas hydrates, the analysis of P- and S-wave reflectivity, which are related to the Poisson's ratio, gives important information on the fluid content and on rigidity of the solid matrix (Carcione and Tinivella, 2000). S-waves do not cross the fluid, so they are independent by the fluid contents showing changes of the solid matrix, which is due to the hydrocarbon hydrate compaction.

We analyze the P and S reflectivity by software Focus (Paradigm), which extract 9 AVO attribute sections from the generation of common angle gathers. For instance, the zero-offset extrapolated amplitude section is created on a sample-by-sample basis by transforming the data to the form of amplitude versus the trigonometric sin of the reflectance angle squared. A linear regression analysis is then performed and the fitted line is extrapolated to zero-offset, which forms the zero-offset section.

Similarly, the program creates a number of other sections, including a slope section (the slope of the fitted line), a product section (slope multiplied by the zero-offset amplitude), a Poisson's ratio section, and S-wave amplitude section. The latter two are formed from the zero-offset amplitude and the slope sections, using assumptions of small change in Poisson's ratio and an average  $V_p/V_s$  ratio of 2.0 (Poisson's ratio = 0.333).

For this analysis we prepared the original CDP by applying a band-pass filtering (cut frequencies 4-8/50-120 Hz) and in particular by the recovering the true amplitude of the reflected signal by spherical divergence correction.

Here we reproduce the results of the P-wave reflectivity and S-wave reflectivity in order to find their correlation. We observe (Fig. 3a) that across the BSR the P wave intercept is mainly characterized by positive values (blue color) and in particular by no relevant polarity inversion. On the other hand, the high amplitude reflection values could be significant of a change of fluids matrix properties of the material.

In Fig. 3b the S wave amplitude section has been obtained: it shows weak reflections in correspondence of the BSR. In association of what we observed on P wave reflectivity along the interface, even a change of density can be assumed.

**Conclusions.** The analysis of the portion of the seismic profile IT95-167 crossing the oceanic Dove Basin, located in the south Scotia Sea, has allowed to identify a high amplitude anomalous reflector that cuts the primary reflections assigned to the sedimentary infilling of the basin and mimic the shape of the seafloor. This type of signal could be interpreted as a BSR due to the gas hydrate layer or to an Opal-A/Opal-CT transformation zone.

Using different approaches to analyze this seismic BSR, we can synthesize our results as following:

- Velocity analysis: the velocity spectrum is ambiguous; a velocity inversion is not clear, but possible. Both the considered causes to explain the presence of the BSR could be realistic.
- Polarity attribute: not negative polarity has been highlighted by the polarity attribute analysis; this suggests an Opal -A/Opal-CT transformation.
- The measured thickness of the sediments above of the BSR seems to be higher than the common values of GHSZ; this turns away the hypothesis that the reflector could be related to gas hydrate.
- AVO: P and S-waves reflectivity only support density change across the BSR.

The comparison and integration of the different obtained results seem to be not sufficient to support the hypothesis of a gas hydrate BSR potentially associated to the presence of abiogenic gas in the sedimentary succession overlying the oceanic basement of the Dove Basin. On the contrary, an Opal-A/Opal-CT transformation seems to be a more plausible hypothesis. We intend to apply further analysis to better clarify the origin of the identified BSR.

**Acknowledgements.** The authors gratefully acknowledge Paradigm through the OGS Focus and Geodepth processing software, and Schlumberger through the University of Trieste Petrel academic grant for interpretation software.

## References

- Barker P.F., Lawler L.A. and Larter R.D.; 2013: *Heat-flow determinations of basement age in small oceanic basins of the Southern central Scotia Sea*. Geological Society, London, Special Publications 381, 139-150.
- Carcione J. M. and Tinivella U.; 2000: *Bottom-simulating reflectors: seismic velocities and AVO effects*. Geophysics, **65**, 54-67.
- Castagna J.P. and Swan H.V.; 1997: *Principles of AVO crossplotting*. The Leading Edge, **16**, 337-342.
- Chopra S. and Marfurt K.J.; 2005: *Seismic Attributes-A historical perspective*. Geophysics, **70**(5), 3-28.
- Del Ben A. and Mallardi A.; 2004: *Interpretation and chronostratigraphic mapping of multichannel seismic reflection profile I95167, Eastern Falkland Plateau (South Atlantic)*. Marine Geology, **209**, 347-361.
- Eagles G., Livermore R.A., Fairhead J.D. and Morris P.; 2005: *Tectonic evolution of the West Scotia Sea*. Journal of Geophysical Research B: Solid Earth, **110**(2), 1-19.
- Etioppe G. and Sherwood Lollar, B.; 2013: *Abiotic Methane on Earth*. Reviews of Geophysics, **51**, 276-299.

- Flörke O. W., Köhler-Herbertz B., Langer K. and Tönges I.; 1982: *Water in Microcrystalline Quartz of Volcanic Origin: Agates*. Contrib. Mineral. Petrol., **80**, 324 - 333.
- Galindo-Zaldívar J., Puga E., Bohoyo F., Gonzales F.J., Maldonado A., Martos Y.M., Perez L.F., Ruano P., Schreider A.A., Somoza L., Surinach E. and de Fenerico Antonio D.; 2014: *Magmatism, structure and Age of Dove Basin (Antartica): A key to understanding South Scotia Arc development*. Global and Planetary Change, **122**, 50-69.
- Lindeque A., Martos Y.M., Gohl K. and Maldonado, A.; 2013: *Deep-sea pre-glacial to glacial sedimentation in the Weddell Sea and southern Scotia Sea from a cross-basin seismic transect*. Mar. Geol., **336**, 61–83.
- Maldonado A., Bohoyo F., Galindo-Zaldívar J., Hernández-Molina F.J., Jabaloy A., Lobo F. J., Rodríguez-Fernández J., Suriñach E. and Vázquez J.T.; 2006: *Ocean basins near the Scotia–Antarctic plate boundary: influence of tectonics and paleoceanography on the Cenozoic deposits*. Mar. Geophys. Res., **27 (2)**, 83–107.
- Rajan A., Mienert J., Bünz S. and Chand S.; 2012: *Potential serpentinization, degassing and gas hydrate formation at a (< 20Ma) young sedimented ocean crust of the Arctic Ocean Ridge system*. J. Geophys. Res., **117**, B03102, doi:10.1029/2011JB008537.
- Somoza L., Leon R., Medialdea T., Perez L.F., Gonzales F.J. and Maldonado A.; 2014: *Seafloor mounds, craters and depressions linked to seismic chimneys breaching fossilized diagenetic bottom simulating reflectors in the Central and Southern Scotia Sea, Antartica*. Global and Planetary Change, DOI: 10.1016/j.gloplacha.2014.08.004.
- Vanneste M., Guilard S. and Mienert J.; 2002: *Bottom-simulating reflections and geothermal gradients across the western Svalbard margin*. Terra Nova, **17**, 510-516.



## sessione 3.2

### **Geofisica applicata superficiale**

Convenor: G. Cassiani e L. Sambuelli

co-organizzata con Sezione Italiana Eage-Seg

---



## STUDY OF A RECONSTRUCTED RIVER EMBANKMENT THROUGH A COMBINATION OF NON-INVASIVE GEOPHYSICAL METHODOLOGIES

L. Busato<sup>1</sup>, J. Boaga<sup>1</sup>, L. Peruzzo<sup>2</sup>, G. Asta<sup>3</sup>, S. Cola<sup>3</sup>, P. Simonini<sup>3</sup>, G. Cassiani<sup>1</sup>

<sup>1</sup> Department of Geosciences, University of Padua, Padua, Italy

<sup>2</sup> ENSEGD, University of Bordeaux, Pessac, France

<sup>3</sup> Department of Civil, Architectural, and Environmental Engineering, University of Padua, Padua, Italy

**Introduction.** In the last decades, frequency and magnitude of extreme flood events on the Italian territory have been rapidly increasing as a consequence of the combination of several factors, such as climate changes and scarce prevention. When river embankments provide the only defence against these phenomena, their characterization and maintenance play a pivotal role in the hydrogeological risk reduction. Usually, embankment monitoring takes place only through visual inspections and punctual measurements that do not allow an extensive and exhaustive characterization. If proper heterogeneities identification is lacking, dramatic water level variations may lead, at worst, to the levee collapse, which then requires rapid emergency interventions. The result usually consists in unsuitable artificial structures that typically require further enhancement interventions and in the overlap of several focused but non-resolving operations developing structures whose features are barely known.

Applied geophysics provides different non-invasive and cost-effective methodologies, whose application overcomes several issues of typical monitoring techniques (e.g., piezometers and geotechnical sounding). The use of electrical resistivity tomography is nowadays state of the art in the levee (and dam) characterization (Cho and Yeom, 2007; Sjödal *et al.*, 2009), together with seismic methods (Karl *et al.*, 2011), ground penetrating radar (Di Prinzio *et al.*, 2010), and self-potential (Panthulu *et al.*, 2001; Moore *et al.*, 2011). But what can actually improve the embankment characterization is the joint use of different geophysical methodologies (Inazaki and Sakamoto, 2005; Cardarelli *et al.*, 2014), also combined with geotechnical soundings to validate the information thus obtained (Perri *et al.*, 2014). These techniques are helpful also when dealing with concrete structures (both in terms of dynamic properties and moisture content distribution analysis) where concrete appears as a relatively conductive mean from an electrical point of view (Turk *et al.*, 1987; Karastathis *et al.*, 2002; Karhunen *et al.*, 2010).

For these reasons, in this work we combine four different non-invasive geophysical methodologies in order to characterize a reconstructed stretch of the Frassine river embankment, whose collapse occurred during a flood event in 2010. Our experimental site, located within the municipality of Megliadino San Fidenzio (Padova province, northern Italy), underwent several further interventions in order to improve the structure stability and impermeability. Nevertheless, several seepage phenomena are currently occurring within this reconstructed sector, resulting in concern about the embankment stability. An appropriate and extensive characterization is then mandatory, and is obtained through the combination of electrical resistivity tomography, multichannel analysis of surface waves, ground penetrating radar, and self-potential. This *modus operandi* provided promising results, whose combination with other information from other techniques (e.g., geotechnical soundings, piezometer measurements, and so on) will lead to a complete site characterization.

**Field site and flood description.** The case study analysed in this work consists in a reconstructed river embankment located within the municipality of Megliadino San Fidenzio (Padova, northern Italy), in the Prà di Botte area (Lat. 45°15'18.3" N, Long. 11°32'35.8" E). From a geological point of view, this site lies in the Adige Alluvial Plain, which is part of the Venetian-Friulian Plain, and therefore is characterized by Tertiary to Quaternary sediments. The entire domain has been strongly influenced by the Last Glacial Maximum (LGM, 30,000-17,000 years B.P.) and the following post-LGM phase, which led to paleosols (e.g., caranto paleosol) and fluvial terraces (Fontana *et al.*, 2008). More in detail, the field site area consists of ancient fluvial ridges now evolved into silty-clayey soils with a low sand content (ARPAV, 2013).

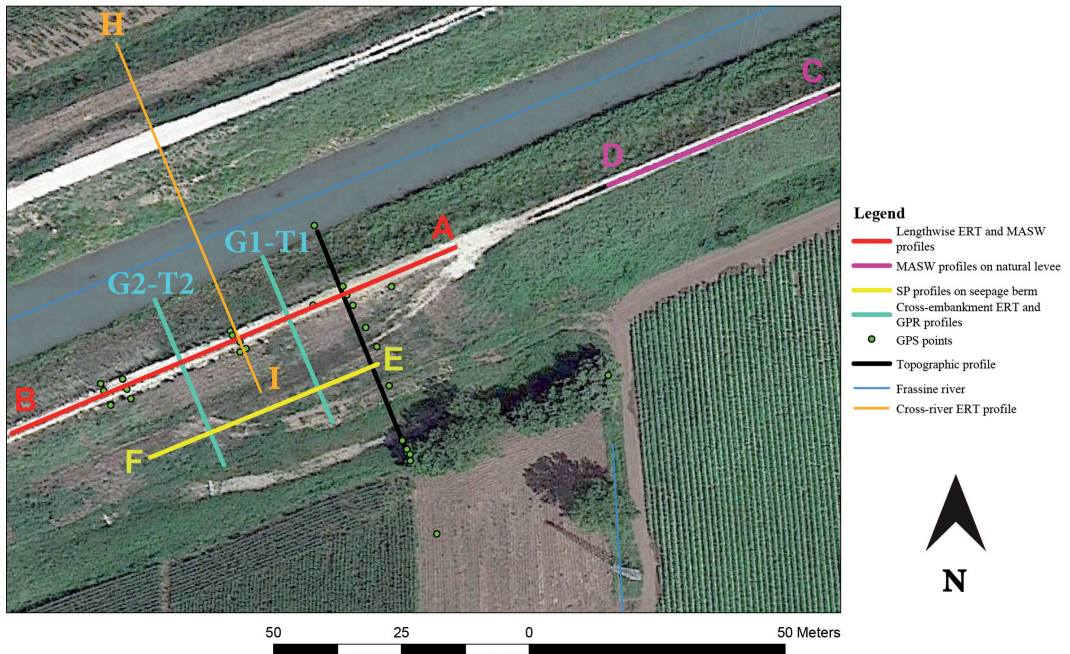


Fig. 1 – Map of all profiles on the Frassine site. The low-outer face SP profiles are not represented.

The Frassine River, to which the reconstructed embankment belongs, is one of the six segments into which the Guà River is divided. It flows between Borgo Frassine (Montagnana, PD) and Brancaglia (Este, PD), with a length of 13.42 km, and is part of the Brenta-Bacchiglione catchment. From a hydrological point of view, this river has a mixed regime that implies higher flow rates during spring and autumn and lower flow rates on the other seasons (Bondesan, 2001).

The flooding event that caused the levee rupture took place in the early afternoon of November 1, 2010, when the water level of the Frassine river reached its historical peak (4.54 m) after a three-day heavy precipitation event that resulted in a cumulative rainfall amount of 300 mm (ARPAV, 2010). The collapse occurred on the right levee and had spread up to a total length of 100 m when a preliminary barrier with boulders of different diameters was built. Then, the positioning of several reinforced concrete bars on the levee outer side increased the structure stability, while the installation of sheet piles on the inner side allowed the stopping of the water flow. Finally, three days after the flood event, the whole preliminary structure was covered with aggregates (tout-venant), thus ending the first step of the embankment restoration.

In order to provide a long-term solution, new reinforcement works from the embankment crest took place in 2012 (second step). They can be divided into three phases: i) concrete injection along the whole preliminary structure (110.0 m length, 9.5 m depth), ii) jet-grouting diaphragm construction, extended also to the undamaged levee (170.0 m total length, 22.0 m total depth) and iii) Tube a Manchette grouting to further waterproof the whole structure. Despite these actions to improve the embankment’s functionality, several water infiltration phenomena occurred during the following months, thus highlighting a lack of homogeneity within the new structure. More in detail, a more diffusive seepage process in the embankment toe marked the upstream sector, while water infiltration in the lower part of the outer face characterized the downstream portion. Therefore, nine geotechnical soundings were carried out in 2013: six of them analysed the reconstructed part, showing a rather complex domain, where the different reinforcing interventions overlap. Since they provide only punctual information, these soundings

dot not allow a complete evaluation of the embankment and lack in identifying the (probable) discontinuities within this segment. The remaining three soundings examined the earthen levee, which is homogeneously composed of silty-clayey sand, as expected. Furthermore, they show a clayey level between 11 m and 13 m depth.

Given the need of dealing with these infiltration events, new interventions modified the outer face of the reconstructed embankment in 2014 (third step). A stability bank with a 0.5 m thick gravel drainage mattress was built, with a seepage berm and a collector ditch to avoid water stagnation. A section of the resulting geometry is outlined in Fig. 2a. The embankment total height from ground level is circa 8.7 m, with a crown 4 m wide, and both inner and upper outer faces have a ratio of width to height of 3:2. The stability bank is 5 m high from ground level, has a ratio of width to height of 2:1 and a 4 m wide crown.

**Methodologies and acquisitions.** The characterization of this site is performed through the application of four different methodologies: electrical resistivity tomography (ERT), multichannel analysis of surface waves (MASW), ground penetrating radar (GPR), and self-potential (SP). Each technique provides different images of the investigated domain (in terms of resistivity, S-wave velocity, dielectric constant, and potential, respectively), whose combination allows a more comprehensive characterization with respect to the single survey.

The first methodology, ERT, is applied with different set-ups, in order to vary depth of investigation, resolution, and section of the embankment. The surveys consisted of:

1. lengthwise profiles: 48 stainless-steel electrodes were placed along the river crest, in correspondence to the reconstructed part. We used two different spacings, 1 m and 2 m, so as to vary both total length (47 m and 96 m, respectively) and depth of investigation (about 10 m and 20 m, respectively). All these surveys share the position of the 23<sup>rd</sup> electrode, which was fixed to guarantee the overlapping of the profiles. Furthermore, we employed both Wenner-Schlumberger and dipole-dipole skip zero acquisition schemes;
2. cross-embankment profiles: we used two different lines (one upstream and one downstream, labelled T2 and T1 respectively), with 48 stainless-steel electrodes spaced 0.75 m each. In both cases the acquisition scheme chosen was dipole-dipole skip 0. They covered the outline of the embankment (from the seepage berm to the water level, via the embankment crest) in two cross-sections, selected according to the results of the lengthwise surveys;
3. cross-river profiles: we placed 72 stainless-electrodes spaced 1 m along a line covering the outline of the reconstructed embankment, the riverbed bed, and the profile of the left bank. Also here, we employed both Wenner-Schlumberger and dipole-dipole skip zero acquisition schemes.

Each ERT sounding is performed with an IRIS Instruments Syscal Pro resistivity meter measuring both direct and reciprocal resistance values (Daily *et al.*, 2004), necessary to assess the measurement error. A summary of date, set-up, and array used for each ERT survey can be found in Tab.1 while Fig. 1 shows the location of these soundings.

Then, we used the MASW technique to compare the reconstructed sector to a natural adjacent one, given the difference in terms of mechanical properties that should arise as a consequence of the different materials involved. More in detail, we took advantage of a seismic streamer, a specific tool composed of several geophones linked together that allows the dragging of the whole equipment along the embankment crest. We carried out 25 measurements, whereof 19 on the reconstructed sector (in correspondence to the ERT lengthwise profiles) and 6 on the earthen levee. In the first case, we energised with a sledge-hammer at both ends of the line (i.e., at 4 m and 6 m downstream, with respect to the first geophone, and at 4 m upstream with respect to the last geophone); in the second case, we energised only at 4 m downstream from the first geophone. For each MASW sounding we used a Geometrics Geode seismograph with sampling rate equal to 250 ns, acquisition time equal to 2 s, and 24 geophones with 4.5 Hz frequency spaced 2 m (i.e., total length of the line equal to 46 m) placed lengthwise on the embankment's

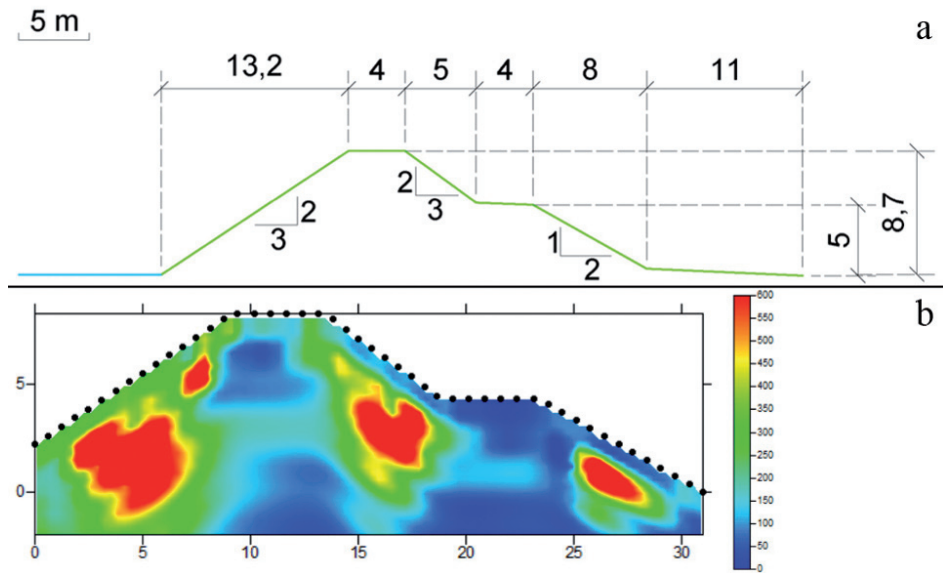


Fig. 2 – a) Topographic profile of the reconstructed embankment. Picture facing downstream. b) T1, resistivity cross-embankment profile. Picture facing downstream. All distances are expressed in meters.

Tab. 1 - Summary of the geophysical measurements realized at the Frassine field site.

Date	Methodology	Set-up and array
October 9, 2014	ERT	Longitudinal profile, 48 elec., 1 m sp., dip-dip
		Longitudinal profile, 48 elec., 1 m sp., W-S
		Longitudinal profile, 48 elec., 2 m sp., dip-dip
		Longitudinal profile, 48 elec., 2 m sp., W-S
November 21, 2014	ERT	Longitudinal profile, 48 elec., 1 m sp., dip-dip
		Longitudinal profile, 48 elec., 1 m sp., W-S
		Longitudinal profile, 48 elec., 2 m sp., dip-dip
		Longitudinal profile, 48 elec., 2 m sp., W-S
	MASW	19 meas. on the reconstructed sector, 6 on the natural levee: 24 geoph., 2 m sp.
SP	Lower outer face profile	
	Seepage berm profile	
February 2, 2015	ERT	Longitudinal profile, 48 elec., 2 m sp., dip-dip
	SP	Lower outer face profile
February 20, 2015	ERT	T1: Cross-embankment profile, 48 elec., 0.75 m sp., dip-dip
		T2: Cross-embankment profile, 48 elec., 0.75 m sp., dip-dip
	GPR	G1: Cross-embankment, ZOP configuration
		G2: Cross-embankment, ZOP configuration
April 9, 2015	ERT	Cross-river profile, 72 elec., 1 m sp., dip-dip
		Cross-river profile, 72 elec., 1 m sp., W-S

crest. Also for the MASW methodology, a summary of date and set-up for each survey can be found in Tab.1 and the profile locations are represented in Fig. 1.

Ground penetrating radar is the third methodology used. Its application took place in correspondence of the cross-embankment ERT lines (T1 and T2), thus resulting in two radargrams, G1 (downstream) and G2 (upstream). In order to gain information regarding the embankment's inner part, we chose a zero offset profile (ZOP) approach, where both the transmitter and the receiver are lowered along the inner and outer embankment faces, respectively. We used a PulseEKKO borehole system with two 100 MHz antennas. All information regarding date and profiling mode can be found in Tab.1 and Fig. 1.

The last technique, SP, was used to monitor the variations in terms of potential along the seepage berm and the lower part of the embankment's outer face. Also in this case all information is summarized in Tab.1 and Fig. 1.

**Data processing, results and discussion. Electrical resistivity tomography.** We performed the inversion of the ERT data at our disposal thanks to two different software, both provided by Lancaster University (UK): Profiler (for lengthwise and cross-embankment profiles) and R2 (for the cross-river profiles). The former creates a quadrilateral finite element mesh, while the latter needs to be fed with a triangular finite element mesh, more suitable for profiles with a more complex topography. The error threshold for the resistance measurements and the error for the inversions are both fixed at 5%.

The lengthwise resistivity cross-sections at our disposal well identify the presence of the reconstructed part within the river embankment, as depicted, for example, in Fig. 3a. This domain is highlighted by relatively higher resistivity values (150-600 Ohm·m, between 24 and 88 m, till a depth equal to circa 8 m from the embankment crest), with respect to the natural levee, which, on the contrary, is characterised by relatively lower resistivity values (50-100 Ohm·m). These values well agree with the materials forming these domains (i.e., reconstructions materials and clayey sand, respectively). The lower part of this cross-section shows rather low resistivity values (50 Ohm·m on average), which may be related to either natural sediments or grouting, according to the site description in section 2. Moreover, the cross-sections with 1 m electrode spacing helped us distinguishing two subdomains within the reconstructed part, thus showing some heterogeneity in this structure. The first, downstream, has an average resistivity of 500 Ohm·m; the second, upstream, has an average resistivity of 300 Ohm·m. These differences led us to the two cross-embankment soundings, T1 and T2 (downstream and upstream, respectively), aimed at identifying the nature of this variation (Fig. 1). First of all, T1 has an average higher resistivity, if compared to T2. More in detail, each cross-section can be divided into two subdomains (Fig. 2b):

- Lateral parts: both inner and outer parts have higher resistivity values because of the ballasts covering the embankment faces. Moreover, these cross-sections well identify also the drainage mattress within the stability bank;
- Central part: in both cases, this subdomain has lower average resistivity values (<150 Ohm·m), likely due to the cement septum, in agreement with other examples in literature (e.g., Sjö Dahl *et al.*, 2009; Karhunen *et al.*, 2010). Furthermore, T1 shows a horizontal zone with resistivity of 150 Ohm·m that does not appear in T2, thus underlying the absence of homogeneity within the reconstructed embankment. These differences may also be the reason behind different seepage phenomena, as described in section 2.

Finally, we decided to combine both dipole-dipole and Wenner-Schlumberger resistance values to obtain the cross-river profile, in order to take advantage of both surveys into a unique resistivity cross-section. The result, shown in Fig. 3b, well represents the difference between the reconstructed embankment (on the left) and the natural one (on the right). The left side shares the same features described for the cross-embankment profiles, but has a lower resolution, given the higher electrodes spacing (0.75 m vs. 1 m); the right side shows the natural levee, marked by a more conductive and homogeneous core (likely clayey sand), covered with more resistive

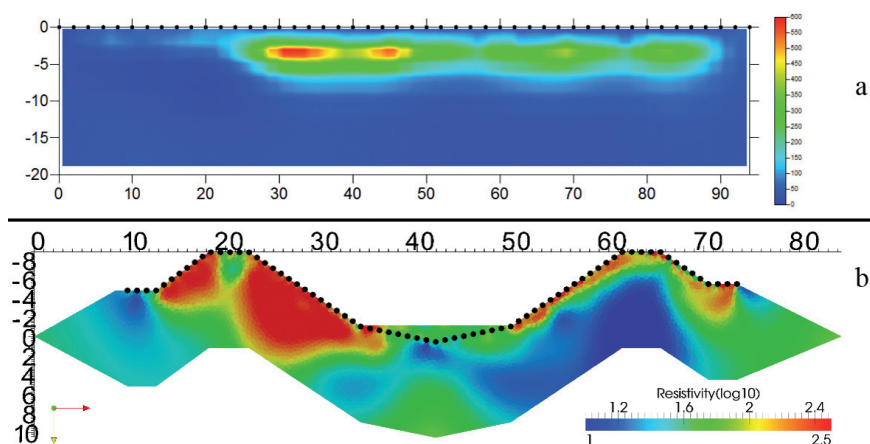


Fig. 3 – a) Lengthwise resistivity profile of the Frassine reconstructed embankment (dipole-dipole skip 0, 48 electrodes spaced 2 m). Water flow is from right to left. b) Cross-river resistivity profile. Picture facing upstream. All distances are expressed in meters.

gravel. A longer profile allows also to reach a deeper investigation depth, thus extending the information provided. Unfortunately, the data at our disposal does not permit us to identify the embankment’s foundations, since they only show a conductive domain.

*Multichannel analysis of surface waves.* Also the MASW data obtained well distinguish the reconstructed embankment from the natural levee. More in detail, the  $V_s$  model of the natural part is characterized by rather low values slightly increasing with depth (from 150 to 260 m/s) that are likely related to the presence of clayey sand, in agreement with both the ERT results and the geotechnical soundings. On the contrary, the frequency-phase velocity diagrams of the reconstructed sector display large energy dispersion, since the propagation of superficial waves is probably strongly influenced by the heterogeneities within this part. Moreover, the stiffening due to the concrete septum is represented by the higher energy in correspondence to velocities close to 1000 m/s (especially for frequencies > 25 Hz). Surface Waves Analysis Wizard, Matlab, and SWAMI allowed the analysis of the MASW data.

*Ground penetrating radar and self-potential.* The analysis of the GPR data was realized thanks to the REFLEX software and to the application of the empirical relation proposed by Topp *et al.* (1980). The results well agree with the ERT data, since G2 and T2 have higher average water content and lower average resistivity, respectively. It is important to underline that the water content distribution within the artificial part is likely irregular, with higher values in the cemented domain. Moreover, the signal to noise ratio is lower in G2 with respect to G1, thus agreeing, at least from a qualitative point of view, with more conductive materials.

On the other hand, the drainage mattress compromised the SP data interpretation, since its position has been communicated only after the acquisitions and then confirmed by the ERT cross-embankment acquisitions. Thus, although the SP profiles show some voltage variations, they are likely due to changes in terms of materials within the mattress itself and not to infiltration phenomena.

**Conclusions.** The characterization of natural and artificial river levee is a tricky challenge with important consequences on hydrogeological risk mitigation. Commonly applied techniques, although widely spread, provide only punctual data that are not adequate to properly describe the whole experimental domain. On the other hand, several geophysical methodologies allow non-invasive, cost-effective, and relatively faster soundings that can be combined in order to observe the same target under different points of view, as presented in this work. The joint use of ERT, MASW, GPR, and SP led to interesting results, from the identification of

heterogeneities within the reconstructed structure to the low electrical resistivity of concrete, a peculiar feature that needs to be taken into account especially in conductive domains, as the one here presented. A further validation of the geophysical data with information provided by geotechnical sounding is currently undergoing with promising results, thus demonstrating once again that the combination of different methodologies into a common framework is a suitable approach to manage river embankment characterization.

## References

- ARPAV; 2010: *Dati alluvione 2010*.
- ARPAV – Servizio Osservatorio Suolo e Bonifiche; 2013: *Carta dei suoli della provincia di Padova*. ISBN: 978-88-7504-163-2.
- Bondesan M.; 2001: *Hydrography. Note illustrative della Carta Geomorfologica della Pianura Padana*. Castiglioni G.B. & Pellegrini G.B. (a cura di), 33-44.
- Cardarelli E., Cercato M. and De Donno G.; 2014: *Characterization of an earth-filled dam through the combined use of electrical resistivity tomography, P-and SH-wave seismic tomography and surface wave data*. Journal of Applied Geophysics, **106**, 87-95.
- Cho I. K. and Yeom J. Y.; 2007: *Crossline resistivity tomography for the delineation of anomalous seepage pathways in an embankment dam*. Geophysics, **72(2)**, G31-G38.
- Daily W., Ramirez A., Binley A. and LeBrecque, D.; 2004: *Electrical resistance tomography*. The Leading Edge, **23(5)**, 438-442.
- Di Prinzio M., Bittelli M., Castellarin A. and Pisa P. R.; 2010: *Application of GPR to the monitoring of river embankments*. Journal of applied geophysics, **71(2)**, 53-61.
- Fontana A., Mozzi P. and Bondesan A.; 2008: *Alluvial megafans in the Venetian–Friulian Plain (north-eastern Italy): evidence of sedimentary and erosive phases during Late Pleistocene and Holocene*. Quaternary International, **189(1)**, 71-90.
- Inazaki T. and Sakamoto T.; 2005: *Geotechnical characterization of levee by integrated geophysical surveying*. In Proceedings of the International Symposium on Dam Safety and Detection of Hidden Troubles of Dams and Dikes.
- Karastathis V. K., Karmis P. N., Drakatos G and Stavrakakis G.; 2002: *Geophysical methods contributing to the testing of concrete dams. Application at the Marathon Dam*. Journal of Applied Geophysics, **50(3)**, 247-260.
- Karhunen K., Seppänen A., Lehtikoinen A., Monteiro P. J. and Kaipio J. P.; 2010: *Electrical resistance tomography imaging of concrete*. Cement and Concrete Research, **40(1)**, 137-145.
- Karl L., Fechner T., Schevenels M., François S. and Degrande G.; 2011: *Geotechnical characterization of a river dyke by surface waves surface waves*. Near Surface Geophysics, **9(6)**, 515-527.
- Moore J. R., Boleve A., Sanders J. W. and Glaser S. D.; 2011: *Self-potential investigation of moraine dam seepage*. Journal of Applied Geophysics, **74(4)**, 277-286.
- Panthulu T. V., Krishnaiah C. and Shirke J. M.; 2001: *Detection of seepage paths in earth dams using self-potential and electrical resistivity methods*. Engineering Geology, **59(3)**, 281-295.
- Perri M. T., Boaga J., Bersan S., Cassiani G., Cola S., Deiana R., Simonini P. and Patti, S.; 2014: *River embankment characterization: The joint use of geophysical and geotechnical techniques*. Journal of Applied Geophysics, **110**, 5-22.
- Sjödahl P., Dahlin T. and Johansson S.; 2009: *Embankment dam seepage evaluation from resistivity monitoring data*. Near Surface Geophysics, **7(5-6)**, 463-474.
- Topp G. C., Davis J. L. and Annan A. P.; 1980: *Electromagnetic determination of soil water content: Measurements in coaxial transmission lines*. Water resources research, **16(3)**, 574-582.
- Turk N. and Dearman W. R.; 1987: *Assessment of grouting efficiency in a rock mass in terms of seismic velocities*. Bulletin of the International Association of Engineering, **36(1)**, 101-108.

## CONTRIBUTION OF THE CLUSTER ANALYSIS OF HVSR DATA FOR NEAR SURFACE GEOLOGICAL RECONSTRUCTION

P. Capizzi<sup>1</sup>, R. Martorana<sup>1</sup>, A. D'Alessandro<sup>2</sup>, D. Luzio<sup>1</sup>

<sup>1</sup> Dip. Scienze della Terra e del Mare, Università di Palermo, Italy

<sup>2</sup> Istituto Nazionale di Geofisica e Vulcanologia, Centro Nazionale Terremoti, Italy

**Introduction.** The use of HVSR technique allows in many cases (Bonnetfoy-Claudet *et al.*, 2006) to obtain detailed reconstruction of the roof of the seismic bedrock (Di Stefano *et al.*, 2014) and to identify areas with similar seismic behaviour. Theoretical considerations (Nakamura, 1989) and experimental tests showed that amplification of horizontal motions between bottom and top of a sedimentary cover is well related to the ratio between the spectra of the horizontal and vertical components of the ground velocity (Nakamura, 2000). This ratio is a measure of ellipticity of Rayleigh wave polarization, overlooking Love and body waves contribution. Assuming that subsoil can be represented as a stack of homogeneous horizontal layers and imposing some geometric and/or physical constraints it is possible to estimate the parameters of the shear wave velocity model (Fäh *et al.*, 2003; Parolai *et al.*, 2000).

The integration of data related to HVSR and active techniques based on the analysis of surface waves can greatly reduce the uncertainties on the interpretation models.

Because the inversion of HVSR curves implies monodimensional distribution of Vs, before inverting the data we used a cluster analysis technique to subdivide them into subsets attributable to areas with low horizontal velocity gradients and therefore similar seismic responses. The data of each cluster were then interpreted by imposing conditions of maximum similarity between the 1D models relating to each measurement point.

Clustering methods are widely used in different research fields (Hartigan, 1975; Adelfio *et al.*, 2012; D'Alessandro *et al.*, 2013). In general, the cluster analysis is a good tool whenever you have to classify a large amount of information into meaningful and manageable groups.

A modified centroid-based algorithm has been applied to HVSR datasets acquired for studies of seismic microzoning in various urban centers of Sicilian towns (Capizzi *et al.*, 2014). The results obtained for Modica and Enna towns are shown. HVSR data were previously properly processed to extract frequency and amplitude of peaks by a code based on clustering of HVSR curves determined in sliding time windows (D'Alessandro *et al.*, 2014).

**The cluster analysis.** The cluster analysis is the procedure that allows to identify within a set of objects some subsets, called clusters, that tend to be homogeneous within them, according to some criteria. The statistical units are divided into a number of groups according to their level of similarity (internal cohesion), evaluated from the values that a number of variables chosen takes in each unit. Generally, in the analysis for grouping is not necessary to have in mind any interpretative model (Fabbris, 1983). The partition is successful if the objects within the clusters are closer to each other than other in different clusters (Barbarito, 1999).

Many clustering algorithms exist (Gan *et al.*, 2007; Everit *et al.*, 2011), and can be categorized into two main types: Hierarchical Clustering (HC) and Non-Hierarchical Clustering (NHC). The HC have numerous advantages compared to the NHC. The HC are explorative methods and is not necessary to define a priori the number of clusters. The HC work with a measure of proximity between the objects to be grouped together. A type of proximity can be chosen which is suited to the subject studied and the nature of the data. One of the results of HC is the dendrogram which shows the progressive grouping of the data. It is then easy possible to gain an idea of a suitable number of classes into which the data can be grouped.

To evaluate the differences between the various clustering techniques, which can also produce results significantly different from each other, the best way is to assess how the different techniques reproduce the structure of known data. These assessments are typically performed on simulated data, and are often difficult to interpret and may be contradictory.

The elements that seem to influence more the results of this analysis are:

- shape, size (absolute and relative) and number of clusters;
- the presence of outliers;
- the level of overlap between clusters;
- the type of measure of similarity / distance chosen.

Various studies (Rand, 1971; Ohsumi, 1980) suggest that different grouping strategies often lead to results not dissimilar while others highlight specific cases of strong divergence (Everitt, 2011; Fabbris, 1983). However, the criteria for choosing between the two types of algorithm (Hierarchical Clustering and Non-Hierarchical Clustering) have not yet been sufficiently explored and literature are very different positions. Anyhow, the criteria suggested by the authors include objectivity, for which researchers working independently on the same set of data must arrive to same results and stability of operating results of the partition of data equivalent (Silvestri and Hill, 1964).

In practice, you should choose the methods that are more insensitive to small changes in the data. For example, it is considered important if, subtracting an individual from the analysis, the partition little change (of course the elimination of outlier produces greater variations within groups), or if, by repeating the analysis without an entire branch of the dendrogram, the structure of the other branches remains unchanged or almost.

Broadly, we can say that, if you seek groups of statistical units, characterized by high internal consistency, hierarchical techniques are less effective than not hierarchical ones.

**Cluster analysis of HVSR data.** Many HVSR data sets were acquired for studies of seismic microzoning in various Sicilian urban centers. After many tests to assess the best clustering techniques for our dataset and purposes, we have chosen to apply an AHC (Agglomerative Hierarchical Clustering) algorithm to extract frequency and amplitude of HVSR curves determined in sliding time windows (D'Alessandro *et al.* 2014) and a HC algorithm to group peaks attributable to the same seismic surface.

The choice is motivated by the fact that the HC are explorative methods, which do not need to define a priori the number of clusters, and allows to use any proximity measure considered suitable for the data. In HC the process of agglomeration or separation is done on the basis of a measure of proximity and of linkage criteria. The proximity between two objects is measured by measuring at what point they are similar (similarity) or dissimilar (dissimilarity). Several measure of proximity was proposed in literature to measure the similarity/dissimilarity between different types of object (Gan *et al.*, 2007; Everit, *et al.*, 2011). Clearly, the choice of the type of measure of proximity must respect specific criteria and would be done on the basis of the main aims of the clusterization (Gan *et al.*, 2007; Everit, *et al.*, 2011).

Windows selection for best average HVSR curve estimation, are generally done by visual inspection of the HVSR curves as function of time. Starting from the full-length records, the HVSR curve are determine in consecutive time windows of appropriate lengths. Time windows that at a simple visual inspection showing HVSR curve considered "anomalous" are generally deleted and therefore not included in the calculation of the average HVSR curve. Often it is very difficult to identify the correct time window to be used for the calculation of the mean HVSR. The lack of a not arbitrary selection criteria making the result clearly operator dependent and therefore not optimal.

To overcome the this problem we applied the AHC to our data, using as proximity measure the Standard Correlation ( $SC_{xy}$ ) defined as:

$$SC_{xy} = \frac{\sum_{i=1}^n x_i \cdot y_i}{\sqrt{\sum_{i=1}^n x_i^2 \cdot \sum_{i=1}^n y_i^2}}$$

where  $x_i$  and  $y_i$  indicate the values of the spectral ratios relative, to the  $i$ -th frequency and the generic pair of analysis windows. The main return of the hierarchical clustering is the dendrogram, which shows the progressive grouping of the data (Fig. 1). The selection of clusters is done cutting the dendrogram at specific level of similarity/dissimilarity. In this application

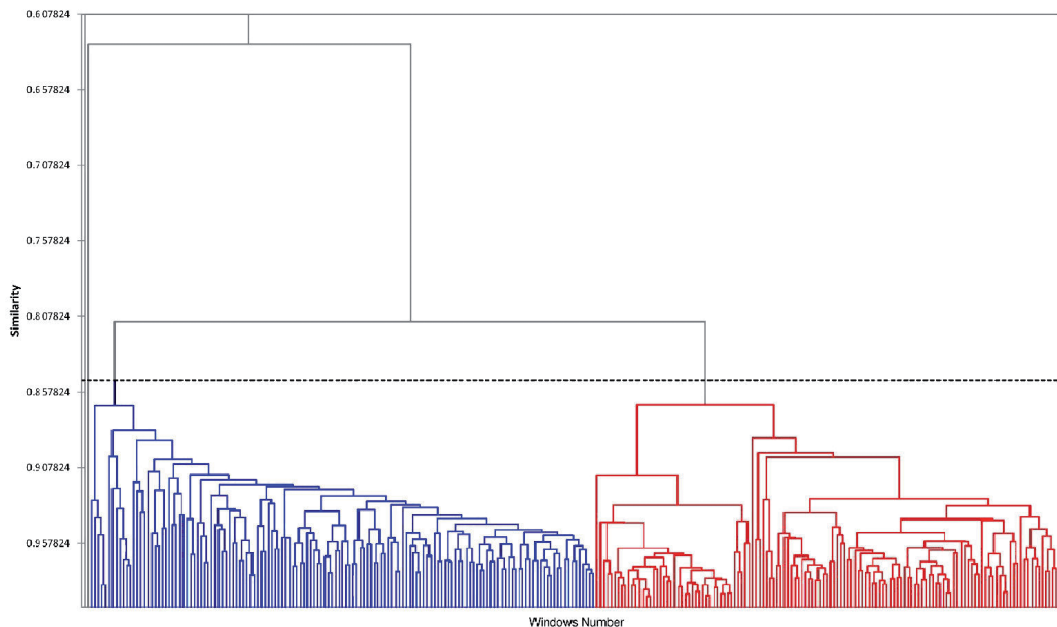


Fig. 1 – Dendrogram relative to HVS curves determined in sliding time windows.

the cutting level was chosen on the basis of some criteria that involve the maximum slope detectable of the level bar chart and the width of the gap identifiable between two successive levels of the hierarchy detectable in the dendrogram (Gan *et al.*, 2007; Everitt, *et al.*, 2011).

After defining the average HVS curves a second multi-parametric clustering procedure has been used to group peaks attributable to the same origin (stratigraphic, tectonic, topographic, anthropogenic or other sources). A nonhierarchical centroid-based algorithm has been implemented (Capizzi *et al.*, 2014). This clustering is carried out in order to delineate the areas inside of which it is possible to assume a continuous trend of the parameters used to describe the subsoil and of the seismic response of the medium. Hypotheses on the cause of the HVS peaks are basic to extract from such kind of data reliable information on the subsurface (Capizzi *et al.*, 2014; Di Stefano *et al.*, 2014; Martorana *et al.*, 2014).

In centroid-based methods, clusters are represented by a central vector, which may not necessarily be a member of the data set. When the number of clusters is fixed, the clustering can be formally regarded as an optimization problem: find the cluster centers and assign each object to the cluster, such that the parameter distances from the cluster centroid are minimized, and calculate the new means to be the centroids of the observations in the new clusters. The algorithm converges to a (local) optimum when the assignments no longer change. In this procedure there is no guarantee that the global optimum is found using this algorithm.

The number of clusters, the presence of outliers and the type parameters used for distance measures mostly affect the results of cluster analysis.

Centroid-based algorithms generally require the number  $k$  of clusters and the initial centroid coordinates to be specified in advance. This aspect is considered one of the biggest drawbacks of these algorithms because an inappropriate choice of  $k$  may yield poor results. Really, is hard to choose the  $k$  parameter when missing external constraints.

The proposed algorithm does not fix the number of clusters and choose automatically, for each possible value of  $k$  the initial centroids from data set. The distance of each unit from the initial centroids and those obtained after each iteration was calculated as the weighted sum of the Euclidean normalized distances of all the variables considered: coordinates ( $x$ ,  $y$  and  $z$ ),

frequency ( $f$ ), amplitude ( $A$ ) and lithology ( $L$ ):

$$D = a\sqrt{(dx^2 + dy^2 + dz^2)} + b\sqrt{df^2} + c\sqrt{dA^2} + d\sqrt{dL^2}$$

where  $a$ ,  $b$ ,  $c$  and  $d$  are the weights. The choice of weights and of the optimal number of  $k$  classes have been optimized maximizing  $R$  parameter, taking into account the intra-cluster ( $DEV_{IN}$ ) and inter-cluster ( $DEV_{OUT}$ ) variances:

$$R = DEV_{OUT} / DEV_T, \quad DEV_T = DEV_{OUT} + DEV_{IN} = 1 .$$

However the use of a priori information especially on stratigraphic data is fundamental for the choice of number of partitions. Generally, experimental tests showed that different weights should be used to identify inclined or sub-horizontal seismic discontinuities.

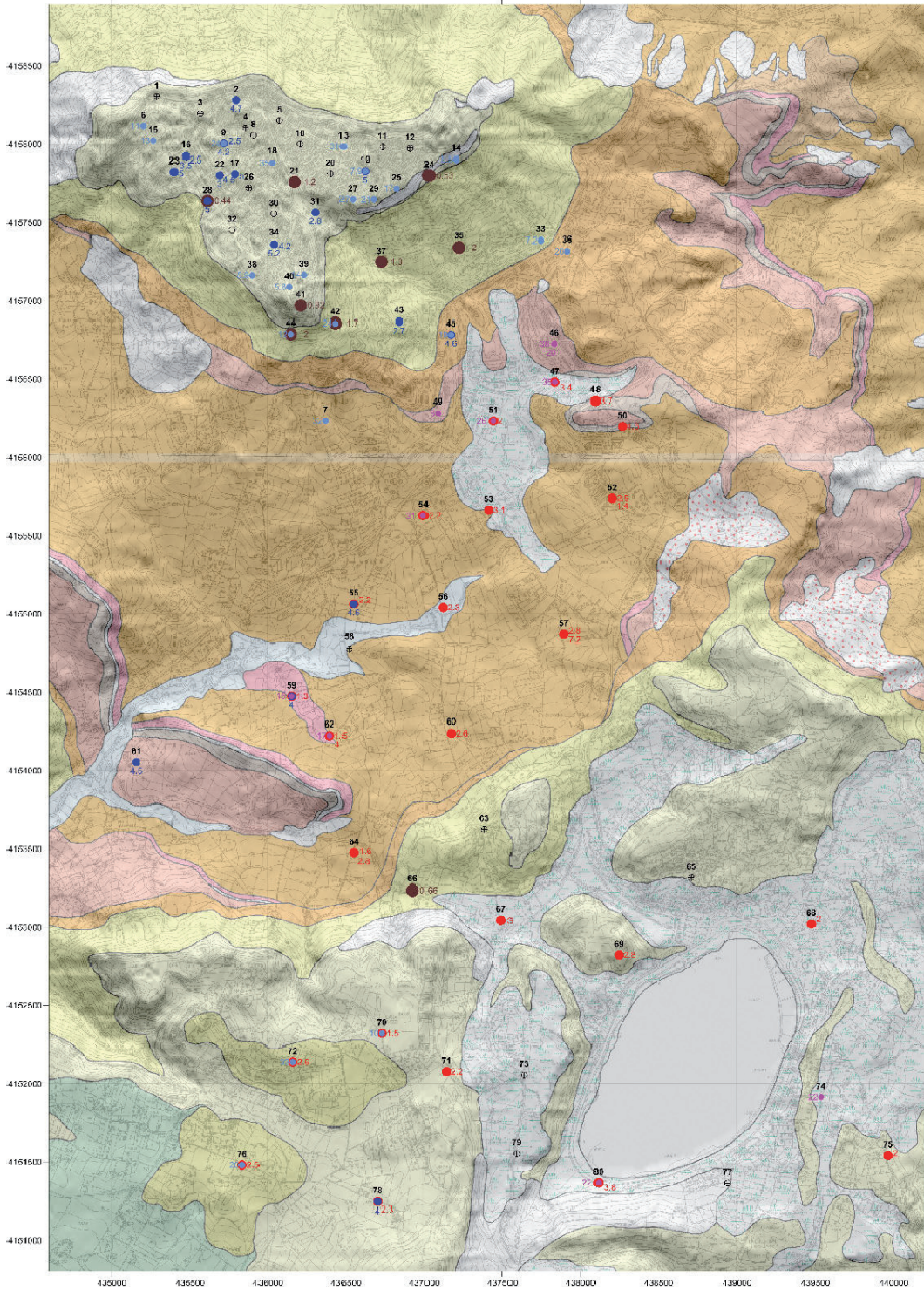
**Application cases.** During 2012, as part of an agreement with the Italian Department of Civil Protection, the expedite seismic microzonation has been performed in 20 municipalities of the Eastern Sicily considered at high seismic hazard. In addition to the collection of all previous geological and geophysical data, we have performed a passive seismic campaign to determine the resonance frequency of the investigated sites by means of the Nakamura technique (Nakamura, 1989). The HVSR cluster analyses were applied to HVSR data acquired in Modica and Enna towns. Multichannel Analysis of Surface Waves (MASW) were acquired in Enna town to constrain the interpretative models and the velocity of shear waves in the subsurface. HVSR data were inverted using similar starting models for each cluster. 1D seismic models were calculated using the code of Lunedei and Albarello (2009) based on the assumption that environmental noise is composed by the superimposition of random multi modal plane waves moving in all the directions at the surface of the Earth and propagating as Rayleigh and Love waves. Since body waves are not considered, this assumption is realistic only if sources are located far enough from the receiver. Consequently, all the time windows of the signal showing noise suspected to be caused by near sources must be removed.

The HVSR clusters of peaks were considered to define the seismic layers, each characterized by a specific range of seismic velocities, and to associate them with the known geological formations. Inversion models of the different partitions obtained using the centroid-based algorithm were superimposed on the geological map of the analysed sites to identify possible correlations with geology and topography.

In the case of Modica town the best cluster results seems to be a three partition, whereas in Enna site the cluster analysis converges to five groups (Fig. 2). In both case the map of the depth of the seismic bedrock (Fig. 3) and 3D model of seismic surfaces were reconstructed.

**Discussion.** One of the typical criticisms to the cluster analysis is to arrive at indeterminate solutions, subject to arbitrary decisions relating to initial information, subjective interpretation of the results, and not statistically verifiable. Contrary to other statistical procedures, cluster analysis is often used when you do not have a priori hypotheses or when you are in the exploratory phase of analysis. However the application of cluster analysis, although falling between the methods of analysis essentially exploratory, should be preceded and accompanied by the definition of interpretative models.

The time windows suitable for the determination of the mean HVSR are generally arbitrarily identified by the operator by a simple visual inspection of the microtremors signals in time or spectral domain. This can lead to an incorrect determination of the mean HVSR curves and to an incorrect interpretation of the main peaks. An automatic procedure, based on clustering analysis, for the determination of the appropriate windows to be used in the average HVSR curve determination has been implemented. This procedure allowed us to easily separate the HVSR curves and peak mainly linked to the site effects from those mainly related to the source effects. The analysis of the HVSR curves as a function of the azimuth result a useful tool for the characterization and discrimination of the major peaks identified on the HVSR curves.



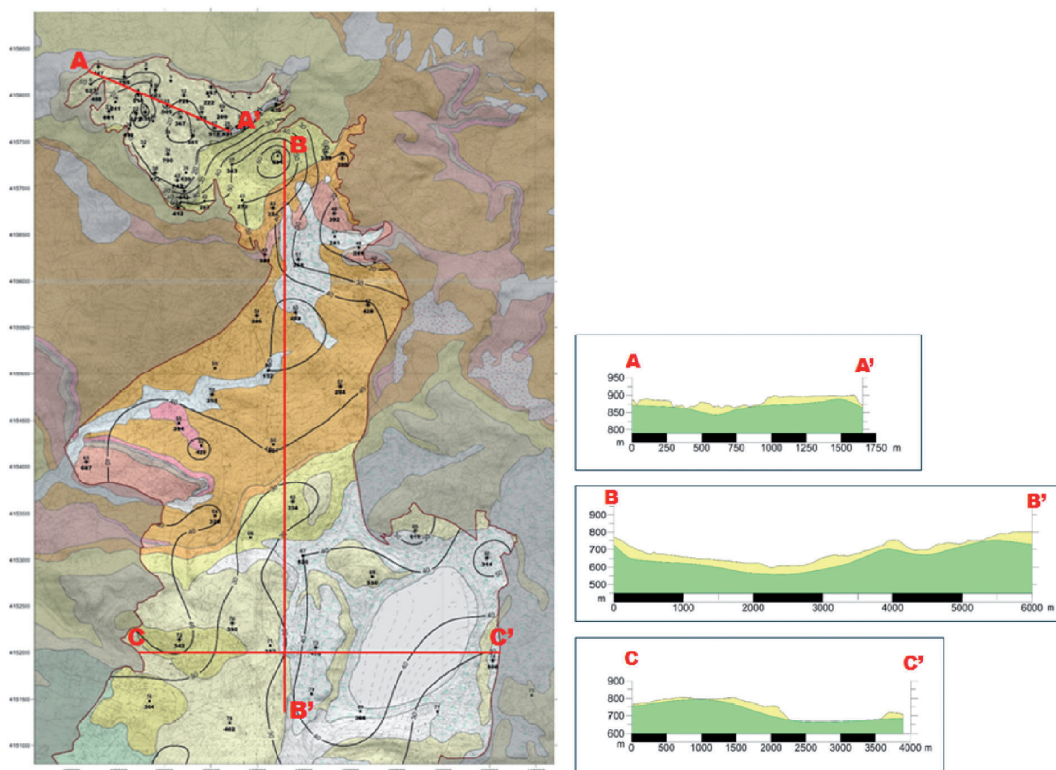


Fig. 3 – Depth of seismic bedrock (left) and seismic sections (right; yellow: seismic soil, green: bedrock).

Furthermore the use of techniques of cluster analysis in the noise processing has enabled to recognize groups of similar HVSR curves and to relate them to similar interpretative seismic models. In many cases, the HVSR cluster analysis applied for microzonation studies of some towns in Sicily, showed good results, allowing to group peaks attributable to the same seismic structures. The comparison of the HVSR pattern with the information about outcropping formations allowed to assess the geological hypotheses on the heavily urbanized investigated areas.

However obtained results underline how the most appropriate clustering algorithm for a particular problem often needs to be chosen empirically and how the choice of the partition is strongly linked to the choice of weights for the calculation of the distance and to the geological and stratigraphic knowledge of the area.

Finally HVSR inversion demonstrates a valuable method, when used in accordance with certain criteria in the acquisition and processing, not only for the estimate of the site amplification effects, but also for the assessment of the main geological and tectonic structures that define the seismic bedrock and coverage deposits.

#### References

- Adelfio G., Chiodi M., D'Alessandro A., Luzio D., D'Anna and G., Mangano G.; 2012: *Simultaneous seismic wave clustering and registration*. Computer and Geoscience, 44, 60-69, doi: 10.1016/j.cageo.2012.02.017.
- Barbarito, L.; 1999. *L'analisi di settore: metodologia e applicazioni*, Milano, Franco Angeli.
- Bonnefoy-Claudet S., Cotton F. and Bard, P.-Y.; 2006: *The nature of noise wavefield and its applications for site effects studies*. A literature review. Earth-Science Reviews, 79, 3-4, 205-227. doi: 10.1016/j.earscirev.2006.07.004.
- Capizzi P., Martorana R., Stassi G., D'alessandro A., Luzio D.; 2014: *Centroid-based cluster analysis of HVSR data for seismic microzonation*. Near Surface Geoscience 2014 - 20th European Meeting of Environmental and Engineering Geophysics, Athens, 14-18 September 2014, We Verg 02, doi: 10.3997/2214-4609.20142095.

- Di Stefano P., Luzio D., Renda P., Martorana R., Capizzi P., D'Alessandro A., Messina N., Napoli G., Todaro S., and Zarcone G.; 2014: *Integration of HVSR measures and stratigraphic constraints for seismic microzonation studies: the case of Oliveri (ME)*. Natural Hazards and Earth System Sciences Discussion, 2, 2597-2637, doi:10.5194/nhessd-2-2597-2014.
- D'Alessandro A., Luzio D., Martorana R. and Capizzi P.; 2014: *Improvement of the Horizontal to Vertical Noise Spectral Ratio technique by cluster analysis*. submitted to Computer and Geosciences.
- D'Alessandro A., Mangano G., D'Anna G. and Luzio D.; 2013: *Waveforms clustering and single-station location of microearthquake multiplets recorded in the northern Sicilian offshore region*. Geophysical Journal International, vol. 194, n. 3, pp. 1789-1809, DOI: 10.1093/gji/ggt192.
- Everitt B.S., Landau S., Leese M., Stahl D.; 2011: *Cluster Analysis*, Wiley Series in Probability and Statistics, 5th Edition, pp. 332, ISBN-10: 0470749911, ISBN-13: 978-0470749913.
- Fabbris L.; 1983. *Analisi esplorativa di dati multidimensionali*, Cleup editore.
- Fäh D., Kind F. and Giardini D.; 2003: *Inversion of local S wave velocity structures from average H/V ratios, and their use for the estimation of site-effects*. Journal of Seismology 7, 449–467. doi: 10.1023/B:JOSE.0000005712.86058.42.
- Gan G., Ma C., Wu J.; 2007: *Data Clustering: Theory, Algorithms, and Applications*, pp. 184, Cambridge University Press, ISBN: 9780898716238.
- Hartigan J.A.; 1975: *Clustering algorithms*. New York, Wiley.
- Lunedei E. and Albarello D.; 2009: *On the seismic noise wavefield in a weakly dissipative layered Earth*. Geophysical Journal International 177, 1001–1014. doi: 10.1111/j.1365-246X.2008.04062.x
- Martorana R., Capizzi P., Avellone G., Siragusa R., D'alessandro A., Luzio D.; 2014: *Seismic characterization by inversion of HVSR data to improve geological modeling*. Near Surface Geoscience 2014 - 20th European Meeting of Environmental and Engineering Geophysics, Athens, 14-18 September 2014, We Verg 01, doi: 10.3997/2214-4609.20142094.
- Nakamura Y.; 2000: *Clear Identification of Fundamental Idea of Nakamura's Technique and its Applications*. 12th World Conference on Earthquake Engineering, 2656.
- Parolai S., Bindi D., Augliera P.; 2000: *Application of the Generalized Inversion Technique (GIT) to a microzonation study: numerical simulations and comparison with different site-estimation techniques*. B. Seismol. Soc. Am., 90, 286–297.
- Oshumi N.; 1980: *Evaluation procedure of agglomerative hierarchical clustering methods by fuzzy relations*. Data Analysis and Informatics, Diday *et al.* (a cura di), North Holland.
- Rand W.M.; 1971: *Objective criteria for the evaluation of clustering methods*. J.A.S.A.
- Silvestri L., Hill I.R.; 1964: *Some problems of the taxometric approach in: Phenetic and Phylogenetic Classification*, Heywood, V.H. Mc Neil, J. (a cura di), Systematic Association Londra.
- Wathelet M., Jongmans D and Ohrnberger M.; 2004: *Surface-wave inversion using a direct search algorithm and its application to ambient vibration measurements*. Near Surface Geophysics, 2, 10 211–221. doi: 10.3997/1873-0604.2004018.

## SEISMIC MEASUREMENTS IN UNSTABLE SEA CLIFF AREAS

R. Iannucci<sup>1</sup>, S. D'Amico<sup>2</sup>, D. Farrugia<sup>2</sup>, P. Galea<sup>2</sup>, S. Martino<sup>1</sup>, A. Paciello<sup>3</sup>

<sup>1</sup> Department of Earth Sciences and Research Center for the Geological Risks (CERI), Sapienza University, Rome, Italy

<sup>2</sup> Department of Geosciences, University of Malta, Msida, Malta

<sup>3</sup> ENEA, National Agency for New Technologies, Energy and Sustainable Economic Development, Rome, Italy

**Introduction.** Sea cliffs are high-risk elements in the Mediterranean area due to the diffused landslide processes that affect sites of touristic relevance as well as buildings which are part of the cultural heritage. The Favignana Island (Sicily, Italy) represents a significant case study as several sea cliffs located in its eastern part are involved in landslide processes where porous carbonate grainstones overlying plastic clay deposits widely outcrop (Falconi *et al.*, 2015). More in particular, the western sector of Cala Rossa Bay was selected as a test site as its geological setting predisposes a large lateral spreading responsible for instabilities of the sea cliff, associated to falls and topples of different-size rock blocks.

This paper reports the preliminary results of a geophysical campaign of seismic noise measurements carried out in May 2015 at Cala Rossa Bay. In recent years, several studies applied ambient noise techniques to investigate landslide-involved slopes (Del Gaudio *et al.*, 2008; Burjáněk *et al.*, 2010, 2012) or to characterize blocks of unstable cliffs (Got *et al.*, 2010; Panzera *et al.*, 2012; Galea *et al.*, 2014), through different approaches among which H/V spectral ratios, f-k analysis, site to reference spectral ratios, polarization analysis, base noise level variations.

The noise measurement stations were distributed in correspondence of the unstable sea cliff as well as on the stable plateau area (i.e. located about 100 m far from the cliff). The seismic noise was recorded for 1 hour and was analyzed by computing the Fast Fourier Transform (FFT) of the three ground-motion components as well as the HVSR. Because of the similar geological and geomorphological setting, the results obtained for the Cala Rossa Bay test site were compared to the ones obtained for Anchor Bay (Malta), reported in Galea *et al.* (2014) and partially reprocessed for the here discussed comparison.

The goal of this research is to provide new evidences about local seismic response in unstable sea cliffs through the analysis of single-station noise records. The relevance of such a geophysical application consists on the possibility to manage the hazard related to sea-cliff landslides in order to mitigate the associated coastal risk.

**Geological and geomorphological setting.** The Favignana Island belongs to the Egadi Archipelago and is part of the NW sector of Sicily (Italy), which represents the emerged western edge of the Sicilian-Maghrebian Chain, originated from the deformation of the Meso-Cenozoic Northern African continental margin (Scandone *et al.*, 1974; Antonioli *et al.*, 2006). Tectonic units, overthrust in the Middle Miocene and Lower Pliocene, compose the Egadi Islands as well as the whole Trapani area (Nigro *et al.*, 2000). The Favignana Island is mainly built-up of Mesozoic-Lower Tertiary carbonate deposits, covered by transgressive Plio-Pleistocene shallow-water marine deposits (Abate *et al.*, 1995, 1997; Catalano *et al.*, 1996). The Lower Pleistocene deposits widespread outcrop along the eastern slope of the emerged paleo-Favignana Island in a pull-apart basin, probably generated by transtensional faults activity (Slaczka *et al.*, 2011).

In Cala Rossa Bay, located in the eastern portion of the Favignana Island, porous carbonate grainstones of the Lower Pleistocene widely outcrop, about 20 m thick and with almost-horizontal strata; these carbonate rocks overlie high-plasticity clays of Pliocene age with a thickness varying from 5 up to 10 m (Fig. 1a). The clays overlie massive carbonate grainstones of the Lower-Middle Miocene, with a thickness varies between 10 and 30 m (Abate *et al.*, 1995, 1997; Tondi *et al.*, 2012), which does not outcrop at Cala Rossa Bay.

This geological setting characterized by the over-position of stiff rocks on a more plastic substratum (Goudie, 2004) leads to a lateral spreading phenomenon which widely involve the sea cliff. More in particular, the horizontal deformations affecting the clayey materials, with a visco-plastic behavior, induce cracks and failures in the overlying stiff rock causing the detachment of single rock blocks and the generation of falls and topples. Lateral spreading processes act selectively, shaping plateau of stiff rocks bordered by unstable cliffs. Lateral spreading phenomena represent a gravity-induced instability highly dangerous respect to the coastal cultural heritages and cause several touristic places in the Mediterranean area (Canuti *et al.*, 1990; Gigli *et al.*, 2012; Falconi *et al.*, 2015) to be inaccessible or avoided for tourists.

**The study area.** In the western sector of Cala Rossa Bay in Favignana Island the ongoing lateral spreading produced a complex ground crack pattern which favors gravitational instabilities also influenced by the presence of an extensive network of underground tunnels related to historical quarry activities in the porous carbonate grainstones and terminated in the latter half of the last century (Falconi *et al.*, 2015).

Based on field surveys, a main gravitational joint system was devised, consisting of three open fractures whose direction is nearly parallel to the coastline (Fig. 1b). Three different unstable zones, separated by the three opened ground cracks, and a fourth stable zone, consisting in the

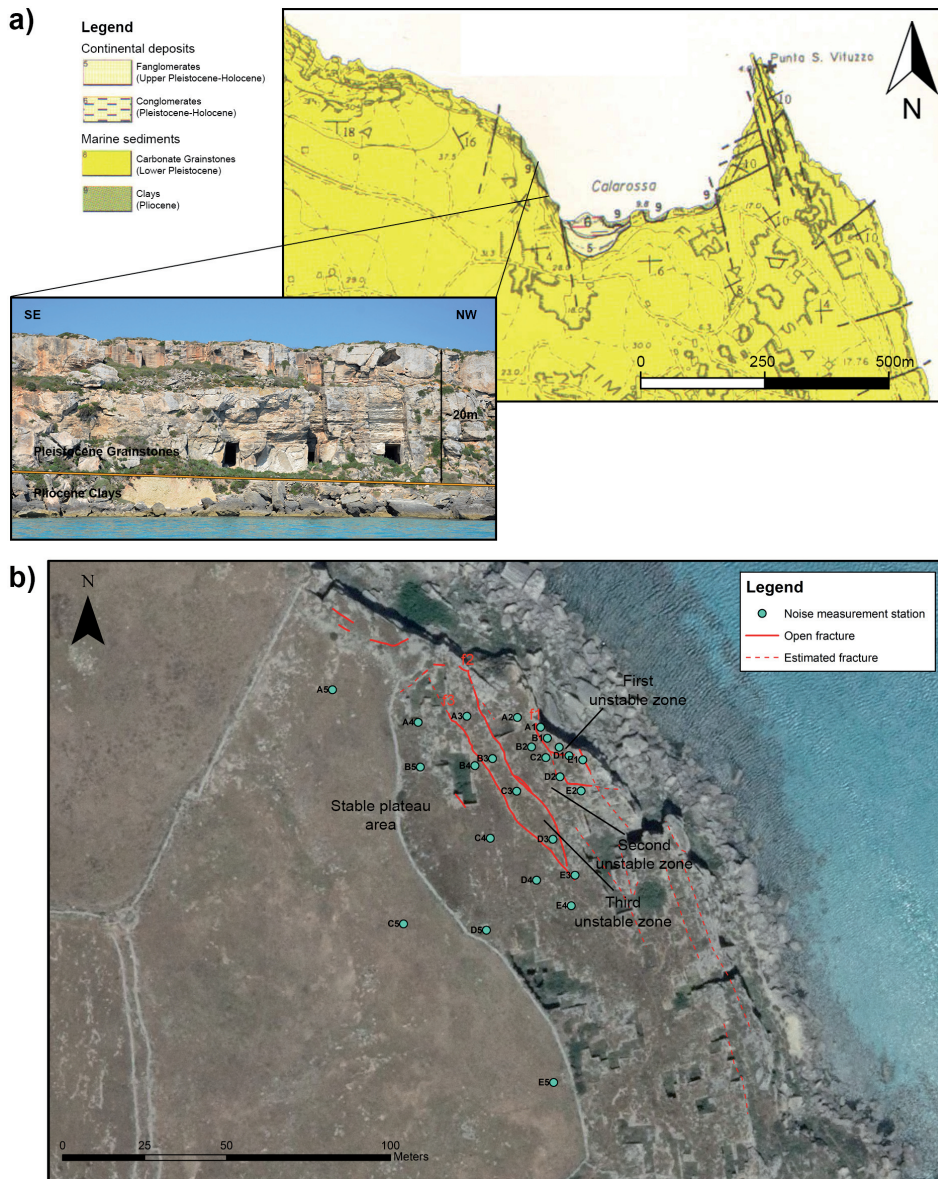


Fig. 1 – Geological and geomorphological setting of Cala Rossa Bay. a) Excerpt of Favignana geological map in the Cala Rossa area (from Abate *et al.*, 1997) and picture of cliff in the Cala Rossa western part that shows the overlapping of the Lower Pleistocene carbonate grainstones on the Pliocene clay deposits. b) Orthophoto of the Cala Rossa western part in which shows: the open fractures with related code, the estimated fractures, the three unstable zones, the stable plateau area, the 25 noise measurement stations.

plateau area, were distinguished. The first zone includes the portion of the slope between the edge of the cliff and the first main fracture (f1) where the rock mass is intensely joined by some additional open cracks related to the stress release. This joint system produces several unstable meter-scale rock blocks. The three deep cracks isolate two large blocks, which correspond to the second and third unstable zone. Where visible, the main cracks have an aperture about 35 cm and a vertical displacement up to 60 cm. A stable plateau area is encountered moving upslope from the third fracture f3.

According to Varnes (1978) and Hutchinson (1988), the resulting landslide process should be defined as a complex-type one since the failure mechanism is a combination of lateral spreading, rock fall and rock topples. Moreover, the two main isolated blocks show a counter-slope top, indicating that a roto-translational component is also present in the spreading process.

**Data acquisition and processing.** In May of 2015, a field-campaign was carried out in the western part of Cala Rossa Bay to record seismic ambient noise. Over an area of approximately 0.01 km<sup>2</sup>, 25 single-station measurements were deployed to cover the aforementioned landslide zones (Fig. 1b). More in particular, 5 stations were placed in each of three unstable zones while 10 stations were deployed on the stable plateau area, at various distances from the f3 ground crack.

Each station was equipped with a 3-component seismometer: 20 measurements were carried out using a LE-3D/5s seismometer by Lennartz Electronic GmbH coupled with a REFTEK 130-01 datalogger, set to a 250 Hz sampling frequency; the other 5 measurements were carried out using a 1.5 Hz SL06 acquisition unit by SARA Electronic Instruments, set to a 200 Hz sampling frequency. Ambient noise records of 1-hour duration were acquired in each station in two days characterized by different weather conditions: on May 27 with a strong wind (on average 20 knots according to the Trapani forecast station) and sea waves directly pounding against the cliff and on May 30 with a weaker wind (on average 15 knots) blowing on the opposite direction and so avoiding the generation of sea waves against the cliff.

The seismic noise records were processed by the use of Geopsy software ([www.geopsy.org](http://www.geopsy.org)). The 1-hour time histories were divided into non-overlapping windows of 40 s and the Fast Fourier Transform (FFT) in the frequency range between 0.4 and 60.0 Hz was computed for each component. By averaging over the windows, the amplitude spectra and the H/V spectral ratio, as well as the distribution of their values in horizontal plane (i.e. spectrum rotate and H/V rotate), were finally achieved for each single record.

The HVSR (Nakamura, 1989) analysis is worldwide used to predict the resonance frequency of a site, particularly when layers having low shear-wave velocity cause a sharp impedance contrast with the bedrock. The presence of a resonance peak in the HVSR curve has been interpreted both in terms of SH-wave resonance in soft surface layers, or in terms of the ellipticity of particle motion when the ambient noise wave train is made up predominantly of surface waves (Bonnefoy-Claudet *et al.*, 2006). In practice, the wavefield is expected to be a combination of both types and the HVSR curve contains information about the shear wave velocity profile in shallow sediments (Galea *et al.*, 2014).

**Results.** By analyzing the FFT of the Cala Rossa Bay records (Fig. 2), a significant energy contribution clearly appears at frequencies lower than 1 Hz in May 27, when a strong wind and sea waves acted against the cliff; on contrary, in May 30, with more favorable weather conditions, such a spectral contribution disappears.

The HVSR curves show a peculiar shape both in the unstable and in the plateau zones, a cave can be observed in the frequency range between 1 and 2 Hz, corresponding to a marked amplification of the vertical ground motion component. The HVSRs also show an asymmetrical peak between 5 and 6 Hz and several peaks at higher frequencies (10-60 Hz). Even though it is not always significant according to SESAME guidelines (Bard, 2005), the HVSR peak at 5-6 Hz frequency is present in the measurements carried out within and in proximity of the unstable zones, while it is not visible in the plateau area.

**Discussion.** *The Anchor Bay test site.* A comparison between the results obtained at Cala Rossa Bay in Favignana Island and the ones of Anchor Bay in Malta was possible taking into account the data already published by Galea *et al.* (2014).

The Anchor Bay test site was chosen for such a comparison because of the lithotechnical setting very similar to the one of Cala Rossa Bay. According to Pedley *et al.* (2002), in Anchor Bay stiff limestones of Late Miocene age (Upper Coralline Limestone, UCL), with a thickness of about 20 m, overlie blue clays of the Middle Miocene (Blue Clay formation, BC) about 30

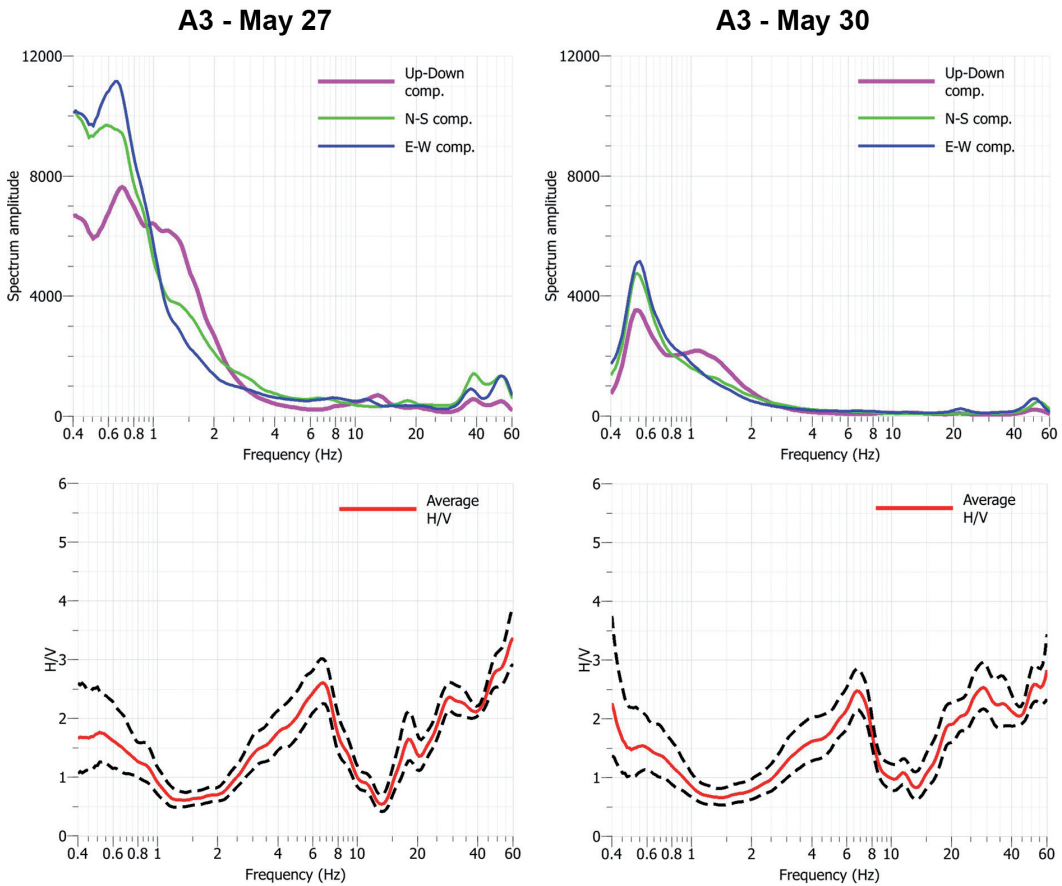


Fig. 2 – Amplitude spectrum and HVSR analysis results at A3 station. Left: results referred to the measurement on May 27 with stronger wind (on average 20 knots) and sea waves pounding directly on the cliff. Right: results referred to the measurement on May 30 with weak wind (on average 15 knots) and low sea waves on the cliff.

m thick. The blue clays lie on top of a not-outcropping stiff limestone of the Lower Miocene (Upper Globigerina Limestone, UGL).

Also in this case, a lateral spreading is generated by the juxtaposition of the stiff limestones over the plastic blue clays. The phenomenon is responsible for the generation of four unstable rock blocks, behind which there is a stable plateau area. Seismic noise measurements were carried out on both the unstable blocks and the plateau area. Time-series of 20 minutes recorded using a three-component seismometer Tromino at a sampling frequency of 128 Hz were reprocessed for this study.

In Anchor Bay, the HVSRs show a ubiquitous resonance peak in a narrow frequency range between 1 and 2 Hz and a following sharp dip of the spectral ratio. As this HVSR feature is widespread present in the Maltese archipelago, the dip of the HVSR curve has been interpreted in terms of a shallow shear-wave velocity inversion, which corresponds to the interface between the competent UCL and the plastic BC (Galea *et al.*, 2014).

*HVSR analysis comparison and interpretation.* Given the similar outcropping lithologies, a similar response in the HVSR results of Cala Rossa Bay and Anchor Bay would be expected (Fig. 3). The HVSR peak at 5-6 Hz observed in Favignana and the peak at 1-2 Hz observed in Malta, as well as the following dips, could be related to a stratigraphic response. According to Galea *et al.* (2014), the HVSR peak can be interpreted in terms of Rayleigh-wave ellipticity and/

**Cala Rossa A3**

**Anchor Bay 11**

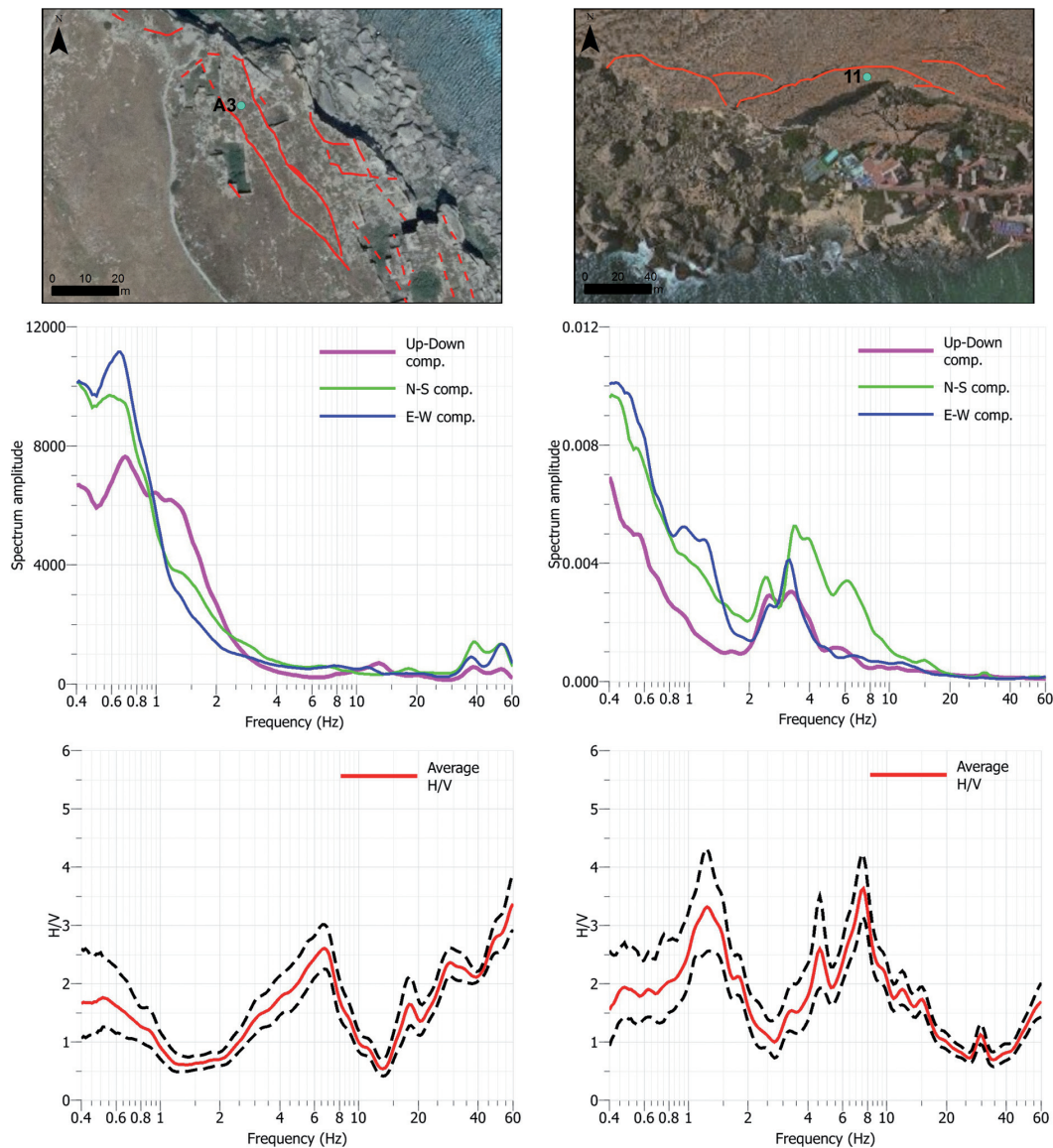


Fig. 3 – Comparison between amplitude spectrum and HVSR results for the A3 station in Cala Rossa Bay (on left) and the station 11 in Anchor Bay (on right).

or trapping of SH-waves, while the dip in terms of a shallow shear-wave velocity inversion, i.e. the same that in Favignana due to the interface between the stiff grainstones and the plastic clays. The shift of the stratigraphic response to higher frequencies at Cala Rossa Bay when compared to Anchor Bay could be related to the different thickness or depth of the clayey deposits. Based on estimated shear-wave velocities and thicknesses, the peak observed in the HVSR curves is compatible with the stratigraphy of Cala Rossa Bay. However, further in-site characterization will be surveyed for future analyses. The HVSR peak generally is visible on the unstable blocks and this could be related to the weakening of the clays in the landslide zone that is responsible for an increasing of the local impedance contrast with the underlying bedrock.

On the other side, the HVSRs at Cala Rossa Bay generally become lower than 1 in the frequency range between 1 and 2 Hz. Such an anomaly respect to the Anchor Bay site could be related to the complex network of man-made tunnels and caves within the Lower Pleistocene carbonate grainstones, which could have a disturbing role in seismic wave propagation, leading to an amplification of the ground motion vertical component.

Finally, the complex behavior of the HVSRs in the higher frequency range (10-60 Hz) can be related to the vibrational behavior of the dislodged rock blocks. The seismic response observed in frequency from 10 to 60 Hz is in agreement with the results published by Got *et al.* (2010) showing that the highest seismic energy was concentrated in specific frequency bands depending on geometrical and mechanical properties of the rock blocks. Polarization analyses (Burjánek *et al.*, 2010, 2012; Galea *et al.*, 2014) will be carried out in order to derive the main modes of vibration for a better comprehension of the seismic response of the cliff slope as well as of its stability in case of earthquake shaking.

**Conclusions.** Preliminary results of seismic noise measurements carried out in the western part of Cala Rossa Bay (Favignana, Italy) show that a site stratigraphic response exists and is characterized by a HVSR peak between 5 and 6 Hz followed by a dip of the HVSR curve. It was also observed a HVSR dip below level 1 in a narrow frequency range, between 1 and 2 Hz, that could be related to the dense network of man-made tunnels and caves within the Lower Pleistocene carbonate grainstones of the Island.

A complex local seismic response was also observed at higher frequencies (10-60 Hz) that can be related to the seismic response of the dislodged rock blocks. The results obtained at Cala Rossa Bay were compared to the ones obtained at Anchor Bay in Malta due to the high similarity of the local geological and lithotechnical setting responsible for ongoing lateral spreading landslide processes.

More-detailed studies will be carry out by experiencing analytical approaches devoted to characterize the vibrational modes of the surveyed rock blocks, in order to evaluate the sea cliff stability conditions during earthquake shaking.

**Acknowledgements.** This study is part of a PhD research (Roberto Iannucci) at the Department of Earth Sciences of Sapienza University of Rome. The Authors wish to thank Luca Falconi, Vladimiro Verrubbi and Augusto Screpanti for data and information provided about the Cala Rossa Bay area and Fabio Martorelli for his useful support in the field geological survey.

## References

- Abate B., Ferruzza G., Incandela A. and Renda P.; 1995: *Tettonica trascorrente nelle Isole Egadi (Sicilia occidentale)*. Studi Geologici Camerti, vol. spec. **1995/2**, pp. 9-14.
- Abate B., Incandela A. and Renda P.; 1997: *Carta geologica delle isole di Favignana e Levanzo (Arcipelago delle Egadi)*, Scala 1:12.500. Dip. di Geologia e Geodesia, Università di Palermo.
- Antonoli F., Kershaw S., Renda P., Rust D., Belluomini G., Cerasoli M., Radtke U. and Silenzi S.; 2006: *Elevation of the last interglacial highstand in Sicily (Italy): A benchmark of coastal tectonics*. Quaternary International, **145-146**, pp. 3-18.
- Bard P.Y.; 2005: *Guidelines for the implementation of the H/V spectral ratio technique on ambient vibrations: measurements, processing, and interpretations*. SESAME European Research Project. WP12, deliverable D23.12, 2004, Available at: <http://sesame-fp5.obs.ujf-grenoble.fr/Deliverables2004>.
- Bonnefoy-Claudet S., Cotton F. and Bard P.Y.; 2006: *The nature of noise wavefield and its applications for site effects studies: a literature review*. Earth-Sci. Rev., **79** (3), pp. 205-227.
- Burjánek J., Gassner-Stamm G., Poggi V., Moore J.R. and Fäh D.; 2010: *Ambient vibration analysis of an unstable mountain slope*. Geophys. J. Int., **180** (2), pp. 820-828.
- Burjánek J., Moore J.R., Yugsi Molina F.X. and Fäh D.; 2012: *Instrumental evidence of normal mode rock slope vibration*. Geophys. J. Int., **188** (2), pp. 559-569.
- Canuti, P., Casagli, N., Garzonio, C. A. and Vannocci, P.; 1990: *Lateral spreads and landslide hazards in the Northern Apennine: the example of M. Fumaiolo (Emilia Romagna) and Chiusi della Verna (Tuscany)*. Proc. 6th International Congress of the International Association of Engineering Geology, Amsterdam (Netherlands), August 1990, **3**, pp. 1525-1533.
- Catalano R., Di Stefano P., Sulli A. and Vitale F.P.; 1996: *Paleogeography and structure of the central Mediterranean: Sicily and its offshore area*. Tectonophysics, **260**, pp. 291-323.

- Del Gaudio V., Coccia S., Wasowski J., Gallipoli M.R. and Mucciarelli M.; 2008: *Detection of directivity in seismic site response from microtremor spectral analysis*. Nat. Hazards Earth Syst. Sci., **8**, pp. 751-762.
- Falconi L., Peloso A., Puglisi C., Screpanti A., Tati A. and Verrubbi V.; 2015: *Rockfalls monitoring along eastern coastal cliffs of the Favignana island (Egadi, Sicily): preliminary remarks*. In Lollino G., Giordan D., Marunteanu C., Christaras B., Yoshinori I. and Margottini C., eds: *Engineering Geology for Society and Territory*, **8**, pp. 287-291. DOI: 10.1007/978-3-319-09408-3\_50
- Galea P., D'Amico S. and Farrugia D.; 2014: *Dynamic characteristics of an active coastal spreading area using ambient noise measurements-Anchor Bay, Malta*. Geophys. J. Int., **199**, pp. 1166-1175.
- Gigli G., Frodella W., Mugnai F., Tapete D., Cigna F., Fanti R., Intrieri E. and Lombardi L.; 2012: *Instability mechanisms affecting cultural heritage sites in the Maltese Archipelago*. Nat. Hazards Earth Syst. Sci., **12**, pp. 1883-1903.
- Got J.-L., Mourot P. and Grangeon J.; 2010: *Pre-failure behaviour of an unstable limestone cliff from displacement and seismic data*. Nat. Hazards Earth Syst. Sci., **10**, pp. 819-829.
- Goudie A.; 2004: *Encyclopedia of Geomorphology*. Routledge, London (United Kingdom), 1156 pp.
- Hutchinson J.N.; 1988: *General Report: Morphological and geotechnical parameters of landslides in relation to geology and hydrogeology*. In Bonnard C., ed: *Proceedings, Fifth International Symposium on Landslides*, **1**, Balkema, Rotterdam (Netherlands), pp. 3-35.
- Nakamura Y.; 1989: *A method for dynamic characteristics estimation of subsurface using microtremor on the ground surface*. Quarterly Report of Railway Technical Research Institute (RTRI), **30** (1), pp. 25-33.
- Nigro F., Renda P. and Arisco G.; 2000: *Tettonica recente nella Sicilia nord-occidentale e nelle Isole Egadi*. Soc. Geol. It., **119**, pp. 307-319.
- Panzerà F., D'Amico S., Lotteri A., Galea P. & Lombardo G.; 2012: *Seismic site response of unstable steep slope using noise measurements: the case study of Xemxija Bay area, Malta*. Nat. Hazards Earth Syst. Sci., **12** (11), pp. 3421-3431.
- Pedley M., Hughes-Clarke M. & Galea P.; 2002: *Limestone Isles in a Crystal Sea: The Geology of the Maltese Islands*. Publishers Enterprises Group Ltd, San Gwann (Malta), 109 pp.
- Scandone P., Giunta G. and Liguori V.; 1974: *The connection between Apulia and Sahara continental margins in the Southern Apennines and in Sicily*. Mem. Soc. Geol. It., **13**, pp. 317-323.
- Slaczka A., Nigro F., Renda P. and Favara R.; 2011: *Lower Pleistocene deposits in East part of the Favignana Island, Sicily, Italy*. Il Quaternario Italian Journal of Quaternary Sciences, **24** (2), pp. 153-159.
- Tondi E., Cilonà A., Agosta F., Aydin A., Rustichelli A., Renda P. and Giunta G.; 2012: *Growth processes, dimensional parameters and scaling relationships of two conjugate sets of compactive shear bands in porous carbonate grainstones, Favignana Island, Italy*. Journal of Structural Geology, **37**, pp. 53-64.
- Varnes D.J.; 1978: *Slope movement types and processes*. In Schuster R.L. and Krizek R.J., eds: *Landslides Analysis and Control, Special Report 176*, National Academy of Science, Washington D.C. (USA), pp. 11-33.

## MARINE GEOPHYSICAL AND GEOLOGICAL INVESTIGATIONS IN SUPPORT TO THE CONSTRUCTION OF NEW HARBOUR INFRASTRUCTURES: THE TRIESTE MARINE TERMINAL EXTENSION

C.A. Masoli<sup>1</sup>, L. Petronio<sup>2</sup>, E. Gordini<sup>2</sup>, M. Deponte<sup>2</sup>, D. Cotterle<sup>2</sup>, R. Romeo<sup>2</sup>, G. Böhm<sup>2</sup>, A. Barbagallo<sup>2</sup>, R. Belletti<sup>2</sup>, S. Maffione<sup>2</sup>, F. Meneghini<sup>2</sup>

<sup>1</sup> Geosyntech srl - Trieste, Italy

<sup>2</sup> OGS (Istituto nazionale di Oceanografia e di Geofisica Sperimentale), Trieste, Italy

**Introduction.** A combination of geographic and historical factors has made the Trieste harbour one of the most important commercial terminals in the Mediterranean sea. Thanks to the deep natural draft (about 18 m) modern high capacity vessels can moor to the piers so this area is subject to a modernization project to improve commercial traffic capability. In this expansion plan, the container Trieste Marine Terminal (TMT) - Molo VII, is interested by an extension of about 200 m. The actual terminal was built upon equal-spaced pillars founded in

the bedrock. To more effectively support this project new bathymetry, geological/geotechnical and geophysical data were collected.

**Geological setting.** The Gulf of Trieste, the northernmost sector of the Adriatic Sea, is part of the Adriatic Apulian foreland. It is composed of the Mesozoic Adriatic Carbonate Platform (Vlahović *et al.*, 2005), Paleocene-Eocene carbonates and Eocene Flysch (Onofri, 1982), a turbiditic sequence composed by an alternation of sandstones, siltstones and marlstones. From a structural point of view, two main patterns interest the Trieste Karst area: the Karst Thrust, developed in Dinaric direction (NW-SE), which forces limestones to overlie the Flysch of Trieste, and some minor thrusts in the turbidites. The Gulf of Trieste was extensively recently explored by several offshore seismic lines (Busetto *et al.*, 2010, 2012) that allow to obtain new information to refine previous geological/structural model (Cavallin *et al.*, 1978; Carulli *et al.*, 1980; Carobene *et al.*, 1981).

The Trieste Marine Terminal (TMT) is located in the southern part of the Trieste harbour. Several seismic acquisition were carried in this area. In the 1950s, a single channel reflection seismic (Mosetti and Morelli, 1968) provided information about the Quaternary sediments covering a drainage pattern superimposed on the Eocene Flysch that during the Messinian were emerged favouring the fluvial erosion (Fantoni *et al.*, 2002). This was the first marine geophysical experiment in Italy followed by two refraction profiles (Finetti, 1965, 1967) and, recently, by some single channel reflection seismic campaigns acquired for geotechnical and environmental studies (unpublished data).

In the studied area the bedrock is represented by the Flysch formation covered by Plio-quaternary sediments (Brambati and Catani, 1988; Masoli and Zucchi, 1968). The bedrock is characterized by an alternation of layer of different geomechanical behaviour and by the presence of a weathered zone. The sedimentary sequence covering the Flysch is characterized by an alternation of levels of silt/sandy clay (greenish gray) with fragments of shells and layers of sand fine to medium, and trace of gravel. Silt/sandy clay are saturated with a very soft consistency and sand has a very loose apparent density.

**Field investigations.** The study area is located on the front of the TMT (about 200,000 m<sup>2</sup>) with an average water depth of 20 m (Fig. 1). The marine bathymetric and geophysical survey was carried out in the Autumn 2014 by the OGS boat “Anthea” equipped for shallow water offshore survey. Underwater refraction seismic requires also the onshore access to the pier to record the hydrophone array data. Data were collected in two phases because of the presence of strong Bora wind that inhibits any offshore activities. In the first part were collected bathymetric, side-scan-sonar, magnetometer and sub bottom profile data, in the second the refraction data.

As the front of the TMT is characterized by an intensive maritime traffic, the acquisition phase required a strong coordination with the local maritime authority and the several operators involved in the different harbour activities (berthing/unberthing, loading/unloading , etc.)

**Navigation and tidal stage.** Navigation data for water-based survey were collected with a Trimble DGPS DSM232 in WGS84 and were passed to the different acquisition tools and the navigational software at a rate of 1 Hz. PDS2000 software with coast line and infrastructure perimeters was used to display the course of the boat and allow real-time navigation along the theoretical predetermined lines.

Tidal stage for data elevation correction were obtained from Trieste Station, belonging to the National Tidegauge Network of “Istituto Superiore per la Protezione e la Ricerca Ambientale – Ispra”. The station is located in Trieste’s seaport, near the “Lega Navale” wharf. The tidegauge station is equipped with altimetric datum. Each datum is referred to the average sea level, measured in Genoa using the ancient Thompson tidegauge. The datums are metallic check tags, used to determinate the altimetric level by means of high precision leveling, following the guidelines fixed by IGM (Italian Military Geographic Institute). From 07/10/2009 the “hydrometric level” is measured with a new high precision radar sensor SIAP+MICROS TLR.

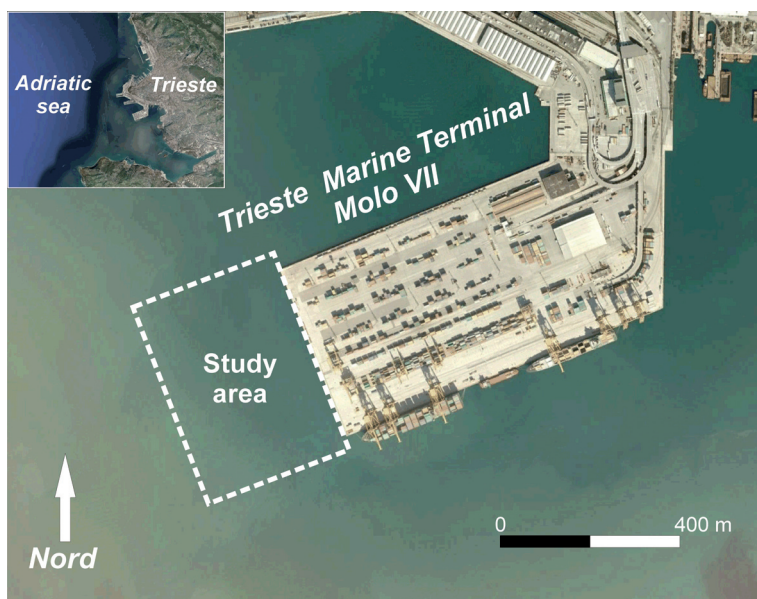


Fig. 1 – Position map.

The data, downloaded from ISPRA web site [www.mareografico.it](http://www.mareografico.it), have been imported in the acquisition software PDS2000, to obtain a full interpolated tidal curve.

**Bathymetry.** Multibeam echo sounders (MBES) emit sound waves in the shape of a fan from directly beneath a ship's hull. These systems measure and record the time it takes for the acoustic signal to travel from the transmitter (transducer) to the seafloor (or object) and back to the receiver; by the analysis in term of amplitude and phase of the received signal, with beam forming techniques, it is possible to detect the incidence angle and the distance. In this way, MBES produce a "swath" of soundings (i.e., depths) for broad coverage of a survey area. The coverage area on the seafloor depends on the depth of the water, typically three to five times the water depth. MBES is an useful tool to acquire water depth information, to determine least water depths over critical items such as wrecks, obstructions, and dangers to navigation and to detect objects in general.

The morpho-bathymetric survey was carried out with multibeam echosounder, Teledyne-Reson Seabat 7125. This dual frequencies (200 and 400 kHz) instrument utilizes 512 equidistant beams with a maximum ping rate of 50 pulse per second. To correct the raw data, the system has to know precisely, for each pulse, the vessel attitude in terms of pitch, roll, heave, yaw; this is the task of the Motion reference unit model MAHRS, produced by TSS-TELEDYNE. The roll value is also used to steer the acoustic pulse so to insonify always the nadir area of the seafloor. Data acquisition was performed at a velocity of 4 knots along parallel lines allow to obtain an overlap of 20%. As the acoustic pulse can be oriented, we obtained images not only the seabed but also the pillars supporting the wharf. Time to depth conversion was made by real time data from Sound Velocity Probe, Reson SVP71, and sound velocity profiles using the YSI CastAway CTD.

**Side scan sonar and magnetometric survey.** The Side Scan Sonar (SSS) is a technique based on the emissions conical or fan-shaped pulses down toward the seafloor across a wide angle perpendicular to the path of the sensor through the water. SSS produces images of the sea floor similar to a large-scale aerial photographs useful to detect seafloor installations (i.e., cables, pipelines, etc.), shipwreck and other obstructions that may be hazardous for navigation. Depending on the different acoustic response it is possible to obtain also indirect information about the nature of the sediment (sand, mud or their mixtures) or the presence of outcropping bedrock, metal bodies, etc.

We utilized the EdgeTech DF-1000 / DCI Digital Side Scan Sonar Sistem (100 and 500 kHz) controlled by CODA DA-50 (Coda Technologies). Data were acquired with the tow fish at the depth of 4 m with a cruise velocity of 4 knots. The investigation involved the generation of six sonograms NW-SE oriented (i.e, parallel to the TMT front) with a length of 500 m and a lateral range of 75 m. The tie line interval was about 50 m that permits a full coverage with overlapping of the study area.

The acquired data were processed through Coda Octopus Geokit Mosaics software and graphically represented in a mosaic in order to locate objects on the sea floor and to define the morphological and sedimentological characteristics of the seabed that confirm/complete the information coming from the bathymetric multibeam survey.

In addition to SSS data acquisition, a magnetometer survey has been carried out to obtain a magnetic map in front of TMT. The survey was conducted from "Anthea" boat with NW-SE tie lines spaced 25 m interval. Magnetic data were acquired using a Marine Magnetics SeaSpy magnetometer towed at a distance of 20 m behind the boat. The sensor elevation was recorded with each magnetic measurement to allow for later correction of the water-depth related changes in magnetic intensity. The magnetometer was cycled at 4 Hz providing about one sample per metre.

The magnetometer survey was preparatory to an UXO (Unexploded Ordinance) survey performed by certified personnel.

**Sub bottom profile.** A dense grid of sub-bottom-profile (SBP) data was recorded to identify recent sediments up to the top of rock basement (Eocene Flysch). A total of about 11 km distributed along 30 lines (11 NW-SE direction and 19 NE-SW direction) was acquired by a Sub Bottom Profiler Edgetech SB-216S (tow fish) and Edgetech 3200-XS topside (control/acquisition unit) with a cruise velocity of 3.5 knots. After several tests we acquire data with the following parameters: up-sweep 2-10 kHz, 20 ms length with a source rate of 2Hz, tow fish depth 1.5 m. SBP data penetration allows to obtain information of sediments/Flysch interface which in the studied area ranges from 30 to 50 m below the sea level.

The two-way-time data were converted in depth below sea level using the velocity of 1530 m/s for the water column and 1610 m/s as an average for the sediments from sea-bottom to the Flysch top. This velocity was obtained by underwater refraction (see next paragraph) and by a check-shot measurement performed in a drilled hole. The SBP lines were analyzed more than once to avoid misinterpretation of multiple events and to test the repeatability of the interpretation. The sediments/bedrock interface were detected and correlated with to the borehole data and to tie-line crossings in correspondence of the line intersections.

In the SW sector, where the bedrock is deeper, we compared SBP data with single channel reflection data acquired with boomer source in a previous unpublished study.

**Underwater seismic refraction.** From a geotechnical perspective a more important problem is that it is very difficult to determine engineering properties from reflection records. Refraction seismic survey are routinely acquired on land for geotechnical purposes. S-wave data are preferred because are strictly connected with geotechnical parameters but the generation of shear wave at the sea bottom is not a trivial issue. To obtain information about the bedrock nature and alteration, an underwater P-wave seismic refraction was planned.

Seismic survey has been carried out along seven profiles with hydrophone cables deployed on the sea-bottom. Acquisition geometry (i.e., trace interval and maximum offset) was defined after a feasibility study to estimate the minimum offset to detect refraction coming from the bedrock. This preliminary analysis was performed by the use of synthetic seismic data computed with different simplified velocity models.

Two 24 channels hydrophone cables, 5 m interval, and a mud gun (Bolt DHS 5500, 7.6280 in<sup>3</sup>) with a pressure of 70 bar were used. Hydrophone cables was deployed by the boat starting from the TMT head along the planned lines. Five to eleven shot points was performed for each line lowering mud gun to the sea bottom. A precise time-break identification was obtained by

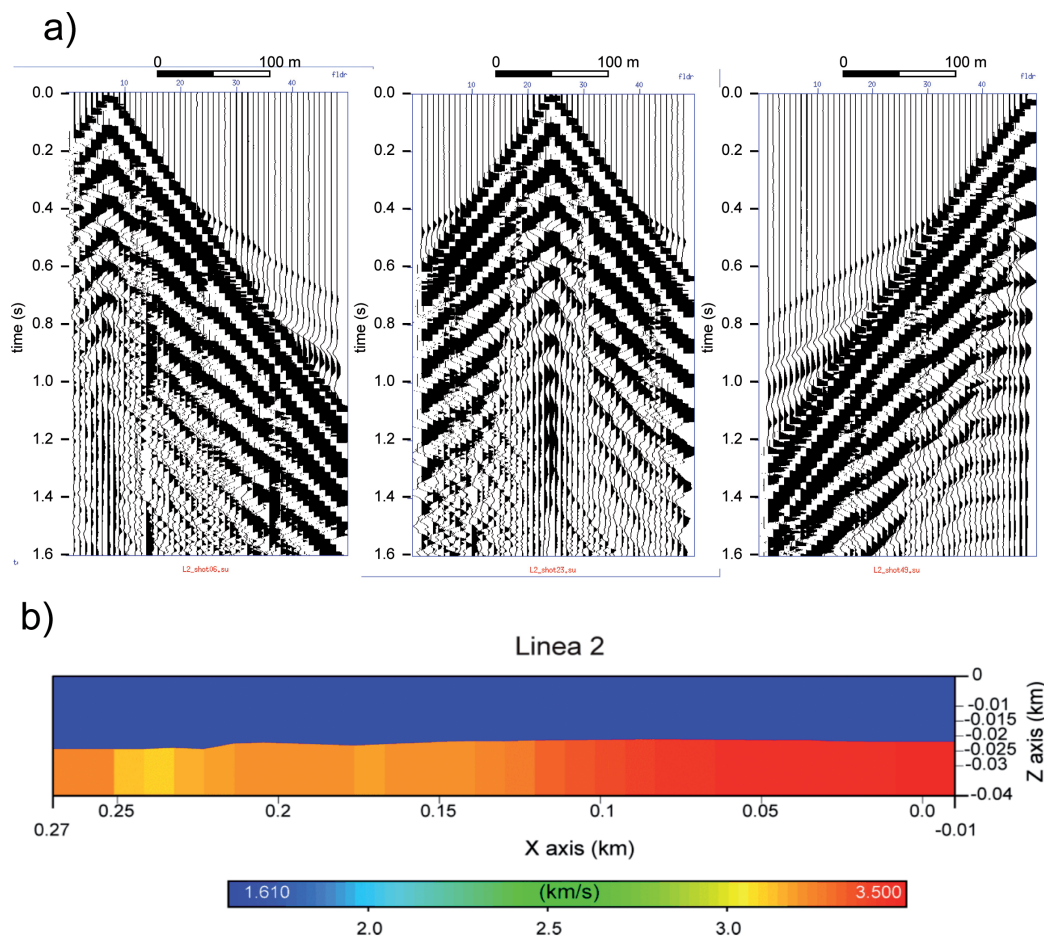


Fig. 2 – Underwater refraction seismic data: a) three common-shot-gathers recorded along the line 2 (perpendicular to the TMT front) and b) P wave velocity model obtained by the first arrivals tomographic inversion (line 2).

the near-field hydrophone. These data were transmitted by a radio-link (RTS-100) to a dedicated onshore seismograph. We used three Seismic Source Daq Link III seismographs (two for the 48 hydrophones, the third one to record the near-field signature and GPS PPS signal) with 0.125 ms sampling rate and 5 s data length.

Underwater seismic refraction data have a good signal to noise ratio and the first arrivals are clearly detectable also a larger offsets (Fig. 2a). Travel time tomography was applied to each seismic line to obtain the corresponding 2D depth velocity section and to estimate the depth of the sediment/Flysch interface. We invert the first arrivals picked in each seismic line. First, we separated two different arrivals in the picked travel times for each common shot gather: the direct arrivals and the refracted arrivals from an horizon below the sea bottom, interpreted as the top of Flysch. For this purpose, we applied a procedure which automatically identifies the knee point (crossover distance) separating the two different arrivals. Then, we inverted the refracted arrivals by using an inversion approach based on minimum dispersion of the refracted points (Carrion *et al.*, 1993): depth and geometry of the refracted horizon are defined by an iterative procedure which minimized the difference between the refracted points and the estimated surface. The same procedure reconstructed also the lateral velocity gradient of the layer below the refracted interface. In the inversion we constrained the sediment velocity (1610 m/s) associated to the first layer below sea bottom.

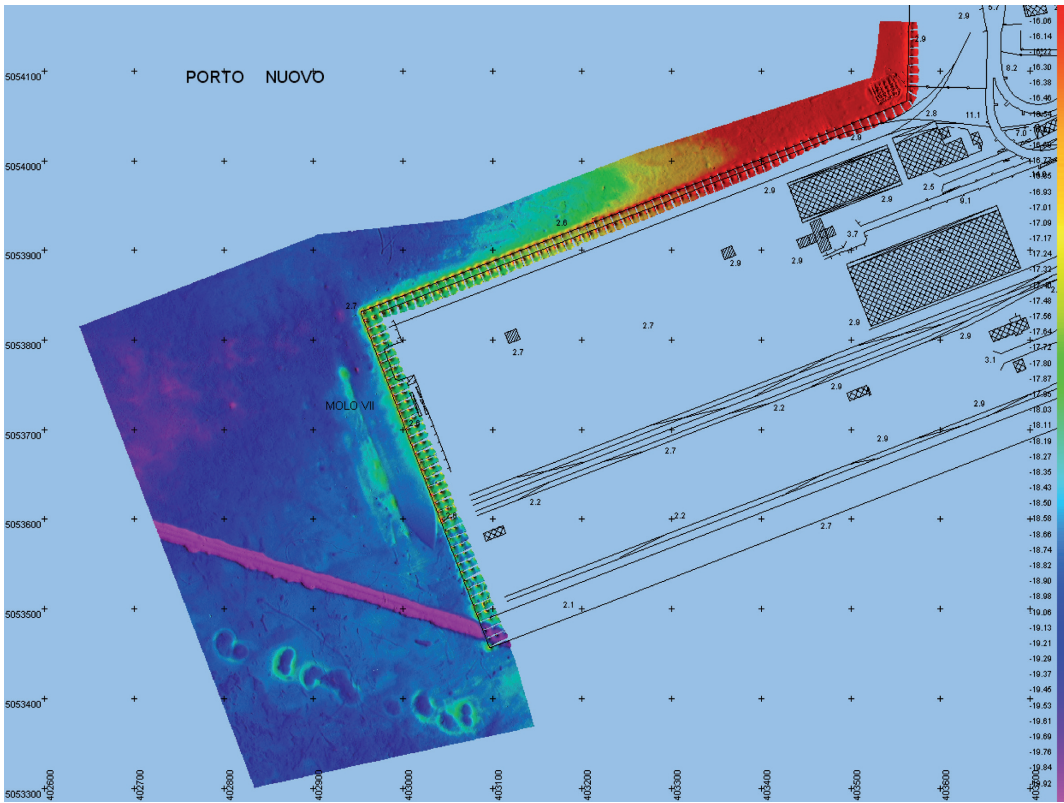


Fig. 3 – Bathymetric map.

We applied the staggered grid method (Vesnaver and Böhm, 2000) for all lines, using a base regular grid with low lateral resolution (28 m) obtaining a final high lateral resolution grid (7 m).

As inversion algorithm we used the SIRT method (Simultaneous Iterative Reconstruction Technique) and the minimum time approach for the ray tracing (Böhm *et al.*, 1999). We estimated the reliability of inversion by computing the time residuals (difference between picked and computed travel times); we obtained 1.4 ms rms residual (equivalent to 2.6 % on picked travel times). An example of 2D velocity model is shown in Fig. 2b.

**Geological/geotechnical borehole data.** In addition to geophysical acquisition, a geological-geotechnical survey and geotechnical laboratory analyses were carried out in order to define the geolithologic, lithostratigraphic and geotechnical features of the area. In particular, eleven sea drillings reaching the first metres of the Flysch bedrock were performed. Of these, four were carried out onshore along the edge of the pier by positioning the drilling rig at the TMT head. The other seven were performed offshore with a barge. In addition to geolithologic and lithostratigraphic identification and classification, various tests were performed on core samples with the use of a pocket penetrometer and pocket vane in order to identify the Uniaxial Compressive Strength (UCS) and Undrained Shear Strength (Su) values and assess the cohesive soils. During the drilling, seventeen undisturbed samples were also extracted, with a Shelby-type tube sampler, along with twelve semi-disturbed samples, which subsequently underwent geotechnical laboratory analyses, as well as twenty Standard Penetration Tests (SPT). The SPT data revealed values between 1 and 32, with rejection on the lithological contact with the Flysch. From the SPT data, Phi values for sandy lithologies were assessed with various methods and revealed an average range of 20°-30° for levels which were less dense, and 30°- 40° for

the remaining. Regarding the finer silt-clay materials, a consistency ranging from soft to plastic was detected.

The Flysch was also classified by the Rock-Quality Designation (RQD) index and, where possible, data regarding sedimentation, fracturing and Joint Roughness Coefficient (JRC) was also collected. The RQD index data revealed that the first metres of Flysch bedrock are characterised by poor quality, which generally moves towards average and, at times, fair quality as further depths are reached.

Based on the assessments carried out, a lithostratigraphic model of the area was defined, and several geological sections were drawn. Specifically, the geolithological features are as follows: 1) from 0.0 to -15.80 / -28.80 m below seafloor (mbsf): silt-clay-sand complex; 2) from -15.80 / -28.80 to -18.80 / -32.00 mbsf: altered marlstone-sandstone Flysch; 3) from -18.80 / -32.00 mbsf: unaltered sandstone-marlstone Flysch.

Geotechnical laboratory tests were performed on the undisturbed and semi-disturbed samples extracted during the drilling, which allowed for the identification of the principal geotechnical parameters. Lastly, regarding the silt-clay-sand complex overlying the Flysch bedrock, the susceptibility to liquefaction based on grain size was assessed (Sherif and Ishibashi, 1978). The results showed that for four samples there is a possibility of liquefaction. Additional tests were performed based on the Liquid Limit (LL) and Plasticity Index (PI) (Seed *et al.*, 2003), which revealed the potential risk of liquefaction of some samples.

**Results and conclusions.** The results of the bathymetry survey are shown in a colour-shaded map in Fig. 3. Seaward of the TMT front, the bathymetry shows a smooth, gently sloping to SW with a water depth ranging from about 18 m to 21 m. Some interesting features can be observed on MBES data as well as on SSS data: a ship footprint located along the pier and an abandoned pipeline channel with NW-SE direction.

SBP data in conjunction with borehole data allow to obtain the depth and the morphology of the top of the bedrock. The assessment of geotechnical conditions was performed mainly on the base of the borehole data and by underwater refraction data.

**Acknowledgements.** TMT personnel for the support and the permission to present these data. Trieste Port Authority for the permission to access in the harbour area. Dr. Roberto Linari for the constructive discussion about seismic refraction data.

## References

- Böhm, G., Rossi G., and Vesnaver A., 1999. *Minimum time ray-tracing for 3-D irregular grids*, J. of Seism. Expl., 8: 117-131.
- Brambati A., Catani G., 1988. *Le coste e i fondali del Golfo di Trieste dall'Isonzo a Punta Sottile: aspetti geologici, geomorfologici, sedimentologici e geotecnici*. Hydrores Information, vol. 6: 13 - 28.
- Busetti M., Volpi V., Nicolich R., Barison E., R. Romeo, L. Baradello, Brancatelli G., Giustiniani M., Marchi M., Zanolla C., Wardell N., D. Nieto, and Ramella R., 2010. *Dinaric tectonic features in the Gulf of Trieste (Northern Adriatic)*. *Boll. Geof. Teor. Appl.*, 51, 2-3, 117-128.
- Busetti M., Zgur F., Romeo R., Sormani L., Pettenati F., 2012. *Caratteristiche geologico-strutturali nel golfo di Trieste*. Meeting Marino ISPRA, Roma, 25-26 Ottobre 2012.
- Carobene L., Carulli G.B. and Vaia F., 1981. *Foglio 25 Udine*. In: *Castellarin A. (ed.) Carta tettonica delle Alpi Meridionali*. CNR ± Progetto Finalizzato Geodinamica Pubbl. 441, 39-54.
- Carrion P., Böhm G., Marchetti A., Pettenati F. and Vesnaver A., 1993. *Reconstruction of lateral gradients from reflection tomography*. *Journal of Seismic Exploration* 2, 55-67.
- Carulli G.B., Carotene L., Cavallin A., Martinis B., Onofri R., Cucchi F. and Vaia F., 1980. *Evoluzione strutturale Plio-Quaternaria del Friuli e della Venezia Giulia*. In: *Contributi alla Carta Neotettonica d'Italia*. CNR ± Progetto Finalizzato Geodinamica Pubbl. 356, 488-545.
- Cavallin A., Martinis B., Carobene L., and Carulli G.B., 1978. *Dati preliminari sulla Neotettonica dei Fogli 25 (Udine) e40A (Gorizia)*. In: *Contributi preliminari alla realizzazione della carta neotettonica d'Italia*. CNR ± Progetto Finalizzato Geodinamica, Pubbl. 155, 189-197.
- Fantoni R., Catellani D., Merlini S., Rogledi S. and Venturini S., 2002. *La registrazione degli eventi deformativi cenozoici nell'avampata veneto-friulano*. *Memorie della Società Geologica Italiana*, 57, 301-313.
- Finetti I.R., 1965. *Ricerche sismiche marine nel Golfo di Trieste (Profilo sismico a rifrazione "Grado-Miramare")*. *Bollettino di Geofisica Teorica ed Applicata* 7(27), 201-217.

- Finetti I.R., 1967. *Ricerche sismiche a rifrazione sui rapporti strutturali fra il Carso e il Golfo di Trieste*. Bollettino di Geofisica Teorica ed Applicata 9(35), 214-225.
- Masoli M., Zucchi M. L., 1968. *Paleontologia ed ecologia dei sedimenti attraversati dal pozzo S. Sabba 2 - Golfo di Trieste* - Estratto dal Bollettino della Biblioteca e dei Musei Civici e delle Biennali d'arte antica.
- Mosetti F. and Morelli C., 1968. *Rilievo sismico continuo nel Golfo di Trieste. Andamento della formazione arenacea (Flysch) sotto il fondo marino nella zona tra Trieste, Monfalcone e Grado*. Bollettino della Società Adriatica di Scienze, LVI(1), 42-57.
- Onofri R., 1982. *Caratteristiche geolitologiche e geomeccaniche del Flysch nella Provincia di Trieste*. Studi Trentini Scienze Naturali, 59, Acta Geol.: 77 - 103.
- Seed R.B., Cetin K. O., Moss R. E. S., Kammerer A. M., Wu J., Pestana J. M., Riemer M. F., Sancio R. B., Bray J. D., Kayen R. E., Faris A., 2003. *Recent advances in soil liquefaction engineering: A unified consistent framework*. Report NO. EERC 2003-06 College of Engineering University of California Berkeley.
- Sherif, M. A., and I. Ishibashi, 1978. *Soil dynamics consideration for microzonation*. Proc. of the 2nd International Conf. on Microzonation, San Francisco, vol. I, pp. 81-96
- Vesnaver A. and Böhm G., 2000: *Staggered or adapted grids for seismic tomography? The Leading Edge*, 9, 944-950.
- Vlahović I., Tišljarić J., Velić I. and Matičec D., 2005. *Evolution of the Adriatic Carbonate Platform: Paleogeography, main events and depositional dynamics*. Paleogeography, Paleoclimatology, Paleocology, 220, 333-360.
- Vrabec M., Slavec P., Poglajen S., and Busetti M., 2012 *Geomorphology of submerged river channels indicates Late Quaternary tectonic activity in the Gulf of Trieste*, Northern Adriatic Geophysical Research Abstracts Vol. 14, EGU2012-8124.

## GEOPHYSICAL INVESTIGATIONS IN A DISMISSED INDUSTRIAL SITE: EX-ESSO (TRIESTE, ITALY)

R. Romeo<sup>1</sup>, L. Petronio<sup>1</sup>, A. Affatato<sup>1</sup>, A. Barbagallo<sup>1</sup>, R. Belletti<sup>1</sup>, G. Boehm<sup>1</sup>, J. Boaga<sup>2</sup>, G. Cassiani<sup>2</sup>, P. Paganini<sup>1</sup>, M.T. Perri<sup>2</sup>, D. Sorgo<sup>1</sup>, M. Rossi<sup>2</sup>

<sup>1</sup> OGS (Istituto nazionale di Oceanografia e di Geofisica Sperimentale), Trieste, Italy

<sup>2</sup> Dipartimento di Geoscienze, Università di Padova, Italy

**Introduction.** The study area is a former polluted industrial area, already home of coastal oil refinery and deposit of hydrocarbons, for which there is a reclamation project. It is owned by the Port Authority of Trieste, in the north-east of the Adriatic sea, Italy. The soils of this industrial area are soaked with hydrocarbons.

In 2004, the engineering company Geosyntech of Trieste has executed a plan of environmental characterization of the area, presenting the first plan of remediation measures for the safety of the territory.

We present the results of a multidisciplinary geophysical survey of the area called Ex-Esso, carried out to define the geometry of the bedrock and the stratigraphic sequence of the surface sediments to provide new information regarding the execution of a containment wall to restrain pollutants and assess the impact of the barrier on the movement of groundwater, analysis carried out with modeling for the analysis of the evolution of the raising of the groundwater level and the design of appropriate drainage.

**Geological setting.** The geology of this area of the NE of Italy is defined by the presence of formations belonging to two major lithoid complexes, limestones of the Adriatic Carbonate Platform (Mesozoic-Paleogene) and the Flysch of Trieste (sandstones and marls alternation in turbidite facies of the Eocene). Rounding out the stratigraphic Quaternary clastic deposits, of both marine and continental origin, which make up the seabed of the Gulf of Trieste and anthropogenic fill soil.

The hills of the province of Trieste are part of the chain of External Dinarides, in particular the west sector chain of Idria Rift. The area is characterized by two main structural reasons. The dominant factor of the tectonic landscape is the Karst Thrust that develops in a Dinaric featuring basically all the Trieste area. The other important is some smaller thrusts that affect extensively the area of Flysch on which stands the city of Trieste and then extend to the base of the coastal slope and within the Gulf (Busetti *et al.*, 2010). The system represents the most external Dinaric thrusts. It is characterized by intense deformation, in particular within the Eocene Flysch sequences, and it is affected by tectonic activity lasting to the Plio-Quaternary. Some sub-vertical faults with an anti-Dinaric NE–SW orientation and a strike-slip activity, cut the previous overthrusts (Carulli, 2011).

The outcrop of Flysch present in the study area, in the southern slope of Mount San Pantaleone, is characterized by a noticeable isoclinal fold, typical of this lithology, which are found in sections throughout the area dominated by the presence of main thrust.

The evolution of the morphology of the land is undoubtedly linked to the interventions of the man who, in order to land use, amended the original morphological detail. The previous location of industrial plants has redesigned over the years the current appearance of the slope.

The current shoreline, south of the study area, is not of natural origin but was generated by the contribution of debris, inert waste and ash landfill of the local dump (Via Errera), who moved the shore line of 150 m by adjusting the trends of natural coast. Along the paleo shoreline there are some outcrops of marine clays mixed with bitumen (anthropogenic) and with the presence of fragments of remains white shells.

Looking at the LIDAR topographic data, it is observed that the Mount San Pantaleone has a share of 40-50 m and its southern side has an average slope of 40°. The shape, probably affected by the dominant human activity, is similar to the forms of coastal shelf and slope, with a cliff at times sub-vertical.

**Field investigation.** As part of the geophysical survey, in view of the peculiar characteristics of the site under study, they were applied both methods of electrical resistivity tomography and the refraction seismic.

*Electrical Resistivity Tomography (ERT).* ERT is a commonly used geophysical method for the imaging of shallow sub-surface target.

The equipment used is called “light 4Point hp” and is produced by L-Gm Lippmann Geophysikalische Messgeräte (Germany).

The location of the electrodes was preceded by a topographic survey to define the alignment and the distance between electrodes. During the prospecting it was adopted configuration Wenner-Schlumberger with the technique of direct measurement and another to estimate the error of the measurement.

The ERT survey was divided into 9 lines, with 550 channels, distance between channels 1 to 4 m and a total length of 1,090 m.

*Refraction seismics.* The acquisition of the seismic data was performed with the recording system Summit - DMT, consisting of a USB interface connected to the PC and from units of A / D conversion arranged on the ground, connected to the individual vertical geophones to 10 Hz.

It was used an accelerated mass seismic source called PWD (Power assisted Weight Drop). This system of energization is made from a steel beam that is accelerated by an elastic strap, tensioning through the hydraulic lift of a piston integral with the mass itself, to increase the speed and generate a seismic signal more impulsive energy. The source is installed on a truck Scam 4WD.

The acquisition parameters are 5 refraction lines, 550 channels, 112 shots, 2 m distance between stations, 0.250 ms sampling, 2 s record length, 1090 m total length. Much of the seismic lines were acquired at the ERT locations.

*Surface wave.* Surface wave methods allow the extraction, and then inversion, of Rayleigh/ Love wave dispersion properties to recover shear-wave velocity profile. In general, the model

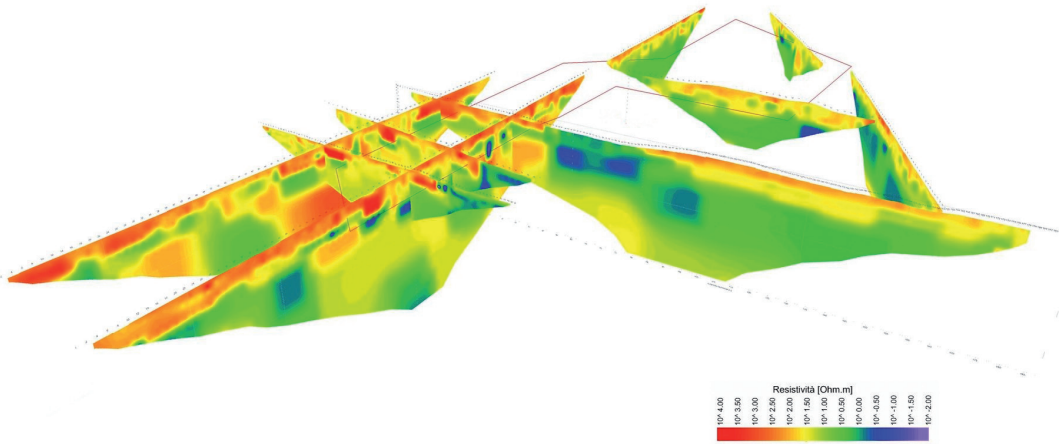


Fig. 1 – Electrical Resistivity Tomography (ERT) tridimensional 2D pseudosection resistivity model of the Ex-Esso industrial site (Trieste, Italy).

used for the dispersion curve interpretation is 1D. Hence, every time the velocity distribution is laterally heterogeneous, and the model errors can have significant consequences on the reliability of resulting shear-wave velocity distributions. For this case studies we the possibility to enhance lateral heterogeneities by an innovative 2D surface wave dispersion analyses inversions with a multi-offset phase analysis (MOPA) able to detect and locate the lateral discontinuities.

In the frequency domain, the surface wave response can be described by the superposition of modal contributions (Aki and Richards, 2002):

$$s(\omega, x) = \sum_m s_m(\omega, x) = \sum_m B_m(\omega, x) e^{j(\omega t - k_m(\omega)x + \varphi_0(\omega))} \tag{1}$$

where:  $j$  is the complex unit,  $x$  is the source-receiver distance,  $\omega$  the angular frequency, and  $k_m(\omega)$  the wavenumber of the  $m$ -th mode. If we disregard the amplitude  $B_m(\omega, x)$  and consider only the modal phase:

$$\phi(\omega, x) = -k_m(\omega) \cdot x + \varphi_0(\omega). \tag{2}$$

The experimental phase can be extracted from time-to-frequency Fourier transform applied on the collected traces. Thus, under the assumption that the  $m$ -th mode carries the largest part of the energy and so the summation in Eq. 1 can be approximated to consist of only its  $m$ -th term, the wavenumber  $k_m(\omega)$  can be recovered by using a simple linear regression (Strobbia and Foti, 2006). Eq. 2 means that phase-offset points lie on a straight line with slope coefficient proportional to  $k_m(\omega)$ . Hence, lateral velocity variations reveal themselves as a slope changes in the presence of lateral heterogeneities. For different subsets of contiguous geophone locations ( $x_i$ ), different values of  $k_m(\omega, x_i)$  are obtained for the same frequency  $\omega$ . Thus, the location of slope changes in the phase-offset piecewise linear function can highlight the locations of lateral discontinuities (Vignoli and Cassiani, 2009; Vignoli *et al.*, 2015). If slope changes occur consistently at the same location for a large frequency range, we can confidently guess that, at that location, there is a lateral velocity variation.

In the Ex-Esso area we adopted the MOPA technique detecting lateral variation using N. 48 4.5 Hz geophones and several sources (vibrois, hammer, seismic gun).

**Geological investigation.** A hydrological study and monitoring of groundwater was carried out for a period of 8 months in 5 piezometric stations, to assess the development of the water table. Pluviometric measurements used are those measured by the regional Civil Protection.

During the project were carried out 12 drilled boreholes (E1 - E12), to reconstruct the stratigraphy of the area and determine the geotechnical parameters. The investigation depth

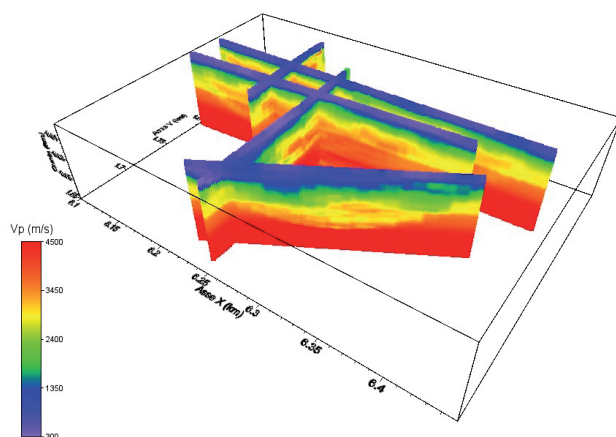


Fig. 2 – Tomographic inversion of refraction seismic survey of of the Ex-Esso industrial site (Trieste, Italy).

automatically determine a 2D pseudosection resistivity model obtained from electrical imaging survey (Fig. 1).

The plotting of data against position along a traverse line, to produce a display of resistivity data in which values are given to the intersection point of 45° lines drawn from mid-points of the current and potential electrode pairs. Depths in the resulting ‘section’ below a transverse bear no simple relationship to the true geology; a pseudosection shows the variation of the measured parameter with position and with effective depth of penetration, rather than with true depth.

*Refraction seismic and tomographic inversion.* For each line we have been executed a tomographic inversion, using the tomographic software Cat3d. The algorithm used is the reverse SIRT (Simultaneous Iterative Reconstruction Technique), based on an iterative process that minimizes the residue of the times. Considering the type of dromocrone, the first arrivals were associated to diving wave.

After analyzing individual lines 2D, it was performed tomography joint of the first arrivals of the times corresponding to all 2D on a 3D model (Fig. 2).

We applied the travel time tomography of first arrivals on all the acquired seismic lines in order to define a precise velocity model of the shallower part of the investigated area. As tomographic volume (350x250x75 m), we used a regular grid (21x15x30 voxels) on which we applied the staggered grid method (Vesnaver and Böhm, 2000), obtaining a more precise final model (63x45x60 voxels) with lateral and vertical resolution of 5.5 m and 1.25 m respectively. We used the SIRT method (Simultaneous Reconstruction Technique) as inversion algorithm and the diving ray paths in the ray tracing approach (Böhm *et al.*, 1999). The picked arrivals of all the lines were jointly inverted in order to preserve the coherency of velocity fields in correspondence of the cross points of the seismic lines. Then, we extrapolated the 2D velocity sections to the whole volume to complete the velocity information of the investigated area. The reliability of the inversion was estimated by the time residuals computation (difference between picked and computed travel times): 1.6 ms rms residual (equivalent to 4.4 % on picked travel times).

**Results.** *Data interpretation and definition of the geological and hydrological model.* The geological model was established by integrating the information obtained with the geophysical surveys and those derived from the geological survey of the land and the stratigraphy of the boreholes (Fig. 3).

The anthropogenic fill is over imposed on the marine clays while in the SE these are emerging to the portion of the ground surface. The calibration of the data with the ERT survey has allowed

varies between 4.90 m and 22.27 m depth. During drilling we have been performed in situ permeability tests.

The diagram summarizing the stratigraphic exploratory drillings carried facies divided into 4 groups: the lithoid Flysch, the altered Flysch, sediments of marine origin and soils of continental and anthropogenic origin.

**Data processing.** *Electrical Resistivity Tomography (ERT).* The geoelectrical tomographic data inversion was performed with the method proposed by Loke and Barker (1996) through the use of the code Res2dinv. This program

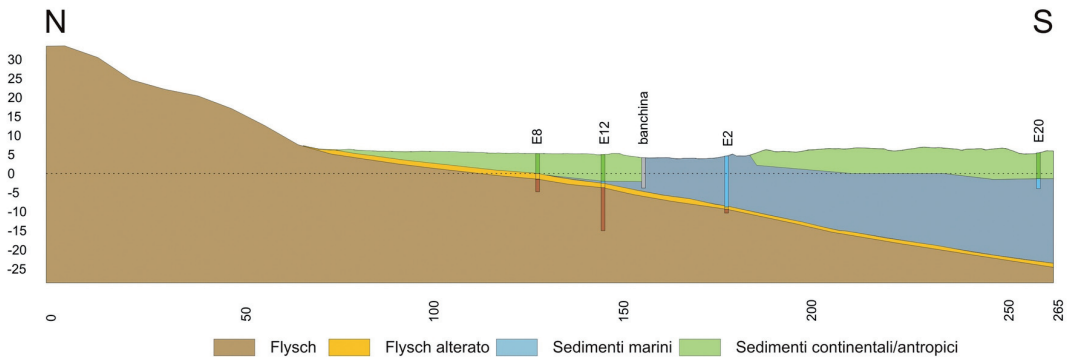


Fig. 3 – Geological section that summarizes the results of geological and geophysical study of the industrial site Ex-Esso (Trieste, Italy): the Flysch in brown, the altered Flysch in orange, the marine silty clay in blue, continental deposits and anthropogenic fills in green.

us to define the pinch-out of marine clays and in the north the covering is in direct contact with the Flysch altered. Due to the low resistivity of the marine clays, ERT measurements did not allow sufficient penetration to image the underlying Flysch.

The advantage of using this method of investigation was to identify the geometry of marine clays in the southern part of the area, clays from 5 m depth coastal seabed that now lie on the surface due to the pressure of the industrial landfill that with its weight has squirt marine sediments upwards.

The ERT survey has also allowed the identification the underground power line high-voltage located in the north part of the area.

The major problem in the analysis of electrical tomographic data was the presence of salty sea water that increases the conductivity and hides the differences lithological.

The refraction seismic survey has extended the exploration at depth allowing to define, with the calibration of the drillings, the interface between the marine clays and the Flysch bedrock.

The transition between the marine clays and the Flysch shows a gradual velocity rise with increasing depth, with a continuous variation of soil properties resulting in a curvature of seismic rays.

The correlation between the velocity model obtained from the inversion of seismic data and the boreholes stratigraphies helped define the top of the altered Flysch, corresponding to an average seismic velocity of about 2300 m/s.

The bedrock Flysch outcrops on the southern slopes of Mount San Pantaleone. The top of the Flysch deepens towards the sea, with a variable slope varying between 6° and 15°, reaching a depth of 19 m from the sea level in the borehole E3, located south of the site. This formation continue to deepen, deduced by drillings made in 1987 that intercept the top of the Flysch at the depth of 55 m below ground level. From marine seismic surveys performed by OGS, the maximum depth of the top of the Flysch in the Zaule Valley reaches the depth of about 80 m.

*Ground flow simulations.* The ground water flow modeling relative to the Ex-Esso area was conducted using MODFLOW, a well-established software produced by the US Geological Survey. This is a 3D finite difference code that reproduces the flow of water in confined and unconfined saturated porous media.

In the specific case, MODFLOW was used in stationary conditions to reproduce the piezometric data measured on the site and then to evaluate the effect that would, in the same conditions of external hydraulic loading, the presence of the planned waterproof excavation as designed in the plan of intervention for the site reclamation.

The model was built by reproducing the three-dimensional geometry obtained from the geophysical and geological surveys, which identifies three main formations (from top to bottom):

- soil anthropic fill / continental deposits;
- silty clay (which outcrops along the SW border of the site);
- Flysch (outcrop along the north edge of the area).

The top of these three groups has been reconstructed on the basis of existing geophysical data and geological surveys. A 3D grid covers an area of approximately 700 m x 800 m, which has at its center the area of the planned excavation. The areal discretization is done with a cell area of 10 m x 10 m.

The trend of contacts between the three groups is complex and highly variable in space, with the closure of the marine clay to the northwest on the top of the Flysch, and a direct contact of the fill in the north of this closure on the Flysch itself, which in turn emerges further north. Towards the SW the soil fill is absent, with an outcrop of the marine clay.

This complex geometry has been reproduced in the 3D grid of the groundwater flow simulator. Contacts between the formations are represented by the finite difference discretization of the numerical model.

The model has been stressed by the following boundary conditions:

- a piezometric level fixed at the average sea level along the coast;
- a height of the water table at the northern end in correspondence of the Flysch outcrop, set at values necessary to achieve the average piezometric level observed in the monitoring wells;
- a conditions of no flow boundary on the east and west sides of the model.

The model is also subjected to a recharge value estimated from average annual rainfall (975 mm/y) and reduced to obtain mean values of piezometric wells comparable with the measured data.

The recharge is imposed zone by zone. Recharge is set to zero in areas where the hydraulic conductivity of the formation outcrops (marine clay) is too low to absorb it. It was also set to zero in correspondence of the planned excavation, for the same reason, in the simulation which represents the presence with a very low hydraulic conductivity.

The main parameter of the hydraulic system is, given the stationary flow conditions, the hydraulic conductivity. Different hydraulic conductivity values are used in different zones. For the anthropogenic fill we used 3.46 m/d, the mean value derived from permeability tests. The area to the east has a larger hydraulic conductivity (15 m/d) that was introduced to adequately replicate the piezometric head distribution. In the area of the excavation, hydraulic conductivity was lowered to 1e-7 m/d.

The marine clay, which outcrops in the south, has a hydraulic conductivity value of 5e-4 m/d. This value is greater than the mean of laboratory data in oedometer (1e-5 m/d) to take account of any inhomogeneity of the system and to reduce numerical problems of the model, but is much lower than the values measured by the permeability Lefranc tests (on average 0.15 m/d) that have been carried out, however, only in the most superficial, almost to the contact between the clay and the fill above. A homogeneous distribution of the hydraulic conductivity was given to the Flysch, estimated on the basis of the evidence given by Lefranc tests at 1.85 m/d (horizontal conductivity), and set anisotropic with a vertical permeability equal to 1/5 of the horizontal.

The simulations predict a maximum rise of the piezometric head, as a result of the remediation action, equal to about 1 m within the very permeable area inside the planned excavation. The water table rise uphill of the excavation reaches about 40 cm. This is the reference value to be considered as a consequence of the excavation on the surrounding area. Note that this value does not pose a risk of raising the water up to ground level. However transient elevations can lead the water to reach the surface temporarily. This fact can happen even in the current situation without this fact represents an effective environmental risk.

**Acknowledgement.** Trieste Port Authority for the support and the permission to present these data.

## References

- Aki K., Richards P. G., 2002. *Quantitative seismology*. 2nd edition, University Science Book, ISBN 0935702962.
- Buseti, M., Volpi, V., Nicolich, R., Barison, E., Romeo, R., Baradello, L., Brancatelli, G., Giustiniani, M., Marchi, M., Zanolla, C., Nieto, D., Ramella, R., Wardell, N., 2010. *Dinaric tectonic features in the Gulf of Trieste (Northern Adriatic)*. Boll. Geof. Teor. Appl. 51, 117–128.
- Böhm, G., G.Rossi, e A. Vesnaver, 1999. *Minimum time ray-tracing for 3-D irregular grids*, J. of Seism. Expl., 8: 117-131.
- Brambati, A., Catani, G., 1988. *Le coste e i fondali del Golfo di Trieste dall'Isonzo a Punta Sottile: aspetti geologici, geomorfologici, sedimentologici e geotecnici*. Hydrores 5 (6), 13–28.
- Carulli G.B., 2011. *Structural model of the Trieste Gulf: A proposal*. Journal of Geodynamics 51, 156-165
- Cucchi F., Piano C., et al., 2013, *Brevi note illustrative della carta geologica del Carso classico italiano*, Progetto GEO-CGT: Cartografia Geologica di sintesi in scala 1:10.000, Regione Autonoma Friuli Venezia Giulia
- GeoSyntech, 2004, *Piano di caratterizzazione ambientale ai sensi del d.m. 471/99 per l'area "ex-Esso" nel Porto di Trieste*, Relazione tecnica di sintesi delle indagini ambientali e delle analisi di laboratorio
- Loke, M.H., 2011. *Electrical resistivity surveys and data interpretation*. in Gupta, H (ed.), Solid Earth Geophysics Encyclopaedia (2nd Edition) "Electrical & Electromagnetic", Springer-Verlag, 276-283.
- Strobbia C., Foti S., 2006. *Multi-offset phase analysis of surface wave data (MOPA)*. J. Appl. Geophys, 59, 300-313.
- Vignoli G., and G. Cassiani, 2009. *Identification of lateral discontinuities via multi-offset phase analysis of surface wave data*, Geoph. Prosp., 58, 389-413
- Vignoli, G., Gervasio, I., Brancatelli, G., Boaga, J., Della Vedova, B. and Cassiani, G., 2015, *Frequency-dependent multi-offset phase analysis of surface waves: an example of high-resolution characterization of a riparian aquifer*. Geoph. Prosp. doi:10.1111/1365-2478.12256
- USGS - MODFLOW <http://water.usgs.gov/ogw/modflow/>
- Vesnaver A. and Böhm G., 2000: *Staggered or adapted grids for seismic tomography?* The Leading Edge, 9, 944-950.

## A 5-KM LONG WATERBORNE CVES SURVEY ON THE PO RIVER IN THE TOWN OF TURIN: PRELIMINARY RESULTS

L. Sambuelli<sup>1</sup>, C. Comina<sup>2</sup>, A. Fiorucci<sup>1</sup>, P. Dabove<sup>1</sup>, I. Pascal<sup>1</sup>, C. Colombo<sup>2</sup>

<sup>1</sup> DIATI – Politecnico di Torino, Italy

<sup>2</sup> DST – Università di Torino, Italy

**Introduction.** The geological imaging and characterization of a riverbed is an essential starting point to determine thickness, lateral continuity and hydrogeological properties of the submerged deposits and to investigate the interconnecting relationship between surface water and groundwater. However, geological prospecting in water-covered areas could be very difficult, expensive and time-consuming with traditional survey techniques. Direct investigations (e.g. continuous core boring) are often neither cost effective nor reasonably quick and adequate in number to cover the whole water stream and to obtain a reliable correlation of data over a wide area. Geophysical methods can therefore be very useful to investigate sediments which are entirely located beneath a water-covered area. Among the available geophysical methods the use of non-seismic methods to study water-covered area is relatively recent (Sambuelli and Butler, 2009).

Focusing on the electrical techniques used for waterborne surveys, Continuous Vertical Electrical Soundings (CVES) using multichannel resistivity meters makes possible to simultaneously perform several resistivity measurements, in a fast and cost-effective way. CVES have been applied in water-covered areas for different purposes and using different electrode configurations a review of successful case histories can be found in Colombo *et al.* (2014). Even if many of the previous studies agree that the use of submerged electrodes allow better penetration in the submerged sediments, the use of floating electrodes seems sometimes

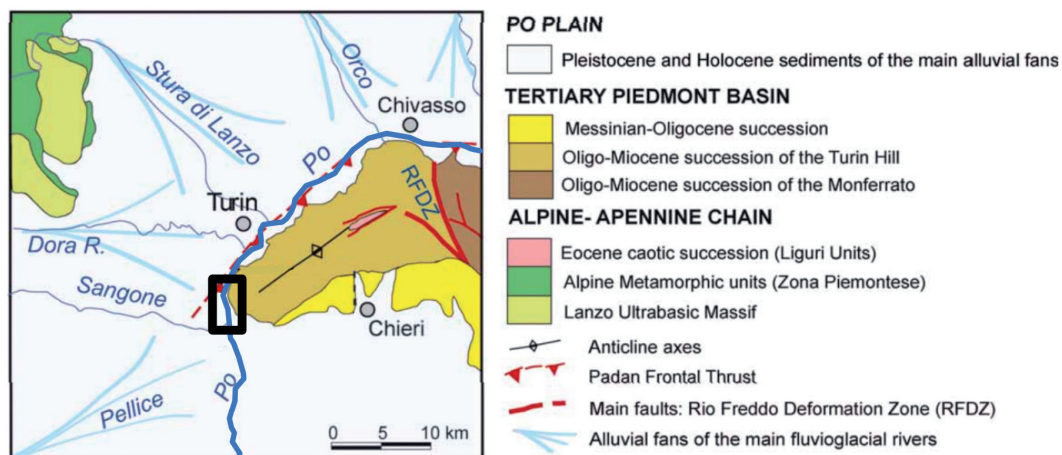


Fig. 1 – Structural geological model of Turin Hill and Po Plain in the area of Turin; the black bold square highlights the study area (modified from Forno and Lucchesi, 2015).

preferable, since data acquisition is faster. With the floating cable arrangement, exponentially spaced electrodes appear to provide the best resolution with depth (Allen and Merrick, 2007).

We preliminarily discuss the results of a continuous electrical resistivity survey carried out on the Po River, in a 5-km long urban sector of its flow across the city of Turin (NW Italy). The main objective of the study was to obtain a first assessment on the characterization of the riverbed sediments, in order to define nature, composition, geometry and spatial relationships of the detected bodies for further geological and hydrogeological reconstruction.

**The geological context.** In the urban area of the city of Turin, the Po River flows at the western edge of the SW-NE-elongated reliefs of the Turin Hill (Fig. 1). The morphology of the relief is remarkably asymmetric, with the presence of a relatively steep north-western slope and a much less inclined southern slope.

From a structural point of view, Turin Hill consists of a marine succession from the Upper Eocene and the Pliocene (Bortolami *et al.*, 1969). This Tertiary sequence lies on a Southalpine metamorphic bedrock (Mosca, 2006). The whole sedimentary succession of Turin Hill is variously deformed, forming an asymmetrical anticline with a SW-NE-oriented axis. This NW verging structure overthrusts onto the Po Plain along the Padan Frontal Thrust currently buried by the Quaternary fluvial sediments of the Po Plain (Castellarin, 1994; Festa *et al.*, 2009).

In particular, for the hillside next to the study area (NW side), the most superficial formation, belonging to the Oligocene-Miocene succession, is the Baldissero Unit (Synthem III Langhian). This Unit consists of marl and sandstones. Arenaceous-conglomeratic bodies with clasts of ophiolite, gneiss and quartzite are present at different levels. Its extension is about several kilometers and thickness varying between 50 and 350 m (e.g. Colle Maddalena). Along the NW side of the Torino Hill, the Baldissero Unit is sometimes covered by deposits belonging to synthems of San Vito (Middle Pleistocene), Cavoretto (Upper Pleistocene) and Monte dei Cappuccini (Upper Pleistocene). These synthems are suspended stream terraces stored on N and NW slopes of the Torino Hill with thicknesses varying between 1 and 5 m and covered by aeolian deposits (Forno *et al.*, 2002; Boano *et al.*, 2004; Forno and Lucchesi, 2005). San Vito Synthem consists of sands, silts and weathered gravels and is located between 175 and 300 m above the current plain. Deposits belonging to Cavoretto Synthem consist of silt and sand weakly weathered and are located between 110 and 175 m above the plain. Monte dei Cappuccini Synthem consists of sand, silt and weakly weathered gravel and is located between 30 and 110 m above the plain. At the foot of the NW side of the Turin Hill, in the right bank of the Po River, extensive fluvial deposits of unknown thickness (Upper Pleistocene - Holocene) is found as a

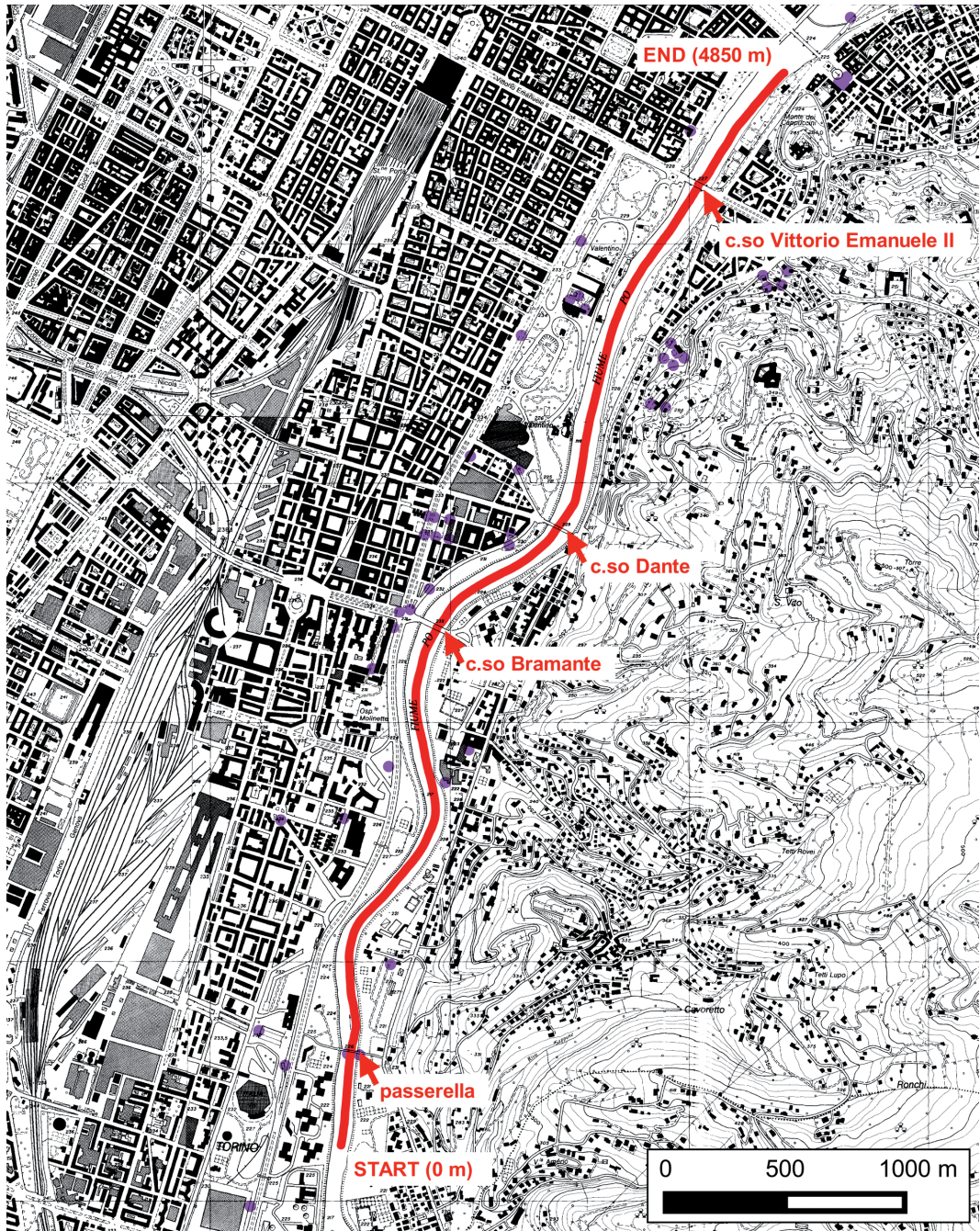


Fig. 2 – Survey line (in red) from the south to the north. Red arrows highlight the location of bridges. Purple dots refer to available geological logs and water wells with stratigraphic information.

cover of Baldissero Unit. These are composed of gravel and fresh or slightly weathered sandy gravel covered across the board by a blanket of sand and silty sands of decimetric or metric thickness. Below this Quaternary covers, the sediments of Turin Hill are expected to continue at depth, progressively deepening towards NW.

**The geophysical acquisition.** A waterborne continuous electrical profile was acquired on the Po River, from the confluence of the Sangone River (south) to the very city centre of Turin (north, Murazzi del Po), for a total length of approximately 4850 m of acquisitions (Fig. 2). The survey line passes throughout four bridges that represented difficult survey points both for the acquisition operations and for the strong electrical anomalies due to pier foundations. An array of nine electrodes fixed on a floating cable (96 m) dragged by a small boat was used for the survey. The array has two current electrodes, in the cable part closest to the boat, followed by eight potential electrodes. The current electrodes are 32 m apart, while the seven couples of potential electrodes had exponentially increasing spacing, from 0.5 m to 32 m. The first potential electrode was 0.5 m from the farthest current electrode. In the continuous profiling set up, dipole-dipole array data are collected measuring voltage potential differences between subsequent couples of potential electrodes given the same current injecting dipole. The towed cable floated on the river surface thanks to plastic floaters fixed near the electrodes that were fully submerged. The cable was kept stretched by a raft fixed at its end. We used a multichannel georesistivimeter (Syscal Pro in Sysmar upgrade – Iris Instruments) which was able to simultaneously acquire the seven potential measurements. The resistivity meter and the end of the cable were connected to a GPS device, in order to accurately record the spatial position of the acquired data. The acquisition step is about 2 seconds which results, on average, in one vertical electric sounding every 4 m. To recover the water depth, in order to constrain the data inversion, we connected to the IRIS georesistivimeter, and fixed to the side of the boat, a 170 kHz Airmar DT800 echo sounder. On average we had a bathymetry measure every 1 m.

We track the boat and the cable as in the following. Two different GNSS (Global Navigation Satellite Systems) instruments were used during the survey: the first one was a dual frequency multi-constellation receiver (Leica 1230+GNSS) that was installed on the main boat, while the second one was a single frequency cartographic receiver (Topcon GRS-1) installed on the raft in order to estimate the direction of the cable where all electrodes are settled. Both real-time and post-processing approaches were followed. The position of the boat was determined in real-time thanks to the Regione Piemonte CORSs (Continuous Operating Reference Stations) network, performing an NRTK (Network Real-Time Kinematic) positioning, obtaining an accuracy of solutions of about 2-4 cm. As far as the scow is concerned, we acquired only the raw data that we post-processed in a single base solution (considering a master station 6 km far from the test-site), thanks to a commercial software, reaching a sub-centimeter accuracy. We considered only positions with fixed phase ambiguities in order to obtain the best accuracy available today with GNSS instruments, at the end of the process we obtained 2 highly accurate positions every second.

**Data processing.** Before the inversion a statistical analysis of the data was performed, in order to evaluate the homogeneity of water resistivity and data variability with depth. The first three potential dipoles with smallest reciprocal spacing mainly investigated the river water, which has a constant resistivity value of 43  $\Omega$  m over the whole travel path. On the other hand, the following four dipoles are expected to give information about the riverbed sediments.

CVES data were inverted using both a classical 2D tomographic processing and a laterally constrained inversion (LCI) approach. The LCI was developed to invert CVES data acquired along a profile by Auken and Christiansen (2004). This approach is based on a pseudo-2D layered parameterization of the investigated geological medium: the inversion result is a set of 1D consecutive resistivity models, each one corresponding to a sounding, composing a pseudo-2D section. All the VES soundings along a profile are inverted simultaneously by minimizing a common objective function, which contains all the acquired data, the available a-priori information and lateral constraints among consecutive models. Through the lateral constraints, information from one vertical electrical sounding are interconnected with the neighbouring ones, producing the final pseudo-2D section. The lateral constraints are chosen in a way to allow for pseudo-2D sections that are more or less homogeneous on the basis of the geological setting of

the investigated area. In particular, the degree of lateral homogeneity of the considered model parameters is controlled by the strength of the constraints. If the expected lateral variability is small, a strong constraint will be applied; conversely if a large variation is expected, the strength of the constraint will be relaxed.

For a reliable inversion auxiliary a-priori data are also fundamental to ensure that as much known information as possible is considered in the inversion process. Crucial information for waterborne surveys includes bathymetry and water resistivity, which describe the properties of the water column. By providing these constraints, the inversion procedure is focused on the deposits beneath the riverbed, thus allowing a more accurate delineation of the sediment's electrical properties.

The conceptual reference model on which the inversion process was based is a three layered medium. For each inversion it was possible to a-priori fix the thickness and the resistivity of the water column (first layer). The first layer thickness was a-priori known thanks to echo sounder measurements of the bathymetry conducted simultaneously to the electrical survey. The first layer resistivity was kept constant ( $43 \Omega \text{ m}$ ) considering the low variation of the mean of the nearest potential dipoles. No constraints were set for the second layer (fluvial deposits) while the electrical resistivity of the third layer (Turin Hill marls) was fixed to the value  $23 \Omega \text{ m} \pm 20 \Omega \text{ m}$  (mean and standard deviation of the whole raw measurements dataset for the seventh dipole) in order to force the inversion to find a lateral continuity for the deepest deposits. An appropriate Matlab code was developed to implement the inversion, similar to the one described in Colombero *et al.* (2014).

On the other hand, classical 2D inversion was carried out using Res2DInv software, in continuous resistivity profiling mode, fixing both the water resistivity and the bathymetry values (Loke and Lane, 2004).

**Preliminary results.** In Fig. 3 the results of the inversion of the whole dataset are shown, both for the LCI approach and for the classical 2D tomography. To maintain a readable vertical scale the profile has been split in 1 km stretches.

The depth of the riverbed varies from a minimum of 2 m to a maximum of 10 m. Below the water layer (blanked in all the sections) a thick layer of sediments with resistivity higher than water resistivity ( $43 \Omega \text{ m}$ ) is found. The layer thickness is not homogeneous, showing irregular depressions and reliefs, but generally it seems to progressively slightly increase towards north. Resistivity values range from the water value up to  $250 \Omega \text{ m}$ . Quite low values are shown in the first 2400 m of the survey line ( $43\text{-}90 \Omega \text{ m}$ ), from this point to the end of the survey the resistivity increases. This first layer of sediments is characterized by the fluvial deposits (mainly silt, sand and gravel) of the Po River. The increase in resistivity from south to north can be linked to a local increase in granulometric size of the sediments or to the presence of more compacted or cemented horizons. Due to the three-layer model assumption, LCI results show for this horizon a unique mean value of around  $150 \Omega \text{ m}$  in the last sections, while 2D tomography results distinguish an upper sub-layer with higher resistivity and a lower horizon with values comparable with the previous sections.

The bottom part of each section is instead characterized by sediments with resistivity values ( $20\text{-}40 \Omega \text{ m}$ ) lower than water resistivity, that could be likely related to the marls of Turin Hill marine sequence. The morphology of this horizon is quite undulating, suggesting strong erosional phenomena both along the main flow of the river and at the confluence of the lateral tributary streams. The depth of the marls ranges from a few meters in the southern sections to more than 15 m toward north.

The geophysical results were compared with direct geological information, consisting of logs and water wells with stratigraphic information in the surroundings of the river banks. Unfortunately, not all the available direct surveys reached the marls, but where the investigation depth was higher, the data were found to be in good agreement (Fig. 3c). A strong electrical anomaly was detected near the first bridge of the survey, due to the pier foundation structure.

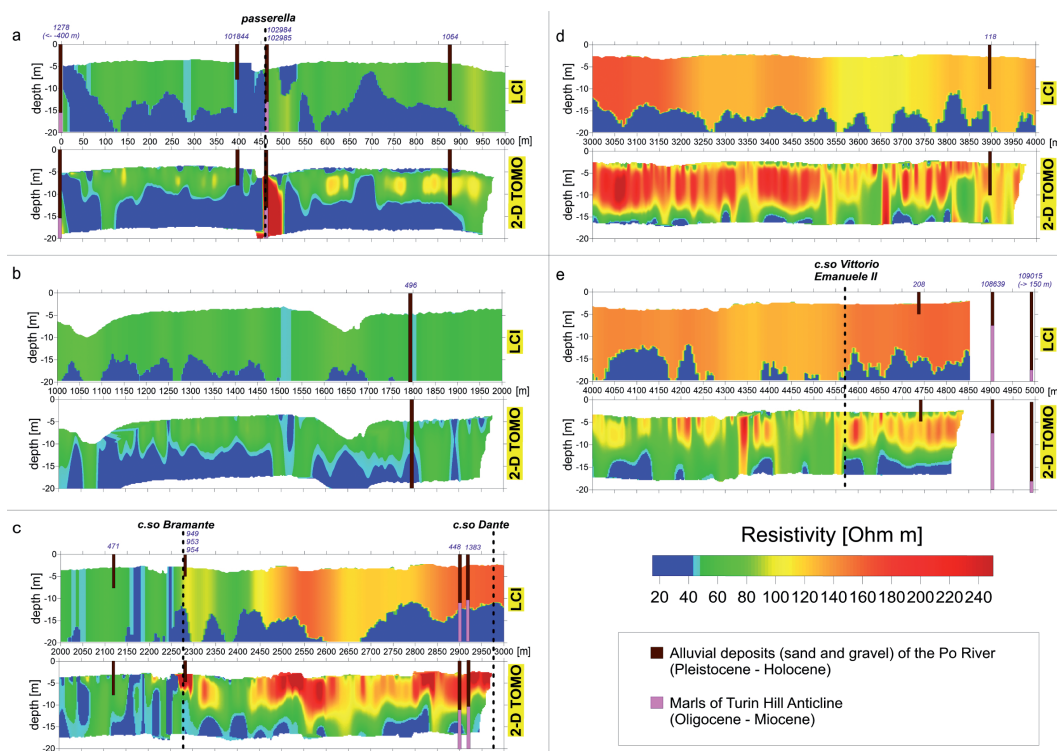


Fig. 3 – Inversion results for the whole dataset. From (a) to (e) consecutive 1-km sections. The first line of each section is the result of the LCI approach, the second refers to the classical 2D tomography. The water layer has been blanked in both sections. Vertical dashed lines highlight the location of bridges. The simplified geological information nearest to the river are plotted in direct comparison with the geophysical results.

These data were rejected for the LCI approach, but remained in the 2D tomographic results (Fig. 3a).

**Conclusions.** This research moved from one main question: how deep is the top of Miocene sediments below the Po River in the city of Turin? The answer would have implications in many fields: it would allow for a better knowledge of the structural geology of Turin Hill, a better understanding of the relationship between surface and groundwater and finally, being the top of Miocene a marly unit (the Baldissero Formation), an interesting indication, from a geotechnical point of view, for every engineering work across or below the river.

Many water wells, drilled in the town, even nearby the left bank of the Po River, did not find the top of the marls, and the depth of the Miocene could only be guessed by outcrops in the hill and some rare information from deeper logs. The asymmetry of the Turin Hill anticline, according to these preliminary results, has been validated for the Miocene, from geophysical data, along a 5-km section parallel to the anticline axis.

According to these preliminary results, the marls below the river are at depth ranging from 3 to 15 m. Only in some short stretches of the survey their depth exceeds the 20 m, a reasonable depth of investigation of CVES. These marls surely have different hydrogeological and geotechnical properties with respect to the Quaternary fluvial sediments. Marls will likely have cohesion and, even if they may have some secondary porosity due to tectonic fractures, a different hydraulic conductivity.

They are the impervious bedrock below the alluvial plane and therefore, in the Turin area, they represent the bottom of the shallowest aquifer that drains into the Po River.

Moreover, according to our preliminary results the depth of the top of the marls could occasionally intersect engineering works across or below the Po riverbed.

The information we obtained, still under process and interpretation, were gathered in a half a day campaign, involving roughly eight people and two boats. Even at this stage of work, considering that the full implication of our findings is still to be exploited, these results seems of interest and another survey along other 5 km of the Po River, to the north of the one presented, is going to be planned.

**Acknowledgements.** The authors wish to thank the “Direzione infrastrutture e mobilità, servizio ponti, vie d’acqua ed infrastrutture” of the Turin municipality and the “Società canottieri Cerea” for their essential logistic support and Diego Franco for his work during data acquisition.

## References

- Allen D. and Merrick N.; 2007: *Robust 1D inversion of large towed geo-electric array datasets used for hydrogeological studies*. Explor. Geophys. (Collingwood, Aust.) 38, 50–59.
- Auken E. and Christiansen A.V.; 2004: *Layered and laterally constrained 2D inversion of resistivity data*. Geophysics 69, 752–761.
- Boano P., Forno M.G. & Lucchesi S. (2004) – Pleistocene deformation of the Collina di Torino inferred from the modelling of their fluvial succession. – Il Quaternario, 17 (1/2): 145-150.
- Bortolami G.C., Crema G.C., Malaroda R., Petrucci F., Sacchi R., Sturani C. and Venzo S.; 1969: *Foglio 56 ‘Torino’ della Carta Geologica d’Italia alla scala 1:1000.000*. Ila ed. Roma: Servizio Geologico d’Italia
- Castellarin A.; 1994: *Strutturazione eo- e mesoalpina dell’Appennino settentrionale attorno al nodo ligure*. Studi Geologici Camerti, special volume CROP 1–1, 99 –108.
- Colombero C., Comina C., Gianotti F. and Sambuelli L.; 2014: *Waterborne and on-land electrical surveys to suggest the geological evolution of a glacial lake in NW Italy*. Journal of Applied Geophysics, 105, 191-202, DOI: 10.1016/j.jappgeo.2014.03.020.
- Festa A., Boano P., Irace A., Lucchesi S., Forno M.G., Dela Pierre F., ... Piana F.; 2009: *Foglio 156 ‘Torino Est’ della Carta Geologica d’Italia alla scala 1:50.000*. APAT, Agenzia per la Protezione dell’Ambiente e per i Servizi Tecnici- Dipartimento Difesa del Suolo, Roma.
- Forno M.G., Ben G., Boano P., Boero V. & Compagnoni R. (2002) – Lembi di depositi fluviali provenienti dai bacini alpini nordoccidentali sulla Collina di Torino presso Villa Gualino (NW Italy) – Il Quaternario, 15 (2): 175-185.
- Forno M.G. & Lucchesi S. (2005) – La successione fluviale terrazzata pleistocenica dei versanti occidentale e nordoccidentale della Collina di Torino. – Il Quaternario, 18 (2): 123-134.
- Forno M. G. and Lucchesi S.; 2015: *Relicts of the Pleistocene Po Plain on the Western and Southern slopes of Turin Hill (NW Italy)*. Journal of Maps, DOI:10.1080/17445647.2015.1027481
- Loke M.H. and Lane J.W.; 2004: *Inversion of data from electrical resistivity imaging surveys in water-covered areas*. Explor. Geophys. (Collingwood, Aust.) 35 (4), 266–271.
- Mosca P.; 2006: *Neogene basin evolution in the Western Po Plain (NW Italy): Insights from seismic interpretations, subsidence analysis and low (U-Th)/He thermochronology* (Ph.D. Thesis). Amsterdam, The Netherlands: Vrije University, 190 pp.
- Sambuelli L. and Butler K.E.; 2009: *Foreword. Special Issue on High Resolution Geophysics for Shallow Water*, Near surface Geophysics, 7, pp. 3-4.

## DIRECT INTERPRETATION OF SURFACE WAVES FOR 2-D AND 3-D SUBSURFACE IMAGING

S. Bignardi, N. Abu Zeid, G. Santarato

Dip. di Fisica e Scienze della Terra, Università degli studi di Ferrara, Italy

**Introduction.** The soil stiffness is routinely evaluated by direct investigation, using geotechnical tests such as CPT-CPTu, SPT. While this approach allows retrieving detailed and reliable information, the procedure is invasive and the result is punctual hence of limited spatial extension. Moreover, the costs of a survey quickly grow with the number of probes. A low

cost, non-invasive, complementary strategy would be the use of methods based on surface waves (SW), such as SASW (Nazarian and Stokoe, 1984) or MASW (Park *et al.*, 1999; Socco and Strobbia, 2004). In the classic SASW and MASW, Rayleigh (and alternatively Love) SW are excited by an active source and recorded by a linear array of receivers deployed on the ground. The dispersive nature of the recorded surface waves is used to derive the vertical (1D) subsurface profile of the shear velocity  $V_s$  by an inversion procedure. In detail, the propagation of SW along the array allows for the construction of a dispersion pattern, which is retrieved by transforming the experimental seismograms from the time-space to a more suitable domain by using a specific numerical transform. For example, in the MASW framework, the frequency-wavenumber ( $f$ - $k$ ) and the frequency-Rayleigh ( $f$ - $V_R$ ) domains are frequently used and also occasionally the  $\tau$ - $p$  transform (McMechan and Yedlin, 1981). The obtained dispersion pattern is then an entire portion of a two parameters domain and in order to capture the dispersion pattern the spectral maxima are picked to yield the so-called dispersion curve. Since SW are multimodal, this approach is capable of separating multiple phase velocity values at the same frequency. In the SASW framework the dispersion pattern is retrieved by calculating the cross spectrum of experimental seismograms recorded at two, opportunely spaced, receivers. The dispersion pattern, in this case, is represented as a cloud of points in the frequency-velocity domain ( $f, V_R$ ). Unfortunately, by this approach a unique value of the velocity is obtained for each frequency, so that when multiple modes contribute to the real propagation these are not identified as separated and misleadingly used as a whole “apparent” propagation mode during the inversion. Despite these differences however, the dispersion pattern is inverted to estimate shear wave velocity distribution.

Unfortunately, available inversion algorithms assume the subsurface model as a stack of homogeneous parallel layers, hence capturing only vertical variations of the subsurface elastic properties (e.g. Aki, 2002; Kausel and Roesset, 1981). Consequently, these algorithms are of limited use when lateral heterogeneities are known to exist. Indeed, there is a growing interest toward applications of the MASW technique for 2-D and 3-D subsurface imaging (Boiero and Socco, 2010; Vignoli *et al.*, 2011, 2015; Bignardi *et al.* 2012, 2014; Masoni, 2014; Socco *et al.* 2014, 2015). Such interest points out how the laterally heterogeneity identification is of primary interest in the near-surface investigations. Dealing with this issue, Bignardi *et al.* (2014) showed that in a MASW survey, the presence of a moderate lateral heterogeneity can be detected in the  $f$ -Offset domain while its effects are difficult to recognize when data are transformed in the  $f$ - $V_R$  domain; i.e. in this domain the information of the “locality” is lost. This leads to the consideration that lateral heterogeneity could be retrieved by separately elaborating the signals recorded at pairs of receivers in a similar way as it is done in the SASW technique.

In what follows we shall use part of the SASW workflow to establish a strategy that can be used both as a feasible inversion strategy or alternatively for the direct interpretation of active-source datasets. Following the second course, we shall show that the Direct Interpretation of Phase Lags (DIPL) (Bignardi *et al.* 2015a, 2015b), which uses the frequency-dependent phase lags among pairs of seismic signals, is capable of retrieving a satisfactory 2-D and 3-D  $V_s$  subsurface image also in complex subsurface environments without the need of inversion. We shall discuss the workflow, the pros and cons of 2-D and 3-D applications. Finally, we shall present and discuss field examples.

**Method.** Let's consider a source  $S$  and two receivers,  $R_1$  and  $R_2$  placed along a line; a SASW-like data processing concerns calculating the phase of the cross spectrum between the signals recorded at the receiver pair. This information can be used to get the local dispersion pattern as a cloud of points (COP) in the  $f$ - $V_R$  domain (see e.g. Fig. 1) through Eq. 1, [please refer to Nazarian's and Stokoe's (1984) paper for the details].

$$\phi(f) = \arg(F_2(f)F_1^*(f)), \quad (1)$$

and

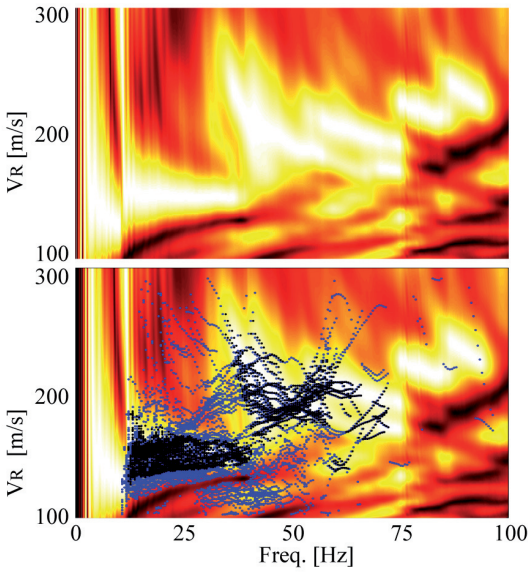


Fig. 1 – An example of the SASW-like cloud of points in the  $f$ - $V_R$  domain. In this example, the blue points are filtered out while the black points are those which comply with Eq. 2. For sake of comparison, the corresponding frequency-velocity transform is shown both clean (above) and with superimposed points (below) to show how the filtered COP adapts to the propagating modes.

$$V_R(f) = \frac{2\pi d}{\phi(f)} f$$

where  $f$  is the frequency,  $\phi(f)$  is the phase lag at the frequency  $f$  and  $d$  is the distance between the two receivers.

This cloud of points, which is just a suitable transformation of the original data, still retains the locality information and to this level, the information regarding different modes of propagation, although mixed. These frequency-dependent phase lags would be suitable to build an objective function to be used during inversion, for example, in a Full Waveform Inversion style (Virieux and Operto, 2009; Masoni *et al.*, 2014; Groos *et al.*, 2014), assuming a suitable forward model is available. In classical SASW, however, this information is usually inverted using a parallel-layered based forward model. In order to avoid introducing such approximation, we proceed without inversion. We rather express the COP in the wavelength-velocity domain ( $\lambda$ - $V_R$ ) which is then associated to the subsurface between the pair.

**2-D approach.** In the two dimensional approach, source and receivers are all placed along the same line. The advantage of this approach is basically that starting from the same data we can compute the frequency-velocity spectrum and use its amplitude to filter out the points in the COP corresponding to harmonics that do not carry a meaningful amount of energy (say less than 5%). To do so, we require

$$E(f, V_{R,p}) > 0.05 E_{max}(f), \tag{2}$$

where  $E(f, V_{R,p})$  is the energy carried by the harmonic wave represented by point  $p$ , having frequency  $f$  and traveling at speed  $V_{R,p}$ , and  $E_{max}(f)$  is the maximum energy transferred by any harmonic wave at the same frequency. An example of the points calculated for a whole linear array of 24, 4.5 Hz proper frequency geophones is shown in Fig. 1. The blue points are the points that are discarded once equation 2 is taken into account, while the valid points are drawn in black. The valid points agree quite well with the frequency-velocity transform obtained for the same data and shown in the background.

The remaining points are then expressed in the wavelength-velocity domain ( $\lambda$ - $V_R$ ). The COP obtained from all receiver pairs, for all the source points and for all the shots (when multiple shots are performed), can now be assembled into one pseudo-section by means of a suitable weighted average algorithm. We refer to this result as a “pseudo-section” because the maximum depth to which each ( $\lambda, V_R$ ) point brings its contribution is associated to a suitable fraction  $\beta$  of

the wavelength, in consideration of the fact that the investigation depth of a (Rayleigh) surface wave is linked to its wavelength. Here we assumed  $\beta = 1$ . For the assembly process we consider the 2-D subsoil as discretized into squared blocks where the value of the velocity for each block is calculated by a weighted average procedure. Averaging has recently proved very useful for immediate (or rough) Vs estimation and allows retrieving very satisfactory results even without inversion (Socco and Comina, 2015). Indeed, we built our weighting strategy based on some phenomenological observations, but better strategies may exist.

$$V_S(x, z) = 1.1 * \sum_{ij} \sum_k^{n_p} b_{ij}(z, l_{k,ij}) V_{R_{k,ij}}, \tag{3}$$

where

$$b_{ij}(z, l_{p,ij}) = \left(\frac{|z|}{l_{p,ij}}\right)^2 \text{ if } |z| \leq l_{k,ij}, \tag{4a}$$

$$b_{ij}(z, l_{k,ij}) = 0 \text{ otherwise}; \tag{4b}$$

$ij$  represent the receiver pair,  $p_{k,ij} = (\lambda_{k,ij}, V_{S_{k,ij}})$  is the corresponding COP,  $k$  is an index running on the accepted points in the cloud and  $l = \beta \lambda$  is a suitable fraction of the wave-length  $\lambda$ . The 1.1 factor is thought to empirically translate  $V_R$  into  $V_S$ .

It is well known that SASW does not allow resolving all the different propagation modes but only one whole apparent mode is retrieved. Note that the weighting average naturally takes into account the presence of multiple modes because multiple values of velocity associated to the same frequency affect different portions of the pseudo-section once expressed in the wavelength-velocity domain. An example of 2-D pseudo-section is shown in Fig. 2a. To judge

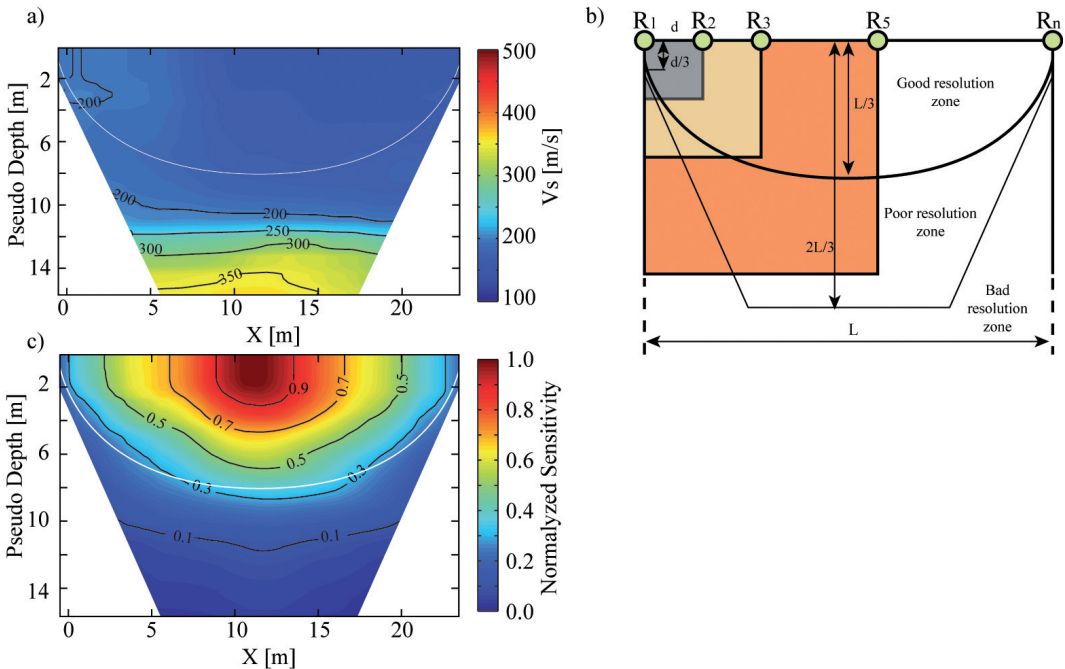


Fig. 2 – a) Obtained 2-D Vs pseudo-section for a MASW-like survey. b) Example of the influence of different receiver pairs on the interpreted profile(a) and sensitivity of the proposed method with depth. The maximum depth showing a reliable resolution is roughly  $\lambda_{max}/3$ , where  $d < \lambda < L$ ,  $d$  is the inter-geophonic distance and  $L$  is the length of the array. Velocities in the poor resolution zone are evaluated using only distant receivers so that deeper velocity values are correct but horizontally stretched. c) Computed normalized sensitivity corresponding to the Vs profile in (a). The white curve in a and b, highlights the portion with “good resolution” (i.e. in this case, the shallower 6 m, with a number of contributions roughly higher than 30%, in this case).

the reliability of such result we can investigate how the final pseudo-section depends on the imputed data. Of course, since this is not an inversion, a traditional definition of “sensitivity” is neither possible nor applicable. To achieve the result in this context, we define “sensitivity to the data” the normalized number of contributions per block. Since the velocity value in each squared block is obtained by averaging multiple contributions, the most the contributions, the most reliable will be the result. The sensitivity corresponding to the pseudo-section of Fig. 2a is shown in Fig. 2c, while Fig. 2b shows a schematic example on how different receiving pairs contribute to the final Vs interpretation and to its sensitivity pattern. The depth, to which lateral heterogeneity is correctly retrieved, is roughly L/3, where L is the array length. Beyond this depth, a result can still be retrieved but, since only distant receivers are involved, the interpreted velocity values are spread horizontally and their exact location under the array is lost.

**3-D approach.** A relevant number of factors come into play when a three dimensional (3-D) subsurface is considered, for instance, near-foundation soils in urban areas. The presence of localized  $V_s$  variations such as the foundation itself, heterogeneities due to excavations and successive replenishments, sewers, fuel tanks, surface velocity inversions due to artificial pavements, or even tree roots, makes up a severe and challenging 3-D subsurface. Furthermore, since the space available at the surface may be insufficient, receivers must be placed keeping into account both the accessibility of the specific site and the need to record a dataset with sufficient wavenumber coverage.

In practice, to tackle the 3-D Vs subsoil reconstruction challenge a method for the elaboration of surface waves recordings unbound from both a rigid field geometry and from the 1D assumption would be highly desirable.

To extend the approach to the three dimensional world, since SW spreading from a point source is cylindrical, we can still use the procedure reported in Eqs. 1-4 under the assumption that the angle  $\alpha$  between  $R_1$  and  $R_2$  is small enough. This enables to link the portion of the cylindrical shell defined by  $R_1$  and  $R_2$  and the angle  $\alpha = R_1SR_2$  (i.e. a portion of the target volume) to the COP obtained for the receiver pair under investigation. Note that the strategy to obtain the COP and its extension to 3-D may represent a very promising strategy for the 3-D inversion of the data.

The assembly process is still performed using the COP’s **relative to all the receiver pairs, all the sources and multiple shots** but the 3-D subsurface is now discretized in cubic blocks where the value of the velocity is calculated according to Eqs. 3, 4a and 4b.

The result is a 3-D pseudo-volume of  $V_s$  where the velocity values are most properly retrieved to a depth roughly equal to L/3, where L is the maximum distance between the two farthest receivers. In the 3-D case with arbitrarily located sources and receivers, it is of course not possible to filter the COP using a frequency-velocity transform, as is allowed by several (usually 24, at least) regularly spaced traces, and this can potentially enable for artifacts introduction. The only constraint we can impose is based on the energy produced by each single shot

$$E(f, V_R)_p > 0.05 E_{max}(r_1, r_2), \tag{5}$$

where, for each pair, is the energy transferred by the most energetic harmonic. For this reason, the 3-D sensitivity with respect to the data is the main tool not only to judge the reliability of the result at any location (x,y,z) but also to have an indication about the spectral accuracy in terms of wavenumber coverage. Finally, Fig. 3 shows a three dimensional survey where the signals recorded at 24 vertical, 4.5 Hz proper frequency geophones and produced by 21 different sources where used to characterize the subsurface under the foundations of a residential building, with particular emphasis to one of its corners, where a settlement occurred. The obtained Vs (Fig. 3a) also presents anomalies due to the sewer system and as expected, a lowering of the shear velocity under the investigated corner where the walls presented some cracks, probably connected to the degradation of the supportive function of the foundation soil.

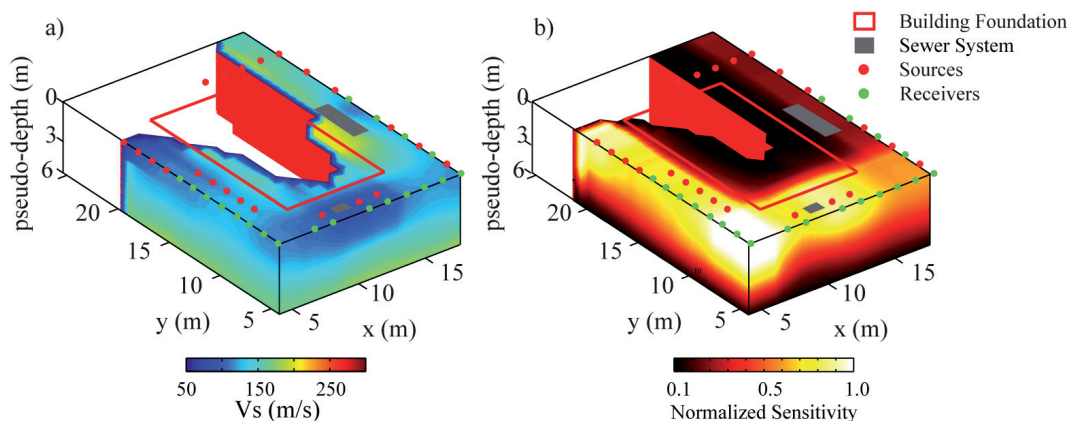


Fig. 3 – Results of the Phase Lag Direct interpretation for a 3-D, near foundation subsurface. The footprint of the building is highlighted in red. a)  $V_s$  distribution beneath a building retrieved using a 2-D array of 24 receivers (showed as green dots) and 21 sources (showed as red dots). The picture highlights two anomalies due to the sewer system (gray squares) and a low velocity zone around the corner ( $x=7, y=7$ ), that was the target of the investigation. b) Corresponding sensitivity pattern. Only the zones with a sufficient spectral resolution, in terms of wavenumber coverage, are shown. The high values around the target corner mean that the result in this portion of the subsurface is reliable while reliability lowers toward the back of the house and at depths higher than three meters.

**Conclusions.** A strategy for the use of the phase lags between pair of signals recorded by either an array or by an arbitrary 2-D distribution of receivers and produced by multiple sources was presented. This strategy could in principle be used to build, in future, an inversion process. However, in this work we rather presented a Direct Interpretation of the Phase Lags (DIPL) to tackle both the 2-D and 3-D investigation of the subsurface. We showed that the use of equations 1-4, coupled with the comparison to the frequency-velocity transform allows retaining the local property of the data and at the same time takes into account both the fundamental and higher modes of the surface wave's propagation, thus enabling the construction of reliable 2-D  $V_s$  pseudo-sections capable of detecting and evaluating lateral heterogeneities below a MASW-like profile. Further, we extended this approach to three dimensions and we discussed the capabilities and limitations of both 2-D and 3-D approaches.

Finally, examples of application to field data were given; where the 2-D case concerns data collected over a regular (i.e. practically 1-D) subsurface while the 3-D data were collected to characterize a very shallow portion of the subsurface under the foundation of a residential building. In both cases we found the results in agreement with both cross-hole and CPT investigations purposely carried-out at the same sites, and whose results cannot be shown here because of the limits imposed on the number figures.

## References

- Aki, K. and Richards, P. G. (2002): Quantitative seismology, Theory and methods (second edition), University Sciences Books, Sausalito, California, pp. 700.
- Bignardi, S., Abu Zeid, N., D'Attoli, M., Morelli, G., Occhi, M., Russo, M., Santarato, G. (2015/a): Near foundation soil stiffening evaluation after resins injection by a novel 3D interpretation of surface waves data: *Near Surface Geoscience 2015 - 21st European Meeting of Environmental and Engineering Geophysics (EAGE)*. September 6-10, 2015, Turin, Italy. DOI: 10.3997/2214-4609.201413799.
- Bignardi, S., Abu Zeid, N., Santarato, G. (2015/b): Direct interpretation of phase lags of MASW data: An example for evaluation of jet grouting for soil stiffening enhancement against soil liquefaction: *SEG Technical Program Expanded Abstracts 2015*: pp. 2218-2223. DOI: 10.1190/segam2015-5925998.1.
- Bignardi, S., Santarato, G. and Abu Zeid, N. (2014): Thickness variations in layered subsurface models - effects on simulated MASW: 76th EAGE Conference & Exhibition 2014 *Experience the Energy*, Amsterdam, The Netherlands.
- Bignardi, S., Fedele, F., Yezzi, A. J., Rix, G. J. and Santarato, G., (2012): Geometric seismic wave inversion by the boundary element method: *Bulletin of the Seismological Society of America*, **102**, 802-811.

- Boiero, D., and Socco, L. V. (2010): Retrieving lateral variations from surface waves dispersion curves: *Geophysical Prospecting*, **58**, 977-996.
- Groos, L., Butzer, S., Forbriger, T., Bohlen, T., 2014, Challenges for 2-D elastic Full Waveform Inversion of Shallow-seismic Rayleigh Waves: 76th EAGE Conference & Exhibition 2014 Experience the Energy, Amsterdam, Netherlands.
- Kausel, E. and Roesset, J.M. (1981): Stiffness matrices for layered soils. *Bulletin of the Seismological Society of America*, **71**, 1743-1761.
- McMechan, G. A., and Yedlin, M. J. (1981): In situ shear wave velocities from spectral analysis of dispersive waves by wave field transformation: *Geophysics*, **46**, 869-874.
- Masoni, I., Zhou, W., Brossier, R., Métivier, L., Operto, S., Virieux, J. M. (2014): Near-surface Full Waveform Inversion Using Surface Waves and Reflected Waves: 76th EAGE Conference & Exhibition 2014 Experience the Energy, Amsterdam, The Netherlands.
- Nazarian, S. and Stokoe, K. H. (1984): In situ shear wave velocity from spectral analysis of surface wave: Proceedings of the 8Th Conference on Earthquake engineering, St. Francisco, Prentice Hall, 3, 31-38.
- Park, C. B., Miller, R. D., Xia, J. (1999); Multichannel analysis of surface waves: *Geophysics*, **64** (3), 800-808.
- Socco, L.V. and Comina, C. (2015): Approximate Direct Estimate of S-wave Velocity Model from Surface Wave Dispersion Curves: *Near Surface Geoscience 2015 - 21st European Meeting of Environmental and Engineering Geophysics (EAGE)*. September 6-10, 2015, Turin. Italy. DOI: 10.3997/2214-4609.201413714.
- Socco, L. V., Bergamo, P., and Garofalo, F. (2014): Surface Wave Dispersion Analysis - From Local 1D Models to Tomography: 76th EAGE Conference & Exhibition 2014 Experience the Energy, Amsterdam, Netherlands.
- Socco, L.V. and Strobbia C. (2004): Surface-wave method for near-surface characterization: a tutorial: *Near Surface Geophysics*, **2**, 165-185.
- Vignoli, G., Gervasio, I., Brancatelli, G., Boaga, J., Della Vedova, B., Cassiani, G. (2015): Frequency-dependent multi-offset phase analysis of surface waves: an example of high-resolution characterization of a riparian aquifer: MOPA of surface waves. *Geophysical Prospecting*. DOI:10.1111/1365-2478.12256.
- Vignoli, G., Strobbia, C., Cassiani, G., Vermeer, P. (2011): Statistical multioffset phase analysis for surface-wave processing in lateral varying media: *Geophysics*, **76** (2), U1-U11.
- Virieux, J. and Operto, S. (2009): An overview of full waveform inversion in exploration geophysics, *Geophysics*, **74**(6), WCC127-WCC152.

## INTEGRATED GEOPHYSICAL PROSPECTING IN THE ARCHAEOLOGICAL SITE OF BADIA

M.T. Giannotta<sup>1</sup>, G. Leucci<sup>1</sup>, L. de Giorgi<sup>1</sup>, R. Persico<sup>1</sup>, M. Leo Imperiale<sup>2</sup>, G. Muci<sup>2</sup>

<sup>1</sup> Institute for Archaeological and Monumental Heritage, IBAM-CNR, Lecce, Italy

<sup>2</sup> Laboratory for Medieval Archaeology, Department of Cultural Heritage, UniSalento, Lecce, Italy

**Abstract.** One of the aims of modern archaeology is the identification of relationships between human communities and their habitat over time. Understanding those links can spread light over the historical development of landscape and the relation between people and environment. In this work, we focus our attention on a settlement in the Apulia region (southern Italy), where remains dating back to Late Antiquity and Early Medieval age have been investigated. The study area, nowadays known as *Contrada Badia*, is located close to the modern town of Cutrofiano (Lecce). The site has been the object of many archaeological investigations concerning the Classical Roman period evidences. On the other hand few investigations focused on the Late Antique and Early Medieval age. However, recent archaeological excavations revealed important features testifying to the dynamic transformations which occurred in these periods. The above described situation represent an ideal context to develop a framework in which integrated archaeological, geophysical and archaeometric investigations could be of great help in the understanding of historical dynamics. In particular an archaeological survey has been performed at *Contrada Badia* over an area of about 50 hectares: this led to the identification of two particularly relevant sites. The first one can be identified as a rural settlement dating back to the Imperial and Late Antique period, whereas the second site is likely referable to a medieval abbey.

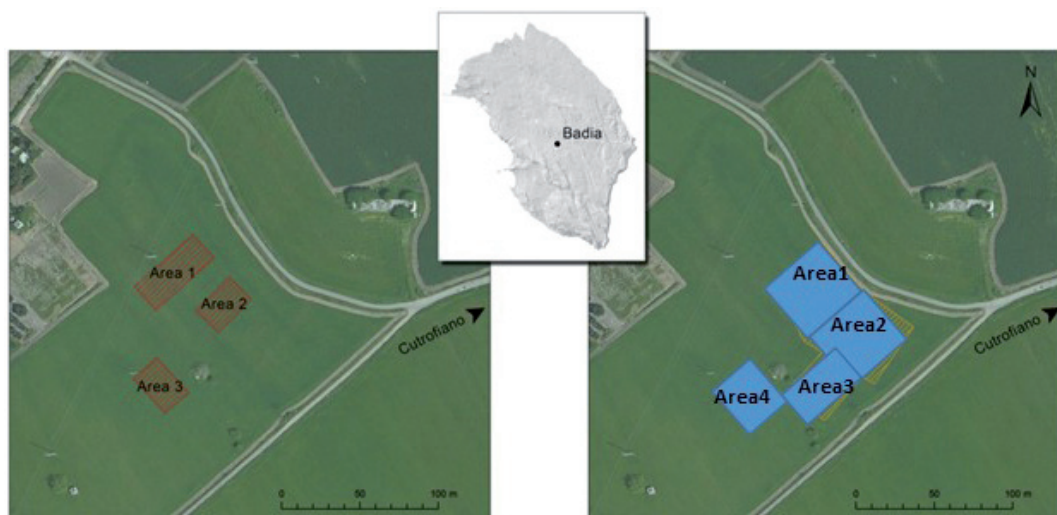


Fig. 1 – Left hand panel: The three rectangular areas in Badia, prospected with a GPR. Righth hand panel: the four rectangular areas in Badia prospected with a magnetometer.

**Introduction.** The Institute for Archaeological and Monumental Heritage IBAM-CNR and the Department of Cultural Heritage, University of Salento have been put in charge, together with other Institution of the PRIN project “Innovative Methods for the Reconstruction of the Landscape of *Terra d’Otranto* between Late Antiquity and Middle Ages”. One of the aims of the project is the characterization of some archaeological contexts in the Salento area, corresponding to the southern part of the Apulia Region, in Italy. In particular, ancient villas, rural settlements and places of worship by the archaeologists in the last few years, as a whole showing that during the Late Ancient Age and Early Medieval Age the landscape in this area was essentially characterized by Roman *latifundia*.

In detail, in the area showed in Fig. 1 the archaeologists performed deeper investigation which provided large information about meaningful landscape transformations, such as changes in cultivations, building of new villages and abandonment of pre-existing ones, foundation of new towns (Arthur, 2006, 2010, 2012a, 2012b). In particular, the 6<sup>th</sup> century A.D. was a moment of intense social and territorial transformation, due to several reasons among which a relevant role was played by the war between Greeks and Goths occurred in the period between 535 and 554 A.D. In the last 15 years medieval archaeologists at University of Salento studied the pattern of early medieval rural settlements through surveys and excavations. For the 7<sup>th</sup> and 8<sup>th</sup> centuries the archaeological record shows a heavy fragmentation of the rural habitat, organized in small villages and farms (Arthur *et al.*, 2008, 2011). One of them, identified and excavated at *Loc. Scorpo* near Supersano, was characterised by residential buildings made of non-durable materials.

Another context of interest in this framework is *Contrada Badia* (Melissano, 1990), close to the modern town of *Cutrofiano*. Some years ago in this area, preliminary aerial photographic investigations and archaeological surveys led to the identification of subsequent phases of frequentation dating back from the Bronze Age (fourteenth-eleventh century B.C.) up to the fifteenth century A.D. (Greco and Lapadula, 2014). A dense scatter of ceramics is located on a 6 hectares plateau: the archaeological record gives evidence of human frequentation in the area during the Hellenistic period and, after a hiatus in the Republican phase, it displays a substantial continuity in the management of rural landscape from the Roman Imperial to the Byzantine period. Late Antique occupation of the site is testified by a large series of finds, such

as architectural elements, rotary querns in volcanic stone, mosaic tiles, slugs from metalworking processes, and an imperial coin.

Aerial photographs and survey data document the existence of a complex *vicus* during the Roman Imperial period. Otherwise, a less wide area was occupied by the Early Medieval settlement. At the same zone the fortuitous finding on the ground surface of a fibula and a bronze buckle allow to hypothesize to be related to the presence of a cemetery area.

The site was still inhabited in the Late Middle Ages: to this period should be attributed some pottery kilns and perhaps an abbey, mentioned in historical documents of the sixteenth century, and then replaced by a farmhouse in the modern period.

It is clear that the site at *Badia* plays a central role for the historical investigation of rural settlements in southern Apulia. In this work we focused our attention on the area where Roman Imperial and Byzantine evidences are mostly noticeable.

Some rectangular transects have been identified as possibly promising zones for near surface geophysical prospecting (Fig. 1). In these areas Ground-penetrating Radar (GPR) and magnetometric (in gradiometry configuration) were undertaken. Due to the complexity of most archaeological environments, the integration of different methods can help to overcome the limitations related to a single method, such as low reflection amplitude in the case of scarce dielectric contrast between archaeological structures and hosting materials or a high level of clutter in strongly heterogeneous terrains for example in GPR. A multimethodological approach, involving GPR and magnetometry, generally reduces the uncertainty in the interpretation of the results, helping to define better the boundaries of individual archaeological buildings or the extent and layout of large settlements (Cammarano *et al.*, 1997; Piro *et al.*, 2000, 2003; Gaffney *et al.*, 2004; Seren *et al.*, 2004; Cardarelli *et al.*, 2008; Giannotta *et al.*, 2014; Leucci, 2015). A good spatial overlap of anomalous zones in different geophysical datasets is generally a powerful indication of the presence of underground bodies with physical properties strongly different from the embedding soil, such as anthropogenic structures. Therefore, the integration of different geophysical surveys can help to better define the location, depth and geometry of archaeological bodies. Being sensitive to different physical parameters, different geophysical methods show anomaly patterns which, in most cases, do not overlap, pointing to features of different origin (Orlando, 2007; Leucci, 2015). As different methods give complementary information, their integration is essential to identify features that otherwise could be undetected and to provide a more comprehensive description of an archaeological site.

**GPR survey.** Ground-penetrating radar (GPR) is one of the faster near surface non-invasive tools, and it provides to best available resolution among the geophysical techniques. Depending on the external conditions and on the central frequency of the antennas, it can allow on average a penetration depth from 1 to 3 m.

It is based on the propagation and scattering of the electromagnetic waves, and consequently it is sensitive to variations of the electromagnetic parameters in the subsoil, especially the dielectric constant and the electric conductivity (Davis and Annan, 1989). The resolution achievable from a GPR ranges about from 40 to 10 cm in archaeological applications, again depending on the kind of soil and on the central frequency of the antennas.

The investigated areas are geo-referenced in Fig. 1. The soil was composed of slimy and quite moist sediments over a calcareous basis. The prospecting was performed with pulsed a RIS H-Mode GPR system equipped with a double antenna at 200 and 600 MHz, in the case at hand the best results were provided by the antennas at 600 MHz, being the depth of the targets of interest smaller than 2 m. In the following, GPR slices and a three dimensional visualization are proposed (Conyers and Goodman, 1997; Leucci, 2002; Goodman and Piro, 2013). The profiles were 0.5 m spaced from each other, for each trace 512 time domain samples were chosen, the bottom scale of the times was 80 ns with regard to the 600 MHz antennas. We adopted a manual gain function to compensate the losses in the soil, and performed a 2D linear processing making use of the GPR-Slice Version 7.0 software ([www.gpr-survey.com/](http://www.gpr-survey.com/)).



Fig. 2 – The GPR and magnetic gradiometric surveys in Cutrofiano allowed the identification of buried walls and structures of probable archaeological interest. Structures seem to have same alignment SE-NW.

The processing consisted in zero time, frequency filtering, manual gain, background removal with moving average, migration in time domain. For the migration and the time domain conversion, we exploited a propagation velocity of 7 cm/ns, worked out from the diffraction hyperbolas present in the data (Conyers and Goodman, 1997; Goodman and Piro, 2013; Persico *et al.*, 2015). Afterward, the migrated data were joined together to form a three-dimensional cube, which allowed in its to visualize flat slices along each of the three coordinative directions. In particular, here we will visualize slices along the depth direction, performed on consecutive time windows 5 ns (about corresponding to 17 cm). Time slices are shown in Fig. 2, that shows that anomalies of interest are present in each of the three areas.

**Gradiometry survey.** Gradiometry (also known as magnetometry or magnetic gradient survey) is a passive geophysical method that detects local variation in the strength of the earth's magnetic field. These variations can be caused by a variety of natural and cultural features that alter the magnetic field emanating from the earth. Typical gradiometers used for archaeological survey allow relatively rapid collection of data (Fassbinder and Reindel, 2005; Silliman *et al.*, 2000). The gradiometer is carried by an operator along a series of transects at a constant speed, collecting data automatically. Data are downloaded from the instrument and used to create magnetic maps of the surveyed area. These maps are processed with software to bring out the anomalies of interest and aid in interpretation.

The gradiometer surveys were carried out using a Bartington Grad 601-2 fluxgate gradiometer. At each site, survey areas were laid out in both 40x40 m and 20x30 m grids oriented to the cardinal directions, with corners established using measurements from the total station. Given the overarching goals of the project (to identify shallow, substantial architectural features) and the time restraints for field collection, we deemed it most productive to use 1 m transect spacing. Although this collection strategy limited the overall level of subsurface resolution achieved, it proved useful for determining broad architectural patterns. Gradiometer survey focused on four areas: one 20x30 m labelled area 4 one 20x40 m labelled area 4 and two 40x40 m collection areas labelled area 1 and area 2 (Fig. 2). Some areas (1 and 4) in the site overlapping with the GPR collection area (2 and 3).

All gradiometer data were processed using TerraSurveyor software (<http://www.dwconsulting.nl/TerraSurveyor3d.html>), and processed data were imported into ArcGIS, with gradiometer grids arranged appropriately. The data were then clipped to three standard deviations and rounded off to  $\pm 12$  nT. Finally, a zero mean filter was used to destripe the data. Gradiometer survey identified archaeological features, some of which coincident with GPR (Fig. 1).

Within survey area 1, is visible a 8nT (red dashed lines) anomaly, labelled R, that was interpreted as related to ancient road. The anomalies labelled A with a negative gradient values (ranging from -10 to -7 nT) could be related to archaeological structures. The high positive anomaly indicated by a red arrow and labelled F could be related to the presence of a furnace.

**Conclusions.** In this paper a combined GPR and magnetic gradiometric prospecting has been presented, applied to a site dating back to Late Antique and Byzantine time in Apulia. Both magnetic gradiometry and GPR allowed us to identify salient aspects of site during a limited window of time. The GPR data allowed to represent time slices and a 3D visualization of the buried context, which has confirmed the presence of anomalies, probably ascribable to some remaining foundations of Late Antique or Early Medieval rural buildings. Indeed, the area has been used for agricultural exploitation for many years now, and frequent ploughings certainly destroyed many archaeological evidences, as proved by the large pottery scatters visible in the fields. Magnetic gradiometry results reveal more anomalies than GPR prospectings and evidenced a probable road, a production area (maybe a kiln) and some other structures that could be of archaeological interest. Relating these data with those coming from archaeological survey and possible future excavations could clarify the functional usage of this part of the Late Antique *vicus*, and his transformation into a byzantine village.

**Acknowledgments.** The work was conducted as part of the PRIN 2010-2011 (2010H8WPKL) “Global Archaeology and history of the rural landscapes of Italy between Late Antiquity and the Middle Ages. Integrated system of sources, methods and techniques for a sustainable development”; financed by Italian MIUR. The authors also thank the Soprintendenza Archeologia della Puglia (Taranto), for the authorization to the surveys and Dr Salvatore Matteo of the municipality of Cutrofiano for his help in the field.

## References

- Arthur P., *L'archeologia del villaggio medievale in Puglia*, in Milanese M. (a cura di), *Vita e morte dei villaggi rurali tra Medioevo ed Età Moderna*, Firenze, 2006, pp. 97-121.
- Arthur P., *Verso un modellamento del paesaggio rurale dopo il Mille nella Puglia meridionale*, in *Archeologia Medievale XXXVII*, 2010, pp. 215-228.
- Arthur P., *Per una carta archeologica della Puglia altomedievale: questioni di formulazione ed interpretazione*, in Bizantini, Longobardi e Arabi in Puglia nell'alto medioevo, Atti del XX Congresso internazionale di studio sull'alto medioevo, Savellettri di Fasano 3-6 novembre 2011, Spoleto, 2012a, pp. 59-85.
- Arthur P., *Villages, communities, landscapes in the Byzantine and Medieval Salento*, in Galetti P. (a cura di), *Paesaggi, comunità, villaggi medievali*, Atti del Convegno internazionale di studio, Bologna 14-16 gennaio 2010, Spoleto, 2012b, pp. 546-563.
- Arthur P., Fiorentino G., Grasso A.M., Leo Imperiale M., *La Storia nel Pozzo. Ambiente ed economia di un villaggio bizantino in Terra d'Otranto –Supersano 2007. Catalogo della Mostra (Museo Storico-Archeologico dell'Università del Salento, 8 ottobre-25 novembre 2011)*. Unisalento Press, Lecce, 2011, ISBN 978-88-9651-508-2, pp. 88.
- Arthur P., Fiorentino G., Leo Imperiale M., *L'insediamento in Loc. Scorpo (Supersano, LE) nel VII-VIII secolo. La scoperta di un paesaggio di età altomedievale*, in *Archeologia Medievale XXXV*, Firenze, 2008, pp.365-380.
- Melissano V., *Ricerche archeologiche nel territorio di Cutrofiano (Lecce)*, in *Studi di Antichità* 6, Galatina 1990, pp. 257-297.
- Greco A., Lapadula E., *L'insediamento di età tardoromana in località Badia, Cutrofiano (Lecce). Dati preliminari sulla ceramica dipinta*, in Museo della Ceramica di Cutrofiano, Quaderno 8-9 (a cura di S. Matteo), Congedo Editore, 2004, pp. 11-38.
- Cammarano F, Mauriello P, Piro S. 1997. Highresolution geophysical prospecting with integrated methods. The ancient Acropolis of Veio (Rome, Italy). *Archaeological Prospection* 4: 157– 164.
- Piro S, Mauriello P, Cammarano F. 2000. Quantitative integration of geophysical methods for archaeological prospecting. *Archaeological Prospection* 7: 203–213.
- Piro S, Goodman D, Nishimura Y. 2003. The study and characterization of Emperor Traiano's Villa (Altopiani di Arcinazzo, Roma) using high-resolution integrated geophysical surveys. *Archaeological Prospection* 10: 1–25.
- Gaffney V, Patterson H, Piro S, Goodman D, Nishimura Y. 2004. Multimethodological approach to study and characterize Forum Novum (Vescovio, central Italy). *Archaeological Prospection* 11: 201– 212.
- Seren S, Eder-Hinterleitner A, Neubauer W, Groh S. 2004. Combined high-resolution magnetics and GPR surveys of the roman town of Flavia Solva. *Near Surface Geophysics* 2: 63–68.

- Cardarelli E, Fischanger F, Piro S. 2008. Integrated geophysical survey to detect buried structures for archaeological prospecting. A case-history at Sabine Necropolis (Rome, Italy). *Near Surface Geophysics* 6: 15–20.
- Orlando L. 2007. Georadar data collection, anomaly shape and archaeological interpretation – a case study from central Italy. *Archaeological Prospection*, 14: 213–225.
- Davis J.L., Annan A.P., Ground-Penetrating Radar for high-resolution mapping of soil and rock stratigraphy, in *Geophysical Prospecting*, 37, 1989, pp. 531-551.
- Conyers L.B., Goodman D., Ground-penetrating radar – An introduction for archaeologists, Alta Mira Press: Walnut Creek 1997.
- Leucci G., Ground-Penetrating Radar Survey To Map The Location Of Buried Structures Under Two Churches, in *Archaeological Prospection*, vol. 9, n.4, 2002, pp. 217-228.
- Goodman D. and Piro S., *GPR Remote Sensing in Archaeology*, Springer, 2013.
- Persico R., Leucci G., Matera L., De Giorgi L., Soldovieri F, Cataldo A., Cannazza G., de Benedetto E., 2015. **Effect of the height of the observation line on the the diffraction curve in GPR prospecting**, *Near Surface Geophysics*, 13, 243-252. DOI: 10.3997/1873-0604.2014042
- Fassbinder JWE, Reindel M. 2005. Magnetometer prospecting as research for Pre-Spanish cultures at Nasca and Palpa, Peru. In *Proceedings of the 6th International Conference on Archaeological Prospection*, Rome. Goodman et al. *Archaeol. Prospect.* 13, 159–163 (2006).
- Silliman SW, Farnsworth P, Lightfoot KG. 2000. Magnetometer prospecting in historical archaeology: evaluating survey options at a 19th-century Rancho Site in California. *Historical Archaeology* 34(2): 89–109;
- Giannotta M.T., Leucci G., Persico R., Leo Imperiale M., The archaeological site of Badia in Terra d'Otranto: contribution of the geophysical prospecting to the reconstruction of the landscape from the Late Antiquity to the Middle Age, in '6th International Congress "Science and Technology for the Safeguard of Cultural Heritage in the Mediterranean Basin', Athens, Greece 22nd-25th October 2013, vol. III, Editore VALMAR, Roma, 2014 (ISBN 978-88-97987-05-5), pp. 41-49;
- Leucci G., 2015. *Geofisica per l'Archeologia e i Beni Monumentali*, Dario Flaccovio Editore, Palermo.

## RILIEVI GEOFISICI IN SITI DI INTERESSE ARCHEOLOGICO IN AGRO DI BAUCINA (PA)

G. Leucci<sup>1</sup>, A. Cubito<sup>2</sup>, L. De Giorgi<sup>1</sup>, S. Pappalardo<sup>2</sup>, T. Giaccone<sup>2</sup>, C. Greco<sup>2</sup>

<sup>1</sup> *Istituto per i Beni Archeologici e Monumentali – CNR, Lecce, Italia*

<sup>2</sup> *Sigeo snc, Catania, Italia*

**Introduzione.** Nel 1991, la Sovrintendenza dei Beni Culturali ed Ambientali di Palermo ha accolto la richiesta del Consiglio Comunale di Baucina di inserire la zona compresa tra Monte Falcone e Monte Carrozza (Fig. 1a) tra le aree a vincolo archeologico. Contestualmente a tale richiesta ha intrapreso una campagna di scavo che ha interessato un settore della necropoli (già scavata negli anni '70) e un settore dell'abitato di Monte Falcone.

Parte dei reperti provenienti da questa campagna di scavo sono attualmente esposti, insieme ad oggetti sequestrati dai Carabinieri a "tombaroli" locali, nel Museo Civico di Baucina (Antiquarium archeologico).

La posizione di questo insediamento è strategica: si trova infatti, sullo spartiacque tra il bacino del Fiume Milicia e quello del San Leonardo, e dai reperti rinvenuti è possibile evidenziare la presenza di rapporti commerciali e/o politici sia con le colonie fenicio-puniche di Palermo e Solunto sia con le polis greche di Himera e di Akragas.

Sulla superficie di questi piccoli rilievi, affiorano resti di antiche strutture e numerosi manufatti in terracotta, tra cui tegole, anfore, ceramica a vernice nera e pesi da telaio. La necropoli è ubicata in parte in corrispondenza delle balze calcarenitiche di Monte Falcone e in parte nelle balze calcarenitiche della collinetta interposta tra i due centri residenziali di Monte Falcone e di Monte Carrozza, quest'ultima probabilmente di pertinenza di entrambe i nuclei abitati.

La necropoli è stata sottoposta negli anni, a numerosi saccheggi, che ne hanno modificato l'aspetto originario: nei pressi delle tombe a grotticella spesso sono presenti numerosi cumuli di terra a testimonianza dell'attività dei "tombaroli".

A seguito dello scavo archeologico del 1991 e ai successivi rilievi e studi condotti dall'archeologo Bordonaro (2011), è emersa la presenza di tombe a fossa intramezzate da sepolture a cappuccina e a enchytrismòs, da incinerazioni e da tombe a grotticella artificiale.

Queste ultime, ancora oggi visibili, ospitavano sepolture plurime accompagnate da corredi costituiti da vasellame di produzione greca e indigena ed erano chiuse da lastre di gesso provenienti dalla vicina contrada Balatelle.

L'esistenza del nucleo abitato di Monte Falcone è messa in risalto dalla presenza di possibili strutture murarie, indiziate da allineamenti di rocce ubicate sul versante meridionale; l'abitato di Monte Carrozza, invece, è testimoniato dal ritrovamento di lastre e pietre squadrate utilizzate presumibilmente nelle costruzioni di edifici.

Su entrambi i rilievi è documentata anche una fase di età preistorica come dimostrano gli strumenti in ossidiana di Pantelleria e sporadici frammenti di ceramica monocroma rossa riconducibili all'età del Rame. Tracce di frequentazioni in età bizantine e araba sono presenti, invece, soltanto a Monte Falcone.

Con lo scopo di realizzare scavi mirati e quindi rivalutare il prezioso sito archeologico è stata intrapresa una campagna di misure geofisiche. E' da sottolineare che i siti archeologici in esame non sono stati mai indagati con metodologie di indagine indiretta e non sono stati mai studiati nella loro totale estensione. L'utilizzo delle prospezioni geofisiche hanno avuto dunque l'obiettivo di mappare gli elementi archeologici ancora sepolti e presumibilmente non violati dai "tombaroli", consentendo al tempo stesso operazioni di scavo archeologico mirate e produttive, nonché la descrizione accurata dell'estensione e delle modalità di sviluppo areale dell'insediamento.

**Inquadramento geologico dell'area indagata.** L'area in cui ricadono i siti archeologici di Monte Falcone e di Monte Carrozza si trova nel territorio del Comune di Baucina (Palermo), che dal punto di vista cartografico risulta compreso nelle tavolette a scala 1:25000 "Ciminna" e "Ventimiglia di Sicilia" edite dall'Istituto Geografico Militare Italiano (Fig. 1b). La zona oggetto di studio si colloca in corrispondenza di un range altimetrico compreso tra circa 580 e 740 m s.l.m., e presenta una morfologia che dipende strettamente dalla litologia delle formazioni affioranti e dall'interazione con le caratteristiche idrologiche e climatiche locali.

In questa zona alto collinare dominano i terreni miocenici di natura biocalcarenitica della Formazione Baucina e il sovrassegno quaternario del deposito di falda a grossi blocchi.

La presenza di copertura vegetale in questi terreni varia con le stagioni ma si rileva quasi sempre la dominanza di cespugli e arbusti.

Nei siti di Monte Falcone e Monte Carrozza, laddove sono presenti affioramenti litoidi (calcarei, conglomeratici o quarzarenitici), la morfologia del terreno si presenta aspra, con scarpate accidentate e talvolta sub-verticali che spesso danno luogo a fenomenologie franose di crollo. Invece, in corrispondenza degli affioramenti prevalentemente argilloso - sabbiosi il terreno mostra minore acclività e le fenomenologie franose prevalenti, descritte nel P.A.I. (ATARS, 2010), sono i colamenti lenti, i fenomeni franosi diffusi, le frane complesse e, in misura minore, i fenomeni di erosione accelerata, soliflusso e scorrimento.

Dal punto di vista idrologico il territorio limitrofo è interessato dalla presenza dei torrenti Acquasanta e Margio. Il regime idrologico è prettamente torrentizio e i deflussi superficiali sono limitati a brevi periodi dell'anno, durante la stagione piovosa ed in concomitanza di precipitazioni intense e concentrate.

Dal punto di vista geologico i due rilievi sono costituiti dalle seguenti formazioni mioceniche, dal basso verso l'alto (Fig. 1b):

Formazione Terravecchia (Tortoniano superiore – Messiniano inferiore): si tratta di conglomerati e sabbie grossolane, peliti sabbiose, sabbie ed arenarie pelitiche, argille sabbiose e peliti, marne grigie o azzurrognole con plancton calcareo. Sono di ambiente fluvio-deltizio fino a piattaforma aperta. Il limite inferiore è inconforme sui terreni più antichi. In particolare sono presenti i seguenti membri:

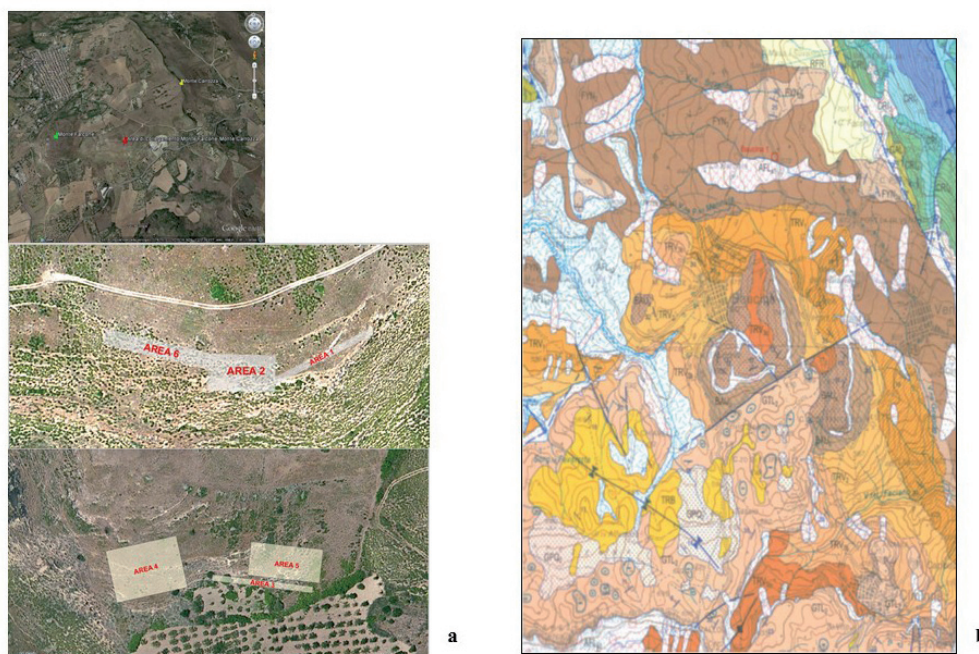


Fig. 1 – a) Ubicazione delle aree di indagine; b) stralcio del Foglio 608 “Caccamo” in scala 1:50.000.

Membro pelitico-argilloso (TRV3): marne grigie, argille grigio-verdastre o azzurrognole (TRV3b) a foraminiferi planctonici (biozone a *Globorotalia suterae* e *Globorotalia conomiozea*) e nannofossili calcarei (biozone da *Minilytha convallis* a *Reticulofenestra rotaria*) e marne marine fossilifere (TRV3c) a *Turborotalia multiloba* (zona non distintiva). Tali depositi poggiano in paraconformità o in eteropia su (TRV2) e sono di ambiente di prodelta.

**I metodi geofisici impiegati nelle campagne di misura a Baucina.** Le condizioni dei terreni da indagare legate alla forte pendenza, alle asperità, all'erba alta, alla presenza di numerosi ostacoli (pietre, alberi, vigne, ecc.) hanno fortemente influenzato la scelta della metodologia geofisica. Pertanto nella campagna di misure è stato impiegato il metodo geoelettrico. Tale metodologia consente di caratterizzare il sottosuolo dal punto di vista del parametro fisico resistività elettrica ( $\rho$ ). Il metodo geoelettrico della resistività si basa sulla circolazione di corrente elettrica stazionaria (continua o a bassissima frequenza, affinché siano trascurabili i fenomeni di induzione) nel sottosuolo.

I mezzi materiali, infatti, rispondono ad un flusso di corrente in maniera diversa, in base al valore che assume il parametro fisico della resistività. Tipicamente, la resistività che i litotipi offrono alla circolazione di corrente elettrica dipende dal contenuto d'acqua interstiziale, dalla temperatura, dal contenuto di gas disciolti nell'acqua, dalla presenza di ioni liberi. La stima dei valori di resistività si realizza mediante un quadripolo elettrico costituito da due elettrodi *A* e *B*, detti di corrente, e due elettrodi *M* ed *N* detti di potenziale. Attraverso gli elettrodi *A* e *B* viene inviata nel sottosuolo una corrente di intensità *I* nota e tramite gli elettrodi *M* e *N* si misura la differenza di potenziale  $\Delta V$ . I quattro elettrodi costituiscono, nel loro insieme, il dispositivo elettrodico di misura, che può presentare diverse geometrie di disposizione sul terreno, ognuna caratterizzata da un parametro *K* che prende il nome di “*fattore geometrico*”.

La relazione che lega i parametri fisico corrente elettrica (*I*), differenza di potenziale ( $\Delta V$ ), resistività elettrica ( $\rho$ ) è la ben nota legge di Ohm:

$$\rho = K \Delta V / I.$$

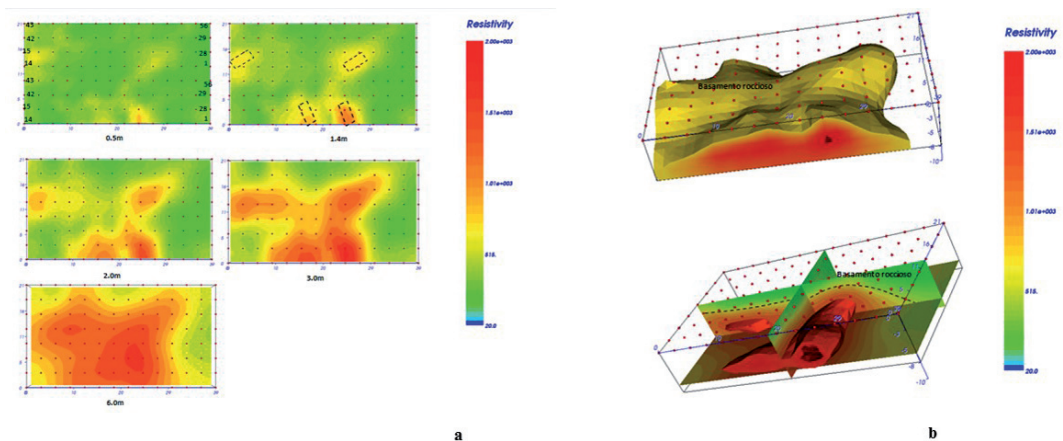


Fig. 2 – a) Modello 3D di distribuzione della resistività a profondità comprese tra 0.5 e 6m; b) isosuperfici di resistività.

Definendo  $\Delta V$  in volt,  $I$  in Ampere e  $K$  in metri, la resistività  $\rho$  viene espressa in Ohm m. In realtà quella che viene calcolata è una resistività apparente ( $\rho_a$ ) ossia è un valore di resistività dovuto ai diversi contributi di tutto il sottosuolo che si sentiranno, in maniera più o meno forte, a seconda della distanza dal dispositivo di misura.

**Risultati.** Per le misure è stato impiegato il georesistivimetro Abem con 64 canali attivi. La massima lunghezza dei profili è stata scelta in base alla massima profondità di interesse (i primi metri dal piano di campagna) e alla probabile risoluzione richiesta. Sono stati pertanto utilizzati un numero di elettrodi variabile e con distanza interelettrodica anch'essa variabile ed adattata al particolare caso di studio. È stato pertanto impiegato il dispositivo elettrodico dipolo-dipolo (Loke, 2001). La disposizione degli elettrodi è stata quella che ha consentito, tramite una particolare procedura di campagna, di ottenere una griglia regolare con distanza interelettrodica variabile tra 1 e 4 m. È stata pertanto utilizzata una geometria di acquisizione che prevede la disposizione sul terreno di una linea elettrica a serpentina che consente un aumento della densità dei dati.

Da questo set di dati si possono quindi estrarre sia Tomografie Geoelettriche Verticali XZ (TGV) che Orizzontali XY (TGO) a varie profondità che rendono un quadro chiaro della distribuzione di resistività nel sottosuolo. Per l'inversione dei dati è stato impiegato il software ERTLab (<http://www.geostudiasier.it/>) che utilizza un algoritmo agli elementi finiti per la modellazione accurata della topografia del terreno. Di seguito vengono commentati i dati relativi alle aree risultate essere più interessanti e che, in seguito ai risultati delle indagini geofisiche, sono state scavate.

Per l'area 2 (Fig. 1a) i modelli di distribuzione della resistività elettrica a varie profondità sono mostrati nelle Fig. 2a

Dal modello di distribuzione della resistività (Fig. 2a) risulta evidente la presenza di un sottosuolo eterogeneo con valori di resistività compresi tra 50 e 2000 Ohm m. In particolare si nota la presenza:

- 1) aree (in rosso), indicate nei riquadri tratteggiati neri, con valori di resistività comprese tra 1800 e 2000 Ohm m; tali valori indicano la probabile presenza di aree in cui è localizzato una probabile struttura di interesse archeologico. I valori relativamente bassi di resistività indicano che tali anomalie non sono da imputare alla presenza di vuoti ma a materiali incoerenti all'interno dei quali sono presenti piccoli vuoti;
- 2) aree (in verde) con valori di resistività compresi tra 50 e 180 Ohm m; tali valori indicano la probabile presenza di materiale di soprasuolo;
- 3) aree relative al basamento roccioso a profondità comprese tra 3.0 e 6.0 m.

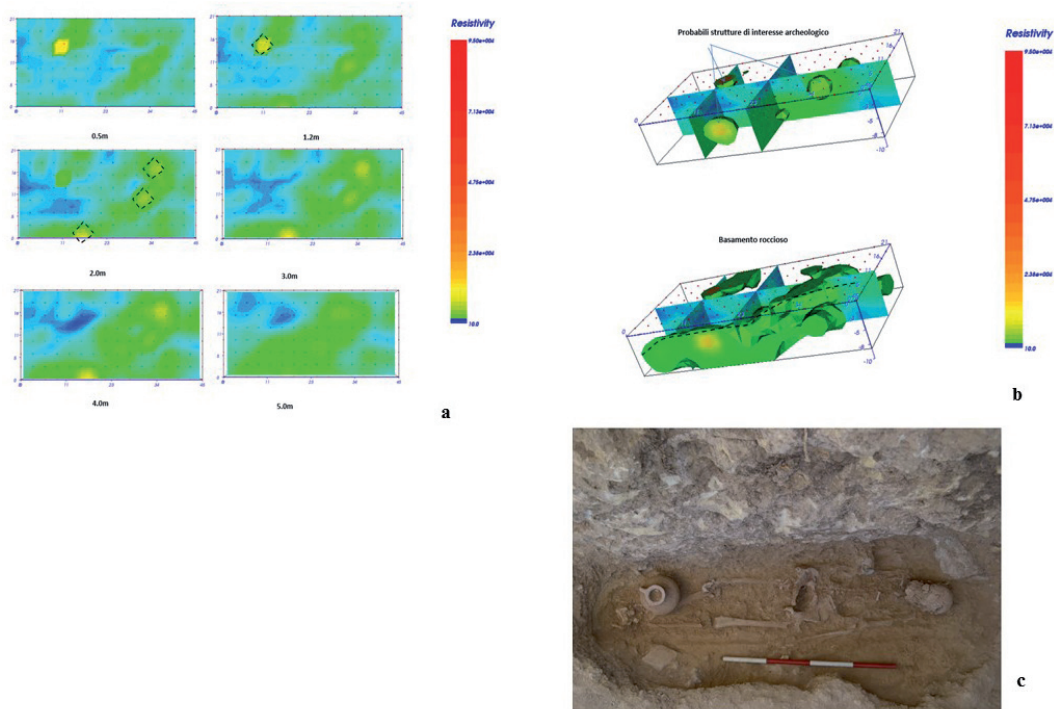


Fig. 3 – Area 5: a) modello 3D di distribuzione della resistività a profondità comprese tra 0.5 e 6 m; b) isosuperfici di resistività; c) foto della tomba scavata successivamente al risultato del rilievo elettrico 3D.

I dati di resistività sono stati inoltre rappresentati in isosuperfici (Fig. 2b). In essa è meglio evidenziato l'andamento del basamento roccioso e le strutture di probabile interesse archeologico.

Per l'area 5 (Fig. 1a) i modelli di distribuzione della resistività elettrica a varie profondità sono mostrati nelle Fig. 3a

Anche in questo caso dal modello di distribuzione della resistività (Fig. 3a) risulta evidente la presenza di un sottosuolo eterogeneo con valori di resistività compresi tra 50 e 90000 Ohm m. In particolare si nota la presenza:

- 4) aree (in giallo), indicate nei riquadri tratteggiati neri, con valori di resistività comprese tra 1800 e 2300 Ohm m; tali valori indicano la probabile presenza di aree in cui è localizzato una probabile struttura di interesse archeologico. I valori relativamente bassi di resistività indicano che tali anomalie non sono da imputare alla presenza di vuoti ma a materiali incoerenti all'interno dei quali sono presenti piccoli vuoti;
- 5) aree (in blu) con valori di resistività compresi tra 50 e 180 Ohm m; tali valori indicano la probabile presenza di materiale di soprasuolo;
- 6) aree relative al basamento roccioso a profondità comprese tra 3.0 e 6.0 m.

I dati di resistività sono stati inoltre rappresentati in isosuperfici (Fig. 3b). In essa è meglio evidenziato l'andamento del basamento roccioso e le strutture di probabile interesse archeologico.

**Discussioni e conclusioni.** Nel mese di luglio 2014 hanno preso il via le indagini archeologiche in un settore della necropoli ubicata lungo il versante meridionale di Monte Falcone, come azione di contrasto al fenomeno degli scavi clandestini. La ricerca è stata condotta dalla Cattedra di Topografia antica dell'Università degli Studi di Palermo, in convenzione e collaborazione con la Soprintendenza dei Beni Culturali di Palermo, e con il sostegno logistico e finanziario del Comune di Baucina.

In considerazione dei risultati del rilievo geoelettrico per lo scavo è stata scelta l'aria 5. In tale area sono state individuate anomalie attribuibili alla probabile presenza di tombe ipogeiche. In aggiunta la scelta di operare nell'area 5 è nata soprattutto dalla possibilità di esplorare una grande tomba a camera parzialmente violata da scavi clandestini. La sepoltura manteneva, infatti, il portale d'ingresso in buone condizioni di conservazione, mentre nella terra di riempimento erano ancora presenti, oltre ad ossa umane, numerosi frammenti di vasi di corredo. Inoltre le tomografie indiziavano ai lati di questa tomba due tracce significative.

Si è iniziato a scavare nella parte inferiore dell'area dove il risultato della tomografia elettrica indicava la presenza di una anomalia (Fig. 3a). Lo scavo ha evidenziato una prima sepoltura entro coppi.

Lo scavo successivamente ha messo in luce una seconda tomba a grotta. Si tratta di una struttura di dimensioni ridotte. Un'altra tipologia tombale attestata durante lo scavo è l'*enchytrismòs*: in totale sono state individuate 4 sepolture tre delle quali localizzate nella balza inferiore e solo una in quella superiore. Per una delle sepolture si segnala l'uso di un'anfora punica. Nessuna delle tombe a *enchytrismòs* presentava corredo (Fig. 3c).

### Bibliografia

- Assessorato Territorio e Ambiente Regione Siciliana, 2010 – I Aggiornamento del Piano Stralcio di Bacino per l'Assetto Idrogeologico: Bacino Idrografico del Fiume Milicia (n. 035), Area territoriale tra il Bacino del F. S. Leonardo e il Bacino del F. Milicia (034), Area territoriale tra il Bacino del F. Milicia e il Bacino del F. Eleuterio (036). <http://www.sitr.regione.sicilia.it>.
- Bordonaro G., 2011 – Monte Falcone e Monte Carrozza. Un insediamento indigeno al confine tra il mondo fenicio-punico e quello greco. *Forma Urbis XVI*, 10: 40-48.
- ISPRA (Servizio geologico d'Italia), 2010 – Carta Geologica d'Italia: Foglio 608 "Caccamo", 1:50.000. Nadir S.a.s. di Antonio D'argenio, Palermo.
- Istituto Geografico Militare Italiano – Foglio 259, IV, SO "Ciminna", 1:25.000.
- Istituto Geografico Militare Italiano – Foglio 259, IV, NO "Ventimiglia di Sicilia", 1:25.000.
- Loke, M. H.: *Electrical imaging surveys for environmental and engineering studies, A practical guide to 2-D and 3-D surveys*: RES2DINV Manual, IRIS Instruments, [www.iris-instruments.com](http://www.iris-instruments.com), 2001.

## INFLUENCE OF DIFFERENT ARRAY DATASETS ON RELIABILITY OF ELECTRICAL RESISTIVITY TOMOGRAPHY

R. Martorana<sup>1</sup>, P. Capizzi<sup>1</sup>, A. D'Alessandro<sup>2</sup>, D. Luzio<sup>1</sup>

<sup>1</sup> Dip. Scienze della Terra e del Mare, Università di Palermo, Italy

<sup>2</sup> Istituto Nazionale di Geofisica e Vulcanologia, Centro Nazionale Terremoti, Palermo, Italy

**Introduction.** Over the past twenty years, progress in electronics and information technology have enabled the development of new geophysical instruments capable of simultaneously performing multiple measurements employing very shorter times than before. This has made possible the development of new methodologies for data acquisition, processing and interpretation, designed to tomographic reconstructions of the subsurface. In recent years, the electrical resistivity tomography has become a popular choice for the investigation of the shallow subsurface. The increasing use of electrical resistivity tomography for different applications is made possible by the use of new instruments and new multi-channel multielectrode sequences. The electrical resistivity tomography (ERT) has become one of the geoelectric methods capable of producing a detailed tomography of the subsoil thanks to the possibility to acquire in a short time a large number of apparent resistivity data.

In electrical tomography, the particular choice of a specific electrode array can substantially influence the final result, depending on the geometry and resistivity of the investigated structures. The main differences in the results obtained are mainly characterized by the resolving power,

by the presence of artifacts in the images, as well as by the deviation from the true resistivity of the subsoil. The resolution of an acquiring sequence of measures is strongly influenced by the sensitivity distribution, which can be very different.

In recent years many authors dealt with the problem of optimization of the data sequences of acquisition, which can be formed by various combinations of measurements with different electrode arrays and/or different dipolar lengths and distances, in order to obtain the best resolution and at the same time the best recovery capacity of the tomographic section. It emerged, therefore, the need of the study of the sequences of measurement, for the choice of optimized dataset, aiming at a higher resolution of investigation and, especially, at a more efficient retrieval of information on the characteristics of the medium investigated.

Recently many studies have been carried out to compare the advantages and limitations of the most common arrays used in electrical tomography. Park and Van (1991) and Van *et al.* (1991) have pointed out the difficulty of acquiring unnoisy field data using the pole-pole array. Sasaki (1992) compared the resolution of pole-pole, pole-dipole and dipole-dipole arrays in cross-hole electrical tomography, ruling that the dipole-dipole array is more suitable for the resolution of complex structures. Comparing the same arrays, Oldenburg and Li (1999) have pointed out the differences in the depth of penetration of each array, considering the inverse models obtained. Studies on the resolving power and reliability of Wenner array (Dahlin and Loke, 1998; Olayinka and Yaramanci, 2000) emphasized the importance of the sampling density to determine the resolution of this configuration.

Over the past two decades, developments in microelectronics have led to major improvements for both acquisition systems and inversion software. Consequently, the tomographic resistivity techniques have achieved remarkable results. Some recent multichannel resistivity-meters enable many simultaneous measurements for each current dipole, significantly reducing the measuring time and, at the same time, allowing the acquisition of big datasets to cover large areas with high sampling density. These multichannel systems consequently has allowed the use of new multielectrode arrays and sequences. Examples of these types of array are the moving gradient and the midpoint-potential-referred. Dahlin and Zhou (2004) have carried out several numerical simulations to compare the resolution and efficiency of pole-pole, pole-dipole, Wenner, Schlumberger, dipole-dipole, moving gradient and midpoint-potential-referred array. They recommend moving gradient, pole-dipole, dipole-dipole and Schlumberger array, rather than the other, although the final choice should be determined by the type of geology expected, the purpose of the survey and other logistical considerations. Martorana *et al.* (2009) have compared various 2D simulations using near surface models, by varying the array type, in order to assess the best resolution.

Despite the flexible nature of these systems, there still is the tendency to acquire apparent resistivity measures using traditional electrode arrays such Wenner, Schlumberger or dipole-dipole. These latter often prove to be a good choice, as their properties are well known, in terms of depth of investigation (Barker, 1989), lateral and vertical resolution (Barker, 1979) and signal-to-noise ratio (Dahlin and Zhou, 2004). However, the choice of these arrays could not be the most efficient if the time or the number of steps permitted for the survey is limited, or if a target of particular interest is spatially localized.

The use of parameters to estimate the reliability of inverse models is crucial to the choice of the measures sequence which provides reliable results, while not entailing excessive costs, that are linked essentially to the number of current dipoles used and survey time.

Recently, there has been a growing interest in the study of the generation of sets of measures for optimizing the resolution tomographic image. One of the benefits of the optimization of the sequential experimental design would be a better reconstruction of the subsurface that aims to reduce the number of acquisitions of the data and, consequently, the cost of the survey, without compromising the quality of the reconstruction itself. In practice the methods of array optimization to maximize the resolution of tomographic image should also take into account the

effect of data errors on the resolution obtained. However, most of the optimization techniques used so far have not sufficiently taken into account the effects of noise on apparent resistivity data.

Generally, in ERT the problem due to errors on data caused by improper electrode positioning is not adequately considered. This error may be higher in steep or heavily vegetated areas and it generates an incorrect estimate of the geometric factor. To reduce the effect of this type of error on the resulting electrical tomography it is possible to select datasets that include arrays with relatively low geometric factors and therefore less sensitive to position errors (Wilkinson *et al.*, 2008).

The study of the influence of errors on the resolution of the inverse model and especially on its ability to retrieve correct information of the subsurface is important to understand how the performance vary from a few simple parameters such as the total number of measurements of the data set and the distribution of the geometric factor values.

The goal of this work is to study how the reliability of inverse model depends on a few basic parameters, as the combination of potential spacing and dipolar distance and, consequently, the number of measurements and of current dipoles, considering also how error affects inversion. The number of current dipole used is crucial, when using multichannel resistivity-meters, because it determines the overall acquisition time.

A systematic comparison is presented between four 2D resistivity models and their images, obtained by the inversion of synthetic datasets relating to four different arrays: dipole-dipole (DD), pole-dipole (PD), Wenner-Schlumberger (WS) and multiple gradient (MG). For DD, PD and WS arrays a progression of eight different datasets are considered, by increasing the number of current dipoles but obtaining approximately the same amount of measures, and so increasing the investigation time. For MG array a progression of six datasets is obtained by increasing the current dipoles and so the lateral coverage. The goal is to study how this affect the resolution and the reliability of the tomographic inversion, particularly in presence of buried structures. Both noise-free and noisy data have been calculated and inverted. The results are compared using quality parameters of the reliability of the inversion. These are calculated for each cell of the first inverse model, and subsequently a mean value is obtained for the entire

Tab. 1 - Parameters used for each data set.

Array	Pattern	parameters
DD PD WS	1	$a_{max} = 1; n_{max} = 35$
	2	$a_{max} = 2; n_{max} = 17$
	3	$a_{max} = 3; n_{max} = 11$
	4	$a_{max} = 4; n_{max} = 8$
	5	$a_{max} = 5; n_{max} = 6$
	6	$a_{max} = 6; n_{max} = 5$
	7	$a_{max} = 7; n_{max} = 4$
	8	$a_{max} = 8; n_{max} = 3$
MG	1	$e = 1-8; c = 1$
	2	$e = 1-8; c = 2$
	3	$e = 1-8; c = 3$
	4	$e = 1-8; c = 4$
	5	$e = 1-8; c = 5$
	6	$e = 1-8; c = 6$

section or for areas coinciding with the abnormal structures. The sequences are also tested with field data to assess the validity of the theoretical results.

**Choice of the acquisition patterns.** Recently many authors have dealt the optimization of acquisition sequences of data, which can be formed by different arrays, dipolar lengths and distances, in order to seek the optimal sequences that ensure a realistic imaging, without the need for an excessive number of measurements. Stummer *et al.* (2004) have experienced an accurate approach that uses sensitivity distributions to calculate an estimate of the resolution matrix of the model. The goal is therefore to seek the optimal sequences that ensure a realistic imaging with high resilience of the subsoil, without the need for an excessive number of measurements that would compromise the economic viability of the survey.

Several simulations on 2D model have been made, using the software RES2DMOD (Loke, 2014), to study the changes in resolution and reliability when the acquisition pattern changes. The choice of the acquisition sequences is based on the variation of the ratio between the maximum dipole length  $a_{max}$  and the maximum dipole order  $n_{max}$ , trying to keep a similar amount of number of measures. Data sets of apparent resistivity values have been calculated using the *multiple gradient* (MG) array (Dahlin and Zhou, 2004; 2006) and the three most common arrays for multichannel measurements: *dipole-dipole* (DD), *pole-dipole* (PD) and *Wenner-Schlumberger* (WS). For DD, PD and WS arrays sequences retain approximately the same depth of investigation and a not so different total amount of data. For these arrays 8 data sets were generated in which the maximum potential spacing  $a$  increases and the maximum  $n$  factor decreases (Tab. 1), so increasing the number of current dipoles and therefore the time of acquisition (Tab. 2).

Tab. 2 - Number of measures and current dipoles for each data set.

Pattern	Nr. of measures				Nr. of current dipoles			
	DD	PD	WS	MG	DD	PD	WS	MG
1	1820	1855	1225	533	69	69	1225	36
2	1887	1938	1479	904	135	69	1479	65
3	1848	1914	1518	1227	198	69	1347	93
4	1784	1864	1504	1596	258	69	1384	122
5	1665	1755	1440	1921	315	69	1320	150
6	1635	1740	1425	2292	369	69	1251	179
7	1512	1624	1344	-	420	69	1082	-
8	1296	1404	1188	.	468	69	1043	-

For the multiple gradient array (MG) we choose particular sequences, in order to minimize the number of current dipoles (and therefore time), but maintaining a resolution comparable to those of the other arrays (Fiandaca *et al.*, 2005). The sequences were determined by subdividing the electrode layout  $AB_{max}$  into equal parts and by locating the current electrodes at the ends of each part:  $AB=AB_{max}/e$ ,  $e$  varying from 1 to 8 (Martorana *et al.*, 2009). However, this sequence does not ensure a uniform lateral coverage comparable to the classical sequences in which all the electrodes are in turn used as the current electrodes. To overcome this drawback, the dipoles of the current are increased by dividing the forwarding step of the current dipole by a coverage factor  $c$ . Six different sequences were considered, with  $c$  ranging from 1 to 6 (Tab. 1).

**Forward modelling and inversion.** The adopted resistivity models are similar to those used by Szalai *et al.* (2013). Model #1 shows ten resistive prisms (100  $\Omega$ m) of the same square section (2m\*2m), equally spaced and a background of 10  $\Omega$ m. The depth of the center of the first prism to the left is 2m and the following prisms are gradually deeper 25 cm until a maximum

depth of 3.75 m. Model #2 has the same patterns (fig. 1 a), but the prisms are conductive (10 Ωm) and the background is resistive (100 Ωm). Models #3 and #4 show respectively a resistive and a conductive buried vertical dyke. 72 electrodes were considered; with a minimum spacing of 1 m. Forward problem was solved using RES2DMOD software.

A fundamental role in the simulation process is the simulation of noise on the predicted data. However, in practice the methods of array optimization to maximize the resolution of tomographic image should also take into account the effect of data errors on the resolution obtained. However, most of the optimization techniques used so far have not sufficiently taken into account the effects of noise on apparent resistivity data.

Generally, in the ERT inverse problem the problem due to error on data caused by improper positioning of the electrodes is not sufficiently considered. This error may be higher in steep or heavily vegetated areas and it generates an incorrect estimate of the geometric factor. To reduce the effect of this type of error on the resulting electrical tomography it is possible to select datasets that include arrays with relatively low geometric factors and therefore less sensitive to position errors (Wilkinson *et al.*, 2008). The study of the influence of errors on the resolution of the inverse model and especially on its ability to retrieve correct information of the subsurface is important to understand how the performance vary from a few simple parameters such as the total number of measurements of the data set and the distribution of the geometric factor values.

For this purpose, noise was added by simulating errors both on electrode spacing and on potential, rather than consider the typical random noise. A standard deviation of 3% was considered to add noise to the electrode positions. The potential errors were generated by simulating the trend showed by Zhou and Dahlin (2003). We used the formula:

$$noisy\ data = U(1+R*\beta/100),$$

where  $U$  is the potential reading,  $R$  is a random number and  $\beta = (c_1/U)^{c_2}$  denotes absolute relative errors of the potential observations (Dahlin and Zhou, 2004). From observed data we considered  $c_1 = 10^4$  and  $c_2 = 0.4$  in order to obtain an average error on resistivity data of approximately 5%.

Inversion was performed using the EarthImager 2D Software (Advanced Geosciences, 2009), considering the same optimized parameter settings, in order to compare the results obtained from the different data sets of noise-free data as well as of noisy and field data.

The evaluation of the results was performed by a quantitative analysis of some parameters that could define the ability of the inverse model to approach to the real situation. Generally, the main parameter used to evaluate the reliability of an inversion is the *RMS error*, which quantifies the misfit between the observed and predicted data. However, simulated models gives the possibility to define quantitative parameters that describe the discrepancy between the tomographic model and the original one. The inversion program uses an arrangement of cells according to the pseudo-section and to the sensitivity function. This is obviously different from the arrangement of the original model. For this reason, in order to evaluate the resistivity mismatch between inverted and original models, a refined mesh was designed, obtained from the superposition of the boundaries of all the blocks of the inverted and the original models.

**Parameters to estimate the reliability of inversion.** For the  $j$ -th refined mesh the *model misfit* is defined as

$$R_j = \frac{|\rho_{j,inv} - \rho_{j,mod}|}{\rho_{j,mod}} \%$$

where  $\rho_{j,inv}$  and  $\rho_{j,mod}$  are the resistivity in the inverse model and in the original model.

A useful parameter to evaluate the model resolution is the *relative model sensitivity*, that can be calculated by expressions for the elements of the Jacobian matrix for the direct problem

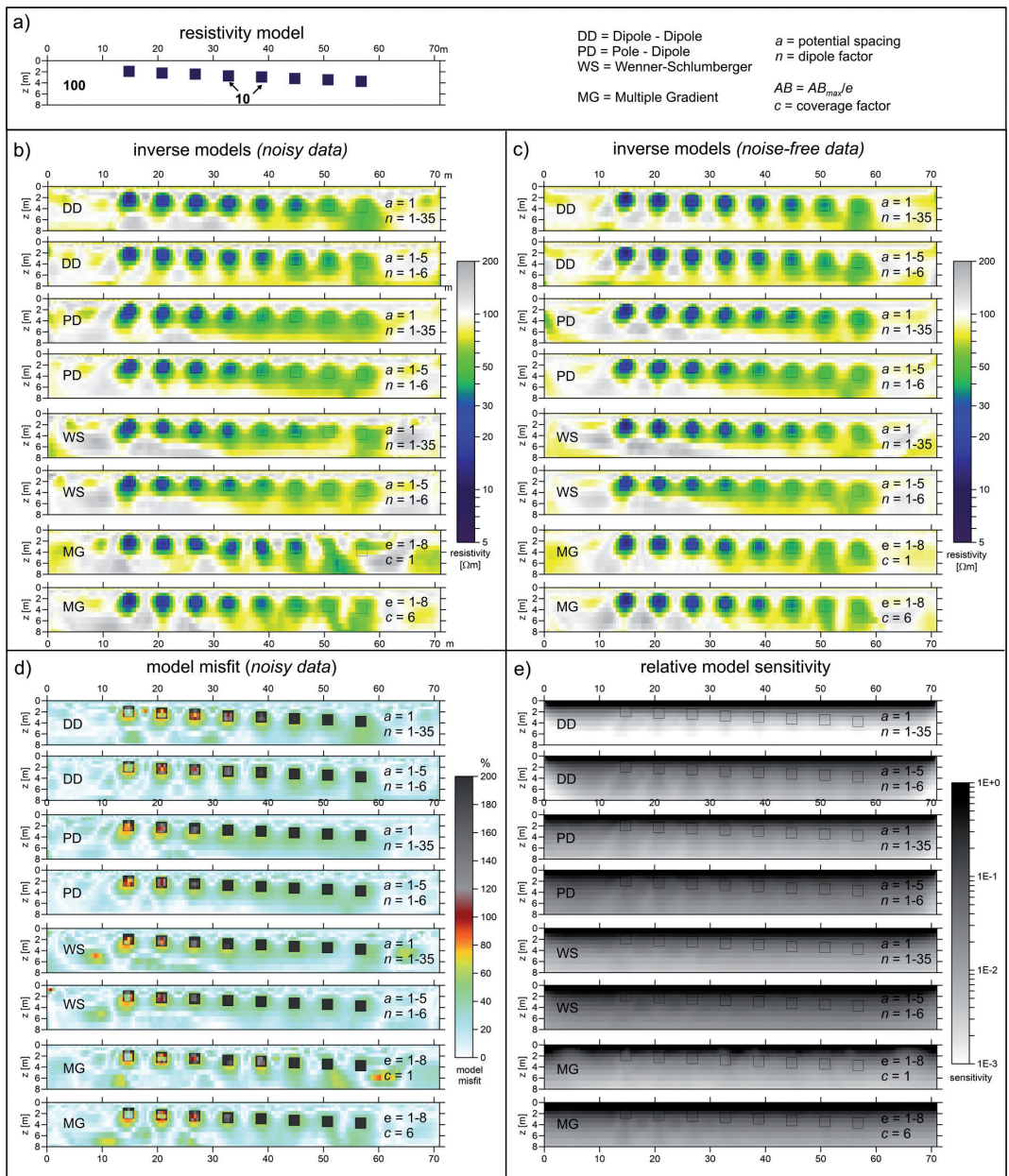


Fig. 1 – Results of the inversion of some data sets starting from the synthetic model shown in (a); b) inverse models for noisy data sets; c) inverse models for noise-free data sets; d) images of the model misfit; e) images of the relative model sensitivity.

(Hennig and Weller 2005). Here we consider the main diagonal of  $\mathbf{J}^T\mathbf{J}$ , where  $\mathbf{J}$  is Jacobian matrix of the inverse model. The inversion process will better resolve model blocks with a higher relative model sensitivity. To obtain inclusive parameters that express the overall effectiveness and resolution of each data set, for each model we calculated the *average model misfit* and the *average sensitivity*. For models #1 and #2 (resistive and conductive targets) we also calculated the average model misfit and the average sensitivity, evaluated on windows of the same size as each resistive square anomaly.

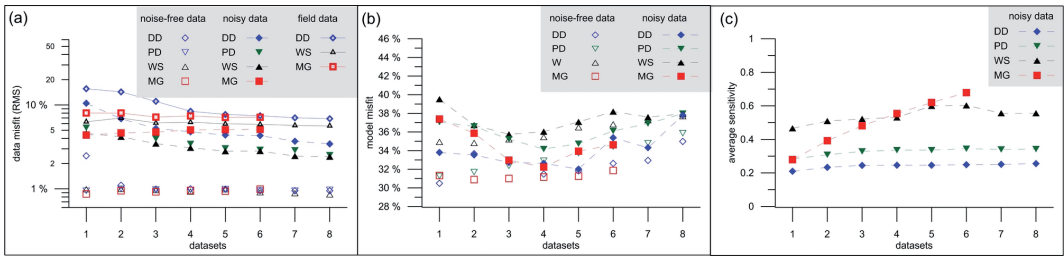


Fig. 2 – Parameters that express the quality of inversions depending on the data set number: a) data misfit (RMS error %); b) average model misfit; c) average relative model sensitivity.

**Results.** The results of the inversions were compared between themselves and with those obtained from a test on field data carried out in Piana degli Albanesi in an area characterized by high heterogeneity. For the inversion of both simulated and experimental data were used the same algorithms and parameters.

Results of model #2 are shown as example (Fig. 1), which highlight how the resolution strongly depends on the choice of the data set and how the information recovery decreases with the target depth. Results obtained by noisy data (Fig. 1b) are poorer of information than noise-free data (Fig. 1a) but the gap between results decreases considering more complex and time requiring data sets. In these examples the comparison is made between data set 1 ( $a_{max}=1$ ;  $n_{max}=35$ ) and data set 5 ( $a_{max}=5$ ;  $n_{max}=6$ ) for DD, PD and WS, and between data set 1 ( $e=1-8$ ;  $c=1$ ) and data set 6 ( $e=1-8$ ;  $c=6$ ) for MG. Generally, as the data set number increases, the model misfit (Fig. 1 d) decreases in correspondence of the targets and overall the shapes are better resolved and artifacts are more limited. This can be explained by the comparison of the correspondent images of relative model sensitivity that show a more uniform distribution and higher values at greater depths (Fig. 1e).

The comparison of the data misfit of inversions for each data set of DD, PD, WS and MG arrays obviously shows sensibly higher values for noisy and field data than for noise-free data (Fig. 2a). Moreover, there is a similar trend for both field and noisy data. As the complexity and time required of data sets increases (data set number increasing from 1 to 8) the RMS% decreases. For DD it starts from high values and decreases rapidly, for WS and PD it starts from lower values and decreases more slowly, instead practically it does not vary for MG. The average model misfit (Fig. 2b) is highly depending on resistivity values of the subsoil. Generally, the trends show a decreasing parameter as data set number increases (very strong for the MG) that probably is related to the increase of number of current dipoles. These trends generally reverse after the data set n. 5 or 6. The average sensitivity (Fig. 2c) is few influenced by the presence of noise and its trend is very similar between noisy and field data because probably the only difference is due to the different resistivity trend in the subsoil. WS data sets show the highest values and DD ones the lowest. In every array, sensitivity increases with data set number, very quickly for MG.

For models #1 and #2 (resistive and conductive targets) we also estimated the trends of the normalized values of the average sensitivity, on windows of the same size of the target, as a function of the depth of the target. Results for model #2 are shown in Fig. 3. Colored zones show the areas of variation of the parameter for each array, from the lower data set number (dotted line) to the highest one (solid line). Trends show the exponential decrease of the sensitivity values as the target depth increases. We note that the slope of the curves decreases considering more complex data sets. This means that not only these latter have a trend for higher sensitivity in every area of the section, but also that they resolve better the deeper cells of the models. Ultimately, the best sensitivity is obtained for WS array, and the worst for DD array.

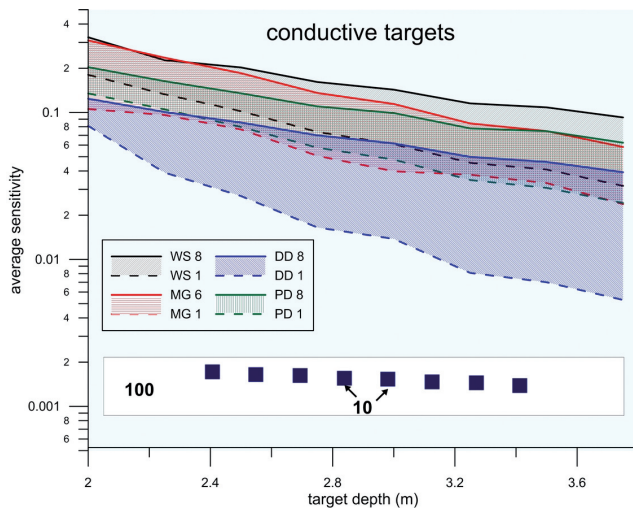


Fig. 3 – Trend of the average relative model sensitivity as a function of the depth of the target. Colored zones show the areas of variation of the parameter for each array, from the lower data.

**Conclusions.** The results show that the reliability of the inverse models depends significantly on the data acquisition pattern. The decrease of sensitivity with depth is lower for those acquisition patterns characterized by a high ratio  $a_{max}/n_{max}$  allowing to resolve deeper targets. Regarding the array type used, the information recovery and the resolution are overall better for WS and worse for DD. Anyway, they can be improved by considering data set with higher numbers of current dipoles but at the expense of the measurement times. In fact, the decrease in sensitivity with increasing depth is less evident for those patterns characterized by a high ratio  $a_{max}/n_{max}$ , that can consequently more easily allow to identify deeper targets. In this context, the MG array is often preferable because it provides comparable results, with a number of current dipoles substantially lower and, consequently a very short survey time.

Tests on field data have allowed a comparison, although limited to the evaluation of the data misfit RMS%. These show higher values than on synthetic data, probably caused by a higher level of noise on the field data. However, the overall trend of the RMS% error as the pattern number is very similar to that shown by synthetic data. For a confirmation of this hypothesis, further simulations will therefore have to be performed with different noise levels on data.

**References**

Advanced Geosciences, Inc.; 2009: *Instruction manual for EarthImager 2D, Version 2.4.0, Resistivity and IP inversion software*, 139 pp.

Dahlin T. and Loke M.H.; 1998: *Resolution of 2D Wenner resistivity imaging as assessed by numerical modeling*, Journal of Applied Geophysics, **38**, 237-249.

Dahlin T. and Zhou B.; 2004: *A numerical comparison of 2D resistivity imaging with ten electrode arrays*. Geophysical Prospecting, **52** (5), 379-398.

Dahlin T. and Zhou B.; 2006: *Multiple-gradient array measurements for multichannel 2D resistivity imaging*. Near Surface Geophysics, **4** (2), 113-123.

Fiandaca G., Martorana R., Cosentino P.L.; 2005: *Use of the linear grid array in 2D resistivity tomography*. Near Surface 2005, A023

Hennig T. and Weller A.; 2005. *Two dimensional object orientated focusing of multi-electrode geoelectrical measurements*. Proceedings of the 11<sup>th</sup> meeting of the EAGE Near Surface Geophysics Conference, Palermo, Italy.

Loke, M.H.; 2014: *RES2DMOD ver. 3.01. Rapid 2D resistivity forward modelling using the finite-difference and finite-element methods*. www.geotomosoft.com.

Martorana R., Fiandaca G., Casas Ponsati A. and Cosentino P.L.; 2009: *Comparative tests on different multi-electrode arrays using models in near-surface geophysics*. Journal of Geophysics and Engineering, **6** (1), 1-20.

Olayinka A.I. and Yaramanci U.; 2000: *Use of block inversion in the 2-D interpretation of apparent resistivity data and its comparison with smooth inversion*. Journal of Applied Geophysics, **45**, 63-82.

Oldenburg D.W. and Li. Y.; 1999: *Estimating depth of investigation in dc resistivity and IP surveys*. Geophysics. **64**, 403-416.

- Park S.K. and Van G.P.; 1991: Inversion of pole-pole data for 3-D resistivity structures beneath arrays of electrodes. *Geophysics*, **56**, 951-960.
- Stummer P., Maurer H. and Green A.G.; 2004: *Experimental design: Electrical resistivity data sets that provide optimum subsurface information*. *Geophysics*, **69** (1), 120-139.
- Szalai S., Koppán A., Szokoli K., and Szarka L.; 2013: *Goelectric imaging properties of traditional arrays and of the optimized Stummer configuration*. *Near Surface Geophysics*, **11** (1), 51-62.
- Van G.P., Park S.K. and Hamilton P.; 1991: *Monitoring leaks from storage ponds using resistivity methods*. *Geophysics*, **56**, 1267-70.
- Wilkinson P.B., Chambers J.E., Lelliott M., Wealthall G.P., and Ogilvy R.D.; 2008: *Extreme sensitivity of crosshole electrical resistivity tomography measurements to geometric errors*. *Geophysical Journal International*, **173** (1), 49-62.
- Wilkinson P.B., Loke M.H., Meldrum P.I., Chambers J.E., Kuras O., Gunn D.A., and Ogilvy R.D.; 2012: *Practical aspects of applied optimized survey design for electrical resistivity tomography*. *Geophysical Journal International*, **189** (1), 428-440.
- Zhou B., and Dahlin T.; 2003: *Properties and effects of measurement errors on 2D resistivity imaging*. *Near Surface Geophysics*. **1** (3), 105-117.

## GROUND PENETRATING RADAR APPLICATIONS FOR ROADS AND AIRPORT PAVEMENTS INVESTIGATIONS

A. Mocnik<sup>1,2</sup>, M. Dossi<sup>1</sup>, E. Forte<sup>1,2</sup>, R. Zambrini<sup>2</sup>, A. Zamariolo<sup>2</sup>, M. Pipan<sup>1,2</sup>

<sup>1</sup> Department of Mathematics and Geosciences, University of Trieste, Italy

<sup>2</sup> Esplora srl, academic spin-off of the University of Trieste, Italy

**Introduction.** In this work we present three examples of application of Ground Penetrating Radar (GPR) method for pavement thickness evaluation and stratigraphic analysis using R.Ex. (Road Explorer), a new system developed by Esplora srl, an academic spin-off of the University of Trieste, in collaboration with the geophysical group of the Department of Mathematics and Geosciences of the same University.

The implementation of this GPR system aims to obtain information that are crucial for the good management and planning of road maintenance, which is fundamental to prevent and minimize the risks to which light and heavy vehicles may be exposed during transit, and ensure the maximum safety for passengers. Nowadays, for testing of pavement of new road infrastructures, direct measurements such as drill cores are performed. Usually drillings reach a depth of about one meter from the road surface and its lateral spacing is variable, basing on the importance of the road and its constructive characteristics, but typically it exceeds some hundreds of meters.

These surveys are primarily aimed at:

- evaluating the thicknesses and local thickness variations;
- collecting all the elements for the definition of the mechanical properties of the road pavement;
- identifying voids, fractures or local defects;
- evaluating the correspondence between the design specifications and the actual work.

Similar surveys are also carried out even after the realization of significant works of maintenance of existing infrastructures or where particular problems have been reported on specific segments of a road infrastructure.

In recent years, such direct investigations, which are necessarily destructive and require the partial or total road block, have been joined with other surveys globally defined as “indirect” that let to obtain information about the subsurface without coring, being not-invasive and not-destructive methods. These methods are used for the extraction of elastic properties of the substrate and aggregates layers as Falling Weight Deflectometer - FWD (Briggs *et al.*, 1991),

and for the water content estimation by means of Time Domain Reflectometry-TDR techniques (Topp *et al.*, 1980). These approaches, while being generally very precise and accurate, provide just punctual information and are also very time consuming and quite expensive.

GPR can provide a continuous survey of a road segment: this is a very important factor since both the moisture content and thickness may have strong lateral variations. Moreover, the GPR is a fast and quite cheap technique.

Applications of GPR on road surfaces can be divided into four main categories: 1- surveys for planning of new roads; 2- investigations for the renovation of existing roads; 3- quality control or security investigations during road projects; 4- targeted surveys to the management of the road surface (Saarenketo, 2009).

In recent years, various applications have been tested for different purposes, ranging from thickness mapping to quality controls, with the development of techniques to achieve an accuracy of 2.5 mm (Maser *et al.*, 2003) and absolute errors of 2.9% by comparing direct data and radar profiles (Al Qadi *et al.*, 2003). Moreover, examples of detection of discontinuities, defects and studies of infiltration are reported (Saarenketo and Scullion, 2000, Grote *et al.*, 2005), as well as measurements aimed to the moisture content and the density estimation and to the quantitative characterization of the materials forming the pavements (Benedetto and Pensa, 2007; Benedetto, 2010; Plati and Loizos, 2013; Shangguan *et al.*, 2014).

In surveys performed on infrastructures with high traffic, the major advantages of GPR surveys are the continuous profiling, as well as the speed and accuracy. Such technique continues to be the only one that can provide meaningful subsurface information at an acquisition speed close to the highway velocity limits. The development of GPR application in infrastructures open to the traffic started in the seventies of last century with systems mounted or dragged by a van; from 1980s in Finland the method become the most popular and used as a routine surveys tool in various road applications (Saarenketo, 1992). Then, it soon developed especially in north Europe and nord America and actually it is a worldwide used technique for different purposes of the roads monitoring.

The GPR hardware is generally mounted on a survey van and made up of a control unit, cables, a positioning System (GPS); air or ground coupled antennas may be mounted on the van or dragged. The instrument is triggered by both constant time intervals or electro-mechanic odometers.

The system can also record simultaneously data using different frequencies. This aspect is very important because the higher frequencies allow to reach higher resolution levels but within limited depths, while antennas transmitting at lower frequencies penetrate deeper even if the degree of detail is reduced.

We describe the method for GPR data acquisition by using the R.Ex. system showing applications for: 1) the analysis of the thickness and the shallow stratigraphy in an airport transit area; 2) thickness evaluation in a newly constructed aircraft apron; 3) thickness lateral changes on recently re-paved roads.

**Method.** Esplora srl and the geophysical group of the Department of Mathematics and Geosciences of the University of Trieste developed a prototype of a GPR equipment support for roads investigation, that has been named R.Ex.-Road Explorer (Fig. 1).

It is composed by a tow entirely made in fiberglass in order to avoid electromagnetic (EM) noises caused by metal supports; it includes special anti-shock boxes to support two ground coupled GPR antennas with different frequencies. The wheels of the tow contain an encoder for the trace positioning, connected to the central unit. The latter is positioned inside the van that drag the R.Ex. system; depending on the conditions of wear and alteration of the surface, the van can reach speeds up to 50-60 km/h, without altering the GPR records.

A Malå ProEx GPR is used to transmit simultaneously two EM waves with different frequencies by connecting two antennas to the central unit. All the antennas are shielded in order to avoid or limit spurious signals. One of them is in the frequency range 800-500 MHz,



Fig. 1 – R.Ex. GPR system and its components connected to a van during a survey.

while the other in the 1.6-2.3 GHz one. In the tow R.Ex., the two antennas are aligned with the truck: at the head the medium frequency antenna is positioned, while on the back the higher frequency one, distant from each other 0.61 m. Depending on the objectives of the investigations and the depth of the targets, we tested that the 2.3 GHz with the 800 MHz couple is used for very high resolution investigations and shallow objectives (determination of the centimetric thickness of aggregate layers), reaching a maximum depth of about 30 cm for the 2.3 GHz and 1m for the 800 MHz. The combination of 1.6 GHz with 500 MHz antennas is generally used to detect structures reaching a depth up to 2 m, like the base and subgrade strata for the 500 MHz antenna, and about 50 cm for the antenna of 1.6 GHz. This is not a standard rule since, as for any practical GPR application, the performance must be tested in situ in order to verify the actual penetration depth and resolution.

One clear advantage of the ground coupled antennas system is the better signal penetration compared with that of the air-coupled ones; another advantage is the better focusing respect air-coupled antennas, that allows an improved pavement cracks or cables detection (Saarenketo, 2009). Laboratory analysis performed on asphalts cores during the R.Ex. system implementation, let us to determine the maximum elevation of the antennas from the ground to obtain the best tradeoff between GPR performances and logistic effectiveness.

The accurate positioning of the GPR data is the most important factor during the data collection phase. Data with incorrect spatial referencing are worthless to the customer and damaging for engineering applications. Positioning can be done using an encoder, that controls the trace interval, or/and using GPS devices; in addition markers at known reference points can be fixed during the data acquisition. The R.Ex. system allows a combination of the previous methods allowing a better control and location of the GPR traces. We install a RTK mode GPS with centimetric precision connected with the GPR control unit, so for each trace of both antennas, we have the coordinates(X, Y and Z). This procedure allows us to geographically locate some defects of the roads, locate specific points of relevant thickness variations, and to associate the position of a drill core to a specific trace, which is useful and necessary for an accurate calibration of the EM velocities.

**Processing and data production.** The processing sequence is aimed at enhance the signal to noise ratio by reducing ringing and low frequency components (DC), as well as the high frequency ones, after the determination of the actual time zero (drift removal).

In the following case histories we adopted a standard processing sequence encompassing: background removal, high-pass filtering, true amplitude recovery and depth conversion. A static correction has not been applied due to the sub-horizontal topographic surface and the sub parallel nature of the imaged horizons.

In relation to the evaluation of the reliability and accuracy of the obtained results, one of the most critical points is the degree of confidence of the thickness values of the different

pavement layers (wear, binder, base). Regarding this point the demand of end-users is a sub centimeter precision. In order to approach such precision is necessary: a) to increase the accuracy in determining the EM wave velocity in the subsurface that allows to convert in depth data originally acquired as a function of traveltime; b) increase the precision of picking the first sample relative to a actual reflection (first break).

The EM wave velocity can be estimated on the basis of the GPR data with different levels of precision (Jol, 2009), but an intrinsic error of the order of 5-10% (Forte *et al.*, 2014) is expected.

For the presented work we used a traditional method for determining the dielectric value of pavement by back-calculating the velocity values by using the drill core data.

*CASE-1: airport pavements.* We tested R.Ex. system on two different sites of an airport pavement in order to: 1) give information of the stratigraphic sequence up to about 2 m of depth from the surface and recognize possible failures or subsidences structures, and lateral variations of the geotechnical properties (Test Site1); 2) verify the thickness of new constructed FRC (Fiber Reinforced Concrete) plates (Test Site 2).

The Test Site 1 is an airport transit area where we used the combination of 500 MHz and 1.6 GHz antennas in order to achieve the better tradeoff between resolution and investigation. The depth conversion has been obtained by diffraction hyperbola analysis and by the available drill cores and continuous penetrometric surveys. In Fig. 2a an example of profile is shown. The lateral contrast between the concrete plates (left of profile) and the bituminous aggregate (right of profile) is clear: in yellow we marked the base of concrete and in green the base of the asphalt. The depth of each layer has been stored in a dedicated database implementing a GIS project, which allows to produce depth maps that can give a global overview of the stratigraphic variations of all the imaged layers. In particular, it was observed that the sedimentary contact between granular sub base and clay-silty levels (light blue) deeps below the concrete reaching a depth close to 2.5 m and it disappears in the central sector of longitudinal profiles (map in Fig. 2b).

The Test Site 2 is a new aircraft apron where we used the 1.6 GHz and 800 MHz antennas couple. We collected longitudinal transects to cross all the length of the aircraft apron for a maximum length of 160 m. The exact location of already drilled cores on some selected plates was available before geophysical data collection and so we designed the GPR survey crossing all the drill locations for a more constrain data calibration.

The GPR analysis evidenced a very strong EM attenuation. This let more difficult and delicate the horizon picking phase aimed at the recognition of the base of the concrete, evidenced by a weak reflector only on the 1.6 GHz data (Fig. 2c). The low reflectivity has been inferred to the high metallic mineral compound within the concrete mixture, as reported by the client.

For the depth conversion, we used a variable lateral velocity field, due to the variation of thickness measured by the cores (range from 32.9 to 37 cm) and because of the variability of reflected traveltimes of the horizons. Thus, maintaining the constraints in correspondence of the cores (generally 2/3 cores for each profile) we calculated the gradient of the resulted velocity value between them.

The intrinsic error of each picked measure is, from the statistical point of view, equal to the  $\pm$  the sampling interval. Considering the frequency of 1.6 GHz, the fixed time sampling interval equal to 0.096 ns and the measured velocity values close to 15 cm/ns, we have assumed that the picked horizon lies in a range of  $\pm 0.0072$  m from the inferred depth.

*CASE-2 highway survey.* 149 Km of recently paved roads were surveyed, recording multi-frequency (800 – 2300 MHz) GPR profiles. We recorded a total of 351 km of data, composed by the acquisition along each road lane in the two track directions.

The aim of these surveys was to measure the thickness of the aggregate layers and the depth of the subgrade, imaging and locating any possible lateral variation of thickness and evidencing the main stratigraphic features.

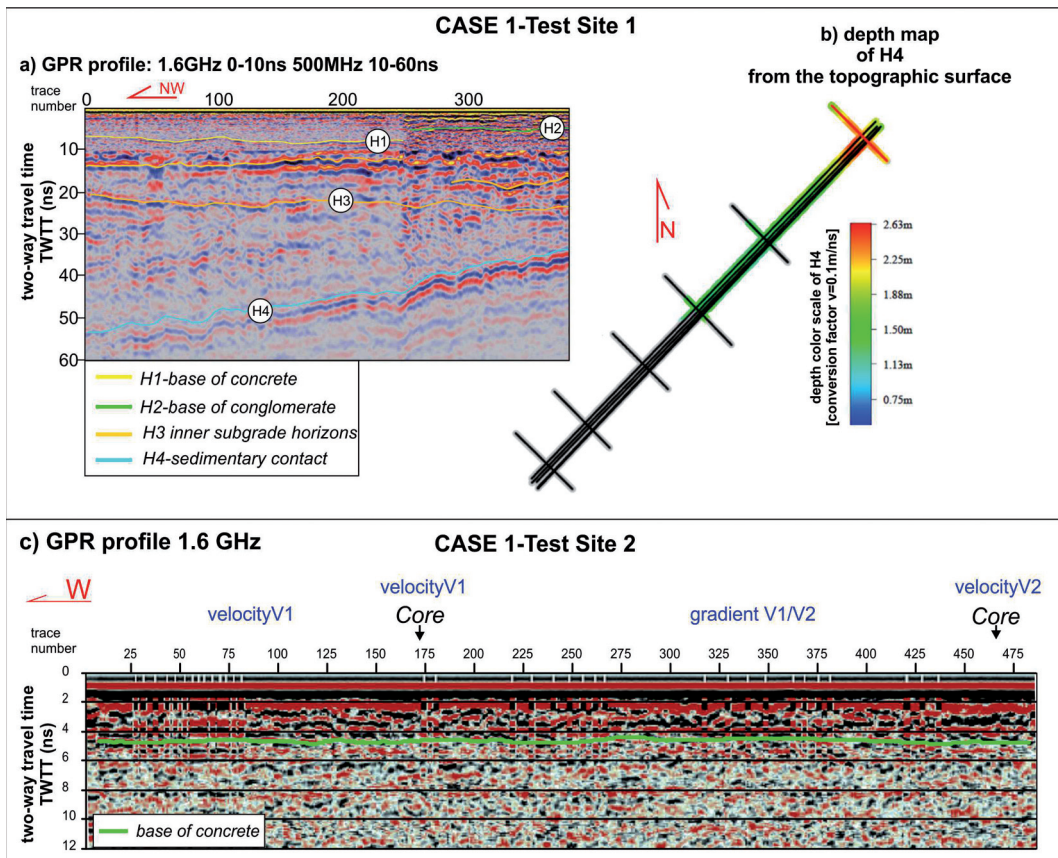


Fig. 2 – example of results from CASE 1 applications of R.Ex. system; a) example of GPR profile acquired in Test Site 1 with 1.6 GHz data till 10ns and 500 MHz data from 10 to 60 ns. b) depth map of sedimentary contact horizon H4 of Test Site 1 where the layer deeps toward north; c) example of GPR profile acquired in Test site 2 where in green color is depicted the weak reflection of the base of the concrete plates.

The GPR survey was joined by FWD performed on the same roads crossed by R.Ex.

Due to the objective of the survey, which was not dedicated to fractures or defects location, we used an horizontal trace spacing of 1m and we fixed a mean acquisition speed of 50 km/h.

In Fig. 3 we show an example; this profile is peculiar because it evidences strong lateral variations of thickness of the aggregates layers. This trend has been also confirmed by the sample cores executed by a geotechnical company, which have been used for velocity calibrations. Along the 2.3 GHz profiles we interpreted the trend of the conglomerate layers (binder and base interfaces, in green and yellow) while along the 800 MHz data we interpreted the horizons associated to the old pavement (in pink) and subgrade (in light blue). Till about trace 2000 from the south, the base of conglomerates lies at an almost constant depth; prosecuting toward the north, the thickness increases and is based on the old pavement not evident southward; the subgrade layer is also irregular. This different behavior from north to south has been observed even by the FWD data response, associated to strong inhomogeneities of the road embankment.

Generally, for this survey, GPR profiles depth conversion has been executed using a vertical variable velocity field: we used a constant velocity for the conglomerate layers derived by the available drill cores, and different velocity values for the subgrade. The latter have been calculated for each road lane based on the building project specifications.

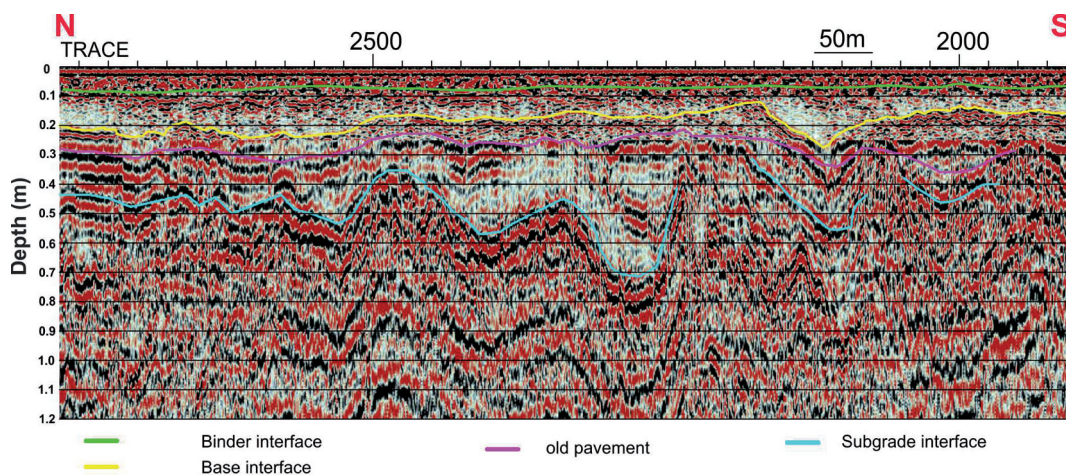


Fig. 3 – Portion of GPR profile of CASE-2 composed by 2.3 GHz till 25 cm from the surface and 800 MHz from 25 cm to 1.2 m of depth; the lateral variation of thickness of the aggregate layers and of subgrade is evident.

**Conclusions.** The R.Ex. system constitutes an acquisition device aimed at obtaining a huge amount of high quality GPR data in a relatively short time. Furthermore, the integration and joining of multi-frequency antennas is essential to obtain high resolution in the shallower portion of paved roads and detailed information down to 2-3 m below the topographic surface.

The methodology described in this work allows to achieve the information that are important for a traffic infrastructure company before maintenance operations planning and after new roads constructions. In Case-1-Test site-1 the interpretation of inhomogeneities of the subgrade let to locate the critical failure points and drive for future maintenance activities; Case-1-Test site 2 and Case 2 report the surveys after pavement and construction works, that has been used as a sort of verification of the layers thicknesses and its analyses between the cores.

Future developments have to be addressed to the improvement in the precision (and the speed) of picking horizons. In this regard, a picking method was recently implemented and tested in different fields of application (Forte *et al.*, 2013; Dossi *et al.*, 2015a) including pavements (Dossi *et al.*, 2015b, 2015c). The obtained results are encouraging allowing to achieve a faster and more accurate picking, diminishing at the same time the subjectivity level of the interpretation.

**Acknowledgments.** We gratefully acknowledge Pavenco srl (Eng. F. Picariello), Emaprice srl (Dr. Eng. M. Grippo Belfi), Elletipi srl (Eng. C. Bratti), Acmar scpa (Eng. M. Lenzi) for the availability of using data for research purpose. All the dataset shown have been acquired by Esplora srl.

## References

- Al-Qadi I., Lahouar S. And Loulizi A.;2003: *Successfull application of GPR for Quality Assurance/Quality control of new pavements*. Paper No. 03-3512, proceedings of Transportation Research Board: 82nd Annual Meeting, January 12-16, 2003 Washington, D.C.
- Benedetto, A.; 2010: *Water content evaluation in unsaturated soil using GPR signal analysis in the frequency domain*. Journal of Applied Geophysics, **71** (1), 26–35.
- Benedetto A. and Pensa S.; 2007: *Indirect diagnosis of pavements structural damages using surface GPR reflection techniques*. Journal of Applied Geophysics, 62, 107-123.
- Briggs R.C., Scullion T., and Maser K.; 1991: *Asphalt thickness variation an effect of backcalculation*. 2<sup>nd</sup> International Conference on Backcalculation. Nashville, USA.
- Dossi M., Forte E., Pipan M.; 2015a: *Automated reflection picking and polarity assessment through attribute analysis: theory and application to synthetic and real GPR data*. Geophysics, **80** (5), H23-H35
- Dossi M., Forte E. and Pipan M.; 2015b: *Auto-picking and phase assessment by means of attribute analysis applied to GPR pavement inspection*. Proceedings of IWAGPR 2015, 3-7 July 2015, Florence, Italy, in press.

- Dossi M., Forte E., Pipan M.; 2015c: *Application of attribute-based automated picking to GPR and seismic surveys*. Proceedings of the 2015 NGGTS, Trieste, 17-19 November 2015.
- Forte E., Dossi M., Colucci R.R., Pipan M.; 2013: *A new fast methodology to estimate the density of frozen materials by means of common offset GPR data*. Special issue of the J. of Applied Geophysics: Forward and Inverse Problems in GPR Research, **99**, 135-145.
- Forte E., Dossi M., Pipan M. and Colucci R.R.; 2014; *Velocity analysis from Common Offset GPR data inversion: theory and application to synthetic and real data*. Geophysical Journal International, **197**, Issue 3, 1471-1483.
- Grote K., Hubbard S., Harvey J. And Rubin Y.; 2005, *Evaluation of infiltration in layered pavements using surface GPR reflection techniques*. Journal of Applied Geophysics, **57**, 129-153.
- Jol, H.M. (ed.); 2009: *Ground Penetrating Radar: Theory and Applications*, Elsevier Science, **524**, pp.
- Maser, K.R., Holland, T.J., Roberts, R. and Popovics, J.; 2003: *Technology for quality assurance for new pavement thickness*. Proceedings of International Symposium on Non-Destructive Testing in Civil Engineering (NDT-CE), September 16–19, 2003, Berlin, Germany.
- Plati C. and Loizos A.; 2013: *Estimation of in-situ density and moisture content in HMA pavements based on GPR trace reflection amplitude using different frequencies*. Journal of Applied Geophysics, **97**, 3-10.
- Saarenketo T.; 1992: *Ground penetrating Radar Applications in road design and Construction in Finnish Lapland*. Geological Survey of Finland. Special Paper 15, 161-167.
- Saarenketo, T.; 2009: *NDT Transportation. Chapter 13 in text book - Ground Penetrating Radar: Theory and Applications*. Ed- Harry M. Jol. Publisher Elsevier, 524 p.
- Saarenketo, T., Scullion, T.; 2000: *Road evaluation with ground penetrating radar*. Journal of Applied Geophysics, **43**, 119–138.
- Shangguan P., Al-Qadi I and Lahouar S.; 2014; *Pattern recognition for density estimation of asphalt pavement during compaction: a simulation study*. Journal of Applied Geophysics, **107**, 8-15.
- Topp G.C., Davis J.L., Annan A.P.; 1980: *Electromagnetic determination of soil water content: measurements in coaxial transmission lines*. Water Resources Research, **16**, 574–582.

## NON-INVASIVE PROSPECTING IN THE OLD TOWN CENTRE OF MESAGNE (BRINDISI, SOUTHERN ITALY)

G. Leucci, L. De Giorgi, L. Matera, R. Persico

*Institute for Archaeological and Monumental Heritage IBAM-CNR, Lecce, Italy*

**Introduction.** Geophysical methods play an important role within many important applications. In particular, it is an important noninvasive technique widely exploited in the contexts of discovery and/or preservation of cultural heritage (Giannotta *et al.*, 2015; Goodman and Piro, 2013; Leucci *et al.*, 2011; Negri *et al.*, 2008; Pieraccini *et al.*, 2006; Matera, 2015) and civil engineering (Cataldo *et al.*, 2014; Piscitelli *et al.*, 2007), that are the most relevant for this contribution. In some cases, the two kind applications can converge together, as e.g. in the case of the investigation of columns (Leucci *et al.*, 2007; Masini *et al.*, 2010). Also in this paper we present a case history where these two kind of interests are joined together. In particular, a multisensory measurement campaign will be presented, including earth resistivity tomography (ERT), spontaneous potential (SP) and ground penetrating radar (GPR) investigations carried out in the old town centre of the town of Mesagne, placed in the outskirts of Brindisi, southern Italy. In particular, after a strong storm a pipe of the aqueduct in Mesagne broke down causing serious subsidence events. Fortunately, no person has been injured during the event, but several buildings have been seriously damaged, and the local municipality has been compelled to vacate several houses that have become definitely dangerous after the event. Moreover, the municipality of Mesagne contacted the Institute for Archaeological and Monumental Heritage IBAM-CNR and committed to it a non-invasive geophysical measurement campaign in order

to provide some insight with regard to the entity and extension of the damages within a part of the old town. The results of these investigation were particularly important because the municipality had to establish whether some tens of people could come back to their houses, or rather they should look for alternative solutions. In particular, the municipality had provided provisional accommodations to several people, which was of course a meaningful cost for them. The situation was made somehow even more complicated by the fact that, indeed, several artificial cavities are present under the houses of the historical center of Mesagne, due to a number of cisterns (whose dating is quite uncertain and variable from case to case, but the most ancient ones are thought to be many centuries old) reused in several ways during subsequent periods (included the exploitation as waste containers) and then definitely abandoned in the 20<sup>th</sup> century and in most cases currently corked. Indeed, in many cases also the memory of the presence of these structures is lost, because the houses changed ownership several times. In particular, the old town of Mesagne was inhabited by the Messapic people since the 6<sup>th</sup> century B.C.. Then, the town passed through the Roman, Greek-Byzantine, Norman, Svevian, French and Spanish dominations that left traces of great historical and artistic value on which, however, the inevitable effects of anthropogenic modifications are evident. In particular, it is probable that important remains are still hidden under the soil, because still in 1999 Messapic tombs dating back to the 5<sup>th</sup> century B.C. were found.

The old town was also affected by significant morphological changes because of occurred leveling, excavations and subsequent debris flows, as it is put into evidence by several documents in the archives of the technical office of the Municipality of the town. The geology of the historic centre and more in general of the town of Mesagne is characterized in the first meters by the presence of clayey weakly cemented sands. The water table is located at an average depth of about 4 m from the current planking level. In particular, the geological substrate, formed by sands, is affected by some degradation processes in its superficial parts whose most significant effect is the gradual removal of the cemented part of the subsoil, due to the rainfall and to the meaningful amount of dropped water from the supply networks and from the drainage systems. Indeed, these degradation processes caused in the old town centre of Mesagne several documented subsidence events also in the past.

In order to probe the current event, an integrated ERT (Loke and Barker, 1996), SP (Fedi and Abbas, 2013) and GPR prospecting was performed, showing one more time the capabilities of the noninvasive techniques in identifying, within the first meters of depth, a number of anomalies, partially ascribable to collapses and of cavities. The paper is organised as follows: In the next section the ERT and SP are presented. In Section 3, the GPR results are presented. Conclusions follow in section 4.

**ERT and SP results.** ERT and SP results have been achieved making use of the same cable displacements. The instrumentation has been supplied to the Laboratory of Applied Geophysics to the Archaeological and Monumental Heritage (IBAM) of Lecce. In particular, the ERT measurements was a SYSCAL kid-switch suitably modified in order to work both as a georesistivimeter and as an equipment for the measure of the spontaneous potentials. An axial dipole (dipole-dipole) configuration was exploited, that allowed (thanks to a suitable procedure set on purpose) to achieve both vertical (TGV) and horizontal (TGO) tomography images, that allowed to achieve a quite clear picture of the subsurface resistivity distribution.

The maximum length of the profiles was chosen based on the required resolution and on the maximum depth of interest, namely the first few meters from the planking level. We made use of 24 electrodes with an electrode distance of 2 m. The inversion of the data has been carried out through an iterative least square minimization process that decreases progressively the difference between the measured apparent resistivity and the model apparent resistivity calculated according to the updated current model of the subsoil. Both the distributions of the electrical resistivity and of the spontaneous potential parameters in the subsurface have been determined in this way. Let us stress, in particular, that a non-standard acquisition geometry

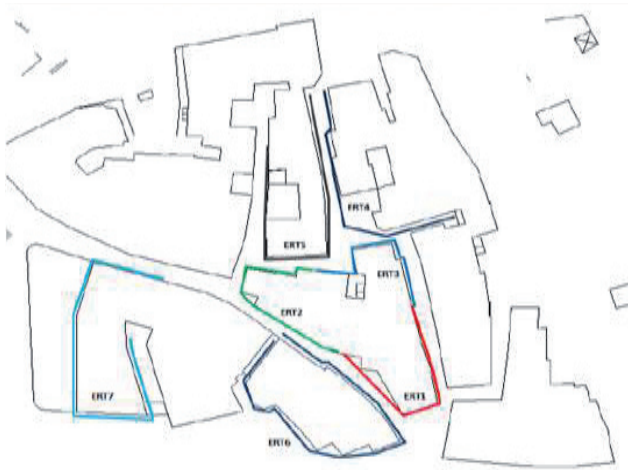


Fig. 1 – Location of the 3D electrical profiles ERT 1-7.

was used, which provided a power line following the boundary line of the buildings. Seven 3D electrical profiles, labeled ERT 1, ERT 2, ...ERT 7, were acquired. Their map is shown in Fig. 1. In this way, an comprehensive area about sized 4960 m<sup>2</sup> was prospected. The resistivity and the spontaneous potential maps were achieved making use of the ERTLlab software and making use also of a specific homemade MATLAB code. In Fig. 2 (left hand panel) the images relating to the profiles ERT 1 and to the homologous measure of spontaneous potential are shown.

The pattern distribution of the electrical resistivity and of the spontaneous potential parameters below the buildings at gradual depth levels (here, for sake of brevity, only one level has been shown) supplied the following considerations:

At first, we have recorded the presence of a heterogeneous subsurface with resistivity values up to 50 and 500 Ω m. Afterwards, it is possible to note the presence of:

- 1) areas indicated with “A”, with resistivity values between 400 and 500 Ω m; these values indicate the probable presence of areas where localized phenomena of instability are present. The relatively low resistivity values indicate that these anomalies are not attributable to the presence of empty volumes, but rather to incoherent materials, probably put there in order fill up previous voids;

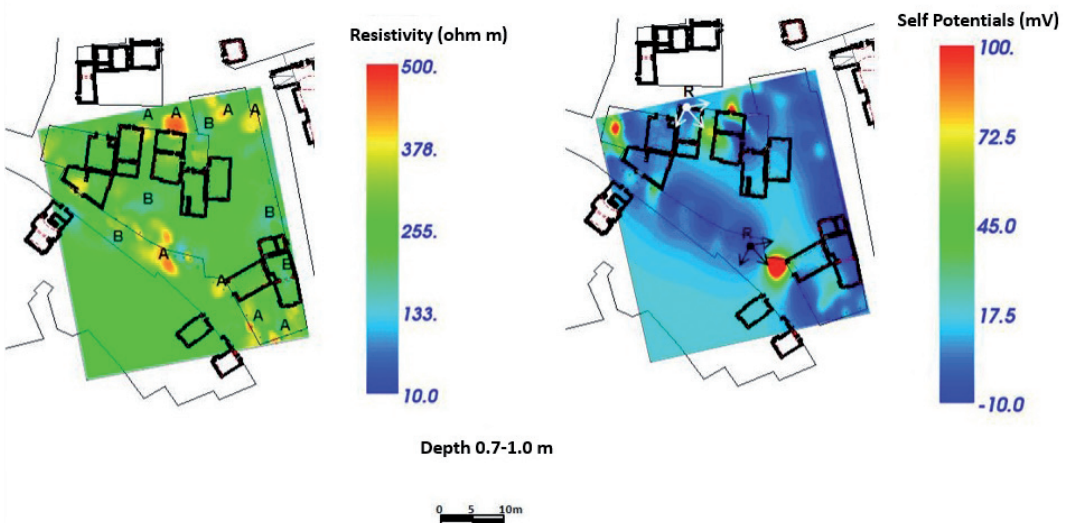


Fig. 2 – Slice of the retrieved resistivity and of spontaneous potential at 70-100 cm.

- 2) areas indicated with “B”, with resistivity values between 50 and 100  $\Omega$  m; these values indicate the probable presence of areas where a phenomenon of instability is present too. The low resistivity values indicate that these anomalies are due to the potential presence of water saturated incoherent materials;
- 3) areas with resistivity values between 150 and 280  $\Omega$  m; these values indicate the probable presence of subsoil zones free of in-homogeneities.

From the right hand panel of Fig. 2, instead, we can notice a quite uneven distribution pattern of the spontaneous potentials. In particular, it is possible to note two points, indicated with “R”, where there is a negative concentration of the spontaneous potential (-10 mV). It is quite probable that, in these points, a flow of materials in the directions indicated by the arrows (that is, towards positive spontaneous potentials values) was occurring at the moment of the measure (March 2014).

**GPR measurements.** A large GPR survey was performed too. In order to carry out it, we made use of a pulsed RIS Hi Mod GPR system, manufactured by the Ingegneria dei Sistemi IDS-Corporation and belonging to the Laboratory of applied geophysics to archaeological and monumental heritage of IBAM-CNR. The system is equipped with a dual antenna with central frequencies at 200 and 600 MHz, plus an antenna at 900 MHz and plus an antenna at 2 GHz. For the case history at hand, in dependence of the several met situations, we have exploited the dual antenna or the antenna at 900 MHz.

In particular, the main targets looked for were subservices and cavities, because possibly related to the present or to future subsidence events. So, the targets looked for were expected to have a size between 0.5 and 2 m, and their depth was expected variable from tens centimeters to a few meters. We set the time bottom scale to 60 ns for the 900 MHz antenna, 80 ns for the 600 MHz and 160 for the 200 MHz antenna.

In the first phase, the GPR surveys were performed in the areas outside the dwellings, in the second phase, instead, inside a number of dwelling, especially those where the most meaningful cracks along the walls were present and those where some of the floor had collapsed in some points. Comprehensively, we gathered 174 Bscans, covering an overall surface of about 964 m<sup>2</sup>. Afterwards, we performed a standard processing sequentially based on zero timing, background removal (Persico and Soldovieri, 2008), declipping, gain variable vs. the depth, one dimensional filtering when needed and finally migration in time domain (Persico, 2014). The processing of the collected data sets was performed making use of the commercial code GPRslice (Goodman and Piro, 2013), which also was exploited in order to achieve depth slices when possible.

A quite good penetration of the signal, that reached (on average) reliably the time level of about 60ns (corresponding on average to a depth of about 2.1m) was recorded.

An average propagation velocity of the electromagnetic waves equal to about 0.07m/ns was evaluated thanks to the presence of the diffraction hyperbolas presumably ascribable to electrically small targets (Mertens *et al.*, 2015; Persico *et al.*, 2015a, 2015b; Soldovieri *et al.*, 2008, 2009).

The profiles obtained with the antenna at 200 MHz showed the same anomalies recorded in the profiles obtained with the antenna at 600 MHz, but did not put into evidence significant deeper targets. Therefore, we will limit to consider the data gathered with the antennas at central frequency 600 MHz because of the obvious better available resolution with respect to the lower frequency antennas.

Depending on the zones and on the exploited antennas, the interline spacing of the Bscan profiles was equal to 50 cm or less (we used a transect of 20 cm for the antennas at 900 MHz). This allowed us to join together the results and work out time depth slices. The time slices were built using a time intervals of 5 ns, about corresponding to 0.17 m. The slides reported in Fig. 3 are not picked up at a unique depth level but rather they are a combination of several slides at different estimated depths level into the different probed areas. This

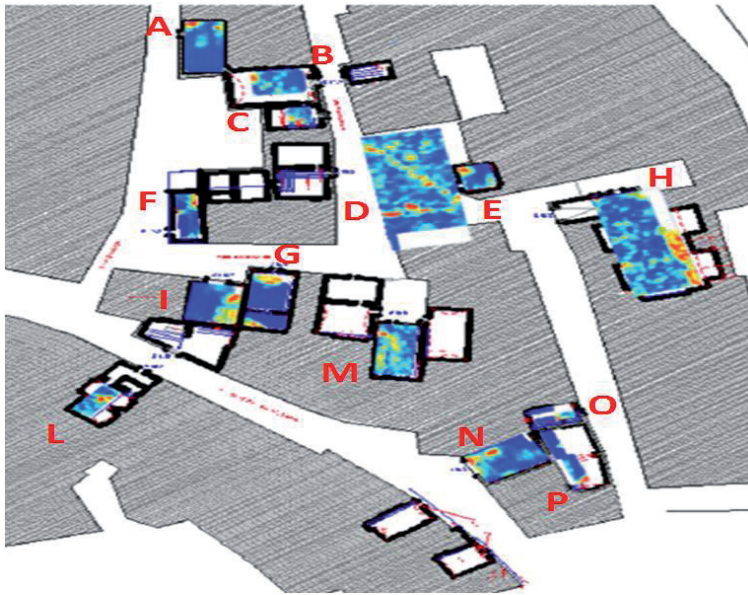


Fig. 3 – GPR slices at the apparently most “interesting” depths. The estimated depths are: A-B-C: 1.9-2.11 m; D: 0.61-0.78 m; E: 0.37-0.54 m; F: 0.25-0.42 m; G: 0.50-0.67 m; H: 0.22-0.37 m; I: 0.25-0.42 m; L: 1.24-1.41 m; M: 0.69-0.78; N-O-P: 1.37-1.54 m.

representation has been chosen in order to put into evidence all the most interesting depth levels in a synthetic way.

The GPR surveys allowed us to highlight the presence of several anomalies (in particular, those in the red colors in Fig. 3) linked to buried critical zones. In such areas, in fact, instability events occurred, due to small voids, cavities and areas where previous artificial changes had been done.

It can be noted that, as expected, in many houses the presence of wells and/or tanks, some of which partially filled with debris materials, was detected.

**Conclusions.** In this contribution we have shown a geophysical case history, where georesistivity, spontaneous potentials and ground penetrating data have been gathered in the historical center of the town of Mesagne, damaged by an exceptional storm that probably caused, among other things, the breaking of a water pipe of the aqueduct. The performed study demonstrates, one more time, the wide range of applicability of the geophysical methodologies. The results of the 3D ERT measurements showed the presence of a highly “disturbed” subsoil and a phase of adjustment still going on at the time of the measurements (March 2014). The SP data showed probable direction of flux of loose materials at the time of the prospecting. The GPR survey campaigns allowed to highlight the presence of several anomalies linked to buried critical zones.

According with the achieved results, it is possible to deem that the instability events have been caused by: 1) losses within both the water supply networks and the drainage systems. 2) The uncontrolled condition of several wells (in particular their high number and above all their state of these wells had never been systematically monitored). 3) Rainwater that infiltrates into the subsoil. In particular, the flowing fluids can saturate the soil and reduce its mechanical resistance. Moreover, the infiltration of superficial runaway water, even in small quantity, can increase the foundation base plastic material quality, lowering the load capacity. Finally, indeed, also modern volumetric changes performed on some houses (e.g. perforation of load bearing walls) have made the structures more prone to damages, but this does not seem to be the main cause of the occurred problems.

## References

- Cataldo A., Persico R., Leucci G., De Benedetto E., Cannazza G., Matera L. and De Giorgi L.; 2014: *Time domain reflectometry, ground penetrating radar and electrical resistivity tomography: a comparative analysis of alternative approaches for leak detection in underground pipes*. NDT & E International, **62**, 14–28, doi: 10.1016/j.ndteint.2013.10.007.
- Fedi M. and Abbas M.A.; 2013: *A fast interpretation of self-potential data using the depth from extreme points method*. Geophysics, **78**, pp. E107-E115, doi: 10.1190/geo2012-0074.1
- Giannotta M.T., De Giorgi L., Leucci G., Matera L., Persico R. and Riccardi A.; 2015: *Preventive Archaeology: the Emblematic Case of Ruvo di Puglia, Italy*. 8<sup>th</sup> International Workshop on Advanced Ground Penetrating Radar (IWAGPR), 7-10 July 2015, Florence (Italy).
- Goodman D. and Piro S.; 2013: *GPR Remote Sensing in Archaeology*, Springer-Verlag ed., ISBN: 978-3-642-31856-6
- Leucci G., Persico R. and Soldovieri F.; 2007: *Detection of Fracture From GPR data: the case history of the Cathedral of Otranto*. Journal of Geophysics and Engineering, **4**, pp. 452-461.
- Leucci G., Masini N., Persico R. and Soldovieri F.; 2011: *GPR and sonic tomography for structural restoration: the case of the Cathedral of Tricarico*. Journal of Geophysics and Engineering, **8**, 3, pp. S76-S92.
- Loke M.H. and Barker R.D.; 1996: *Rapid least-squares inversion of apparent resistivity pseudosections using a quasi-Newton method*. Geophys. Prosp., **44**, 1, pp. 131–152, doi: 10.1111/j.1365-2478.1996.tb00142.x.
- Masini N., Persico R., Rizzo E., Calia A., Giannotta M.T., Quarta G. and Pagliuca A.; 2010: *Integrated Techniques for Analysis and Monitoring of Historical Monuments: the case of S.Giovanni al Sepolcro in Brindisi (Southern Italy)*. Near Surface Geophysics, **8**, 5, pp. 423-432, doi: 10.3997/1873-0604.2010012.
- Matera L.; 2015: *Theoretical/Technical aspect and comparative analysis of the GPR methodology (Part I)*. PhD thesis at the Department of Earth and Geoenvironmental Sciences of the University of Bari “Aldo Moro”, Doctoral Research School (XXVII cycle). Mistral service, ISBN: 978-88-98161-29-4.
- Mertens L., Persico R., Matera L. and Lambot S.; *Smart automated detection of reflection hyperbolas in complex GPR images*. Submitted to IEEE Transaction on geosciences and Remote Sensing.
- Negri S., Leucci G. and Mazzone F.; 2008: *High resolution 3D ERT to help GPR data interpretation for researching archaeological items in a geologically complex subsurface*. Journal of Applied Geophysics, **65**, pp. 111-120.
- Persico R. and Soldovieri F.; 2008: *Effects of the Background Removal in Linear Inverse Scattering*. IEEE Trans. on Geos. and Rem. Sens., **46**, 4, pp. 1104-1114, doi: 10.1109/TGRS.2007.910223.
- Persico R.; 2014: *Introduction to Ground Penetrating Radar: Inverse Scattering and data processing*. Wiley and Sons, doi: 10.1002/9781118835647.ch10.
- Persico R., Matera L., Mertens L., Lambot S. and Ciminale M.; 2015a: *Enhanced Strategies for the Retrieving of the Propagation Velocity in the Soil from the Shape of the Diffraction Curves*. 21<sup>st</sup> European Meeting of Environmental and Engineering Geophysics (EAGE), 6 - 10 September 2015, Turin, Italy, DOI: 10.3997/2214-4609.201413839.
- Persico R., Leucci G., Matera L., De Giorgi L., Soldovieri F., Cataldo A., Cannazza G. and De Benedetto E.; 2015b: *Effect of the height of the observation line on the diffraction curve in GPR prospecting*. Near Surface Geophysics, in print.
- Pieraccini M., Noferini L., Mecatti D., Atzeni C., Persico R. and Soldovieri F.; 2006: *Advanced Processing Techniques for Step-frequency Continuous-Wave Penetrating Radar: the Case Study of “Palazzo Vecchio” Walls (Firenze, Italy)*. Research on Nondestructive Evaluation, **17**, 2, pp. 71-83, doi: 10.1080/09349840600689475.
- Piscitelli S., Rizzo E., Cristallo F., Lapenna V., Crocco L., Persico R. and Soldovieri F.; 2007: *GPR and Microwave Tomography for Detecting shallow Cavities in the Historical Area of Sassi of Matera (Southern Italy)*. Near Surface Geophysics, **5**, 4, pp. 275-285, doi: 10.3997/1873-0604.2007009.
- Soldovieri F., Prisco G. and Persico R.; 2008: *Application of Microwave Tomography in Hydrogeophysics: some examples*. Vadose Zone Journal, **7**, 1, pp. 160-170, doi: 10.2136/vzj2006.0147.
- Soldovieri F., Prisco G. and Persico R.; 2009: *A strategy for the determination of the dielectric permittivity of a lossy soil exploiting GPR surface measurements and a cooperative target*. Journal of Applied Geophysics, **67**, 4, pp. 288-295, doi: 10.1016/j.jappgeo.2008.09.007.



## sessione 3.3

### **Modelling e aspetti teorici**

Convenor: G. Florio e P. Mazzucchelli

co-organizzata con Sezione Italiana Eage-Seg

---



## SINGLE-PASS SURFACE RELATED 3D MULTIPLE ESTIMATION FOR OBS DATA WITH DATA DRIVEN + BATHYMETRY APPROACH

M. Codazzi, P. Mazzucchelli

Aresys, Milano, Italy

**Introduction.** Ocean Bottom Seismic is a type of survey where recording nodes are laid out on sea-floor and seismic sources are energized at sea surface and it is an alternative acquisition method in marine environments when the presence of obstacles or a shallow water layer prevents the conventional seismic acquisition by towed streamers. Despite higher acquisition costs, OBS data compare favorably to conventional surface marine acquisitions because of their inherently full azimuth coverage (as OBS geometries usually show similarity to land acquisition geometries), providing better illumination of complex subsurface structures.

Furthermore, OBS surveys record both pressure and particle motion through hydrophones and geophones respectively: the multicomponent nature of OBS data broadens the number of applicable processing algorithms. More specifically, the availability of different recordings of the wavefield allows to process OBS data for the separation of up-going and down-going wavefields.

OBS data suffer from the contamination by surface-related multiple reflections exactly like conventional marine data, amplified by the shallow water environment where OBS acquisitions are employed: it must be noted that surface related-multiple reflection estimation is tightly joined to up-going and down-going wavefield separation.

However, taking advantage of the multicomponent nature of OBS data is not straightforward, because of the different technologies of hydrophones and geophones that imply a tricky calibration process. Moreover the sparse sampling of sea bottom nodes (compared to conventional surface marine acquisitions) prevents the direct application of multidimensional filtering algorithms, usually available for surface marine acquisition geometries, that cannot cope with aliased wavefields (at least in CSG -Common Shot Gather- subdomain).

**Surface related multiple suppression for OBS data.** Surface related multiples can occur both at source side and at receiver side: examples of surface related multiple travelpaths are sketched in Fig. 1. More complex patterns can be generated while dealing with higher order multiples. Each travelpath have been visually separated into three different sub-paths: red and blue sub-paths represent recorded OBS data (source and receiver related, respectively), while the “missing” water-layer propagation is shown in green.

A well-known and widely-used way to deal with multiple wavefields and multicomponent data is the so-called PZ summation: the multicomponent nature of OBS data is exploited in order to separate up-going and down-going wavefields, as multiples contaminating pressure and vertical particle velocity data have opposite polarity. However, PZ summation can correctly handle only receiver-side surface-related multiples (or equivalently, ghosts, corresponding to travelpaths *a*, *c*, *d*, *f* in Fig. 1). Thus, up-going and down-going wavefields after separation are still contaminated by source-side multiples, and further processing is needed. Moreover, an effective PZ summation requires the calibration of geophones and hydrophones, that is known to be generally difficult because of differences in frequency responses and signal to noise ratios, and their variability with respect to emerging angles.

Different techniques based on the adaptation of the standard data-driven SRME approach (Berkhout *et al.*, 1997) have been proposed to address the estimation and suppression of surface related multiples while dealing with OBS acquisitions: in fact, multiple estimation techniques that are generally used in the processing of conventional streamer acquisitions cannot be applied to OBS data, as the assumption that both sources and receivers are located at the sea surface is not met by this type of acquisition geometries. However, in case that conventional streamer data are available in the same acquisition area, a full data-driven approach can still be implemented by combining them with the OBS data (Verschuur *et al.*, 1999).

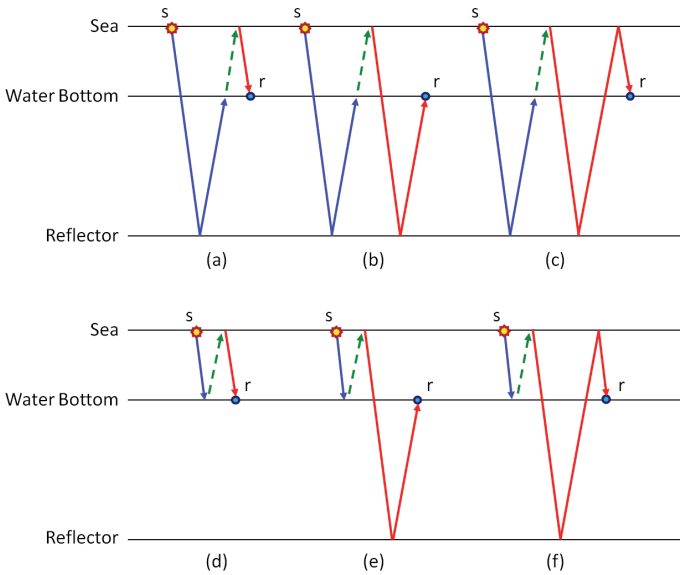


Fig. 1 – OBS SRME multiple generation schemes: a) first order downgoing multiple (receiver ghost); b) first order upgoing multiple; c) second order downgoing multiple; d) water layer multiple; e) first order upgoing multiple (source side reverberation); f) second order downgoing multiple (source side reverberation).

Unfortunately, this situation does not usually happen. When only OBS data are available, missing surface traces can be obtained by transforming OBS data in surface data with a datuming process: a quite expensive preprocessing step (both in terms of computational cost and I/O overburden) is required to apply standard data-driven demultiple techniques. Any additional I/O is a manifest drawback, especially when dealing with the dimensionality of modern 3D acquisitions.

Conversely, a fully model-driven approach has been proposed by Pica *et al.* (2006), extending to OBS data their approach based on wavefield modeling. While data-driven methodology requires only a description of the water layer (implicitly needed in the datuming step), the latter requires a good-quality reflectivity model (i.e., migrated data volume, that cannot be available in the early processing steps).

Another OBS data demultiple algorithm has been proposed by Jin *et al.* (2012) by extending the MWD technique to OBS geometries (requiring the knowledge of the water layer only). This technique can predict only source-side and receiver-side water layer reverberation (travelpaths *a, c, d, e, f* in Fig. 1). Even if the MWD approach cannot predict all multiple paths, it must be noted that water-layer related multiples (also defined as *source-side* or *receiver-side* water-layer reverberations) prevail over the other interfering wavefields, at least in the shallow water environment. Furthermore, its computational cost is smaller than those of the approaches previously discussed and it proves to be an alternative method to perform up-down separation without the need of different wavefields recorded by hydrophones and geophones (the quality of the separation relies on a subsequent adaptive subtraction processing step).

Unfortunately, none of the proposed techniques can deal with all the different multiple travelpaths (source-side and receiver-side) in a single processing step, without requiring a full reflectivity volume or an intermediate 3D surface acquisition.

We propose a hybrid approach that blends OBS data and computed travelpaths in water layer and that is able to estimate all the possible source-side and receiver-side surface related multiples shown in Fig. 1.

**Single-pass OBS surface related multiple estimation.** We introduce a (partially) data-driven method for the estimation of multiple reflections for OBS data that neither requires integration of surface data nor reflectivity models, but only the knowledge of the bathymetry (information that, if missing, can be anyway extracted from the geometry of OBS data). Unlike the techniques based on a separate datuming step, this method has also the advantage to perform

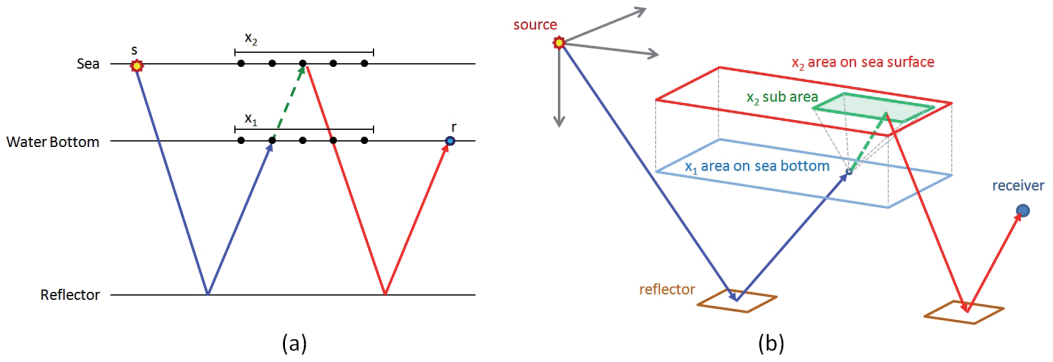


Fig. 2 – Single-pass OBS SRME algorithm schematics: a) path of multiple decomposed in three contributions, with a set of DRPs  $x_2$  at sea surface and a set of P-DRPs  $x_1$  at sea bottom; b) practical implementation of multiple estimation for a 3D OBS geometry: for each  $x_1$  point, only a sub-area of  $x_2$  is taken into account in the summation.

the multiple estimation in a single pass, without the need of any intermediate output. Moreover the data-driven nature of this approach allows to inherently handle both P and P-S converted waves.

Similarly to 3D SRME, for each input trace s-r, OBS multiple estimation involves the convolution and subsequent stacking of OBS trace couples s- $x_1$ ,  $x_2$ -r, where  $x_2$  is any possible Downward Reflection Point (DRP) belonging to a regularly sampled surface, while  $x_1$  belongs to an analogous surface laid on the sea bottom (Fig. 2a). Thus, for each trace two sets of points must be defined: one set of Downward Reflection Points (DRPs) at the sea level, between the source and the receiver, and one set of Projected DRPs (P-DRPs) with the same horizontal coordinates of DRPs and the same depth of the water bottom.

As shown in Fig. 2a, the path of any surface-related multiple can be split in three parts: s- $x_1$ ,  $x_1$ - $x_2$ ,  $x_2$ -r (where  $x_1$  identifies the P-DRPs and  $x_2$  the DRPs). A possible OBS multiple contribution is given by the convolution of interpolated traces s- $x_1$  and  $x_2$ -r (blue and red solid lines in Fig. 2a respectively) shifted by the travel-time of the direct ray in the water layer from  $x_1$  to  $x_2$  (green dashed line in Fig. 2a), which can be easily computed on-the-fly (assuming a known water-layer velocity model).

The estimated multiples  $M$  are computed as a summation of the contributions of all possible P-DRPs and DRPs combinations as:

$$M(t, \mathbf{s}, \mathbf{r}) = \sum_{\mathbf{x}_1} \sum_{\mathbf{x}_2} D(t, \mathbf{s}, \mathbf{x}_1) * \delta(t - \tau_{\mathbf{x}_1, \mathbf{x}_2}) * D(t, \mathbf{x}_2, \mathbf{r}) \quad (1)$$

where  $D$  is the OBS data,  $*$  represent the convolution along time axis,  $\delta$  is the Dirac Delta function,  $s$ ,  $x_1$ ,  $x_2$  and  $r$  are the source, the P-DRP, the DRP and the receiver respectively, and  $\tau_{x_1, x_2}$  is the travel time in the water layer from  $x_1$  to  $x_2$  (that is simply computed as ratio between the distance  $x_1$ - $x_2$  and the water velocity  $V_w$  when a constant velocity assumption can be done for the water layer).

The computational cost of the double summation involved in Eq. 1 is greater than SRME approach for conventional streamer data, as it implies multiple contribution gathers with double dimensionality. The multiple contribution gather for 2D OBS multiple estimation is a 3D sampled volume, while 3D OBS multiple estimation requires a 5D MCG data volume. One can notice similarities between OBS SRME MCGs and the data driven techniques for internal multiples estimation, that share the same increased dimensionality. However, stationary points are minima for OBS SRME MCGs (all terms in Eq. 1 delay the events), while they are saddle points for internal multiple MCGs (as a cross-correlation term, or time advance is implied in the corresponding expression).

Eq. 1 can be recasted to a fully data-driven approach, by substituting the travel-time with a third OBS data contribution  $D(t, x_2, x_1)$ , as proposed in (Ma *et al.*, 2010). Nonetheless, the proposed “hybrid” approach (where the knowledge of the bathymetry and the velocity model for the water layer are required) compares favorably to the fully data-driven approach: it proves to be less computationally expensive and more accurate than the convolution of three different traces (as time delay is replaced by full trace convolution, then additional I/O is mandatory to retrieve the seismic trace at  $x_2, x_1$ ). Furthermore, estimated higher order multiples are less prone to source wavelet and relative amplitude distortion. Finally, the fully data-driven approach strictly relies on the quality of direct wavefield recorded in OBS data to correctly estimate both water-layer reverberations and first-order multiples).

**Practical implementation issues.** As well-known, for an efficient 3D SRME implementation (Moore *et al.*, 2008), an optimized interpolation strategy that allows a simple on-the-fly data regridding to required geometries  $s-x_1, x_2-r$  is implemented. This strategy must allow to cope with sparse and irregular sampling and avoid operator aliasing (Bienati *et al.*, 2012). The interpolation scheme involves the retrieval of one (or more) neighbouring traces, and the computation of a differential correction (i.e., differential moveout) or a weighted stack (i.e., continuation operators). The neighbourhood selection rule must minimize the sensitivity of the interpolation kernel to model errors, taking into account both azimuth and offset differences:

$$d_w = \alpha \cdot |m_1 - m_2| + \beta \cdot |h_1 - h_2| + \gamma \cdot (h_1 + h_2) |\theta_1 - \theta_2| \quad (2)$$

where  $m_i$  is the midpoint,  $h_i$  is the offset and  $\theta_i$  is the azimuth of  $i$ -th trace;  $\alpha$ ,  $\beta$  and  $\gamma$  are weights that must be chosen in some heuristic way.

Note that any data regridding strategy (implied in all 3D SRME practical implementations) may introduce a mild model dependency, even for fully data-driven approaches. Furthermore, another subtle dependency on a-priori knowledge of subsurface structure is implied in the choice of the integration area.

However, both the selection of neighboring traces, and the computation of a differential correction must be modified according to OBS geometry.

First of all, the different depths of sources (at sea surface) and receivers (at sea bottom) must be taken into account in Eq. 2. While for surface data the azimuth terms ( $\theta_i$ ) is considered without signum within the range  $[0^\circ, 180^\circ]$  (i.e. it is possible to exchange sources with receivers and viceversa), for OBS data the same terms specify the azimuth with signum within the full range  $[-180^\circ, 180^\circ]$ . Also the values of weights  $\alpha$ ,  $\beta$  and  $\gamma$  can be slightly modified for minimizing the interpolation error of OBS traces.

Then, an adapted differential correction must be defined in order to compensate the different depths of input and output trace receivers, as water bottom is a generally varying surface. A simple differential correction with constant velocity is implemented, where the interpolated traces time  $t_{out}$  is approximated by:

$$t_{out} = \frac{1}{V} \sqrt{h_{out}^2 + \left( z_{in} - z_{out} + \sqrt{V^2 t_{in}^2 - h_{in}^2} \right)^2} \quad (3)$$

where  $V$  is the constant reference velocity,  $t_{in}$ ,  $h_{in}$  and  $z_{in}$  are the time, the offset and the receiver depth of input trace respectively, and  $t_{out}$ ,  $h_{out}$  and  $z_{out}$  are the time, the offset and the receiver depth of output trace respectively.

In practice, in order make the algorithm less expensive, the terms of summation 1 associated to highly unlikely  $x_1-x_2$  patterns that give incoherent contributions to the result can be discarded, as shown in Fig. 2b. The correct choice of valid patterns depends on both the depth and smoothness of water bottom and the complexity of the subsurface.

It must be noted that direct wavefield contributes to both source and receiver sides ghost thereby it must not be removed from the data before the processing: in fact, the proposed approach still relies on the quality of direct wavefield recorded in data to correctly estimate

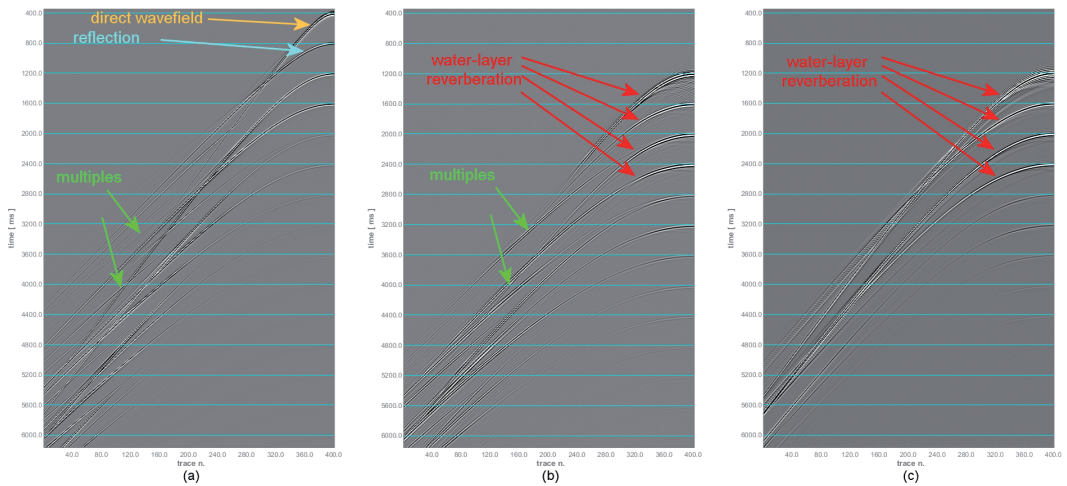


Fig. 3 – Simulated data example: a) input (reference) data; b) estimated multiples by OBS SRME: all multiples events are correctly predicted c) estimated multiples by OBS MWD: only water layer reverberation are correctly predicted.

water layer reverberations only (i.e., travelpaths a, c and f for receiver-side reverberations, and d, e, f for source-side reverberations in Fig. 1).

However, the water layer reverberations only can be separately estimated by a model based approach (Jin *et al.*, 2012). Then, the different estimations can be jointly subtracted from OBS data by cooperative matched filtering (Costagliola *et al.*, 2015), allowing to cope with the potential weaknesses of the different algorithms.

Coarse receiver spacing are often encountered in OBS acquisition geometries. A pre-processing interpolation step can be required in order to improve the result of the multiple estimation approach. For example, compressing sensing based interpolation schemes (Fioretti *et al.*, 2015) can be pursued to obtain a well-sampled wavefield.

**Synthetic data example.** The proposed approach has been tested with a synthetic OBS dataset to prove the feasibility of the technique. An OBS acquisition has been simulated, using a finite difference kernel and a free surface constraint to allow the correct recording of multiples. The average water-layer depth is 600 m, the shot interval (at surface) is 50 m and the hydrophones spacing (at sea-floor) is 20 m.

A receiver line for a selected Common Shot Gather is shown in Fig. 3. Input data is shown in Fig. 3a, the multiple estimation result obtained with the proposed approach is shown in Fig. 3b and it is compared to the result obtained applying the OBS adapted MWD technique (Jin *et al.*, 2012) that is shown in Fig. 3c.

The comparison of estimated multiples (Fig. 3b), obtained by the proposed approach, and the reference input data shown in Fig. 3a, proves that all OBS multiples are correctly predicted (water layer reverberations – red arrows, and deeper reflections – green arrows), at least from a kinematic point of view. In fact, the proposed algorithm is not strictly amplitude consistent, and the seismic wavelet is distorted in respect to input data (a squared source wavelet is superimposed to seismic reflectivity, due to the data convolution): an adaptive subtraction step is required as post-processing to obtain the up-going demultiplied wavefield only. The comparison of the results in Figs. 3b and 3c proves how the MWD method cannot predict all the multiples except for water-layer reverberations (red arrows). The two different algorithms can however complement each other (especially when the direct wavefield is not correctly recorded in seismic data): joint adaptive subtraction of both multiple estimations can improve the overall quality of the resulting seismic data. The processing of real OBS acquisitions (not shown) leads to the same conclusions.

**Conclusions.** A single-pass surface related multiple estimation method has been described for OBS data: no generation of intermediate new datasets is needed, and no model information other than water layer description is required.

Results obtained on synthetic data demonstrate that the proposed technique can achieve the task of estimating both source-side and receiver-side surface related multiples, without requiring additional surface data (both recorded or simulated), and favorably compares to conventional multi-step approaches that involve OBS geometry transformations (i.e. datuming). The minimization of I/O overburden is obtained accepting an increased computational cost, as a higher dimensionality of multiple contribution gathers is required (as two unknown control points are involved instead of one single downward reflection point). Thus, the viability of the algorithm implies a careful implementation that contributes to reduce the increased computational costs in respect to standard 3D SRME approach. Moreover, the same computational kernel can be adapted to separate up-going and down-going wavefields, without the need of multicomponent data.

**Acknowledgments.** The authors would like to thank Nicola Bienati (Eni Upstream and Technical Services) for fruitful discussions and valuable suggestions and Laura Fioretti and Sathya Costagliola (Aresys) for support in data processing.

### References

- Berkhout, A.J., and Verschuur, D.J., 1997, Estimation of multiple scattering by iterative inversion, Part I: Theoretical considerations: *Geophysics*, 62, 1586-1595.
- Bienati, N., Mazzucchelli, P., Codazzi, M., 2012, 3D-SRME Antialiasing in the Multiple Contribution Gather Domain: 74<sup>th</sup> Conference & Exhibition, EAGE, Expanded Abstracts, Y009.
- Costagliola, S., Codazzi, M., Mazzucchelli, P., Bienati, N., 2015, Improving Multiple Removal by Cooperative Matched Filtering: 77th Conference and Exhibition, EAGE, Expanded Abstracts, Th P4 14.
- Fioretti, L., Mazzucchelli, P., Bienati, N., 2015, Stagewise Conjugate Gradient Pursuit for Seismic Trace Interpolation, 77th Conference and Exhibition, EAGE, Expanded Abstracts, We N112 05.
- Jin, H., Wang, P., 2012, Model-Based Water-Layer Demultiple (MWD) for Shallow Water: From Streamer to OBS: 82th Annual International Meeting, SEG, Expanded Abstracts, 1-5.
- Ma, J., Sen, M. K., Chen, X., Liu, Y., 2010, OBC Multiple Attenuation Technique Using SRME Theory: 80th Annual International Meeting, SEG, Expanded Abstracts, 3473-3477.
- Moore, I., Dragoset, B., 2008, General surface multiple prediction: a flexible 3D SRME algorithm, *First Break*, Volume 26, 89-100.
- Pica, A., Manin, M., Granger, P.Y., Marin, D., Suaudeau, E., David, B., Poulain, G., Herrmann, P. h., 2006, 3D SRME on OBS Data Using Waveform Multiple Modelling: 76th Annual International Meeting, SEG, Expanded Abstracts, 2659-2663.
- Verschuur, D. J., Neumann, E.L., 1999, Integration of OBS data and surface data for OBS multiple removal: 69th Annual International Meeting, SEG, Expanded Abstracts, 1350-1353.

## AUTOMATIC V<sub>RMS</sub> BUILDER

S. Costagliola, P. Mazzucchelli

*Aresys, Milano, Italy*

**Introduction.** Velocity analysis plays an important role in seismic imaging. In general, the problem of estimating velocity from seismic data is an ill-posed inversion problem, in the sense that the data do not contain all the necessary information to define a velocity function with arbitrary variations with depth and along the horizontal directions (Biondi, 2006).

Therefore, for the velocity updates derived with this procedure to be accurate, the current migration velocity must be close to the correct one, or the reflectors cannot be steeply dipping and the velocity have strong lateral variations.

Fortunately, in many practical situations we have a priori information about the velocity model that complements the information contained in the seismic data. The combination of these two sets of information (the information contained in the data and the a priori one) are often sufficient to constraint adequately the problem.

From an historical point of view, the conventional velocity analysis for each common-mid-point (CMP) section is defined by the following steps (Yilmaz, 2001):

- 1) semblance analysis is performed in the time and root-mean-square (RMS) velocity domain by computing a normalized coherency coefficient of the data along each hyperbolic time trajectories, this produce a map  $S(t_0, V_{RMS})$ ;
- 2) manual picking is performed on the semblance map for each specific stacking time  $t_0$ ;
- 3) interval velocities ( $V_i$ ) are computed based on the picked  $V_{RMS}$  to construct earth velocity time model;
- 4) time-to-depth conversion is performed to get the earth velocity model in depth.

In more recent years, the main effort in velocity model building techniques has been directed towards the improvement of depth migrated images. In particular, we can affirm that tomographic inversion forms the basis of all contemporary methods of updating velocity models for depth imaging. Over the past 15 years, tomographic inversion has evolved (from ray based travel time tomography in data domain and image depth domain to full waveform techniques – a quite complete reference can be found for example in Jones (2010) to support the production of reasonably reliable images for data from complex environments, taking advantage of both the increased quality and dimensionality of seismic data (from millions of traces to currently billions of traces) and the increased computing power dedicated to seismic processing.

Less appealing novelties have appeared in the “time processing world”, especially for processing steps related to time domain imaging. Nonetheless, data images obtained in the time domain (from the simplest volume stack to a more accurate pre-stack time migration) are still the most powerful QC -Quality Check- tools that any geophysicist can apply to evaluate the results of any time processing tool (i.e., denoising, multiple subtraction, ...). Indeed, as the current dataset magnitude of seismic data prevents anyone from a direct and complete inspection of pre-stack gathers, time domain images are a truly unique opportunity for data QC. Nonetheless, the “resolving power” of such time domain processes demands for a high quality velocity model, that should be available from the very early processing steps, and that should not require any intensive human interaction to be built.

Since its introduction by Taner and Koehler (1969), the semblance measure has been an indispensable tool for velocity analysis of seismic records. The drawback of this methodology is that a visual interpretation of the semblance map is necessary for all (or many of) the common-mid-points sections. Moreover a localized mispick along a velocity trend can yield anomalous interval velocities. In particular, picks at too close time intervals can yield physically implausible interval velocity values; therefore, they should not be taken into account.

The problem of automatic velocity picking has been studied by many authors. Toldi (1989) and Viera *et al.* (2011) built an a-priori constrained interval-velocity model such that the stacking velocities calculated from that model give the most powerful stack. In Fomel (2009) an algorithm based on the AB semblance proposed by Sarkar *et al.* (2001, 2002) is derived while Li and Biondi (2009) developed an automatic velocity picking technique based on the Simulated Annealing Algorithm.

The present study is to propose a total or partial elimination of the manual picking step, by setting up a data driven  $V_{RMS}$  model building strategy. The developed model building technique, uses the time migration and/or normal moveout outputs with an additional parameter scan, trading currently available computing power for intensive human interaction, while taking advantage of the compressive sensing framework (e.g. Candès *et al.*, 2006). Indeed, a non-linear inversion, constrained by interval velocity bounds, provides a sparse and robust solution.

**Time migration vs. normal moveout.** Time migration proves to be a great tool for processing data coming from areas where lateral velocity changes are not too severe, but structures are complex. Time migration has the effect of moving dipping events on a seismic surface from apparent locations to their true locations in time. The resulting image is shown in terms of travel-time rather than depth, and must then be converted to depth with an accurate velocity model to be compared to well logs. When velocity variations are sufficiently strong to create non-hyperbolic diffraction surfaces, canonical time migration cannot focus the data properly, and depth migration could become necessary.

However, if interval velocity estimates are inaccurate, depth migration not only mispositions the reflectors in depth but also misfocuses the data. Its robustness makes time migration an essential imaging tool. However, it has to be applied within the limitation imposed by its underlying assumptions. Time migration in his isotropic version assumes that the diffraction surfaces are hyperbolic, and that the corresponding time-shift can be reasonably well described by the following equation:

$$\tau = \sqrt{\left(\frac{t_0}{2}\right)^2 + \frac{|\mathbf{m} - \mathbf{s}|^2}{V_{RMS}(t_0, \mathbf{m})^2}} + \sqrt{\left(\frac{t_0}{2}\right)^2 + \frac{|\mathbf{m} - \mathbf{r}|^2}{V_{RMS}(t_0, \mathbf{m})^2}} \tag{1}$$

where s, r and m represent source, receiver and image point coordinates on the surface respectively. Time migration is very sensitive to the choice of the velocity function and the irregular sampling of the data. An approximate method for imaging prestack data that is less expensive and often more robust than full prestack migration is based on the transformation of prestack data to equivalent zero-offset data. This is accomplished by the application of normal moveout (NMO):

$$\tau = \sqrt{t_0^2 + \frac{|\mathbf{s} - \mathbf{r}|^2}{V_{RMS}(t_0, \mathbf{m})^2}} \tag{2}$$

At first order, NMO transforms data collected at a finite offset to equivalent zero-offset data. The transformation to zero-offset is only kinematic and approximate; even in constant velocity, the NMO time is exactly equivalent to zero-offset time only when reflectors have no dip component along the trace source-receiver azimuth.

The NMO and stack sequence can be seen as an approximate partial prestack time migration that focuses data along the offset axes. The only velocity information that NMO and stack needs to focus the data along offsets is the average velocity corresponding to the midpoint which can be directly measured from the data. Because NMO is a trace-to-trace transformation, with no spreading of energy across midpoints, NMO and stack is immune from operator aliasing across midpoints (Biondi, 2006).

**Anisotropy.** Anisotropic models are recognized as a more realistic representation of the subsurface where complex geological environment exists. However, anisotropic model building is still a challenging problem in the industry.

Currently, many seismic processing and inversion methods utilize anisotropic models, thus providing a significant enhancement over the seismic imaging quality and resolution. The existing anisotropic model-building schemes are mostly based on measuring the non-hyperbolic moveout along the travelttime curve to flatten the common image gathers (Li and Biondi, 2011).

Considering horizontal layers only, the medium can be defined as vertical transverse isotropic (VTI). In case of weak anisotropy the NMO curve can be approximated by Taylor expansion using an extra term depending on the anisotropy parameter  $\eta$  (Alkhalifah and Tsvankin, 1995). Time migration using such approximation can be rewritten as:

$$\tau = \sqrt{(t_0/2)^2 + \frac{|\mathbf{m} - \mathbf{s}|^2}{V_{RMS}(t_0, \mathbf{m})^2} \left( 1 - \frac{2\eta|\mathbf{m} - \mathbf{s}|^2}{V_{RMS}(t_0, \mathbf{m})^2(t_0/2)^2 + (1 + 2\eta)|\mathbf{m} - \mathbf{s}|^2} \right)} + \sqrt{(t_0/2)^2 + \frac{|\mathbf{m} - \mathbf{r}|^2}{V_{RMS}(t_0, \mathbf{m})^2} \left( 1 - \frac{2\eta|\mathbf{m} - \mathbf{r}|^2}{V_{RMS}(t_0, \mathbf{m})^2(t_0/2)^2 + (1 + 2\eta)|\mathbf{m} - \mathbf{r}|^2} \right)} \quad (3)$$

**V<sub>RMS</sub> builder.** The main assumption under V<sub>RMS</sub> builder is that once the pre-stack data has been corrected by moveout or migrated using an accurate velocity model, all the traces of a CMP gather have a reflector located at the same time  $t_0$ , producing a flat event that sums constructively. Conversely, when the events are not flat, the corresponding stacked trace has a lower energy and the velocity model can be improved.

When a V<sub>RMS</sub> model has been already computed manually, the observed non-flatness or residual normal moveout may be used to refine that model slightly perturbing it, thus avoiding the time-consuming operation of re-picking and re-analyzing velocities.

If the signal-to-noise ratio of the input data is poor, then the stacked amplitude may not be the best display quantity (Yilmaz, 2001). The aim in velocity analysis is to obtain picks that correspond to the best coherency of the signal along a NMO trajectory over the entire spread length of the CMP gather. (Neidell and Taner, 1971) described various alternative types of coherency measures that can be used as attributes in computing velocity spectra.

In practice, data is migrated (or NMO corrected) for a set of velocity variations. This produces a semblance-like map. This map is positive and multimodal because of the velocity local maxima. Besides this difficulty, the inversion is classified as an ill-posed problem. Therefore, the optimization needs a priori information and constraints, that could be implicit and explicit, for the solution characterization.

Geological knowledge on the subsurface structure and on the behavior of the velocity function are used to constrain the components of the velocity model that are not sufficiently determined from the data alone. Such prior knowledge facilitates the automatic picking to get the refined model.

Migrating the data with the updated velocities produces flatter events and the process can be iterated few times to reach the converge.

Following the same approach, anisotropy parameter can also be estimated. One way to obtain velocities and anisotropy values that produce flat gathers is a cascaded approach where as first step the long offsets are muted and the gathers flattened simply by assuming isotropy and fine-tuning the V<sub>RMS</sub> velocity only. Then the far offsets are re-introduced and the “hockey stick” effect can be corrected by choosing an effective eta value controlling the far offset behavior (Alkhalifah, 1997).

**Monotonic constraint.** Because of the V<sub>RMS</sub> formulation, not all the solutions are physically consistent. A non strictly physical constraint (but realistic in most of the practical scenarios) is to force the solution to be monotonically increasing. The monotone solution  $V_M$  can be found solving a non-linear optimization (Hastie *et al.*):

$$V_M = \arg \min_x \left\{ \|\mathbf{V} - \mathbf{x}\|_2^2 + \lambda \left[ \sum_k \max(0, V_k - V_{k+1})^2 + \sum_k \max(0, V_{k-1} - V_k)^2 \right] \right\} \quad (4)$$

where  $V_k$  is the  $k^{\text{th}}$  element of the non-monotonic starting RMS velocity vector  $\mathbf{V}$  and  $\lambda$  is a Lagrange parameter that allow to weight the strength of the constraint. Introducing a differentiable approximation of  $\max(\cdot)$ , the gradient of the cost function can be computed and the solution can be obtained by a steepest descent algorithm. However, since the minimization problem is in general non-convex, convergence is not guaranteed. An alternative procedure considers a

compressive sensing approach such that invalid solutions are preliminarily discharged. This procedure abandons the global optimization in exchange for lower computational costs and a more robust estimation.

**Interval velocity consistency constraint.** Interval velocity is directly related to the geological formation, rock properties, stack, and migration (Buland *et al.*, 2011; Claerbout, 1985). Therefore a prior rough model is usually available. Moreover it can be limited between boundaries and this is intrinsically translated in a corresponding smooth RMS velocity. If we assume the  $V_{RMS}$  at location  $t_0$  to be known, the  $V_{RMS}$  at location  $t_0 + \Delta t$  has to be ranged as:

$$\sqrt{\frac{V_{RMS}^2(t_0) \cdot t_0 + \min(V_i^2) \cdot \Delta t}{t_0 + \Delta t}} < V_{RMS}(t_0 + \Delta t) < \sqrt{\frac{V_{RMS}^2(t_0) \cdot t_0 + \max(V_i^2) \cdot \Delta t}{t_0 + \Delta t}} \quad (5)$$

An analogues condition can be written also for a passed time location ( $t_0 - \Delta t$ ). By means of a matching pursuit approach, outliers can be preliminarily discharged and a valid solution can be obtained iteratively. By using this scheme a new double constraint is added at each iteration so that convergence to the solution is accelerated.

**Synthetic example.** We tested  $V_{RMS}$  builder on the synthetic Pluto data set. Pluto data set is one of several test sets released by the Subsalt Multiples Attenuation and Reduction Technology Joint Venture (SMAART JV). It is designed to emulate deep water subsalt prospects as found in the Gulf of Mexico. Depth true model and corresponding  $V_{RMS}$  are represented in Fig. 1a and Fig. 1b respectively.

The processing flow is set up by the following steps:

- 1) at the first iteration no a-priory model is used. Data is binned, NMO and stacked using a set of constant velocities profiles ranging from 4500 to 13500 ft/s;
- 2) coherency panels are produced and local maxima time locations are extracted starting from the water bottom position (assumed to be known);
- 3) for each location, RMS velocity corresponding to the maxima is computed;
- 4)  $V_{RMS}$  builder uses both monotonic and interval velocity consistent constraints to redefine valid picked time locations. A greedy approach starts from the global maxima of the entire panel. The following time location is chosen by a maximum energy criteria and, if constraints are fulfilled, the corresponding element of the solution is stored. This algorithm produces more and more constraints at each step leading to a stable convergence. The process ends when all the time locations selected at point 3) are processed;
- 5) RMS velocities at valid time locations are interpolated in time to get the final velocity profile;
- 6) once estimation has been done for all CMP locations a smoothing spatial filter is applied;
- 7) data is time migrated with the updated  $V_{RMS}$  model with about 10% of perturbation;
- 8) steps 2 to 6 are iterated to refine the model.

Test shows that two iterations are enough to reach convergence. Final  $V_{RMS}$  model is represented in Fig. 1c. This result shows that, even with such a complex model, automatic  $V_{RMS}$  builder performs a good job and the low-medium frequencies of the velocities are well retrieved.

In Fig. 2 we show a sub-sampled set of CRPs obtained by migrating the data using: a) uniform mean velocity (9000 ft/s); b) final resulting  $V_{RMS}$  model; c)  $V_{RMS}$  model obtained from true depth model. We can see that CRP are correctly aligned and they considerably differ from the ones computed using the true model just under the salts.

In Fig. 3 we show time migrated panels using: a) uniform mean velocity (9000 ft/s); b) final resulting  $V_{RMS}$  model; c)  $V_{RMS}$  model obtained from true depth model. Once again the panel obtained with the automatic  $V_{RMS}$  builder looks extremely coherent and very similar to the one computed using the true model.

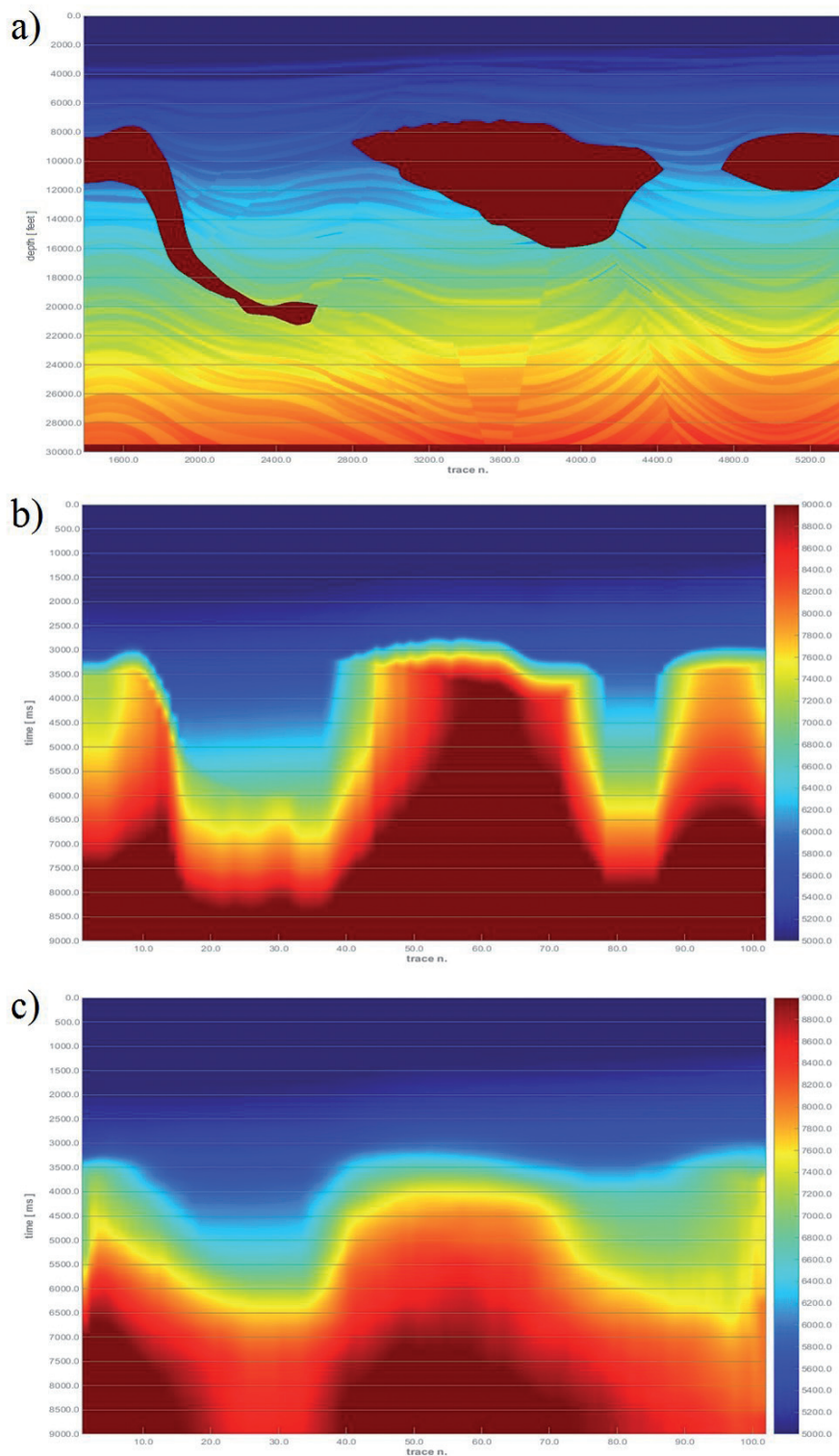


Fig. 1 – Velocity models: a) true depth model; b)  $V_{RMS}$  obtained from the true model; c) automatic  $V_{RMS}$  Builder result.

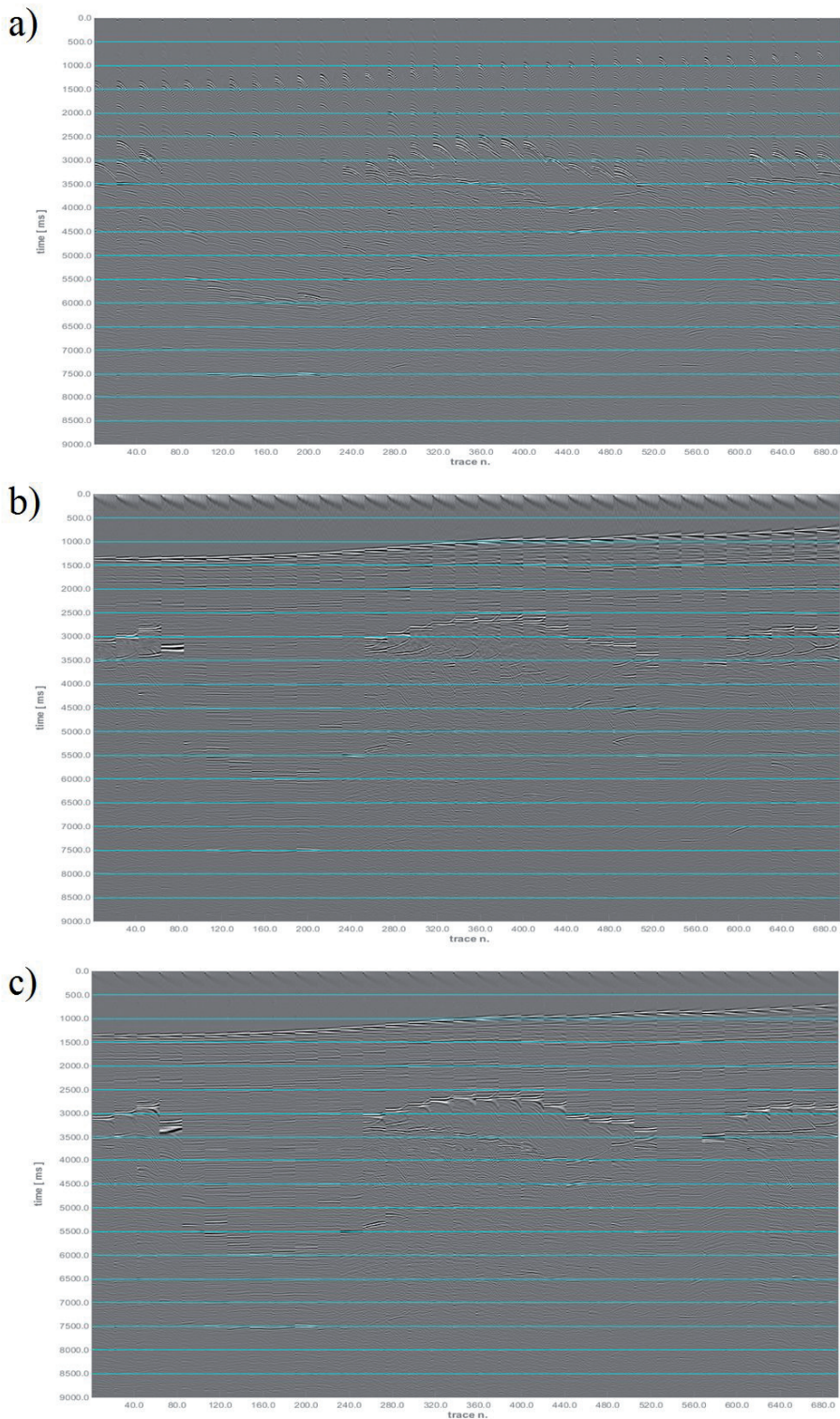


Fig. 2 – CRPs obtained by time migrating the data using: a) uniform velocity model; b) automatic  $V_{RMS}$  builder result; c)  $V_{RMS}$  obtained from the true model.

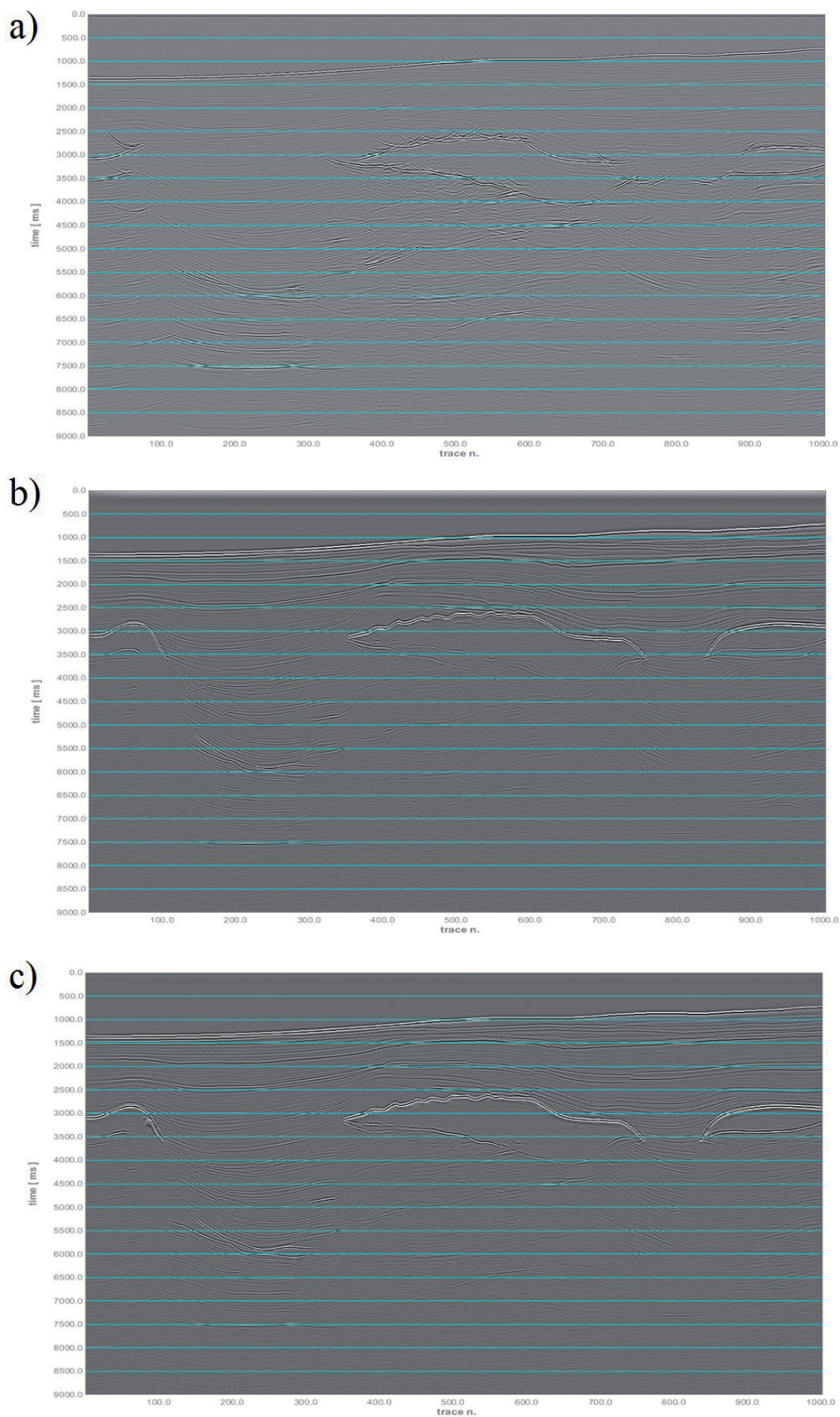


Fig. 3 – Stacked time migration of the data using: a) uniform velocity model; b) automatic  $V_{RMS}$  builder result; c)  $V_{RMS}$  obtained from the true model.

**Conclusions.** We described a method that allow to eliminate (or at least reduce) semblance manual picking. We developed a data driven  $V_{\text{RMS}}$  model building strategy that automatically pick velocity profiles giving flat CRP events. This is done by means of an iterative matching pursuit approach that allow to preliminarily discharge invalid outliers leading to a performing solution.

Results obtained from Pluto data set show that  $V_{\text{RMS}}$  builder allow to obtain good results also in complex velocity model scenarios with a consequent improving for the imaging.

**Acknowledgements.** The authors would like to thank Nicola Bienati (Eni Upstream and Technical Services) for fruitful discussions and the SMAART JV for providing the Pluto dataset.

## References

- Alkhalifah T.; 1997: *Velocity analysis using nonhyperbolic moveout in transversely isotropic media*. Geophysics, **62**, pp. 1839-1854.
- Alkhalifah T. and Tsvankin I.; 1995: *Velocity analysis for transversely isotropic media*. Geophysics, **60**, pp. 1550–1566.
- Biondi B.; 2006: *3D seismic imaging*. Society of Exploration Geophysicists, **14**, pp. 147.
- Buland A., Kolbjørnsen, O., and Carter, A. J.; 2011: *Bayesian dix inversion*. Geophysics, **76**, pp. R15-R22.
- Candès E. J., Romberg J. K. and Tao, T.; 2006: *Stable signal recovery from incomplete and inaccurate measurements*. Communications on pure and applied mathematics, **59**, pp. 1207-1223.
- Claerbout, J.; 1985: *Imaging the earth's interior*. Blackwell Scientific Publications,
- Fomel, S.; 2009: *Velocity analysis using AB semblance*. Geophysical Prospecting, **57**, pp. 311–321.
- Hastie T., Tibshirani R. and Wainwright M.; 2015: *Statistical Learning with Sparsity: The Lasso and Generalizations*. Chapman & Hall/CRC Monographs on Statistics and Applied Probability, **143**, pp. 83.
- Jones, I. F.; 2010: *Tutorial: Velocity estimation via ray-based tomography* First Break vol. **28**, February 2010
- Li Y. E. and Biondi B.; 2009: *Automatic velocity picking by simulated annealing*. Stanford Exploration Project, **138**, 1–10.
- Li Y. E. and Biondi B.; 2011: *Migration velocity analysis for anisotropic models*. 2011 SEG Annual Meeting. Society of Exploration Geophysicists.
- Neidell N. S. and Taner M. T.; 1971: *Semblance and other coherency measures for multichannel data*. Geophysics, **36**, pp. 482-497.
- Sarkar D., Baumel R. T. and Larner K. L.; 2002: *Velocity analysis in the presence of amplitude variation*: Geophysics, **67**, pp. 1664-1672.
- Sarkar D., Castagna J. P. and Lamb W.; 2001: *AVO and velocity analysis*: Geophysics, **66**, 1284-1293.
- Taner M. T. and Koehler F.; 1969: *Velocity spectra-digital computer derivation applications of velocity functions*. Geophysics, **34**, pp. 859-881.
- Toldi, J. L.; 1989: *Velocity analysis without picking*. Geophysics, **54**, pp. 191-199.
- Vieira, W. W., Leite, L. W. and Nunes, F. S.; 2011: *Automatic Picking in the Semblance Domain*. 12th International Congress of the Brazilian Geophysical Society.
- Yilmaz Ö.; 2001: *Seismic data analysis*. Society of Exploration Geophysicists, vol. **I**, pp. 292)

## LESS IS MORE: FROM VAN DER ROHE TO THE 4-CHANNEL SYSTEM FOR THE EFFICIENT AND HOLISTIC ACQUISITION OF SURFACE WAVES: AN URBAN CASE STUDY

G. Dal Moro<sup>1\*</sup>, S.R. Moustafa<sup>2,3</sup>, N. Al-Arifi<sup>2</sup>

<sup>1</sup> Department of Seismotectonics, Institute of Rock Structure and Mechanics, Prague, Czech Republic

<sup>2</sup> Geology and Geophysics Department, Faculty of Sciences, King Saud University, Riyadh, Saudi Arabia

<sup>3</sup> Seismology Dept., National Research Institute of Astronomy and Geophysics, Cairo, Egypt

**Introduction.** Nowadays, the analysis of surface wave propagation for depicting the shear-wave velocity ( $V_s$ ) vertical profile is routinely performed for a large number of applications ranging from crustal studies to Non-Destructive Testing (e.g. Ryden *et al.*, 2004; Prodehl *et al.*,

2013). In the last decade, several methods have been actually proposed in order to acquire data to analyze according to different (active and passive) procedures.

The critical point that must be considered in order to retrieve a reliable  $V_s$  profile, is that because of the intrinsic non-uniqueness of the solution that inevitably characterizes any methodology, the use of a single component cannot provide a fully constrained subsurface model (e.g. Scales *et al.*, 2001; Dal Moro, 2014).

For this reason, over the years, a number of solutions capable of handling and jointly analyze various datasets and components have been proposed (e.g. Arai and Tokimatsu, 2005; Picozzi and Albarello, 2007; Dal Moro, 2014; Dal Moro *et al.*, 2015a).

As a matter of facts, the design of acquisition and analysis procedures which are efficient (limited equipment and straightforward field procedures) and capable of providing a sufficiently large amount of data necessary for a robust inversion process, represents a challenging task which can be seen also from a so-to-speak aesthetic point of view.

The work and philosophical approach of the well-known German architect and designer Mies van der Rohe, who adopted minimalistic elements with multiple functional purposes, inspired the holistic acquisition and analysis system here briefly introduced. The pursued goal is to obtain the maximum possible outcome out of an extremely-light equipment and field efforts. The proposed *system* consists of a simple 4-channel seismograph, one 3-component (3C) geophone and four vertical-component geophones.

The acquired (active and passive) data, are used to determine up to six independent (but mutually related and complementary) objective functions that, altogether, fully describe the surface-wave propagation.

It is important to point out that, in general terms, an *acquisition system* is composed by the combination of several elements: the A/D (Analog-to-Digital) conversion unit (usually referred to as seismograph), a certain number of sensors (geophones or accelerometers), the seismic cables that transmit the signal to the A/D unit and the acquisition software that handles the data also possibly computing some quality check to ensure that no major problems occur during the acquisition procedures. The overall efficiency of the adopted *acquisition system* is determined by the combination of all these elements and actually depends on the quality of the weakest component so that, for instance, very high-quality geophones risk to be quite useless when a poorly designed and engineered A/D unit is used to convert and acquire the signals.

Data acquired while considering the considered system, are eventually jointly used to set up an extremely-constrained inversion, thus giving no room to ambiguities in the obtained  $V_s$  subsurface model.

After briefly introducing the fundamentals of the designed system and approach, we also present the analyses performed on a dataset acquired in a NW-Italy urban area.

**The designed system.** The design of the acquisition and analysis system described in the present paper represents the concrete realization of the paradigmatic van der Rohe's motto: *less is more*.

Differently than the standard multi-channel approach (24 vertical geophones actually provide a single *component*), here, the mindful use of a simple 4-channel seismograph, one 3C geophone and four vertical geophones, allows the determination of four components from active acquisitions and two from passive seismics.

In order to properly appreciate the value of the four components extracted from the active acquisitions, a clear understanding of the concept of *component* (with respect to the one of *number of geophones*) is crucial, and Fig. 1 will help clarifying the point.

If we consider the data that can be acquired by a 3C geophone in the framework of an active survey, we can define up to four *components* (for further details see Dal Moro *et al.*, 2015b):

- the THF (Love waves) group velocity spectrum;
- the group-velocity spectra of the Radial (RVF) and Vertical (ZVF) components of Rayleigh waves;

- the *Radial-to-Vertical Spectral Ratio* (RVSR) describing (clearly in relative terms) the amplitude ratio of the two components as a function of the frequency (thus enabling us to go behind the analysis of the velocities alone).

Since these four components are capable of fully describe the surface wave propagation, such a methodology [which can be used as a purely-active stand-alone application - see Dal Moro *et al.* (2015a, 2015b)] is here indicated as Holistic analysis of Surface waves (for the sake of brevity hereafter HS).

It must be clearly underlined that the radial and vertical components of Rayleigh waves are, in general terms, different, and such a difference is a crucial point that enables more-constrained analyses based on the multi-component *Full Velocity Spectrum* (FVS) approach (Dal Moro *et al.*, 2015b, 2015c).

On the other side, while considering the multi-channel data recorded for instance by 24 or 48 vertical-component geophones for MASW (*Multichannel Analysis of Surface Waves* - see e.g. Dal Moro, 2014) or ESAC (*Extended Spatial Auto-Correlation* - Ohori *et al.*, 2002), we are actually dealing with less information with respect to the described HS approach, since such classical multi-channel techniques actually provide information on just one component (in this case the phase velocities of the vertical component of Rayleigh waves).

Being an active methodology, the depth investigated through the HS approach will clearly depend on the adopted offset (Dal Moro *et al.*, 2015a, 2015b). From the logistical point of view it must be anyway considered that moving a single geophone is definitely faster and easier than moving an array of geophones. Considering for instance an urban environment, it is clearly possible to set the source on one side of a road and the geophone on the opposite, without significantly interfering with the circulation of traffic.

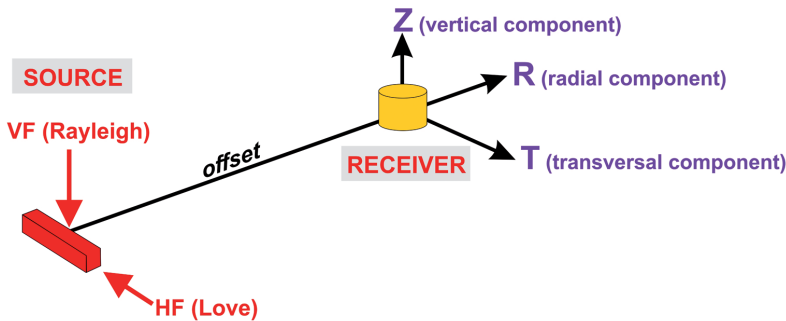


Fig. 1 – Active seismics (HS multi-component approach): the components acquired in case a single 3C geophone is used to record the signals produced while considering both Vertical and Horizontal forces (Rayleigh and Love waves, respectively). Further details in Dal Moro (2014) and Dal Moro *et al.* (2015b).

In addition to such a multi-component active dataset, for the present work we also considered two passive datasets/components acquired with the same 4-channel acquisition system: the HVSR curve (Arai and Tokimatsu, 2004) and the Rayleigh-wave (vertical component) effective dispersion curve (phase velocities) retrieved via *Miniature Array Analysis of Microtremors* (MAAM - see Fig. 2) (Cho *et al.*, 2013).

This latter technique relies on the passive data collected by an uneven number of vertical-component geophones deployed along a small-radius circular array (the triangle is the easiest and quickest solution), with an additional central geophone used for the noise compensation (Cho *et al.*, 2013). The frequency range where the retrieved phase velocities are properly defined is a function of the adopted radius (Fig. 2). For the most common near-surface applications that require the investigation of some tens of meters, the typically radii range from 0.5 up to about 5 m.

By fully and efficiently exploiting the data that can be collected through a simple 4-channel (triggerable) acquisition system, we are then able to collect a considerable amount of active and passive data then used to perform a joint analysis based on the following objective functions:

- 1) *Horizontal-to-Vertical Spectra Ratio* (HVSr) [3-channel passive seismics];
- 2) phase-velocity Rayleigh-wave dispersion curve from *Miniature Array Analysis of Microtremors* (MAAM) [4-channel passive seismics];
- 3) Active HS data recorded by means of the 3-component geophone and used for the holistic analysis of the group-velocity spectra of Rayleigh and Love waves (defined according to the *Multiple Filter Analysis* - e.g. Bhattacharya, 1983) also jointly with the RVSr (i.e., altogether, four components).

Since the phenomenology of Love waves is typically by far simpler than that of Rayleigh waves (Dal Moro, 2014; Dal Moro *et al.*, 2015c) but their analysis via miniature array techniques does not provide highly accurate results (Tada *et al.*, 2009), we decided to analyze their propagation from the active dataset (THF component depicted in Fig. 1).

By properly combining the data acquired by means of these three procedures (for which we just need a 4-channel acquisition system), we can potentially jointly analyze up to 6 components.

Since this would result in a so-to-speak *extreme* inversion procedure, here we decided to limit the presented analyses to just three components, chosen with the goal of anyway ensuring the most robust solution. The here-considered components are the HVSr curve, the effective dispersion curve of the vertical component of Rayleigh waves as defined via MAAM and the Love-wave group velocities (from the active acquisitions) here analyzed according to the FVS approach.

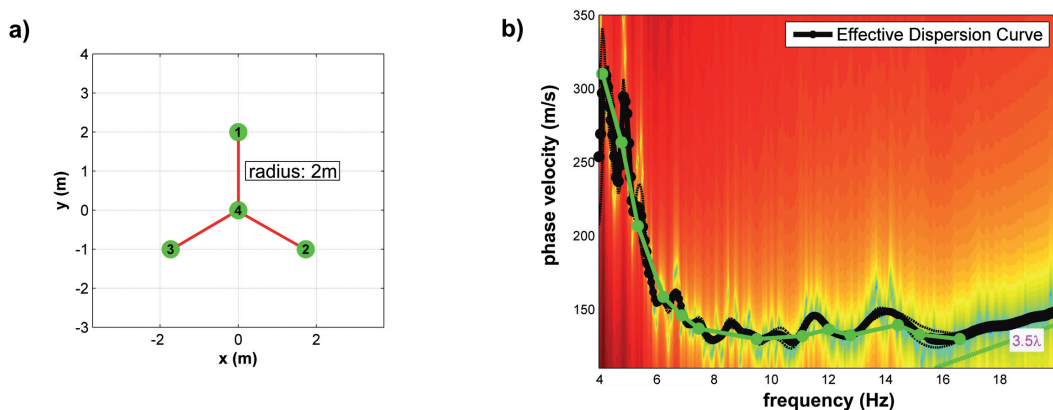


Fig. 2 – MAAM (passive seismics): a) acquisition setting (in this case the four vertical-component geophones are deployed along a 2-m radius circle); b) Rayleigh-wave effective dispersion curve (vertical component) determined while considering the data acquired for the case study illustrated in the present paper. The  $3.5\lambda$  line reports the upper frequency limit determined by spatial aliasing effects.

**An urban case study.** The site considered for this pilot study is located in the city center of La Spezia (NW Italy) where, as common for any urban area, logistical problems (related to the lack of available spaces) and a considerable amount of noise (related to several human, commercial and industrial activities), make the acquisition procedures quite challenging. Local stratigraphy is superficially dominated by a mixture of soft alluvial and marine sediments that, at deeper layers, turn into gravel-like materials.

The active (HS) and passive (MAAM) data to consider for the previously-described joint analyses were acquired according to the parameters reported in Tabs. 1 and 2. Passive data used

for determining the H/V spectral ratio were acquired (recording time 20 min; sampling rate 64 Hz) with the same 3C geophone used for the active HS acquisitions.

The source considered for the active data was a standard 8-kg sledgehammer and for the HF acquisition we used a simple and classical wooden beam.

As previously stated, for the sake of brevity here we will consider just three components: the HVSR, the Rayleigh-wave effective dispersion curve (i.e. the phase velocities defined via MAAM) and the Love wave group velocities (from the active dataset).

As also pointed out by Cho *et al.* (2013), during the analyses (being a pilot project data were acquired using various seismographs) we verified that the *Signal-to-Noise* (S/N) ratio determined by the adopted *acquisition system*, reveals as crucial in the acquisition of the data then used for the *Miniature Array Analysis of Microtremors*. The noise inevitably introduced in the data by non-optimized A/D units, can in fact represent a serious problem that cause incorrect (lower) phase velocities in particular in the low-frequency range (see the theoretical description in Cho *et al.*, 2013), being the noise compensation procedure capable of compensating the noise only when its level does not reach extreme values.

Following the procedure suggested by Cho *et al.* (2013), we divided the data into small windows and, in order to remove the possibly-pernicious effects of large-amplitude transients, removed all the segments having an average amplitude larger than a threshold fixed on the basis of the mean *root-mean-square* (*rms*) values of the acquired traces.

While the highest frequency which can be analyzed is limited by mere spatial aliasing effects and is then related to the adopted radius of the array [its value can be estimated in about 3.5 times the wavelength  $\lambda$  as defined in Cho *et al.* (2013): see the 3.5- $\lambda$  line reported in Fig. 2b], the lowest frequency that can be soundly determined depends also on the quality of the adopted acquisition system (that determines the amount of *electronic noise* that can significantly pollute the data and analyses, especially in the low-frequency range).

For the present pilot survey, we actually acquired 2 MAAM data sets (according to two different radii - see acquisition parameters reported in Tab. 1): while the 2-m radius allowed to retrieve the dispersion curve in the 4÷16 Hz frequency range (see Fig. 2b), the 5-m radius array provided reliable phase velocities approximately in the 2÷10 Hz range.

Tab. 1 - MAAM acquisition parameters (see also Fig. 2a).

sampling rate	4 ms (Nyquist frequency 125 Hz)
acquisition length	30 min
radius	2 m; 5 m
sensors	four vertical 2Hz geophones

Tab. 2 - HS acquisition parameters.

sampling rate	1 ms (1000 Hz)
acquisition length	1 s
offset	40 m
sensor	one 3-component 2Hz geophone (used also for the acquisition of the microtremor data used to define the HVSR)
stack	4

For validation purposes, MAAM analyses were compared with the results obtained from standard passive multi-channel bidimensional array (L-shaped 18-channel configuration), processed according to the ESAC methodology and the obtained dispersion curves resulted perfectly consistent.

HVSR curve was modeled according to Arai and Tokimatsu (2004), thus considering the amount of Love waves as one of the variables (for details see Dal Moro, 2014). The Rayleigh-wave effective dispersion curve (retrieved from MAAM and confirmed by the ESAC) was modelled according to Tokimatsu *et al.* (1992) and Love waves (from the active acquisition) via FVS analysis.

The outcomes of the performed joint analysis are summarized in Fig. 3, where the overall good agreement for all the three considered components is quite apparent (the identified  $V_s$  model is summarized in Tab. 3).

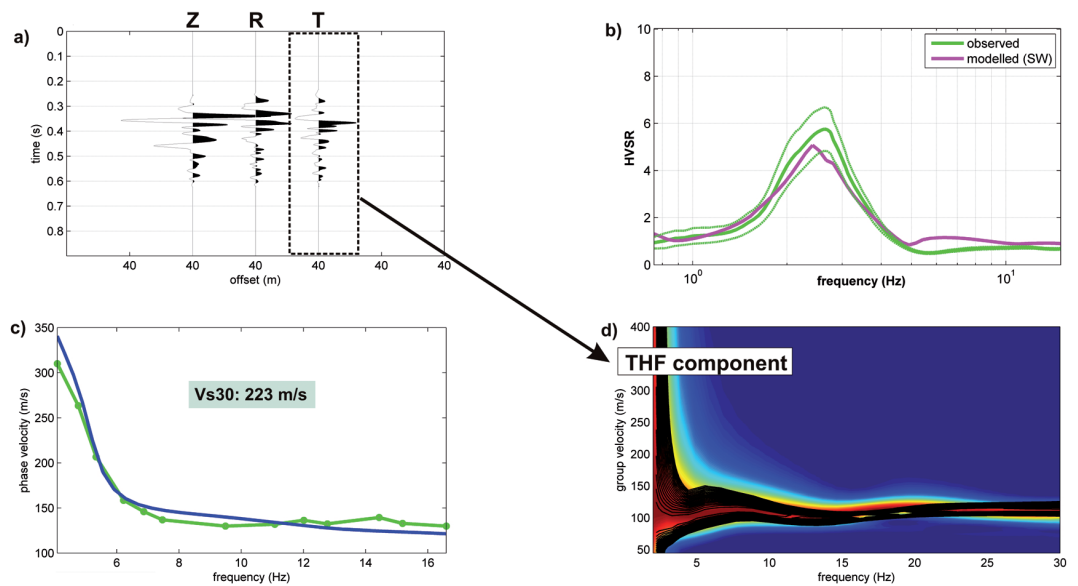


Fig. 3 – Joint analysis of the three considered components (the retrieved model is reported in Tab. 3): a) acquired active traces (vertical Z, radial R and transversal T components); b) field and synthetic HVSR curves; c) field (from MAAM) and synthetic Rayleigh-wave (vertical component) effective dispersion curves; d) field (background colors) and synthetic (overlain black contour lines) Love-wave group velocity spectra from the active acquisition (FVS analysis).

Tab. 3 - Retrieved  $V_s$  model down to a depth of 50 m.

thickness (m)	$V_s$ (m/s)
0.2	88
0.4	118
1	105
0.8	115
1	117
1	119
4.5	150
5.2	170
4	381
31.9	488

**Some conclusions.** In spite of the limited adopted equipment (one 4-channel seismograph, one 3C geophone and four vertical-component geophones) and the simple and straightforward field procedures, the proposed acquisition and analysis procedures can provide a significant amount of data to jointly analyze in order to fully constrain an inversion procedure eventually capable of providing a robust subsurface model free from ambiguities and non-uniqueness of the solution.

The adopted procedures appear particularly relevant especially in case of surveys to accomplish in urban areas (for instance for seismic-hazard studies), characterized by heavy logistical problems and limited room to deploy and move the sensors.

While the determination of the HVSR curve and the active acquisitions are not significantly influenced by the electronic noise produced by the acquisition system, the analyses performed according to the *Miniature Array Analysis of Microtremors* result instead strongly affected by this sort of noise and the use of high-quality A/D units results then mandatory.

Furthermore, an improper geophone coupling (in urban areas planting a geophone can be quite tricky) can determine low-quality data that would then mirror in poor analyses. In fact, because of the mathematics intrinsically involved in the *Miniature Array* analyses, even relatively-small differences in the amplitudes of the acquired traces can produce major problems and prevent from the determination of fully reliable dispersion curves. Data quality should be then checked already on the field even by simply computing the *rms* values for all the acquired traces. If the *rms* amplitude of one trace significantly deviates from the median value, that is the evidence that some problem occurred during the acquisition of that trace. Common causes are represented by a bad coupling, problems with the geophone-cable connections or, finally (worst case), by the fact that the coil of that geophone is not consistent with that of the other geophones (in this case the geophone must be substituted).

From the practical point of view is important to underline that while the HVSR and MAAM data necessarily refer to very local conditions, the active data refer instead to the average subsurface conditions between the source and the receiver. In case of significant superficial lateral variations, at the high frequencies (i.e. the shallowest layers) it is then possible a relatively poor match for the three objective functions here considered. For this reasons, HVSR and MAAM data should be considered only in the low-frequency range (incidentally often poorly defined in the active data).

**Acknowledgements.** The present work was partially supported by the *Visiting Professor Program* of the King Saud University (Riyadh, Saudi Arabia) and the authors are grateful to the *Deanship of the Scientific Research* of the King Saud University (Riyadh, Saudi Arabia) for the financial support (PRG-1436-06 Research Grant).

## References

- Arai H. and Tokimatsu K.; 2004: *S-wave velocity profiling by inversion of microtremor H/V spectrum*. Bull. Seism. Soc. Am., **94**, 53–63.
- Arai H. and Tokimatsu K.; 2005: *S-Wave velocity profiling by joint inversion of microtremor dispersion curve and horizontal-to-vertical (H/V) spectrum*. Bull. Seism. Soc. Am., **95**: 1766–1778
- Bhattacharya S.N.; 1983: *Higher order accuracy in multiple filter technique*. Bull. Seismol. Soc. Am., **73**: 1395–1406.
- Cho I., Senna S. and Fujiwara H.; 2013: *Miniature array analysis of microtremors*. Geophysics, **78**, KS13–KS23.
- Dal Moro G., Moura R.M. and Moustafa S.R.; 2015c: *Multi-component Joint Analysis of Surface Waves*. J. Appl. Geophysics, **119**, 128–138.
- Dal Moro G., Moustafa S.R. and Al-Arifi N.; 2015b: *Efficient acquisition and holistic analysis of Rayleigh waves*, Proceedings of the Near-Surface EAGE 2015 (Turin - Italy)
- Dal Moro G., Keller L. and Poggi V.; 2015a: A Comprehensive Seismic Characterization via Multi-Component Analysis of Active and Passive Data. First Break, 33, 45-53.**
- Dal Moro G.; 2014: *Surface Wave Analysis for Near Surface Applications*. Elsevier, ISBN 9780128007709, 252pp
- Ohori M., Nobata, A. and Wakamatsu K.; 2002: *A comparison of ESAC and FK methods of estimating phase velocity using arbitrarily shaped microtremor analysis*. Bull. Seism. Soc. Am., **92**, 2323–2332.
- Picozzi M. and Albarello D.; 2007: *Combining genetic and linearized algorithms for a two-step joint inversion of Rayleigh wave dispersion and H/V spectral ratio curves*. Geophys. J. Int., **169**, 189–200.

- Prodehl C., Kennett B., Artemieva I.M. and Thybo H.; 2013: *100 years of seismic research on the Moho*. Tectonophysics, **609**, 9–44.
- Ryden N., Park C.B., Ulriksen P. and Miller R.D.; 2004: *Multimodal Approach to Seismic Pavement Testing*. Journal of Geotechnical and Geoenvironmental Engineering, **130**, 636-645.
- Scales J.A., Smith M.L. and Treitel S.; 2001: *Introductory Geophysical Inverse Theory*. Open file, Samizdat Press, 193 pp. <http://samizdat.mines.edu>
- Tada T., Cho I. and Shinozaki Y.; 2009: *New Circular-Array Microtremor Techniques to Infer Love-Wave Phase Velocities*. Bull. Seism. Soc. Am., **99**, 2912–2926.
- Tokimatsu K., Tamura S. and Kojima H.; 1992: *Effects of Multiple Modes on Rayleigh Wave Dispersion Characteristics*. Journal of Geotechnical Engineering, **118**, 1529-1543.

## APPLICATION OF ATTRIBUTE-BASED AUTOMATED PICKING TO GPR AND SEISMIC SURVEYS

M. Dossi, E. Forte, M. Pipan

*Department of Mathematics and Geosciences (DMG), University of Trieste, Italy*

**Introduction.** An accurate reflection picking, as independent as possible from the subjectivity of the interpreter, is of paramount importance when performing both qualitative (e.g. stratigraphic interpretation) and quantitative (e.g. amplitude inversion) analyses of several wave-field geophysical surveys. Automated picking processes can be used to facilitate interpretation and to recover several parameters and attributes (Chopra and Marfurt, 2005) from the recorded profile, most importantly the reflected amplitudes and the two-way traveltimes, which can then be used to estimate the main impedance contrasts in the subsurface. In ground penetrating radar (GPR) surveys, examples of application include the identification of contaminants in near-surface hydrogeological settings (Backer, 1998; Babcock and Bradford, 2013); the inspection and maintenance of roads through the identification of damaged sections (Saarenketo and Scullion, 2000); and the monitoring of glaciers in terms of their temporal variations in stratigraphy and water content (Forte *et al.*, 2014a, 2014b; Colucci *et al.*, 2015). In seismic surveys, an accurate picking can be used for first-breaks detection and data processing (Sabbione and Velis, 2010); amplitude-versus-offset analysis (AVO; Castagna and Backus, 2007); and the identification of faults in a profile, which are characterized by discontinuities in the picked events (Hoyes and Cheret, 2011).

Several picking techniques exist (Dorn, 1998), and they differ in terms of 1) their adopted picking criteria, like for example manual picking, amplitude cross-correlation, or interpolation between control points (seeds); 2) the assumptions made with regards to the analyzed data set, for example that the recorded events are locally smooth; 3) the accuracy of the picked results and their dependence on the interpreter's subjectivity and experience. We developed an automated process designed to accurately detect, and mark as a horizon, any event that shows lateral phase continuity, and to select specific reflection phases for subsequent analysis and interpretation. In this paper, we give a short description of the main features of the implemented algorithm (more details in Dossi *et al.*, 2015a, b; Forte *et al.*, 2015), and show a few examples of its application to both GPR and seismic data sets.

**Automated picking.** The algorithm starts by performing attribute analysis on the recorded data set, also known as complex trace analysis (Taner *et al.*, 1979; Barnes, 1996, 2007), separating the signal into its reflection strength (also referred to as instantaneous amplitude, or trace envelope) and the cosine of its instantaneous phase (also referred to as cosine phase). The cosine phase profile allows to follow reflections more accurately with respect to the

original amplitude section. The algorithm uses this feature to track any event with lateral phase continuity, connecting signal phases with the same polarities and close arrival times. Given its independence from the reflection strength, the system can even track events characterized by lateral amplitude variations or changes in the shape of the reflected wavelet. The picking procedure is nevertheless sensitive to the presence of noise and interference in the recorded profile. For example, a hyperbolic diffraction can intersect an unrelated reflection and deform horizons originating from such reflection, while noise-related distortions of the signal phases can interrupt the tracking of an event. Therefore, the analyzed profiles may require a certain degree of processing before picking. The algorithm itself can reduce such effects by automatically connecting horizons which belong to the same coherent event but were separated by a few distorted phases. This is done by using close parallel horizons as patches across the gaps, and it has the effect of reducing the total number of horizons, while increasing their average length. Once all possible horizons have been constructed, they are superimposed on the recorded profile for visual interpretation. Optional constraints on the reflection strength can be set, in case the interpreter wants to selectively display events that reach specific energy thresholds.

After picking, the algorithm automatically analyzes each horizon, searching for close sub-parallel events that can be considered part of the same reflection. The aim is to obtain single horizons representing each reflection, using either phase or energy-based constraints, in order to reduce the total number of displayed picked events, and therefore improve the interpretation. The phase-based method groups together sub-parallel horizons by reconstructing the reflected wavelet in each of them and then confronting their shapes. The wavelets are reconstructed by averaging the cosine phase along each horizon, which preserves the reflected signal while removing other unrelated events. If the two shapes are similar by means of cross-correlation, the two sub-parallel horizons are considered to be part of the same reflection. Under favorable conditions of high signal-to-noise ratio and absence of interfering events, this process (also called phase assessment) can be used to identify the initial phase (as well as later ones) in each reflection, and therefore its polarity, which allows to reconstruct the subsurface reflectivity. Specific phases can then be selected for further analysis and interpretation. The energy-based method is instead used when lateral signal variations, caused by either dispersion, noise, or interference, do not allow the accurate reconstruction and comparison of the reflected wavelets. In this case the recorded profile is separated into energy packages by defining the main peaks of the reflection strength. Sub-parallel horizons from the same package are then grouped into the same event using statistical analyses of their arrival times. Specific horizons can then be selected by using either energy or time-related constraints with respect to the peak reflection strength in each energy package.

**Examples of application.** *Stratigraphic interpretation (reflection seismics).* In this section, we apply the automated picking to a seismic profile acquired in 2010 in the west Mediterranean Sea by the Istituto Nazionale di Oceanografia e Geofisica Sperimentale (OGS), as part of the WS10 exploration project (Geletti *et al.*, 2014). Attribute analysis allows to clearly define the subsurface structures by disregarding the amplitude information, as it can be noticed from the cosine phase profile in Fig. 1A. In the analyzed pre-stack time migrated profile, three different domains can be identified, namely a sedimentary basin (S), the seismic basement (B) and a salt dome (D), all showing slightly different seismic signatures. As previously discussed, we applied the energy-based grouping method, due to the inherent variation of the reflected wavelet caused by seismic processing (e.g. stacking), which prevents its accurate reconstruction through cosine phase averaging. The horizon grouping results are shown in Fig. 1B, superimposed on the amplitude section. The algorithm divided the profile into energy packages and selected from each reflection those horizons with an average energy equal to at least 50% of the peak reflection strength in the respective package. This selection method can be sensitive to vertical resolution, which can cause close parallel reflections to be grouped into the same energy package so that, although accurately picked, the weaker one is not automatically displayed after grouping (e.g.

white arrow in Fig. 1B). Nevertheless, the results are consistent in all the domains, and allow to correctly mark the sedimentary sequence, its lateral boundaries, and even the salt dome intrusion. Such area is indeed a complex target for all the existing picking procedures, due to the high velocity contrast between the salt and the intruded sediments, as well as the abrupt lateral changes in the horizon continuity.

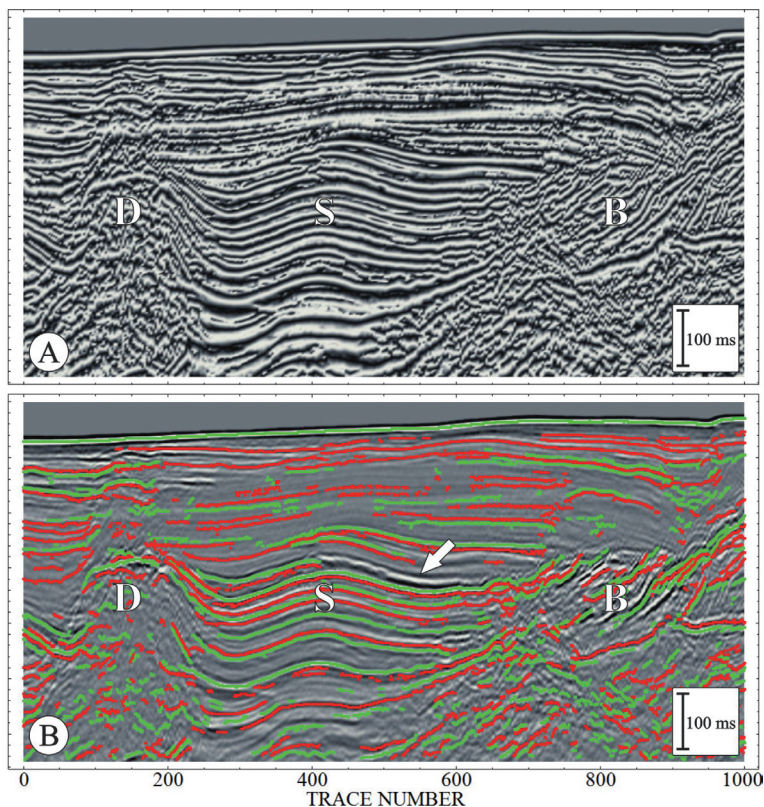


Fig. 1 – Application of the picking procedure to a reflection seismic profile. The figure shows: A) the cosine phase section, and B) the resulting picked reflections, superimposed on the amplitude profile, after applying on the horizons energy thresholds equal to 50% of the peak reflection strength in each energy package. Positive amplitudes are marked in green, negative amplitudes in red. The profile images a sedimentary basin (S), the seismic basement (B) and a salt dome (D). The white arrow indicates an example of distinct parallel reflections automatically grouped within the same energy package, preventing the weaker one from being displayed. Refer to the text for further details.

*Road inspection (GPR).* In this section, we analyze a common offset (CO) GPR data set acquired over an airport runway. The recording system was a Malå Geoscience ProEx GPR, connected to 500 MHz ground-coupled bistatic shielded antennas. An exemplary profile, acquired using a 0.185 ns sampling interval and an average 0.19 m trace spacing, is shown in Fig. 2A. The applied processing sequence consists of DC removal, drift correction, background removal, and band-pass filtering. Amplitude recovery algorithms were not used, and so the signal shows a steady decrease of amplitude with depth (Fig. 2A). Nevertheless, as previously discussed, the cosine phase allows to correctly track laterally continuous events (Fig. 2B), even without any applied gain function. More chaotic results can be noticed in the deeper part of Fig. 2B, where the signal-to-noise ratio is lower, preventing the identification of clear coherent structures. However, most of these artificial horizons are automatically disregarded during the described phase-based horizon grouping process, whose results are displayed in Fig. 2C. In fact,

the figure shows those horizons which were automatically identified as part of the first three phases of reflections with at least two identified phases, which means that each horizon must have at least one recognized sub-parallel event in order to be displayed. These requirements remove noise-related horizons, but they can also affect areas characterized by interference or overlapping. For example, some recognizable structures in the shallow region (0-15 ns), clearly marked by the algorithm in Fig. 2B, are not automatically displayed in Fig. 2C, because the local quality of the recorded signal prevents such horizons from meeting the thresholds set for the phase-based grouping method. The horizons shown in Fig. 2C are the result of a totally automated procedure, with only a few required control parameters and thresholds being set by the interpreter. However, the algorithm is able to identify the base of the runway pavement (H1), made by concrete plates, as well as other features interpreted as natural sedimentary contacts, with the two most apparent layer interfaces marked as H2 and H3.

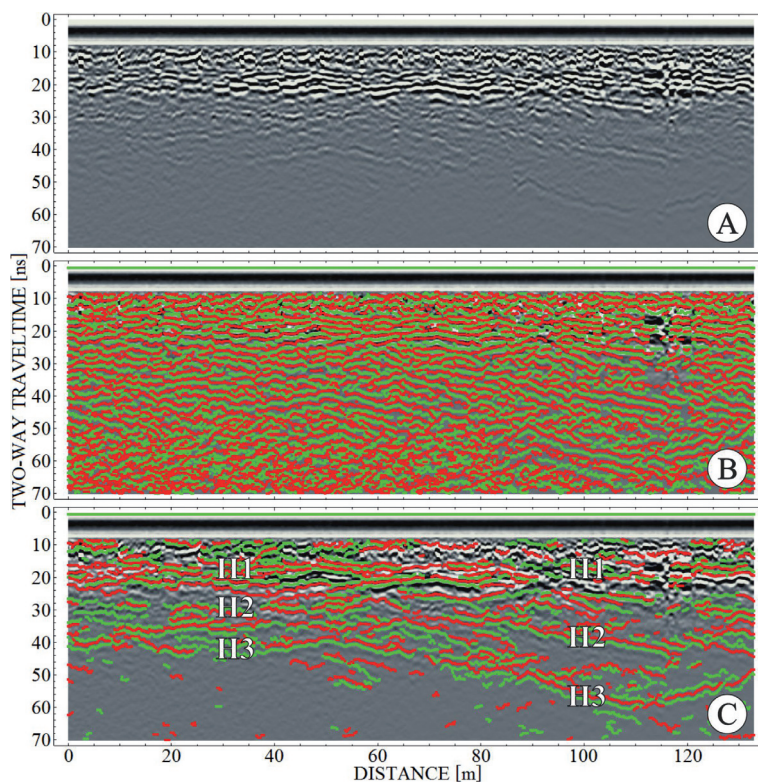


Fig. 2 – Application of the picking procedure to an airport runway 500 MHz CO GPR profile. The figure shows: A) the processed profile; B) all the resulting picked horizons; and C) those horizons automatically identified as one of the first three phases of reflections with at least two recognized phases. Positive amplitudes are marked in green, negative amplitudes in red. The labels H1, H2 and H3 highlight the three main layer interfaces described in the text.

*Glacier monitoring (GPR).* In this section, the picking algorithm is applied to a CO GPR data set acquired over the Prevala glacieret (Forte *et al.*, 2014a), which is located at an elevation of 1830-1960 m a.s.l. in the Julian Alps, near the border with Slovenia. The recording system was a ProEx Malá Geoscience GPR equipped with 250 MHz shielded antennas, with a 0.4 ns sampling interval and an average 0.2 m trace spacing. The latter parameter was measured with an odometer that was also used as a triggering device. The recorded profile is shown in Fig. 3A, and contains several features, including a well stratified surface layer (L), a central debris layer (D) producing several hyperbolic diffractions, and older deeper ice reaching the glacieret base

(B). The applied processing sequence consists of DC removal, drift removal, spectral analysis and band-pass filtering, spatial filtering to remove ringing and late arrivals of the ground wave, spherical divergence correction, and time migration. In the last two steps, a constant velocity equal to  $20 \text{ cm}\cdot\text{ns}^{-1}$  was used: this value was estimated by integrating the analysis of dedicated common mid-point (CMP) gathers with direct measurements obtained in a nearby snow pit dug concurrently with the GPR survey. The results of the picking and phase-based grouping method are shown in Fig. 3B, and include those horizons automatically identified as part of the first three phases of reflections with at least three identified phases, which means that each horizon must have at least two recognized sub-parallel event in order to be displayed. The complex nature of the analyzed data set offers an interesting test for the picking procedure, since the profile contains not only laterally continuous sub-horizontal reflectors, but also discontinuous reflections and interfering diffractions caused by the debris layer, some of which are not fully corrected by the applied migration algorithm. Moreover, in the deepest part of the profile there are low amplitude discontinuous reflectors, which were interpreted as the internal ice layering and the glacieret base. Although with different levels of accuracy in different parts of the profile, all the main features have been properly detected by the applied procedure.

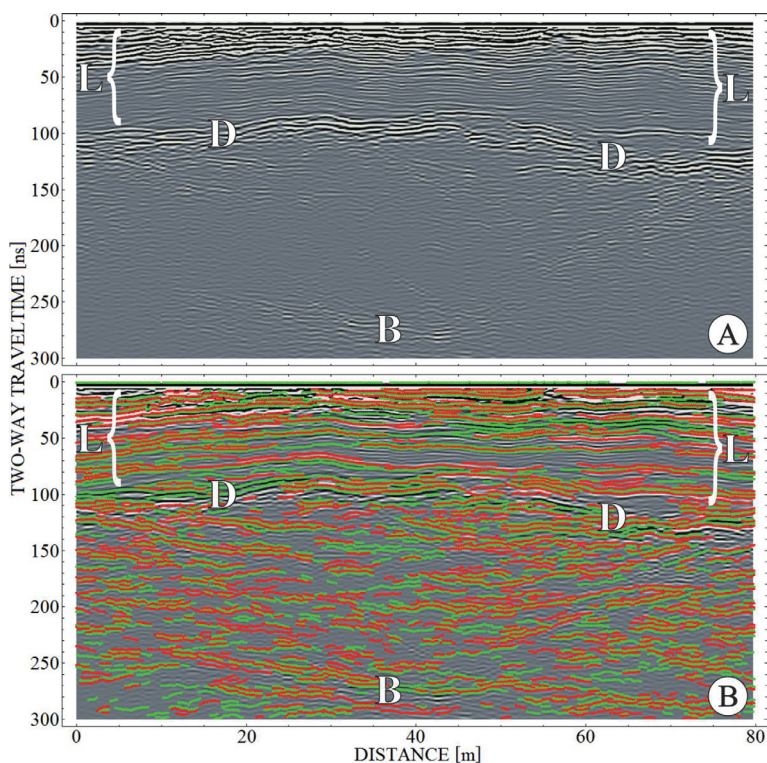


Fig. 3 – Application of the picking procedure to a glaciological 250 MHz CO GPR profile. The figure shows: A) the processed GPR profile; and B) those horizons automatically identified as one of the first three phases of reflections with at least three recognized phases. Positive amplitudes are marked in green, negative amplitudes in red. The applied labels highlight the layered firm (L); a mixed ice and debris layer (D); and the glacieret base (B), respectively.

**Discussion.** The proposed picking method presents two main advantages with respect to other commonly used techniques: 1) it is mostly independent from the interpreter, not needing any initial manually picked seed for horizon tracking, and with just a few required control parameters and thresholds; 2) the interpreter can check the results at each step in order to evaluate the performance, manually intervene in complex areas where the algorithm might fail,

and change parameters or even the used approach (e.g. by switching between the energy-based and the phase-based grouping methods). Indeed, the entire procedure (i.e. picking, grouping, and even the phase assessment) is implemented as an interactive process rather than a “black box”.

We showed the versatility of the algorithm, which can be successfully applied to both reflection seismic and GPR data sets, as well as to both CO and CMP gathers. Furthermore, the process can equally perform at different levels of complexity in terms of structural domains and subsurface material variations. We demonstrated that data processing is not a critical issue for the procedure, although both picking and grouping performances are improved with higher signal-to-noise ratios. Nevertheless, the algorithm can be applied to data sets with just basic processing and without (or with limited) amplitude recovery, which allows it to pick amplitudes free from possible subjective distortions caused by the interpreter’s assumptions regarding the propagation velocity and signal dissipation in the subsurface materials. This is very important in case the picking results are to be used for further analysis (e.g. AVO) or inversion processes (e.g. amplitude inversion).

**Conclusion.** We presented a few examples of application of an automated process designed to detect and track, in an accurate and objective way, reflections inside a recorded data set by exploiting their lateral phase continuity. The results, obtained in different profiles from both reflection seismic and GPR surveys, are quite accurate, since they are able to mark most of the recorded reflections and their different phases, with only a few exceptions in more complex areas characterized by noise or interference. Although the presented examples were limited to just 2D sections, the procedure can be easily extended to 3D data sets. A few input parameters must be selected and carefully evaluated by the interpreter, nevertheless the degree of subjectivity is greatly reduced with respect to other commonly used picking algorithms, leading to a faster and more objective process. Further improvements can be achieved by using integrated attributes as additional thresholds, or by evaluating the behavior of other physical parameters, such as changes in the spectral distribution.

**Acknowledgments.** This research is partially funded by the “Finanziamento di Ateneo per progetti di ricerca scientifica – FRA 2014” of the University of Trieste. We thank Dr. Renato R. Colucci for his contribution in the acquisition and interpretation of the glaciological survey. The airport runway GPR section is property of Esplora srl, which is gratefully acknowledged. We also thank the “Istituto Nazionale di Oceanografia e Geofisica Sperimentale - OGS” for the permission to use and publish their proprietary seismic data, which can be purchased from them for scientific or industrial purposes.

## References

- Babcock E., and Bradford J., 2013, “Detecting subsurface contamination using Ground Penetrating Radar and Amplitude Variation with Offset analysis”, Proceedings of the 7th International Workshop on Advanced Ground Penetrating Radar, Nantes, France, pp. 1-5, ISBN 978-1-4799-0937-7
- Baker G.S., 1998, “Applying AVO analysis to GPR data”, Geophysical Research Letters, vol. 25, no. 3, pp. 397-400
- Barnes A.E., 1996, “Theory of 2-D complex seismic trace analysis”, Geophysics, vol. 61, no. 1, pp. 264-272
- Barnes A.E., 2007, “A tutorial on complex seismic trace analysis”, Geophysics, vol. 72, no. 6, pp. W33-W43
- Castagna J.P., and Backus M.M. (Eds.), 2007, “Offset-dependent reflectivity: Theory and practice of AVO analysis”, SEG, Investigations in Geophysics, vol. 8, 7th edition, 348 pp., ISBN 978-1-5608-0059-0
- Chopra, S., and Marfurt K.J., 2005, “Seismic attributes - A historical perspective”, Geophysics, vol. 70, no. 5, pp. 3SO-28SO
- Colucci R.R., Forte E., Boccali C., Dossi M., Lanza L., Pipan M. and Guglielmin M., 2015, “Evaluation of internal structure, volume and mass of glacial bodies by integrated LiDAR and Ground Penetrating Radar surveys: The case study of Canin Eastern Glacieret (Julian Alps, Italy)”, Surveys in Geophysics, vol. 36, pp. 231-252
- Dossi M., Forte E., and Pipan M., 2015a, “Automated reflection picking and polarity assessment through attribute analysis: Theory and application to synthetic and real ground-penetrating radar data”, Geophysics, vol. 80, no. 5, pp. H23-H35
- Dossi M., Forte E., and Pipan M., 2015b, “Auto-picking and phase assessment by means of attribute analysis applied to GPR pavement inspection”, Proceedings of the 8th International Workshop on Advanced Ground Penetrating Radar, Florence, Italy, *in press*
- Dorn, G.A., 1998, “Modern 3-D seismic interpretation”, The Leading Edge, vol. 17, pp. 1262-1269

- Forte E., Dossi M., Pipan M., and Colucci R.R., 2014a, "Velocity analysis from common offset GPR data inversion: theory and application to synthetic and real data", *Geophysical Journal International*, vol. 197, pp. 1471-1483
- Forte E., Dossi M., Colle Fontana M., and Colucci R.R., 2014b, "4-D quantitative GPR analyses to study the summer mass balance of a glacier: a case history", *Proceedings of the 15th International Conference on Ground Penetrating Radar*, Brussels, Belgium, pp. 352-356, ISBN 978-1-4799-6789-6
- Forte E., Dossi M., Pipan M., and Del Ben A., 2015, "Automated phase attribute-based picking applied to reflection seismics", *Geophysics*, *submitted*
- Geletti, R., Zgur F., Del Ben A., Buriola F., Fais S., Fedi M., Forte E., Mocnik A., Paoletti V., Pipan M., Ramella R., Romeo R., and Romi A., 2014, "The Messinian Salinity Crisis: new seismic evidence in the West-Sardinian Margin and Eastern Sardo-Provençal basin (West Mediterranean Sea)", *Marine Geology*, vol. 351, pp. 76-90
- Hoyes J., and Cheret T., 2011, "A review of 'global' interpretation methods for automated 3D horizon picking", *The Leading Edge*, vol. 30, pp. 38-47
- Saarenketo T., and Scullion T., 2000, "Road evaluation with ground penetrating radar", *Journal of Applied Geophysics*, vol. 43, no. 2-4, pp. 119-138
- Sabbione J.I., and Velis D., 2010, "Automatic first-breaks picking: New strategies and algorithms", *Geophysics*, vol. 75, no. 4, pp. V67-V76
- Taner M.T., Koehler F., and Sheriff R.E., 1979, "Complex seismic trace analysis", *Geophysics*, vol. 44, no. 6, pp. 1041-1063

### 3D MAGNETOTELLURIC RESPONSE IN PRESENCE OF RESISTIVITY DISPERSION: SNAKE RIVER PLAIN (IDAHO) EXAMPLE

R. Esposito<sup>1</sup>, A. Troiano<sup>2</sup>, M.G. Di Giuseppe<sup>2</sup>, D. Patella<sup>3</sup>, C. Troise<sup>2</sup>, G. De Natale<sup>2</sup>, R.M. Castelo Branco<sup>1</sup>

<sup>1</sup> Federal University of Ceará, Fortaleza, Brazil

<sup>2</sup> Istituto Nazionale di Geofisica e Vulcanologia - Osservatorio Vesuviano, Naples, Italy

<sup>3</sup> Department of Physical Sciences, University Federico II, Naples, Italy

**Introduction.** Resistivity dispersion is a known phenomenology, which in geophysics constitutes the basis of the Induced Polarization (IP) prospecting method (Seigel, 1959; Wait, 1959; Bertin and Loeb, 1976; Sumner, 1976; Fink *et al.*, 1990). In the frequency domain (FD), the dispersion consists in a variation of the resistivity parameter as the frequency of the exciting current is changed. The dispersive resistivity, called impedivity (Patella, 1993), is a complex function of frequency. At vanishing frequency, however, the impedivity is real and coincides with the classical resistivity parameter used in DC geoelectrical methods. A real asymptote is also approached by the impedivity as frequency tends to infinity.

It has been shown that the electrical dispersion phenomenology can influence the magnetotelluric (MT) response (Stoyer, 1976; Patella, 1987). The detection and spatial definition of impedivity effects by MT can give a notable contribution to the understanding of the rock physical properties, well beyond the limited exploration depths of some tens m, reachable by the standard Induced Polarization (IP) equipments. Hydrocarbon and geothermal exploration are application fields, where MT is an ideal approach to detect dispersion-affected zones. These zones are fractured portions of rock, which have undergone diffuse alterations due to chemical interaction with uprising light hydrocarbons and hot fluids. These altered zones are considered reliable markers of the presence of exploitable reservoirs underneath. Dispersion effects in MT were experimentally recognized and modeled by 1D and 2D tools in volcanic and geothermal areas (Coppola *et al.*, 1993; Patella *et al.*, 1991; Giammetti *et al.*, 1996; Di Maio *et al.*, 1997, 2000; Mauriello *et al.*, 2000, 2004), and in hydrocarbon exploration (e.g., He *et al.*, 2010).

The paper analyses the 3D magnetotelluric (MT) response in presence of resistivity frequency dispersion. The aim of this paper is to further study the influence of the electric dispersion on MT, by analyzing the synthetic responses generated by a 3D body. 3D IP effects have

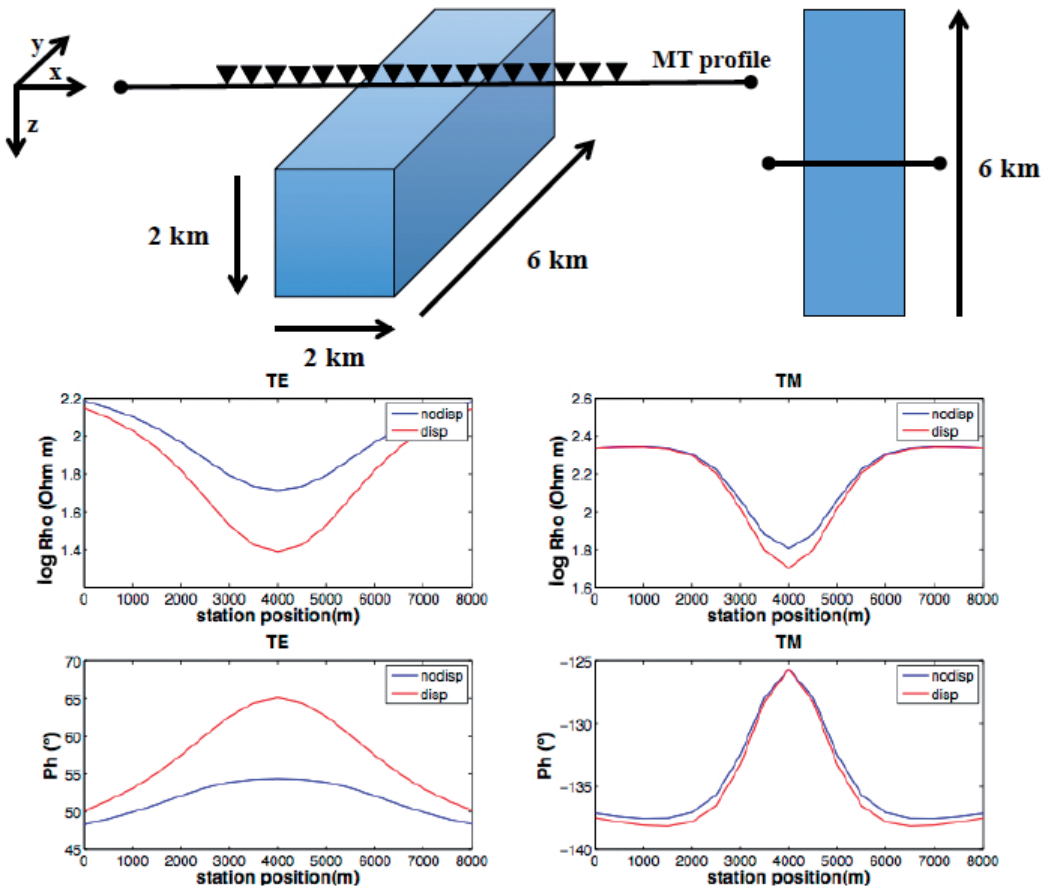


Fig. 1 – At the top the 3D model and the selected profiles with corresponding station sites on the left, on the right the model seen from above. At the bottom modulus (top diagrams, in  $\Omega$  m) and phase (bottom diagrams, in deg.) of the two orthogonal TM and TE modes of the MT apparent impedivity response against distance (in m) along the profile. The blue curves refer to the reference non dispersive response, while the red curves to the dispersive case.

gained widespread interest also in TDEM, FDEM and LOTEM prospecting, as documented in many papers, recently appeared (e.g., Chang-Chun and Bin, 1994; Hoheisal *et al.*, 2004; Zaslavsky *et al.*, 2011; Marchant *et al.*, 2014). In the present MT simulations, the 3D body is a dispersive conductive prism immersed in a non-dispersive resistive half-space. This resistivity contrast is motivated by previous simulations on 1D and 2D models. Dispersive conductive layers sandwiched between dispersion-free resistive layers (1D), and dispersive conductive, infinitely long prisms hosted in a dispersion-free resistive half-space (2D) have shown the most remarkable distortions (Mauriello *et al.*, 1996; Esposito and Patella, 2009). Moreover, such a model, by a proper choice of the prism’s size and depth, can be useful to interpret MT data in the prospection for oil and geothermal reservoirs (Pellerin *et al.*, 1996; Zhdanov and Keller, 1994). A MT field dataset, related to a geothermal exploration program in the eastern Snake River Plain, Idaho, (Stanley, 1982), is re-analyzed within a 3D framework, in order to highlight the greater interpretative potential that rises from the inclusion of 3D dispersion effects in MT data analysis.

**3D simulation of dispersive effects in MT.** Fig. 1 shows the 3D model assumed for studying the IP effects in MT and the responses generated by the body. A horizontal dispersive prism with resistivity  $\rho_0=10 \Omega\text{m}$  is buried in a non-dispersive half-space with resistivity  $200 \Omega\text{m}$ . The

3D body has horizontal length of 6 km along the  $y$ -axis and square edges of  $2 \times 2$  km<sup>2</sup>. The top face is located at 2 km depth. The simulations have been done along a 8 km long profile parallel to the  $x$ -axis which crosses the prism's mid-length. 17 MT station points, spaced 500 m from each other, have been assumed along the profile.

The IPFD spectrum in rocks is mostly modeled using the Cole-Cole type impedivity function  $\rho^{CC}(\omega)$  (Cole and Cole, 1941), given as

$$\rho^{CC}(\omega) = \rho_0 \{1 - m [i\omega\tau^c / (1 + i\omega\tau^c)]\}. \quad (1)$$

In Eq. 1,  $i = \sqrt{-1}$ ,  $\omega$  is the angular frequency,  $\rho_0$  is the DC resistivity, and  $m \in [0,1]$ , known in mining geophysics as chargeability (Seigel, 1959), is the IP amplitude, defined as  $m = (\rho_0 - \rho_\infty) / \rho_0$ , where  $\rho_\infty \in [0, \rho_0]$  is the resistivity at infinite frequency. Moreover,  $c \in [0,1]$  is the decay spectrum flattening factor and  $\tau \geq 0$  is the main time constant.

For the sake of conciseness, only one example of simulation is presented, which refers to the following Cole-Cole parameter set for the dispersive prism:  $m=0.9$ ,  $\tau=10$  s and  $c=0.75$ , the blue line refers to the reference non-dispersive case and the red lines to the dispersive assumption. Along the profile, centered over the prism (Fig. 1), the departure of the red lines from the reference blue lines, for both modulus and phase of the TE and TM modes, is very evident. The IP effect manifests with a more pronounced minimum of both the TE and TM apparent impedivity modulus, centered above the median axis of the 3D dispersive body. The amount of distortion of the MT response over a polarizable body depends on the values assigned to the Cole-Cole parameters,  $m$ ,  $\tau$  and  $c$ . Mauriello *et al.* (1996) gave a detailed overview on this topic, and inferred from 2D simulations that high values of  $m$  (not less than 0.75) and  $\tau$  (not less than 100 s) are ideal for dispersion effects to be recognizable in MT measurements. They also showed that the TE is always the most distorted MT mode. Esposito and Patella (2009) showed that  $c$  has practically no remarkable distortion effect in MT on 1D structures. The low influence of  $c$  was also inferred by Mauriello *et al.* (1996) in 2D cases.

The results from a great number of simulations above the model in Fig. 1, carried out following the same approach as in Mauriello *et al.* (1996) by changing  $m$  and  $\tau$  with fixed  $c$ , fully confirm all of the above conclusions. A further consideration is that visible distortion effects can be obtained even when the  $m$  and  $\tau$  vary in opposite directions. The sense is that the choice of an exceedingly low value of one of them must be compensated by a quite high value of the other one.

**Snake river plain example.** We now show a field example already studied by Mauriello and Patella (1999) in the frame of the probability tomography imaging. The area is the eastern Snake River Plain (SRP), Idaho, where a MT profile was performed by Stanley (1982), near the Idaho National Engineering and Environmental Laboratory. The SRP is an arcuate depression bounded on both sides by the Basin and Range structures, and for much of its extent it is underlain by basalt and interbedded continental Quaternary and Tertiary sediments (Mabey, 1982). Mauriello and Patella (1999) applied the 2D probability tomography imaging to the SRP TM and TE pseudosections in Fig. 2 and evinced within the SRP depression a laterally bounded conductive slab with lateral extension of about 17 km and a mean depth to its top of about 2 km.

Dispersion effects were also admitted, in order to explain the occurrence of a charge polarity inversion at the top edges of the slab and a tightening of the same edges as frequency decreases. Using the 2D dispersive MT forward modeling by Mauriello *et al.* (1996), the 2D structure depicted in Fig. 2 was then proposed, as best conforming to the large-scale geometry and dispersion inferences from the probability tomography sections. Finally, by comparing the synthetic TM and TE pseudosections from the 2D model in Fig. 2 with the original ones, Mauriello and Patella (1999) found a good matching of the two TM pseudosections, while the TE ones were judged not properly conforming to each other. They attributed this discrepancy to the circumstance that the TE mode is much more affected than the TM mode whenever

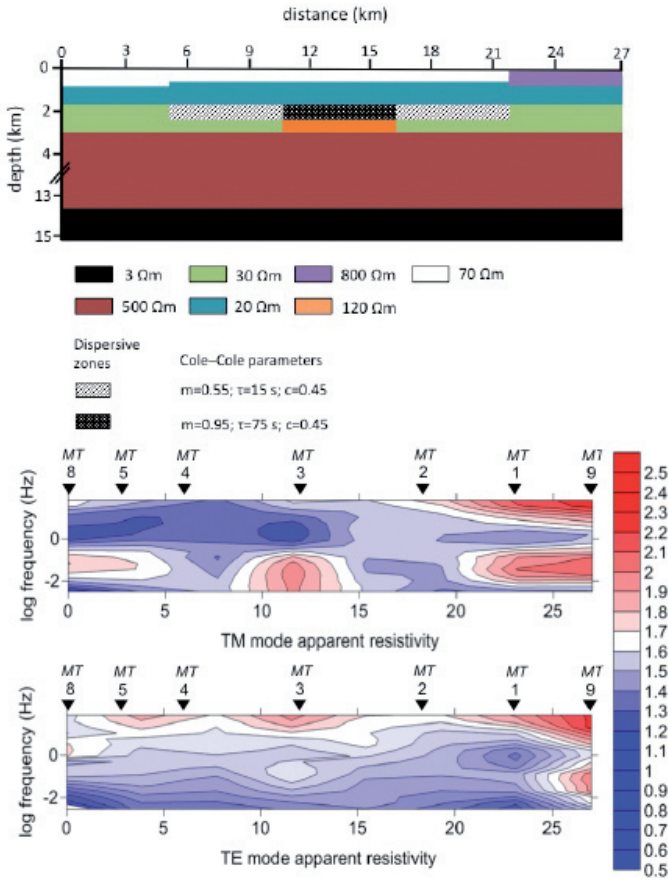


Fig. 2 – At the top the NW-SE section of the interpreted Snake River Plain structural model across the MT profile by Stanley (1982), The 3D conductive slab (15 km wide in the direction normal to the section) is assumed to be affected by resistivity frequency dispersion. At the bottom the Snake River Plain MT TM and TE field pseudosections with the MT stations (redrawn after Stanley, 1982). The color scale is in  $\Omega$  m.

a 2D geometry is assumed to approximate a limited strike length slab (Wannamaker *et al.*, 1984,1997; Livelybrooks *et al.*, 1996).

We propose now a 3D refinement of the 2D section in Fig. 2, using the same resistivity sequence and Cole-Cole parameters as in the 2D model and assigning after trial-and-error a final strike length of 15 km to the horizontal slab, shorter than the width of the infinite length slab in the original 2D model. Fig. 3 shows the TM and TE original and synthetic apparent resistivity pseudosections and the misfit between them. The misfit has been plotted by assigning at each point of the pseudosections the modulus of the discrepancy index  $r_i$ , given by (Troiano *et al.*, 2014)

$$r_i = |(d_i - m_i) / \epsilon_i|, \tag{2}$$

where  $d_i$  are the observed data,  $m_i$  are model responses and  $\epsilon_i$  are the data errors with  $i=1,2,\dots,M$ ,  $M$  being the total number of measured data.

The normalized root mean square (*rms*) misfit has been calculated using the formula (Gabàs and Marcuello, 2003)

$$rms = \sqrt{(\sum_M r_i^2 / M)}. \tag{3}$$

Average *rms* values have been obtained equal to 2.6 for the TM section and 3.1 for the TE section.

Following a previously suggested interpretation paradigm (Mauriello *et al.*, 1996, 2004),  $m$  and  $\tau$  seem to play an important role mostly in the evaluation of IP effects in volcano-geothermal areas. In fact,  $m$  can be associated to the degree of alteration and mineral particle deposition

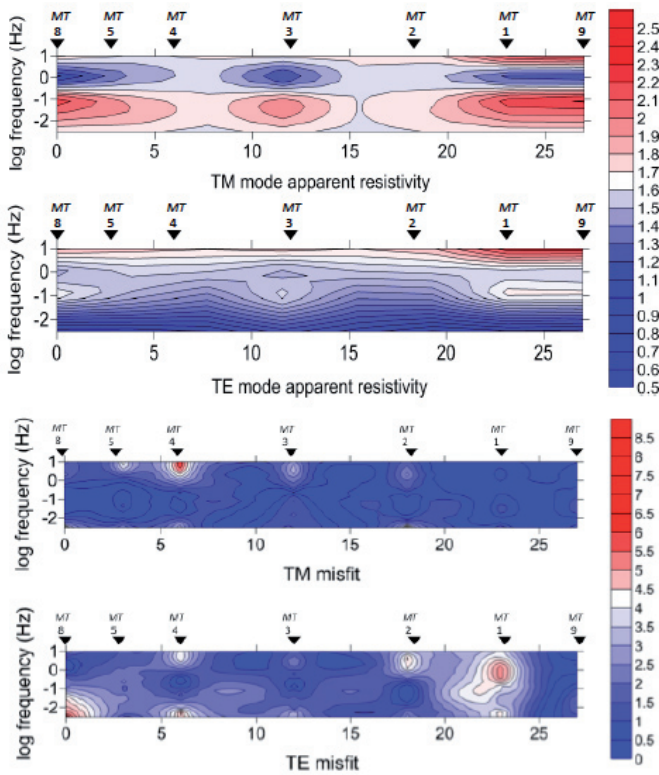


Fig. 3 – The Snake River Plain MT TM and TE synthetic pseudosections, reconstructed from the 3D model in Fig. 2 at the top and at the bottom the misfit between the observed MT TM and TE pseudosections and the synthetic ones.

due to rock-fluid interaction. Within certain limits, the higher is the volume percent of alteration products occluding rock fissures and pores, the higher is  $m$ . For the examined SRP field case, high  $m$  values, up to 0.95, have been required to model the MT profile, fully consistent with values found in other volcanic and geothermal environments (Patella *et al.*, 1991; Coppola *et al.*, 1993; Giammetti *et al.*, 1996; Di Maio *et al.*, 2000; Mauriello *et al.*, 2000, 2004).

We thus feel we can consider the 3D refinement of the original 2D model as an evidence of the greater accuracy that can be reached by a 3D approach to the interpretation of MT data supposed to be affected by dispersive effects.

**References**

Berton, J. and J. Loeb, 1976, Experimental and Theoretical Aspects of Induced Polarization, Gebrüder-Borntraeger, Berlin-Stuttgart.

Chang-Chin, Y., and L. Bin, 1994, The research on the 3D TDEM modeling and IP effect, Chinese J. Geophys., S2, P.631.3, CJFDTotol-DQWX4S2.053.

Cole, K.S. and R.H. Cole, 1941, Dispersion and absorption in dielectrics. Part I. Alternating current characteristics, J. Chem. Phys., 9, 341-351, do: 10.1063/1.1750906.

Coppola, B., R. Di Maio, I. Marini, A. Merla, D. Patella, G. Pulelli, F. M. Rossi, and A. Siniscalchi, “Study of the Simplon area geothermal anomaly in the frame of a transalpine deep railway tunnel feasibility project,” Underground Transportation Infrastructures, 93-102, ed. J. L. Reith, Balkema, Rotterdam, 1993.

Di Maio, R., P. Mauriello, D. Patella, Z. Petrillo, S. Piscitelli, A. Siniscalchi, and M. Veneruso, “Self-potential, geoelectric and magnetotelluric studies in Italian active volcanic areas,” Ann. Geofis., Vol. 40, 519-537, 1997.

Di Maio, R., D. Patella, Z. Petrillo, A. Siniscalchi, G. Cecere, and P. de Martino, “Application of electric and electromagnetic methods to the study of the Phlegrean Fields caldera,” Ann. Geofis., Vol. 43, 375-390, 2000.

Esposito, R., and D. Patella, 2009, The role of the impedivity in the magnetotelluric response, PIER, 89, 225-253, doi: 10.2528/PIER081 21203.

Fink, J.B., E.O. McAlister, B.K. Sternberg, W.G. Wieduwilt and S.H. Ward (eds.), 1990, Induced Polarization: Applications and Case Histories, Investigations in Geophysics, 4, SEG, Tulsa, Oklahoma.

- Gabàs, A., and A. Marcuello, 2003, The relative influence of different types of magnetotelluric data on joint inversions, *Earth Planet. Space*, 55, 243-248, doi: 10.1186/BF03351755.
- Giammetti, S., D. Patella, A. Siniscalchi, and A. Tramacere, "The Siena Graben: Combined interpretation of DES and MT soundings," *Ann. Geofis.*, Vol. 39, 189–200, 1996.
- He, Z., Z. Hu, W. Luo and C. Wang, 2010, Mapping reservoirs based on resistivity and induced polarization derived from continuous 3D magnetotelluric profiling: Case study from Qaidam basin, China, *Geophysics*, 75, B25-B33, doi: 10.1190/1.3279125.
- Hoheisel, A., A. Hördt and T. Hanstein, 2004, The influence of induced polarization on long-offset transient electromagnetic data, *Geophys. Prospect.*, 52, 417-426, doi: 10.1111/j.1365- 2478.2004. 00426.x.
- Livelybrooks, D., M. Mareschal, E. Blais and J.T. Smith, 1996, Magnetotelluric delineation of the Trillabelle massive sulfide body in Sudbury, Ontario, *Geophysics* , 61 , 971-986, doi: 10.1190/1.1444046.
- Mabey, D.R., 1982, Geophysics and tectonics of the Snake River Plain, Idaho, in B. Bonnicksen and R.M. Breckenridge, *Cenozoic Geology of Idaho*, Idaho Bureau of Mines and Geology Bulletin, 26, geology.isu.edu/B-26Ch3-1.
- Marchant, D., E. Haber and D.W. Oldenburg, 2014, Three-dimensional modeling of IP effects in time- domain electromagnetic data, *Geophysics*, 79, E303-E314, doi: 10.1190/geo2014-0060.1.
- Mauriello, P., D. Patella and A. Siniscalchi, 1996, The magnetotelluric response over two-dimensional media with resistivity frequency dispersion, *Geophys. Prosp.*, 44, 789-818, doi: 10.1111/j.1365- 2478.1996.tb00174.x.
- Mauriello, P., and D. Patella, 1999, Principles of probability tomography for natural-source electromagnetic induction fields, *Geophysics*, 64, 1403-1417, doi: 10.1190/1.1444645.
- Mauriello, P., D. Patella, Z. Petrillo, and A. Siniscalchi, "An integrated magnetotelluric study of the Mt. Etna volcanic structure," *Ann. Geofis.*, Vol. 43, 325–342, 2000.
- Mauriello, P., D. Patella, Z. Petrillo, A. Siniscalchi, T. Iuliano, and C. Del Negro, "A geophysical study of the Mount Etna volcanic area," *Mt. Etna: Volcano Laboratory*, Vol. 143, 273–291, ed. A. Bonaccorso, S. Calvari, M. Coltelli, C. Del Negro, S. Falsaperla, American Geophysical Union, *Geophysical Monograph Series*, 2004.
- Patella, D., 1987, Tutorial: Interpretation of magnetotelluric measurements over an electrically dispersive one-dimensional earth, *Geophys. Prosp.*, 35, 1-11, doi: 10.1111/j.1365-2478.1987. tb00799.x.
- Patella, D., A. Tramacere, R. Di Maio, and A. Siniscalchi, "Experimental evidence of resistivity frequency-dispersion in magnetotellurics in the Newberry (Oregon), Snake River Plain (Idaho) and Campi Flegrei (Italy) volcano-geothermal areas," *J. Volcanol. Geoth. Res.*, Vol. 48, 61–75, 1991.
- Patella, D., 1993, I principi metodologici della magnetotellurica su mezzi generalmente dispersivi, *Ann. Geophys.* , 36 , 147-160, earth-prints.2122.3658.1.
- Pellerin, L., J.M. Johnston and G.W. Hohmann, 1996, A numerical evaluation of electromagnetic methods in geothermal exploration, *Geophysics*, 61, 121-137, doi: 10.1190/1.1443931.
- Seigel, H.O., 1959, Mathematical formulation and type curves for induced polarization, *Geophysics* ,24 , 547-565, doi: 10.1190/1.1438625.
- Stanley, W.D., 1982, Magnetotelluric soundings on the Idaho National Engineering Laboratory facility, Idaho, *J. Geophys. Res.*, 87, 2683-2691, doi: 10.1029/JB087iB04p02683.
- Stoyer, C.H., 1976, Consequences of induced polarization in magnetotelluric interpretation, *Pure Appl. Geophys.*, 114, 435-449, doi: 10.1007/BF00876943.
- Sumner, J.S., 1976, *Principles of Induced Polarization for Geophysical Exploration* , Elsevier, Amsterdam.
- Troiano, A., M.G. Di Giuseppe, D. Patella, C. Troise and G. De Natale, 2014, Electromagnetic outline of the Solafatara-Pisciarelli hydrothermal system, Campi Flegrei (Southern Italy), *J. Volcanol. Geoth. Res.* , 277 , 9-21, doi:10.1016/j.jvolgeores.2014.03.005.
- Wannamaker, P.E., J.M. Johnston, J.A. Stodt and J.R. Booker, 1997, Anatomy of the southern Cordilleran hingeline, Utah and Nevada, from deep electrical resistivity profiling, *Geophysics*, 62 , 1069-1086, doi: 10.1190/1.1444208.
- Zaslavsky, M., V. Druskin and L. Knizhnerman, 2011, Solution of 3D time-domain electromagnetic problems using optimal subspace projection, *Geophysics*, 76, F339-F351, doi: 10.1190/geo 2011-0088.1.
- Zhdanov, M.S., and G.V. Keller, 1994, *The Geoelectrical Methods in Geophysical Exploration*, Elsevier, Amsterdam.

## OPTIMAL PARAMETERS FOR FINITE DIFFERENCE MODELING OF 2D SEISMIC WAVE EQUATION

B. Galuzzi<sup>1</sup>, E. Stucchi<sup>1</sup>, E. Zampieri<sup>2</sup>

<sup>1</sup> Dipartimento di Scienze della Terra "A. Desio", Università degli Studi di Milano, Italy

<sup>2</sup> Dipartimento di Matematica "F. Enriques", Università degli Studi di Milano, Italy

**Introduction.** Full waveform inversion is a classical contest of data inversion in which the numerical solution of the wave equation is compared with one or more seismograms to obtain information on the Earth's subsurface (Tarantola, 1986), (Virieux and Operto, 2009). Consequently, accurate and efficient numerical implementation of the wave equation is still an active research field and involves sampling quantities such as time, space and physical properties of the subsurface, along with choosing an appropriate numerical method of resolution and writing an efficient resolution code. Approximation error and execution time determine the effectiveness of the implementation. An effective code exhibits the right balance between these two factors because the use of high-resolution parameters to decrease the approximation error causes a large execution time, which, for seismic inversion applications, should remain in the order of a few seconds or lower. For example it may be necessary to use about ten thousand or one hundred thousand synthetic seismograms to resolve a problem of seismic inversion by global optimization algorithms (Sajeva *et al.*, 2014).

In this work we study the relationship between these two factors in the contest of the numerical solution of the 2D acoustic wave equation. The numerical solution is obtained from finite difference software, written at the University of Milan, in which the implementation parameters can be set in order to get an efficient solution. At the beginning we derive the 2D acoustic seismic wave equation and explain the numerical implementation and the parameters of modeling used. Then, we analyze which parameters cause the highest approximation error and find that they are the space step size and the order of approximation of space derivatives. We study their behavior in a simple constant-velocity model as a function of the maximum frequency of the source signal and we analyze the relation with the execution time. Finally, we apply these considerations on a complex-velocity model and find the right parameters of modeling to get the optimum trade-off between the approximation error and the execution time.

**The 2D acoustic seismic equation.** The seismic wave propagation in a geological medium is often modeled by the acoustic 3D equation (Fichner, 2010)

$$\frac{\partial^2 p(x, y, z, t)}{\partial t^2} = c(x, y, z)^2 \left( \frac{\partial^2 p(x, y, z, t)}{\partial x^2} + \frac{\partial^2 p(x, y, z, t)}{\partial y^2} + \frac{\partial^2 p(x, y, z, t)}{\partial z^2} \right) + f(x, y, z, t),$$

with  $p$  acoustic pressure of the wave,  $f$  seismic source and  $c$  acoustic wave speed. A realistic range for wave speed can be between 1500 m/s (water) and 7000 m/s (granite). Since the seismic source has a space dimension much smaller than the geological medium, it can be approximated by a point source in space

$$f(x, y, z) = \delta(x - x_0)\delta(y - y_0)\delta(z - z_0)s(t),$$

where  $s(t)$  is the seismic wavelet, describing the variation of seismic source in time. One important aspect of the modeling is the maximum frequency  $f_{max}$  of the wavelet. Since many source-receiver geometries are often confined to a plane (for example  $y=0$ ), it is possible to use the acoustic 2.5-D equation (Bleistein, 1986)

$$\frac{\partial^2 p(x, y, z, t)}{\partial t^2} = c(x, z)^2 \left( \frac{\partial^2 p(x, y, z, t)}{\partial x^2} + \frac{\partial^2 p(x, y, z, t)}{\partial y^2} + \frac{\partial^2 p(x, y, z, t)}{\partial z^2} \right) + f(x, y, z, t),$$

which differs from the 3D equation only for the fact that  $c$  varies only as a function of the depth  $z$  and the length  $x$ . Finally, because of the large computational cost of 3D modeling, we consider the 2D acoustic wave equation

$$\frac{\partial^2 p(x, z, t)}{\partial t^2} = c(x, z)^2 \left( \frac{\partial^2 p(x, z, t)}{\partial x^2} + \frac{\partial^2 p(x, z, t)}{\partial z^2} \right) + \delta(x - x_0)\delta(z - z_0)s(t).$$

In general a 2D modeling of wave propagation cannot be used in general to make a direct quantitative comparison, including amplitude information, with seismic data acquired along a line and assumed to be 2.5-D, but there are many strategies that make the passage from 2D to 2.5-D possible (Liner, 1991; Williamson and Pratt, 1995; Song and Williamson, 1995).

**Modeling of the acoustic seismic equation.** In our numerical implementation of the acoustic wave equation we use an explicit finite difference method (Cohen, 2002), with uniform time step and uniform space step (with the same step for depth and length). In order to approximate the time and space derivatives we use different finite difference operators.

We implement a second order operator to approximate the time-derivative

$$\frac{\partial^2 p(x, z, t)}{\partial t^2} = \frac{p(x, z, t + dt) - 2p(x, z, t) + p(x, z, t - dt)}{dt^2} + O(dt^2),$$

and implement a 2n-order space operator to approximate the space derivatives

$$\frac{\partial^2 p(x, z, t)}{\partial x^2} = \frac{\sum_{i=1}^n c_i (p(x + idx, z, t) + p(x - idx, z, t))}{dx^2} - 2 \frac{(\sum_{i=1}^n c_i) p(x, z, t)}{dx^2} + O(dx^{2n}),$$

$$\frac{\partial^2 p(x, z, t)}{\partial z^2} = \frac{\sum_{i=1}^n c_i (p(x, z + idz, t) + p(x, z - idz, t))}{dz^2} - 2 \frac{(\sum_{i=1}^n c_i) p(x, z, t)}{dz^2} + O(dz^{2n}),$$

where the  $c_i$  are the coefficients for the 2n-order of approximation of derivatives (Cohen, 2002). Tab. 1 lists the values of  $c_i$ , obtained as a function of the order of approximation  $ord_s = 2n$ , for some values of  $n$ .

Tab. 1 - Values of the coefficients for different order of approximation of spatial derivative.

ords	c1	c2	c3	c4	c5	c6
2	1	0	0	0	0	0
4	4/3	-1/12	0	0	0	0
6	3/2	-3/20	1/60	0	0	0
8	8/5	-1/5	8/135	-1/560	0	0
10	5/3	-5/21	5/126	-5/1008	1/3150	0
12	12/7	-15/56	10/189	-1/112	2/1925	-1/16632

In the interest of computational efficiency, the limitation of the computational domain to only a part of the true physical domain introduces reflecting boundaries that do not exist. We use the Gaussian taper method (Cerjan *et al.*, 1985) to suppress the undesired reflections, in which we introduced a thin absorbing region along the artificial boundary where the wave field is attenuated.

**Approximation error of the implementation.** There are four main parameters that influence the approximation error of the implementation: the time step  $dt$ , the space step  $dx$ , the order of approximation of the space operator  $ord_s = 2n$  and the size of the absorbing region, expressed as the number of grid nodes. To focus the attention only on the first three parameters, we can choose an absorbing region so large as to make irrelevant the error introduced by the boundaries of the model. There are two main relations between these three parameters. The first is numerical stability (Courant *et al.*, 1967)

$$dt < \frac{dx}{c_{max}} \lambda,$$

with  $\lambda = \lambda(ord_s) \in [0.5, 1]$ , that is the Courant number. This relation limits the maximum possible

Tab. 2 - Values of  $n$  as a function of ords, to obtain an error below 1%.

$ord_s$	2	4	6	8	10	12	14	16	18	20	22	24
$n$	18	6.3	4.5	3.75	3.5	3.25	3	2.9	2.8	2.7	2.6	2.5

time step as a function of the space step size  $dx$  and the maximum velocity  $c_{max}$ . The second is the numerical dispersion (Alford *et al.*, 1974)

$$dx < \frac{c_{min}}{f_{max}n},$$

where  $n=n(ord_s)$  is the number of points per wavelength. Grid dispersion limits the maximum possible space step by the minimum velocity  $c_{min}$  and the maximum frequency  $f_{max}$  of the source signal  $s(t)$ . We consider the function  $\cos\left(\frac{2\pi x}{l}\right)$ , where  $l$  denotes the wavelength, to estimate the values of  $n$ . If we calculate the second derivative of this function analytically at  $x=0$ , and we set  $l=1$ , we obtain  $-4\pi^2$ . The numerical solution can be obtained by sampling the function with different sampling intervals  $dx=l/n$ , where  $n$  is the number of points per wavelength and by using different  $2n$ -order operators. Tab. 2 lists the values of  $n$ , as a function of the order of approximation  $ord_s$ , to obtain an error below 1%.

Numerical stability is a necessary condition to implement any explicit finite difference method. Because of the order of magnitude of the wave speed in rocks, the stability condition implies that the maximum possible time step must be approximately three order of magnitude at least lower than the minimum possible space step size  $dt_{max} \approx 10^{-3} dx_{min}$ ; if this condition is met, the error of approximation is more sensitive to spatial parameters ( $dx, ord_s$ ). For this reason, we study the error of approximation and execution time as a function of  $dx$  and  $ord_s$ .

**A constant-velocity test.** To simulate a simple seismic acquisition, we consider a rectangular region with dimensions  $X=3240$  m and  $Z=1620$  m, with a constant velocity of  $c=1500$  m/s (water velocity). We choose a seismic source located in  $(x_0, z_0)=(27$  m, 27 m), characterized by a Ricker wavelet

$$s(t) = (1 - 2a(t - t_0)^2)e^{-a(t-t_0)^2},$$

with  $a=\pi^2 f_0^2$  and  $t_0=0.2$  s. The choice of this wavelet is so because it is simple to control its maximum frequency, that is  $f_{max} \approx 3f_0$ . The recording spread is composed of 119 receivers, equally spaced by 27 m, with a depth of 27 m and also an offset of 27 m to the first receiver. In the case of constant velocity model without boundary, the solution of the equation is (Aki and Richards, 2002)

$$p(x, z, t) = \frac{1}{2\pi c^2} \int_0^{t_s} s\left(t - \frac{\sqrt{(x - x_0)^2 + (z - z_0)^2 + s^2}}{c}\right) \frac{ds}{\sqrt{(x - x_0)^2 + (z - z_0)^2 + s^2}},$$

with  $t_s$  that depends on the duration of the wavelet, usually much smaller than the duration of registration  $T$ . If we use a quadrature formula to approximate the integral, we have a solution of the problem whose accuracy is independent of distance and time, but depends only on the accuracy of the quadrature formula. This procedure allows building an “exact” solution that can be compared with our numerical solutions (we can consider our model as unbounded using a large absorbing boundary condition). A numerical implementation of this problem was made with a fixed time step of  $dt=0.0005$  s and a recording length of  $T=2s$ . To study the behavior of the approximation error and execution time, we consider two different grid cell size  $dx=[27$  m, 9 m], twelve different space orders of approximation  $ord_s=[2,4\dots 24]$  and three different wavelets with  $f_s=[5$  Hz, 10 Hz, 15 Hz] (which correspond to  $f_{max}=[15$  Hz, 30 Hz, 45 Hz]). To compare the numerical solution with the “exact” solution, we use the following measure of

numerical error:

$$err = \frac{1}{temp * nric} \sum_{i=1}^{temp} \sum_{j=1}^{nric} |real_{i,j} - sint_{i,j}|,$$

where  $temp=4000$  is the number of time samples,  $nric=119$  is the number of receivers,  $real_{i,j}$  is the “exact” seismogram and  $sint_{i,j}$  is the numerical one. Both seismograms are normalized to their maximum value.

Fig. 1a shows the six curves (two for each frequency  $f_s$ ) of the approximation error as a function of  $ord_s$ . It is possible to see that the error increases with  $dx$  and  $f_{max}$ , according to the relation of grid dispersion. We note also that the curves of approximation decrease, in general with  $ord_s$ , but this behavior depends also on  $dx$  and  $f_{max}$ . In particular, for frequency  $f_{max}=45$  Hz (the green curves), we note that the curve with  $dx=27$  m slowly decreases as a function of  $ord_s$ , while the one with  $dx=9$  m decreases fast until  $ord_s \approx 8$ . Then we notice that the error remains stable around  $5 \cdot 10^{-5}$ . Similarly, for frequency  $f_{max}=30$  Hz (the blue curves), the curve with  $dx=27$  m slowly decreases as a function of  $ord_s$ , while the one with  $dx=9$  m decreases fast until  $ord_s=6$ . Here the error remains stable around  $2.5 \cdot 10^{-5}$ . Finally, for frequency  $f_{max}=15$  Hz (the red curves), the curve with  $dx=27$  m decreases fast as a function of  $ord_s$  until  $ord_s=8$  and then remains stable around an error of  $2 \cdot 10^{-4}$ , while the curve with  $dx=9$  m, decreases fast until  $ord_s=6$ , it remains nearly constant until  $ord_s=12$  and finally increases slowly. Overall it remains stable around an error of  $1 \cdot 10^{-5}$ . Therefore the whole behavior of the curves does not appear to be simple. However, for high frequencies, the better way to reduce the error is to decrease  $dx$  and slightly increase  $ord_s$ . Increasing only the order of approximation  $ord_s$  seems to bring only minor improvements. Instead, for low frequencies, there is no need to use short step sizes:  $dx=27$  m with  $ord_s \approx 8$  gives a sufficiently low approximation error, without the necessity to further increase  $ord_s$ . For middle frequencies, the error appears to be more complex. However, using a short  $dx$  with a low  $ord_s$  is a good compromise, while an equally valid solution is to use a high order of approximation  $ord_s$  with higher space step sizes  $dx$ .

The behavior of modeling as a function of  $dx$ ,  $ord_s$  and  $f_{max}$  can be explained by the grid dispersion relation. If we place  $c_{min}=1500$  m/s and  $f_{max}=45$  Hz, (green curves in Fig. 1a) we obtain

$$n < \frac{33.3}{dx}.$$

Therefore, if we want to use a space step size with  $dx=9$  m (the dashed green curve in Fig. 1a) it is sufficient to have  $n \approx 3.7$ , which corresponds from Tab. 2 to an  $ord_s \approx 8$ ; greater order of approximation will not produce significant improvements, because the curve remains almost

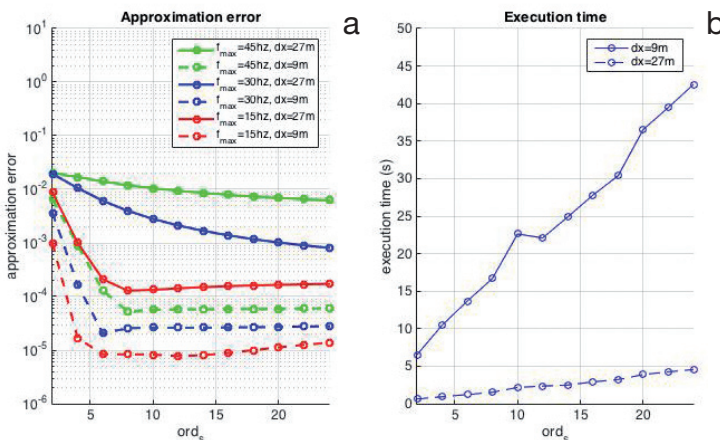


Fig. 1 – Approximation error (left) and execution time (right) for different modeling parameters.

constant. On the contrary, if we want a space step size of  $dx=27$  m (the continuous green curve), it would be necessary that  $n \approx 1.2$ . However, this is not possible because of the Nyquist theorem and consequently the solution will have a great numerical dispersion. If we place  $c_{min}=1500$  m/s and  $f_{max}=15$  Hz, (red curves in Fig. 1a) we obtain

$$n < \frac{100}{dx}.$$

Therefore, if we want to use a space step size of  $dx=9$  m, (the dashed red curve) it is sufficient to have  $n \approx 11.1$ , which corresponds from Tab. 2 to  $ord_s \approx 4$ ; a greater order of approximation will not produce significant improvements because the error remains almost constant hereafter. On the contrary, if we need to use a space step of size  $dx=27$  m, we must set  $n \approx 3.7$ , so it will be necessary a higher order  $ord_s$ .

As a final consideration the error, especially for low  $dx$ , seems to converge to a low constant value different from zero for each maximum frequency. This is due to the fact that the error related to time discretization takes over when the error related to space discretization decreases. This error is low for low maximum frequency  $f_{max}$ , and increases with  $f_{max}$ .

In addition to this consideration about approximation error, it is important to evaluate the execution time. In Fig. 1b we represent the two execution time curves, in function of  $ord_s$ , related to  $dx=[27$  m, 9 m] with  $f_{max}=15$  Hz (for different maximum frequency the execution time did not change). We can note that execution time increases in function of  $dx$  and  $ord_s$ . In particular the curve with  $dx=27$  m is always below that with  $dx=9$  m. This is due to the numerical method implemented, since we have

$$T \propto nx * nz * ord_s$$

where  $T$  is the execution time and  $nx*nz$  is the number of grid nodes.

Then, the execution time increases quadratically as a function of  $dx$  and only linearly with  $ord_s$ . Therefore it can be more convenient to increase  $ord_s$  rather than decreasing  $dx$ , to obtain comparable error but with a lower execution time. As an example, the modeling with  $dx=9$  m and  $ord_s=4$  has an error comparable with the modeling with  $dx=27$  m and  $ord_s=24$ . Moreover the first has an execution time of 11 s, while the second of only 5 s.

**A complex-velocity test.** We simulated another seismic acquisition with the same parameters of acquisition as the previous one: one point source, the same numbers of receivers, a registration time of  $T=2$  s and a time step  $dt=0.0005$  s. We now assumed that the velocity varies as a function of the depth and length  $c=c(x, z)$  (Fig. 2a), with a range between 1500 m/s and about 4500 m/s. This velocity model is a readjustment of a portion of the Marmousi model

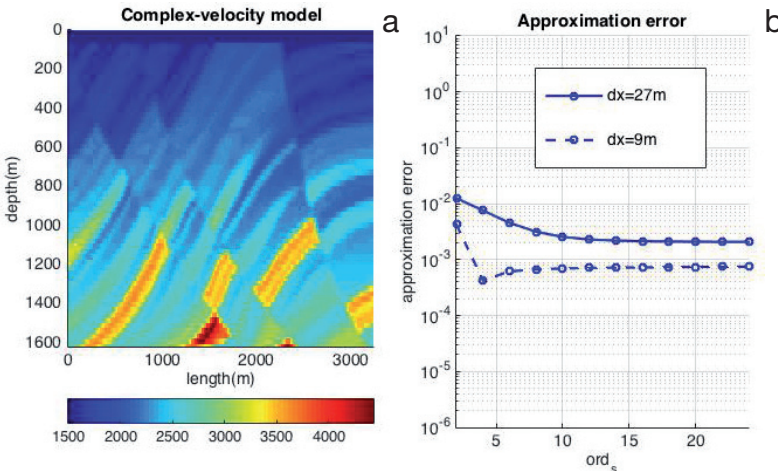


Fig. 2 – Complex-velocity model (left) and its approximation error (right).

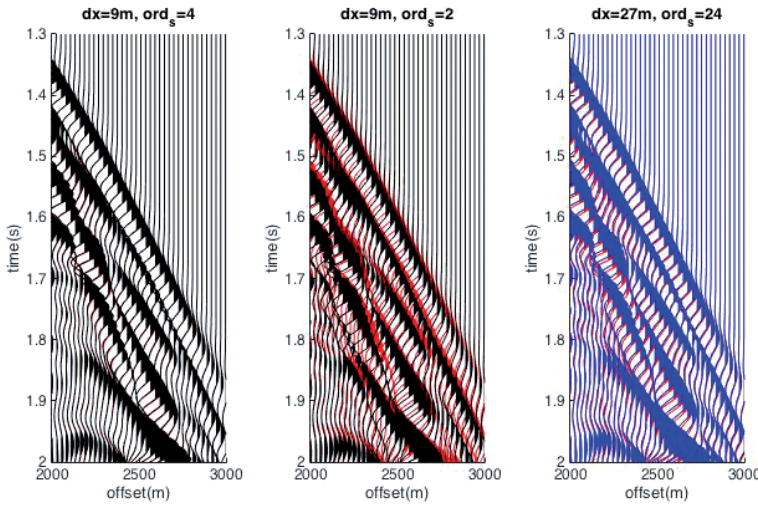


Fig. 3 – Three portions of three different seismicograms for different modelling parameters. On the left  $dx=9$  m,  $ord_s=4$ . In the center  $dx=9$  m,  $ord_s=2$ . On the right  $dx=27$  m,  $ord_s=24$ . All of them are confronted with the exact seismicograms, in red.

(Bourgeois *et al.*, 1991). We considered absorbing boundary conditions for lateral and bottom sides. On the contrary, for the topside we considered a reflective boundary condition (expressed by  $p(x, 0, t)=0, \forall x, t$ ) to simulate the high contrast of velocity and density between air and water. For this modeling there is not an exact solution to be compared with the numerical ones. So as “exact” solution we use a numerical one with  $dx=1$  m,  $dt=0.000125$  s and  $ord_s=4$ . To study the behavior of error and execution time, we consider again two different grid cell size  $dx=[27$  m, 9 m], twelve different space orders of approximation  $ord_s=2,4,\dots,24$  and a wavelet Ricker with  $f_s=10$  Hz ( $f_{max}=30$  Hz). The two execution time curves as a function of  $ord_s$  are the same of Fig. 1b (execution time is not influenced by the velocity  $c$ ), while the two curves of error are represented in Fig. 2b.

The behavior of these curves is similar to that of the previous test, but the error is higher. Indeed there are more seismic events in the seismicogram for this test (reflected and refracted arrivals) than in the previous one. The curve of  $dx=27$  m decreases slowly as a function of  $ord_s$ , while the one of  $dx=9$  m decreases fast until  $ord_s=4$ , with the error remaining stable. We can note that, also in this case, it can be more convenient to use a space step of  $dx=27$  m with high order  $ord_s$ , rather than a space step of  $dx=9$  m and low  $ord_s$ . The errors we obtained in fact are comparable, but the execution time of the first case is lower (Fig. 1b).

In Fig. 3 we reported a portion of three numerical seismicograms we obtained. The first, on the left, is the seismicogram obtained with  $dx=9$  m and  $ord_s=4$ , that corresponds to the better solution obtained with  $dx=9$  m. The second, in the center, is the seismicogram obtained with  $dx=9$  and  $ord_s=2$ . The third, on the right, is the seismicogram with  $dx=27$  and  $ord_s=24$ , that corresponds to the best solution obtained with  $dx=27$ . All of them are confronted with the “exact solution” (the red seismicograms on the graphics). We note that the third seismicogram is better than the second one and, from Fig. 1b, it also has a lower execution time. On the other hand the first seismicogram is better than the third one, even if the differences are not so pronounced, but it has a higher execution time. Therefore it can be more convenient to choose the modeling parameters used to compute the third seismicogram instead of using the modeling parameters of the first one, especially if a huge number of forward modeling is required.

**Conclusions.** Using a constant velocity model and a portion of the Marmousi model, we studied the 2D acoustic seismic wave equation and the parameters of modelling necessary to implement an efficient numerical solution as a function of approximation error and execution time. The approximation error depends on the stability condition and the grid dispersion relation. We found that under the stability condition, the approximation error is above all influenced by the space step size  $dx$  and the order  $ord_s$  of the finite difference approximation of spatial

derivatives. Therefore an optimal trade-off between these two parameters is required in order to reduce the approximation error.

This approximation error can also be analysed in terms of the grid dispersion relation and therefore in terms of the ratio between the minimum velocity  $c_{min}$  in the model and the maximum frequency  $f_{max}$  of the wavelet. If the ratio is low, it is necessary to use a low spatial step size and a medium order of spatial derivative approximation (for instance:  $dx=9$  m and  $ord_s=6,8$ ). If the ratio is high, it is possible to use a greater spatial step size, but with a higher order of spatial approximation (for instance:  $dx=27$  m and  $ord_s=22,24$ ). As a final consideration, if there are combinations of these two parameters that cause comparable errors, it is convenient to use the one with the greater space step size to reduce the execution time, especially in application such as the Full Waveform Inversion where a large number of forward modelling may be needed.

## References

- Williamson, P. R., & Pratt, R. G. (1995). A critical review of acoustic wave modeling procedures in 2.5D dimensions. *Geophysics*, 60, 591-595.
- Virieux, J., & Operto, S. (2009). An overview of full waveform inversion in exploration geophysics. *Geophysics*, 127-152.
- Aki, K., & Richards, P. G. (2002). *Quantitative Seismology* (2nd ed.). University Science Books.
- Alford, R. M., Kelly, K. R., & Boore, D. M. (1974). Accuracy of finite difference modeling of the acoustic wave equation. *Geophysics*, 39 (6), 834-842.
- Bleistein, N. (1986). Two-and-One-Half Dimensional in-Plane Wave Propagation. *Geophysical Prospecting*, 34, 686-703.
- Bourgeois, A., Bourget, M., Lailly, P., Ricarte, P., & Versteeg, R. (1991). Marmousi, model and data. *European Association of Exploration Geophysicists*.
- Cerjan, A., Kosloff, D., Kosloff, R., & Reshef, M. (1985). A non reflecting boundary condition for discrete acoustic and elastic wave equations. *Geophysics*, 50, 705-708.
- Courant, R., Friedrichs, K., & Lewy, H. (1967, March). On the partial difference equations of mathematical physics. *IBM Journal*, 215-234.
- Cohen, G. (2002). *Higher-order Numerical Methods for Transient Wave Equations*. Berlin: Springer-Verlag.
- Fichner, A. (2010). *Full Seismic Waveform Modelling and Inversion*. Berlin: Springer-Verlag.
- Liner, C. L. (1991). Theory of a 2.5-D acoustic wave equation for constant density media. *Geophysics*, 56 (12), 2114-2117.
- Sajeva, A., Aleardi, M., Galuzzi, B. G., Mazzotti, A., & Stucchi, E. M. (2014). Comparison of stochastic optimization methods on analytic objective function and on 1D elastic fwi. *European Association of Geoscientists and Engineers Conference and Exhibition*, (pp. 1893-1903). Amsterdam.
- Song, Z., & Williamson, P. R. (1995). Frequency-domain acoustic wave modelling and inversion of crosshole data; Part 1, 2.5-D modelling method. *Geophysics*, 60 (3), 784-795.
- Tarantola, A. (1986). A strategy for nonlinear elastic inversion of seismic reflection data. *Geophysics*, 51, 1893-1903.

## APPLICATION OF THE RECONFIGURABILITY OF THE INTEGRATION TIME IN STEPPED FREQUENCY GPR SYSTEMS: FIRST EXAMPLES IN THE FIELD

R. Persico<sup>1</sup>, D. Dei<sup>2</sup>, F. Parrini<sup>2</sup>, L. Matera<sup>1</sup>, S. D'Amico<sup>3</sup>, A. Micallef<sup>3</sup>, P. Galea<sup>3</sup>

<sup>1</sup> Institute for Archaeological and Monumental Heritage IBAM-CNR, Lecce, Italy

<sup>2</sup> Florence Engineering s.r.l., Florence, Italy

<sup>3</sup> University of Malta, Msida, Malta

**Introduction.** Ground Penetrating Radar (GPR) is the tool that allows the best available resolution within the non-invasive subsurface geophysical techniques, as well known (Daniels, 2004; Jol, 2009; Persico 2014). In particular, possibly integrated with other geophysical techniques (Matera *et al.*, 2015), a GPR can provide information of geological, cultural, and structural interest (Ranieri *et al.*, 2015; Sambuelli *et al.*, 2014; Castaldo *et al.* 2009; Masini *et*

*al.*, 2010; Pieraccini *et al.*, 2006; Piscitelli *et al.*, 2007). On the other hand, several sources of uncertainty can affect the data, among which clutter (van der Merwe and Gupta, 2000), several kinds of noises (Ouadfeul and Aliouane, 2014), model errors (Pierri *et al.*, 2001; Persico *et al.*, 2002) and interferences from other electromagnetic devices (Goodman and Piro, 2013).

In this contribution, we propose some results regarding the reconfiguration of the integration time of the harmonic tones radiated and received by a stepped frequency ground penetrating radar (GPR) system in a way programmable vs. the frequency. As will be shown, this can allow an efficient rejection of narrow band electromagnetic interferences on the GPR signal without erasing the disturbed frequencies.

In fact, as well known (Noon, 1996), by prolonging the integration time, the spectrum of the real radiated harmonic tone becomes narrower, and by means of a suitable filtering in the receiving chain the signal becomes cleaner with respect to noise and interferences. Moreover, this goal is achieved without increasing the transmitted power (because what is increased is the transmitted energy) On the other hand, this achievement is paid with a prolongation of the time required for the measure, but as far as one can prolong only the disturbed tones, the overall prolongation of the measurement time is customarily not critical. However, this implies that the system satisfies some hardware and software requirements that commercial systems usually do not satisfy. In particular, the availability of the management of the integration time tone by tone is not a standard tool for stepped frequency systems, that in general allow (at most) to prolong in the same way all the radiated tones together, so that the extension of the integration time is performed also at frequencies that do not need it. Moreover, this hardware requirement is not sufficient if one does not set an algorithm able to recognize in the field the most meaningful interferences (if any) so to set the prolongation of the default integration time accordingly in an automatic way. The hardware for having selectively extensible integration times has been made available by the research project AITECH (<http://www.aitech.net.com/ibam.html>), thanks to which the Institute for Archaeological and Monumental Heritage IBAM-CNR, together with the University of Florence and the IDS corporation, had the possibility to implement a reconfigurable stepped frequency GPR system. Then, the algorithm has been found thanks to subsequent more recent research activities, also performed within the European Cost Action TU1208.

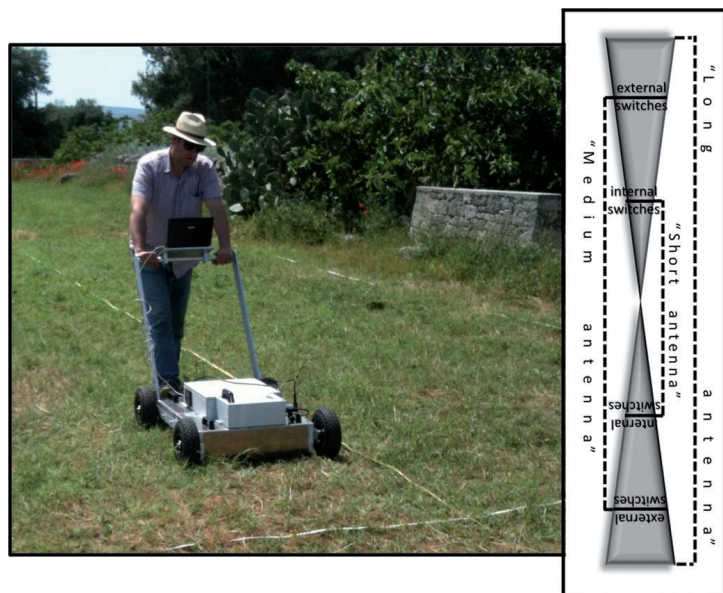


Fig. 1 – Left hand panel, the prototypal reconfigurable stepped frequency system. Right hand panel: diagram of the reconfigurable antennas.

In the following, the reconfigurable system will be briefly described in section 2, then the algorithm for the reconfiguration of the integration times is exposed in section 3. Some preliminary experimental results achieved in the field are then exposed in section 4. Conclusions follow in section 5.

**The reconfigurable system.** A prototypal reconfigurable GPR system (Persico and Prisco, 2008) has been implemented within the research project AITEACH, as said. Several tests on real sites in Italy and abroad (Norway and Malta) have been performed within a Ph.D. course handled within a collaboration by the Department of Earth Science of the University of Bari and the Institute for Archaeological Heritage of the Italian Research National Council (IBAM-CNR). Fig. 1 (in the left hand panel) offers an image of the system, that allows to reconfigure vs. the frequency the length of the antennas, the power radiated at each frequency and the integration time of the received harmonic tones.

The length of the equivalent antennas of the prototypal reconfigurable GPR system can be modified by using special switches that can make the arms “longer” or “shorter” as shown in Fig. 1 (in the right hand panel).

The arms of the antennas can be electronically reduced by means of two internal switches (*is*) and two external switches (*es*). When both the *is* and the *es* are switched on, the antennas are “long”, when the *is* are switched on and the *es* are switched off, the antennas are “medium”, if both the *is* and the *es* are switched off, the antennas are “short”. Of course, the switches of the equivalent antennas are synchronised so that the lengths of the transmitting and receiving antenna are constantly equal to each other. The reconfigurable antennas are comprehensively sized about 80x45 cm times 25 cm for the height. The central unit is attached to the antennas, so that no external cable is needed to connect them to each other. The frequency interval that the system can sweep ranges from 50 MHz to 1 GHz with a frequency step of 2.5 MHz or (optionally) of 5 MHz. In the second case, the measure can be performed in a slightly faster way, but the risk of aliasing in frequency domain increases (Persico, 2014). The three central frequencies of the equivalent antennas can be evaluated from the data. In previous works, as (Persico *et al.*, 2014; Matera *et al.*, 2015), some possibilities related to the variable length of the arms of the antennas were shown and discussed. Here, we focus on the reconfiguration of the integration times whereas, at the moment, the possibility of reconfiguring the radiated power vs. the frequency has not been deeply investigated yet.

**The reconfiguration of the integration times.** The algorithm for the reconfiguration works analyzing a first calibration Bscan, possibly coinciding with the first Bscan of interest for the prospecting at hand. This preliminary Bscan is exploited in order to evaluate and quantify the presence of meaningful (if any) interferences. This aim is pursued as follows: for all the traces and for each tone within the trace,  $N$  samples of the in phase and in-quadrature ( $I$  and  $Q$ ) components are retrieved and stored, by means of the customary heterodyne demodulation receiving chain of any stepped frequency system. Indeed, this is not a procedure conceived on purpose for the scopes of this paper, but is the normal praxis customarily adopted in stepped frequency systems. Usually, however, one accepts as  $I$  and  $Q$  components the algebraic average value of the  $N$   $I$  and  $Q$  samples gathered at that frequency in that position. Here, we propose to exploit another information related to these  $N$  samples, namely their variance. In particular, in Fig. 2 we show the results of an experimental test performed in Florence by the Florence Engineering s.r.l., relatively close to a repeater of FM broadcast radio transmissions. In abscissa there are the subsequent  $I$  and  $Q$  samples frequency per frequency (but indexed after their sequential number). In correspondence of the frequencies not much disturbed, the samples are substantially equal to each other within the tone, thus resulting in a step like diagram. However, when the tones are disturbed by external electromagnetic devices, then the behaviour of the samples within the tone is quite variable and noise-like.

This has suggested to deal the in-phase and in-quadrature components as the samples of two random variables. Since the algebraic average is an estimation of the statistical average, we can

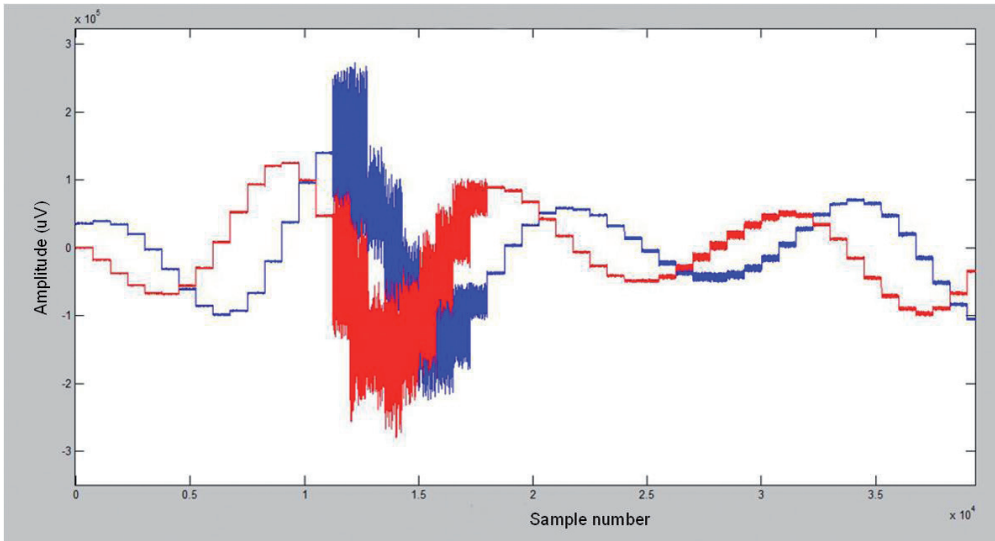


Fig. 2 – Experimentally measured I and Q components close to an FM broadcast radio repeater. The disturbed tones (that correspond to the FM band 88-110 MHz) are characterised by a strongly oscillating behaviour.

estimate the variance of the  $I$  and  $Q$  components at each tone as follows:

$$\begin{cases} \sigma_{I;f_k,t_h}^2 = E\left[\left(I_{f_k,t_h}\right)^2\right] - \left[E\left(I_{f_k,t_h}\right)\right]^2 \\ \sigma_{Q;f_k,t_h}^2 = E\left[\left(Q_{f_k,t_h}\right)^2\right] - \left[E\left(Q_{f_k,t_h}\right)\right]^2 \end{cases} \quad (1)$$

where  $E$  indicates the algebraic average value,  $k$  and  $h$  are the tone and the trace indexes, respectively. The generic comprehensive variance of the tone  $k$  of the trace  $h$  can be naturally defined as

$$\sigma_{f_k,t_h}^2 = \frac{\sigma_{I;f_k,t_h}^2 + \sigma_{Q;f_k,t_h}^2}{2} \quad (2)$$

Then, as an index of the intensity of the interference on the tone  $k$  (independently of the trace along the calibration Bscan) we have chosen the quantity

$$\sigma_{f_k}^2 = \max_h \left( \sigma_{f_k,t_h}^2 \right) \quad (3)$$

The choice of the maximum is conservative, in the sense that it is based on the most disturbed  $k^{\text{th}}$  tone along all the traces of the Bscan. Indeed, since the selected frequency step was 2.5 MHz, the sequence  $\sigma_{f_k}^2$  vs.  $f_k$  can be reliably confused with the graph of the continuous function  $\sigma_f^2(f)$ , so that the quantity in Eq. 3 can be regarded as the variance vs. the frequency, evaluated all over the calibration Bscan.

So, from the calibration Bscan we can work out and visualize automatically the behaviour of the variance of the tones vs. the frequency, and from this one we can decide whether the reconfiguration is needed or not. This decision is left as a heuristic choice here, on the basis of the comparison (done ones at for all) between some Bscan gathered two times, once with the default integration times and once with reconfigured integration times. We do not have and so can not give a general quantification, because the default integration time is variable from instrument to instrument, and in general also the amplification and quantization chain depend from the equipment at hand. So, the calibration is to be meant as referred to the system at hand, and the order of magnitude of  $\sigma_f^2(f)$  is meaningful or less meaningful only in relationship

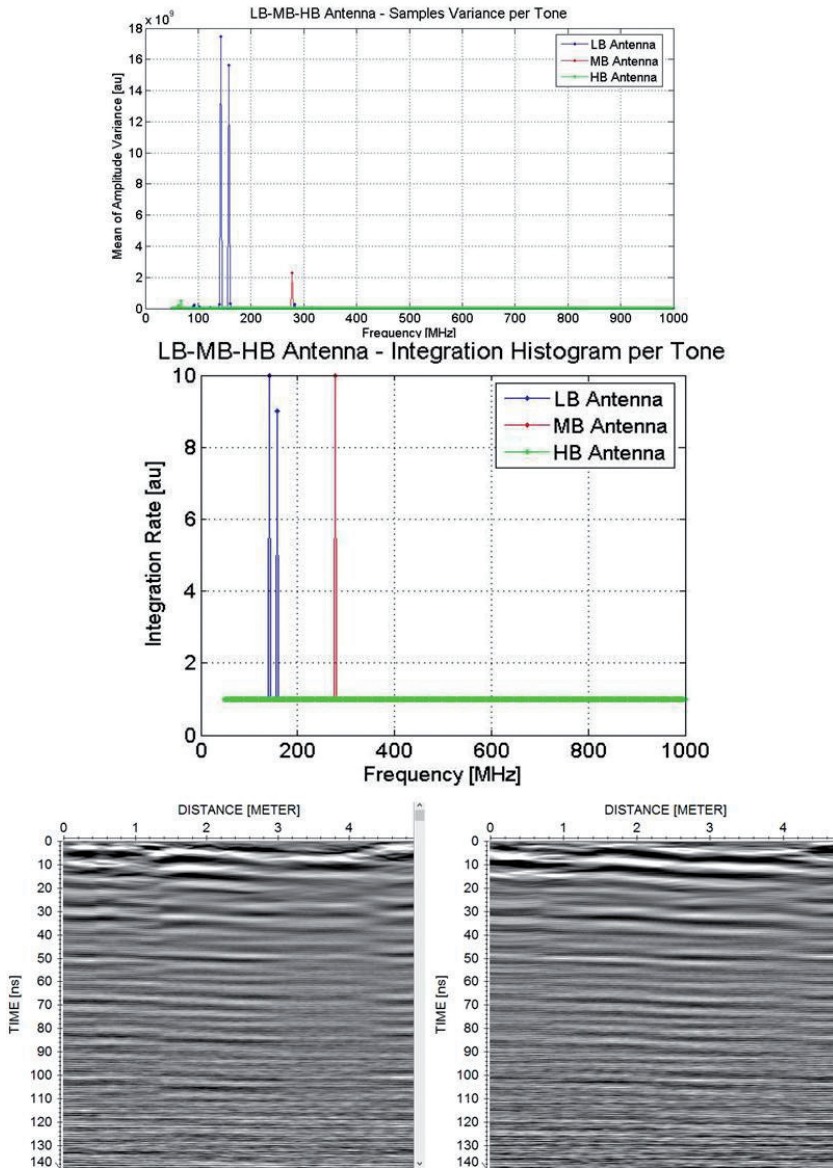


Fig. 3 – Upper panel: recorded variance vs. the frequency, for each couple of antennas. Medium panel: the extension of the integration times vs. the frequency for each antenna. Lower panel: on the left hand side is represented Bscan achieved with default integration times. On the right hand panel is represented the Bscan achieved with reconfigured integration times.

to the specific equipment at hand. For the prototypal system at hand, we have seen that if the maximum level of  $\sigma_f^2(f)$  is higher than  $10^{10}$  some effects begin to be perceivable and a reconfiguration of the integration times provides some meaningful benefits.

Said that, if in the field we see that the variance of the tones is negligible, we can just continue our work with the default integration times. If we evaluate that the variance of the tones is not negligible, the reconfiguration algorithm asks us to set an integer number  $M > 1$ . This number quantifies the maximum “degree” of reconfiguration needed in the case at hand. In particular, the reconfiguration code calculates a factor of enlargement for each integration time

according to the low:

$$W_k = \min \left\{ \text{Ceil} \left( M \frac{\sigma_{f_k}^2}{\max_k (\sigma_{f_k}^2)} \right), 10 \right\} \quad (4)$$

where  $W_k$  is the factor of enlargement for the  $k^{\text{th}}$  tone and *Ceil* stands for the minimum integer not smaller than the argument. In other words, initially an enlargement factor equal to *Ceil*( $M$ ) will be calculated for the most disturbed tone, while the other ones will be about proportionally less enlarged with the care that the reconfiguration will never shorten the integration time of any harmonic tone (which is guaranteed by the *Ceil* function). However, the hardware of the system does not allow an enlargement of the default integration time beyond a factor equal to 10, and therefore in Eq. 4 includes a saturation to 10 if the set prolongation factor of the integration time is longer than 10 times the default integration time at some frequency.

**Experimental results.** The results exposed in the following are relative to two measurement campaigns performed in the framework of the scientific short term mission “Use of GPR and standard geophysical methods to explore the subsurface”, supported by the European Cost Action TU1208 “*Civil Engineering Applications of Ground Penetrating Radar*” and performed between July 14 and 24, 2015.

Here we will show some results achieved in the site of Laferla Cross. The site is located outside an historical church, where we have checked the presence of cavities and buried subsidences. In particular, there is a project of moving the church from its current position in order to preserve it from some sliding phenomena of the soil, that indeed have already meaningfully damaged it. In this paper, we will show data gathered with the “long” antennas of the system, according to the explanation provided with regard to Fig. 1. The central frequency is about 130 MHz. More details about the purposes of these campaigns are available in Persico *et al.* (2015). Here it is sufficient to say that six Bscans have been gathered, and the Bscan n. 1, has been repeated twice in order to calibrate the integration times. The variance vs. the frequency is shown in Fig. 3 (upper panel). As can be seen, the most disturbed frequencies are around 100 MHz, because there is the range reserved to the broadcast FM radio transmissions. Moreover, also the shielding of the antennas is in general less efficient at low frequencies. As can be seen from the upper panel of Fig. 3, the higher levels of the variance is recorded at two frequencies between 100 and 200 MHz. The order of magnitude reached by the variance is about 1.8 times  $10^{10}$ , this means that some effect from these interferences can be perceived. We have reconfigured the integration times with a factor  $M=10$  both for the long and medium antennas, whereas a factor 1 has been left for the high frequency antennas because we do not see any meaningful disturbance for it. In the medium panel of Fig. 3, the graph of the produced elongations is shown. When the value of the function is equal to 10, it means that the integration times has been prolonged up to 10 times the default integration time, when the value is 9, the extension has been equal to 9 times the default integration time and so on. As can be seen, the extension factor is never smaller than 1, so that no harmonic has been integrated for a time shorter than the default value. Finally, in the lower panel of Fig. 3, the two radargrams with the default integration time and the reconfigured integration times are shown.

Seeing at the two figures, we can appreciate that some reflections appear as interrupted of two-piece-like in the left hand panel and continuous in the right hand panel.

**Conclusions.** In this paper, some effects of electromagnetic interferences on GPR data have been shown, and above all a possible counteraction based on the reconfiguration of the integration times of the harmonic tones of a stepped frequency (reconfigurable) GPR system has been described. Preliminary experimental tests at a site of cultural interest have been shown. Indeed, the effect of the disturbance in the presented example was visible but not much strong. Indeed, this happens because the default integration times of the prototypal system are intrinsically quite high, of the order of 100  $\mu\text{s}$  as said. However, this has a meaningful price in terms of practicality of the measure. In particular, at the moment the system does not allow to

visualize the gathered data in real time, and compels to walk quite slowly when performing a measurement campaign. Moreover, such a long integration time would constitute an even worse technological problem for a system equipped with an array of antennas. Therefore, indeed commercial stepped frequency systems usually works with meaningfully shorter integration times. This makes consistent a question about the investigation of the possibilities offered by a reconfiguration of the integration time starting from a shorter default basic integration time. At the conference, some results also in this sense will be shown.

**Acknowledgements.** The authors mentions with gratitude the Puglia Region, that funded the Aitech Project and the TUCost Action 1208, that funded two Short Term Scientific Missions (STMS) in Norway and in Malta, that allowed us the understand, implement and test the reconfiguration of the integration times.

## References

- Castaldo R., Crocco L., Fedi M., Garofalo B., Persico R., Rossi A. and Soldovieri F.; 2009: *GPR Microwave Tomography for Diagnostic of Archaeological Sites: the Case of a high-way construction in Pontecagnano (Southern Italy)*, *Archaeological Prospection*, **16**, 203-217.
- Daniels D. J.; 2004: *Ground penetrating radar 2<sup>nd</sup> edition*, IEE press.
- Jol H.; 2009: *Ground Penetrating Radar: Theory and applications*, Elsevier.
- Goodman D. and Piro S.; 2013: *GPR Remote Sensing in Archaeology*, Springer-Verlag ed..
- Masini N, Persico R., Rizzo E, Calia A, Giannotta M. T., Quarta G. and Pagliuca A.; 2010: *Integrated Techniques for Analysis and Monitoring of Historical Monuments: the case of S.Giovanni al Sepolcro in Brindisi (Southern Italy)*, *Near Surface Geophysics*, **8**, 423-432.
- Matera L. , Noviello M., Ciminale M. and Persico R.; 2015: *Integration of multisensor data: an experiment in the archaeological park of Egnazia (Apulia, Southern Italy)*, accepted for publication on *Near Surface Geophysics*.
- Noon D. A.; 1996: *Stepped-Frequency Radar Design and Signal Processing Enhances Ground Penetrating Radar Performance*, Ph.D. Thesis, Department of Electrical & Computer Engineering, University of Queensland, Australia.
- Ouadfeul S. A. and Aliouane L.; 2014: *Noise Attenuation from GPR Data Using Wavelet Transform and Artificial Neural Network*, *IJAPM*, **4**, 426-433.
- Persico R.; 2014: *Introduction to Ground Penetrating Radar: Inverse Scattering and data processing*, Wiley.
- Persico R., Ciminale M. and Matera L.; 2014: *A new reconfigurable stepped frequency GPR system, possibilities and issues; applications to two different Cultural Heritage Resources*, *Near Surface Geophysics*, **12**, 793-801.
- Persico R., D'Amico S. and Matera L.; 2015: *Report for the Scientific Short Term Mission "Use of GPR and standard geophysical methods to explore the subsurface"* granted by the European Cost Action TU1208.
- Persico R., Prisco G.; 2008: *A Reconfigurative Approach for SF-GPR Prospecting*, *IEEE Trans. on Antennas and Propagation*, **56**, 2673-2680.
- Persico R., Soldovieri F., Pierri R.; 2002: *Convergence Properties of a Quadratic Approach to the Inverse Scattering Problem*, *Journal of Optical Society of America Part A*, **19**, 2424-2428.
- Pieraccini M., Noferini L., Mecatti D., Atzeni C., Persico R. and Soldovieri F.; 2006: *Advanced Processing Techniques for Step-frequency Continuous-Wave Penetrating Radar: the Case Study of "Palazzo Vecchio" Walls (Firenze, Italy)*, *Research on Nondestructive Evaluation*, **17**, 71-83.
- Pierri R., Leone G., Soldovieri F. and Persico R.; 2001: *Electromagnetic inversion for subsurface applications under the distorted Born approximation*, *Nuovo Cimento*, **24C**, 245-261.
- Piscitelli S., Rizzo E., Cristallo F., Lapenna V, Crocco L., Persico R. and Soldovieri F.; 2007: *GPR and Microwave Tomography for Detecting shallow Cavities in the Historical Area of Sassi of Matera (Southern Italy)*, *Near Surface Geophysics*, **5**, 275-285.
- Ranieri G., Trogu A., Loddo F., Piroddi L. and Zucca R.; 2015: *Geophysics - An Essential Tool for Modern Archaeology. A Case from Monte Prama (Sardinia, Italy)*, Proc. 21<sup>st</sup> European Meeting of Environmental and Engineering Geophysics, Turin.
- Sambuelli L., Elia D., Meirano V. and Colombero C.; 2014: *Case history : a magnetic and GPR prospection on a Roman rural villa in western Piedmont (Italy )*, Proc. of 33th Convegno Nazionale Gruppo Nazionale di Geofisica della Terra Solida, Bologna.
- van der Merwe A, and Gupta . J.; 2000: *A Novel Signal Processing Technique for Clutter Reduction in GPR Measurements of Small, Shallow Land Mines*, *IEEE Trans. on Geoscience and Remote Sensing*, **38**, 2627-2637.

## A NEW INVERSION METHOD OF VERTICAL GRAVITY AND MAGNETIC SOUNDINGS

A. Vitale, D. Di Massa, M. Fedi, G. Florio

*Dipartimento di Scienze della Terra, dell'Ambiente e delle Risorse, Università Federico II, Napoli, Italy*

**Introduction.** The purpose of this work is to present a new method for the inversion of potential fields (gravity or magnetic anomalies).

The inverse problem is solved by determining the set of parameters that describes the sources of the field due to the experimental data.

If the unknown parameters are the density or the magnetization this type of problem is linear and in most cases it is an indeterminate problem, since the data are less in number than the number of unknown parameters. The use of constraints, which define models geologically valid, such as intervals of maximum variation of the model parameters, can manage to reduce the ambiguity.

One of the greatest difficulties in the inversion of the potential field is to obtain satisfactory information about the characteristics of the sources of interest, which may be the top and the bottom of the structures that generate anomalies plus estimates and trends of density values (or intensity of magnetization, in the case of magnetic fields) relating to them.

The scientific literature is extraordinarily rich in both 2D and 3D gravity and magnetic data inversion algorithms.

All these methods provide density/magnetization distributions at depth having certain properties.

Green (1975) searched for a density model that minimizes its weighted norm to some reference model. Safon *et al.* (1977) used the method of linear programming to compute moments of the density distribution. Fisher and Howard (1980) solved a linear least-squares problem constrained for upper and lower density bounds. Last and Kubik (1983) introduced a 'compact' inversion minimizing the body volume.

Guillen and Menichetti (1984) assumed as a constraint the minimum momentum of inertia. Barbosa and Silva (1994) suggested allowing compactness along given directions using a priori information. Li and Oldenburg (1996, 1998) introduced model weighting as a function of depth using a subspace algorithm.

Pilkington (1997, 2002) used preconditioned Conjugate Gradients (CG) method to solve the system of linear equations. Portniaguine and Zhdanov (1999, 2002) introduced regularized CG method and focusing using a reweighted least squares algorithm with different focusing functional. Li and Oldenburg (2003) use wavelet compression of the kernel with logarithmic barrier and conjugate gradient iteration. Barbosa & Silva (2006) proposed a 2D method to invert potential field data by a procedure incorporating a priori knowledge.

Wijns and Kowalczyk (2007) propose a semi-automatic procedure that allows defining solutions geologically reasonable. Pilkington (2009) used data space inversion in Fourier domain. Barnes and Barraud (2012) have developed instead an inversion algorithm to solve geometrical interfaces between different geological bodies, through the introduction of information concerning the depth and regularizing the solution.

However, there are no 1D algorithms, since the forward problem in this case should be referred to infinite layers, which produce a constant field in space and, therefore, could not explain any gravity anomaly.

Fedi and Rapolla (1990) explored for the first time the possibility to perform the inversion of "vertical gravity soundings", which refers to a 1D inversion method. The forward problem consisted in assuming a volume of layers of different densities. The volume is however finite vertically and horizontally, this last condition is necessary to avoid the Bouguer slab effect, which would make impossible the inversion of field anomalies. The other main feature of this approach is that a multiscale dataset is inverted. The data at various altitudes are obtained by

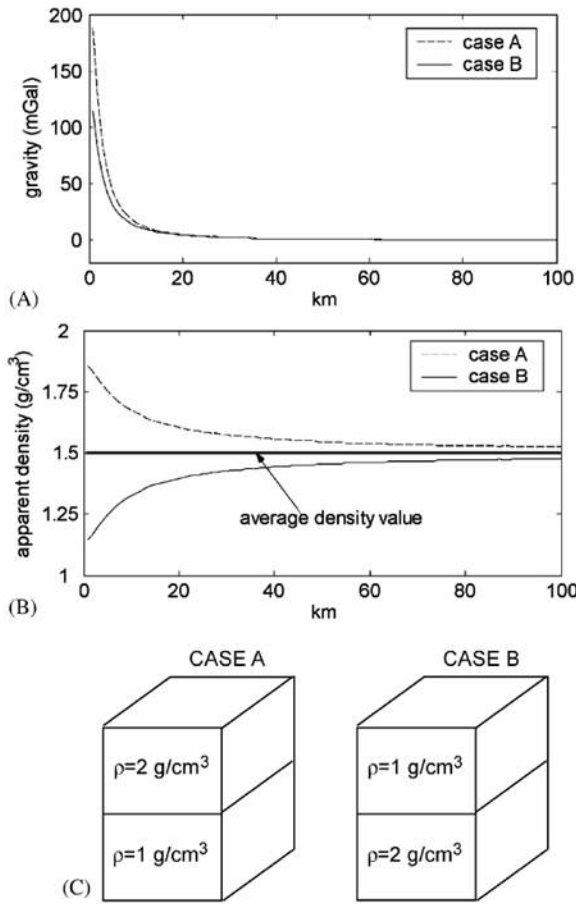


Fig. 1 – Vertical variations of gravity field (a) and of the apparent density (b) of a two-layered source (c) with an upper layer more dense (case A) or lesser dense (case B) (from Fedi and Rapolla, 1990).

upward continuation of the original survey. The vertical sounding is central with respect to the layers volume, so yielding a 1D density/magnetization distribution at depth.

Inspired by this method, in this work we propose the inversion of multiple one-dimensional vertical gravity/magnetic soundings.

The major change that we made to the existing 1D method of Fedi and Rapolla (1990) consists in extracting the soundings are at different horizontal positions, and no more just at the centre of the volume.

We tested our method by analyzing both synthetic perfect data, to simulate data measured at different levels, and upward continued data.

**Method.** The basic idea is that the vertical distributions of density and/or magnetization could be deduced by the field known at different heights.

We started from the relation defining the gravitational field generated at a point  $P(x_k, y_k, z_k)$  by a distribution of mass density  $\rho(\vec{r})$  in a volume  $V$ .

$$g(P) = \gamma \int_V \rho(\vec{r}) \frac{z-z_k}{|\vec{r}-\vec{r}_k|^3} dv \tag{1}$$

where  $\gamma$  is the gravity constant and

$$|\vec{r} - \vec{r}_k| = \sqrt{(x - x_k)^2 + (y - y_k)^2 + (z - z_k)^2} \tag{2}$$

If the density varies just vertically:

$$\rho(\bar{r}) = \rho(z), \tag{3}$$

and if we consider a vertical sounding with  $N$  measurements  $\{P_{k1}, \dots, P_{kj}, \dots, P_{kN}\}$ , then Eq. 1 becomes:

$$g(P_{kj}) = \gamma \int_V \rho(z) \frac{z-z_{kj}}{|\bar{r}-\bar{r}_{kj}|^3} dv \tag{4}$$

This equation describes the 1D forward problem of a continuous unknown function  $\rho(z)$  linearly related to the gravity data. If we assume a discrete number  $M$  of layers, where in each of them the density is homogeneous, we have:

$$g(P_{kj}) = \sum_{i=1}^M \rho_{ij} G_{ij}(P_{kj}) \tag{5}$$

where:

$$G_{ij}(P_{kj}) = \gamma \int_{V_i} \frac{z-z_{kj}}{|\bar{r}-\bar{r}_{kj}|^3} dv \tag{6}$$

and  $\{\rho_{1j}, \dots, \rho_{ij}, \dots, \rho_{Mj}\}$ ,  $\{V_1, \dots, V_i, \dots, V_M\}$  are respectively the densities and the volumes of the  $M$  layers.

with  $i=[1, \dots, M]$ .

Fedi and Rapolla (1990) showed that, normalizing the field in Fig. 1a with that produced by the same volume with unit-density, the resulting quantities (apparent densities, Fig. 1b) are strongly related to the behavior of density, that is decreasing (left model, Fig. 1c) or increasing (right model, Fig. 1c).

We now turn on the inversion of 1D gravity soundings. We here use the method, called “Minimum Length with Inequality Constrains” or IML. It is used to solve indeterminate linear problems such as:

$$\mathbf{g} = \mathbf{G}\boldsymbol{\rho} \tag{7}$$

where  $\mathbf{g}$  represents the data vector referred to the  $j^{th}$  sounding,  $\boldsymbol{\rho}$  represents the density vector referred to the volume and  $\mathbf{G}$  represents the matrix of the theoretical kernel, defined by the Eq. 6.

This kind of estimation model is also known as “minimum length” of the solution for indeterminate problem.

The presence of experimental errors ( $\Delta\mathbf{g}$ ), implies that the fitting between experimental data and theoretical data ( $\mathbf{G}\boldsymbol{\rho}$ ) is searched according to:

$$\mathbf{g} - \Delta\mathbf{g} \leq \mathbf{G}\boldsymbol{\rho} \leq \mathbf{g} + \Delta\mathbf{g} \tag{8}$$

Besides, to reduce the number of possible models that are solution to our problem, constraints can be used to express our a priori information on the density of each layer:

$$\rho_L \leq \rho_i \leq \rho_H \tag{9}$$

With these inequalities, the problem is first transformed into a non-negative *least squares problem*, according to a technique described in Menke (1984):

minimize  $\|\mathbf{m}\|_2$  subject to:  $\mathbf{F}\mathbf{m} \geq \mathbf{h}$

This problem may be transformed into:

$$\mathbf{G}'\mathbf{m}' = \mathbf{g}' = \begin{bmatrix} \mathbf{F}^T \\ \mathbf{h}^T \end{bmatrix} \mathbf{m}' = \begin{bmatrix} \mathbf{0} \\ 1 \end{bmatrix} \tag{10}$$

$$\mathbf{F}^T\mathbf{m}' = \mathbf{0}, \mathbf{h}^T\mathbf{m}' = 1 \tag{11}$$

And find the solution  $\mathbf{m}'$  that minimizes:

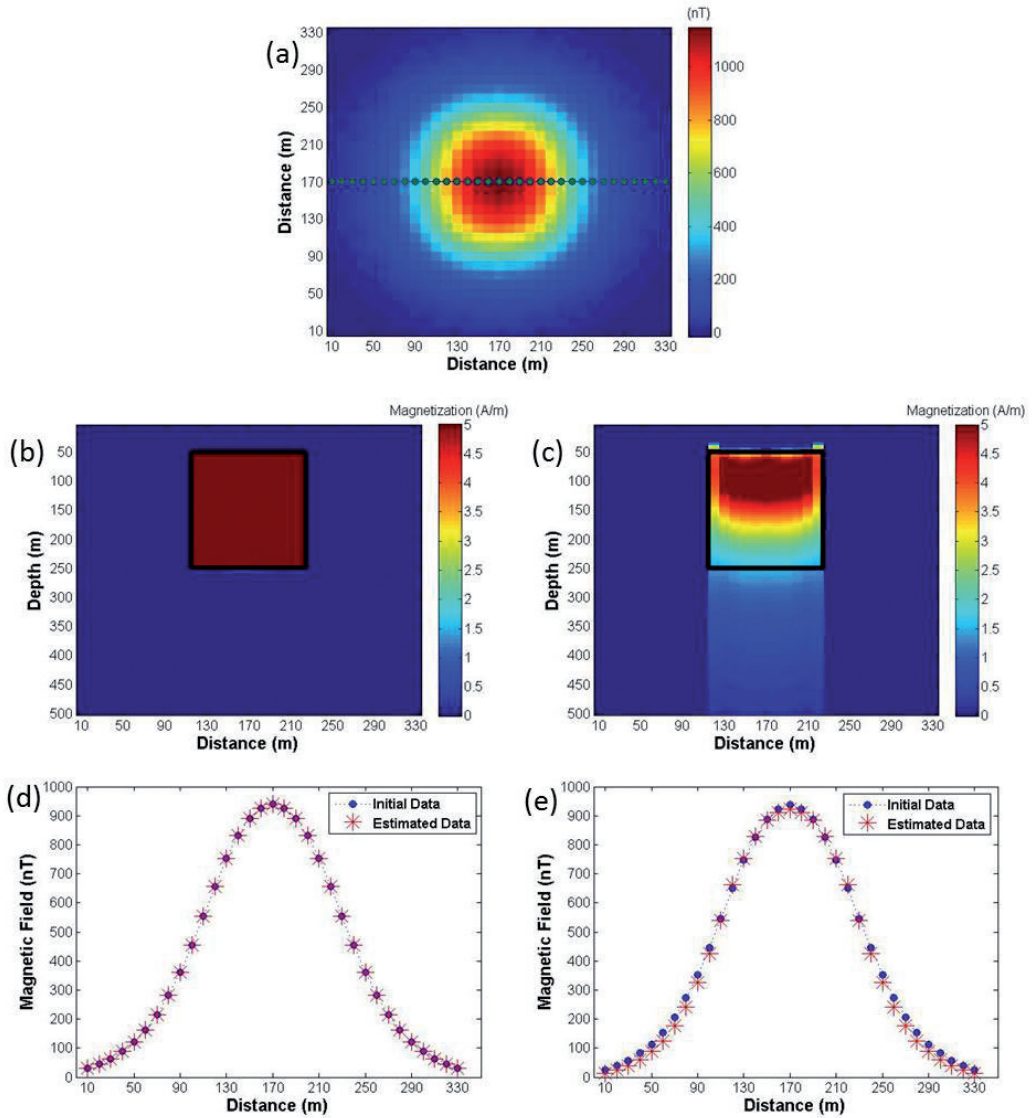


Fig. 2 – a) Magnetic anomaly map for buried body, the green points are related to the position of the vertical soundings; b) inverse model obtained from the calculated data; c) inverse model obtained from the continued data; d) comparison between initial data and estimated data for the calculated data; e) comparison between initial data and estimated data for the continued data.

$$\|g' - G'm'\|_2 \text{ subject to } m' \geq 0.$$

The matrix  $F$  contains both the kernel  $G$  relative to the vertical sounding data  $g$  and matrices associated with additional constraints. Similarly, the vector  $h$  contains both the data vector  $g$  and the values of the constraints.

It can be shown that if the prediction error,  $e' = \|g' - G'm'\|_2$  is null then the constraints  $Fm' \geq h$  are inconsistent, but if  $e \neq 0$ , constraints  $Fm' \geq h$  are consistent and the solution of the problem is:

$$m_i = -\frac{e'_i}{e'_{M+1}} \text{ with } i = 1, \dots, M \tag{12}$$

So, inequalities 8 and 9 allow to manage the overall tolerance of this particular technique.

The problem thus posed is the resolution of a single sounding. In the cases shown below, each sounding is resolved independently of each other.

The role of matrices  $\mathbf{F}$  and the vector  $\mathbf{h}$  is important because they allow to solve the problem by mitigating the effect of a trend or data errors.

**Synthetic example.** We tested the IML method on synthetic magnetic data obtained from the calculation of the magnetic effect of a single body in the investigated volume. The data at different heights were generated thanks to an algorithm that calculates the magnetic response, at a fixed altitude, of a prismatic sources for which are defined physical (magnetization or susceptibility) and geometrical properties.

The vertical profiles are selected by field measurements at  $N$  altitudes.

For real cases it is quite unlikely to collect data at different heights; in this case the vertical sounding is built by using a property of the potential field that allows the computation of the data at different altitude starting from those at a fixed level, namely upward continuation (Fedi and Rapolla, 1993). The use of an upward continuation algorithm introduces an error, that may be managed by using a third-order polynomial, as shown in Castaldo *et al.* (2014) during the inversion process.

From the anomaly maps, calculated and continued at fixed altitudes, we have extracted the values of the field along the points of a profile, which passes centrally on the analyzed anomaly. The set of points of the profile at different levels defines the vertical soundings (Fig. 2a).

For the calculation of the kernel a theoretical volume has been defined with horizontal dimensions that are in agreement with those of the body that generates the anomaly. These dimensions may be estimated using a technique of boundary analysis (Fedi and Florio, 2001): by calculating the module of horizontal derivative field along the two horizontal directions and selecting the distance between the identified maxima. The vertical dimension of the theoretical volume is defined so as to completely contain the source of anomaly and it is discretized, with a high number of layers (up to 99) of the same thickness.

For this test we used a single body with horizontal dimension equal to  $110 \text{ m} \times 130 \text{ m}$  at depths from 50 m to 250 m. The magnetization contrast with the surrounding volume is 5 A/m. The vertical soundings consist of magnetic data calculated and continued at 20 different altitudes from the first level at 5 m up to the last level at 100 m with a 5 m constant step. For this test, we used the real magnetization contrasts, setting the lower bound equal to 0 and the upper bound equal to 5 A/m.

For the experimental error data, we noticed that the continued data need a higher tolerance value to get results. In this experiment we have set, for the calculated data, an experimental error data equal to  $10^{-6}$  nT while for the continued data we used a value equal to  $10^{-2}$  nT.

Fig. 2 shows the inversion results obtained from the calculated data (Fig. 2b) and the continued data (Fig. 2c). The black rectangle identifies the exact location of the buried body. For both cases the algorithm provides excellent results in estimating the position and the magnetization contrast of the body. As regards the results obtained from the inversion of continued data, the depth of the bottom is not so well defined in comparison with that for calculated data.

From the estimated parameters, we calculated also the estimated data along the considered profile, at a fixed altitude, and we compared them with the initial data related to the same profile. As we can see in Figs. 2d and 2e, the fitting is really good for both kinds of data. These results are not trivial if we consider that the inversion method is applied on vertical soundings of field data, each one inverted independently.

**Case history.** We applied this particular inversion method to a dataset over the sedimentary basin of the Frenchman Flat Basin, Nevada Test Site, USA (Phelps and Graham, 2002).

According to Phelps and Graham (2002), the basin's bottom is located at 2.4 km depth in the northeast sector of the basin, and the maximum density contrast, between less dense sediments and the basement, is about  $0.4 \text{ g/cm}^3$ .

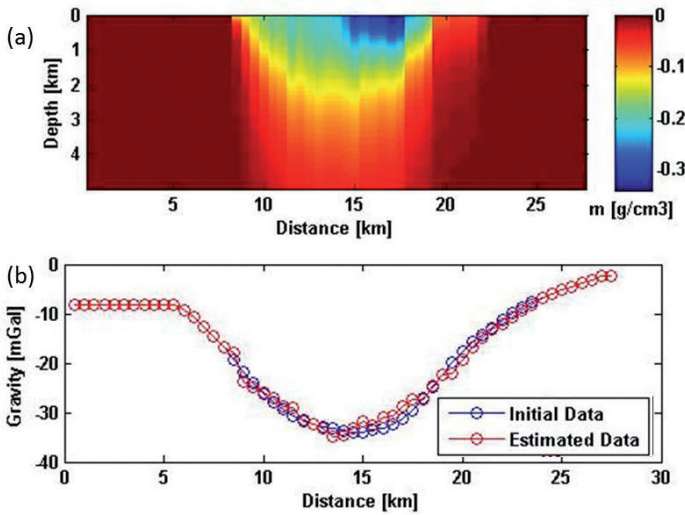


Fig. 3 – Results of the inversion process and the comparison between data and estimated data.

A profile was extracted, running through the gravimetric low from the isostatic gravity map and then we upward continued the data at 81 different heights (from 0.001 to 0.081 km), in order to be able to build 55 vertical soundings of gravity.

Therefore, we had 55 points with step size of 0.5 km, so getting 55 vertical soundings with 81 measures each. As we said previously, a boundary analysis was used to identify the horizontal dimensions of the sedimentary basin, in order to be able to build the theoretical volume needed for the inversion process, as shown in Bott (1962). At this point a theoretical volume was build of 199 layers and horizontal dimensions of 15 km along the direction of the strike and around 10 km in the direction orthogonal to it.

The bottom of the theoretical volume was located at 5 km of depth, so that we could compare our results with those obtained by Phelps and Graham (2002).

We used a density contrast range between -0.4 and 0.0001 g/cm<sup>3</sup>; this information is derived from the apriori geological knowledge of the Frenchman Flat Basin. About the experimental error data, and following what synthetic cases shown, we used the lower value in the inversion process to obtained a good resolution of the inverse model. We have set this value equal to 10<sup>-2</sup> mGal.

As we can see from the results (Fig. 3a) our estimates of depth at the deepest portion of the basin is around 2.4 km in agreement with the previous work. Even our estimates of density contrasts are consistent with the previous work. The particular asymmetric shape of this sedimentary basin is due to structural and tectonic origins.

Note that the data are very well reproduced, as the fitting is very good, along all the profile. This result confirms what seen in analysis of synthetic data: even building a section by joining independent models related to several 1D inversions, we get a good data fitting along the entire profile. This means that the results obtained from a single 1D inversion are validated also along a profile, and opens new horizons to this kind of method.

**Conclusions.** In this work we have presented a new inversion algorithm for potential field data, which consists in the inversion of vertical soundings of data collected at different altitudes. This is quite unusual for potential field data, but rather common for other geophysical methods, as geoelectrics, electromagnetics and seismics.

Starting from the boundary analysis of the data map, we estimated the horizontal dimensions of the anomaly source. The inversion algorithm was tested on synthetic magnetic data, produced by a single buried body and on a real case, relative to gravity data referred to a sedimentary basin in Nevada, US.

The data at different heights, for the synthetic case, were generated in two different ways. The first approach, i.e. theoretical approach, consists in measuring the field response at different altitude, the second one, uses a property of the potential field that allows calculating the data at different heights starting from a fixed base level, i.e. the upward continuation.

However, the upward continuation introduces an error in calculated field values that can be removed using a third-order polynomial in the inversion process.

For the synthetic case, for both calculated and continued data, the inverse models represent the correct position and the true magnetization contrast of the anomaly source. The inversion of the continued data did not provide a good definition of the bottom of the source probably because of the upward continuation errors.

For the real case the obtained result are in good agreement with those retrieved by Phelps and Graham (2002).

In both cases, even if the algorithm is dealing with a mono-dimensional vertical inversion, we are able to obtain a really good fitting among the measured and the estimated data along the horizontal profile.

## References

- Barbosa V. C. F. & Silva J. B. C. , 1994. Generalized compact gravity inversion, *Geophysics*, 59, 57–68.
- Barbosa, V.C.F. & Silva, J.B.C., 2006. Interactive 2D magnetic inversion: a tool for aiding forward modeling and testing geological hypotheses, *Geophysics*, 71 (5), 43–50.
- Barnes G. & Barraud J., 2012. Imaging geologic surfaces by inverting gravity gradient data with depth horizons. *Geophysics*, 77, G1–G11.
- Bott M. H. P., A Simple Criterion for Interpreting Negative Gravity Anomalies, *Geophysics*, VOL. XXVII, No. 3 (JUNE 1962); P. 376-381
- Castaldo R., Fedi M., Florio G., Multiscale estimation of excess mass from gravity data, *Geophys. J. Int.* (2014) 197, 1387–1398
- Fedi, M., & Florio, G. (2001). Detection of potential fields source boundaries by enhanced horizontal derivative method. *Geophysical Prospecting*, 49(2001), 40–58.
- Fedi, M., Rapolla, A., 1993. I metodi gravimetrico e magnetico nella geofisica della Terra solida, Liguori Editore, 322 pp.
- Fedi, M., Rapolla, A., Vertical Gravity an Magnetic Soundings: forward problem formulation and data inversion, *Bollettino di Geofisica Teorica ed Applicata* Vol. XXXVII, N.147 – September 1995
- Fisher, N. J., and Howard, L. E., 1980, Gravity interpretation with the aid of quadratic programming: *Geophysics*, 45, 403-419.
- Menke, W., 1984. *Geophysical Data Analysis: Discrete Inverse Theory*, Academic Press (Elsevier), 260 pp.
- Guillen A. & Menichetti V., 1984. Gravity and magnetic inversion with minimization of a specific functional, *Geophysics*, 49, 1354–1360.
- Last B.J. & Kubik K., 1983. Compact gravity inversion, *Geophysics*, 48, 713–721.
- Li Y., and Oldenburg D., 1996, 3D inversion of magnetic data: *Geophysics*, 61, 394-408.
- Li Y., and Oldenburg D., 1998, 3D inversion of gravity data: *Geophysics*, 63, 109–119.
- Li Y., and Oldenburg D., 2003, Fast inversion of large-scale magnetic data using wavelet transform and logarithmic barrier method: *Geophysical Journal International*, 152, 251-265.
- Phelps G. A. & Graham S. E., 2002. Preliminary gravity inversion model of Frenchman Flat basin, Nevada Test Site, Nevada, U.S. Geological Survey Open-File Report 02-363
- Pilkington, M., 1997, 3-D magnetic imaging using conjugate gradients: *Geophysics* 62, 1132-1142.
- Pilkington M., 2009, 3D magnetic data-space inversion with sparseness constraints: *Geophysics* 74, L7-L15
- Portniaguine, O., and Zhdanov, M. S., 1999, Focusing geophysical inversion images: *Geophysics* 48, 713-721.
- Portniaguine, O., and Zhdanov, M. S., 2002, Magnetic inversion and compression: *Geophysics* 67, 1532-1541.
- Safon, C., Vasseur, G., and Cuer, M., 1977, Some applications of linear programming to the inverse gravity problem: *Geophysics*, 42, 1215-1229.
- Silva J.B.C. & Barbosa V.C.F., 2006. Interactive gravity inversion, *Geophysics*, 71, J1–J9.
- Vadim A. Litinsky, Concept of effective density: Key to gravity depth determinations for sedimentary basins, *Geophysics*, Vol. 54, No. 11 (NOVEMBER 1989); P. 1474-1482
- Wijns, C. & Kowalczyk, P., 2007. Interactive geophysical inversion using qualitative geological constraints, *Exploration Geophys.*, 38, 208–212.

## Indice degli autori

---



**A**

Abu Zeid N. 82  
 Affatato A. 70  
 Aiello G. 5  
 Al-Arifi N. 134  
 Aleardi M. 11, 20  
 Asta G. 43

**B**

Barbagallo A. 63, 70  
 Belletti R. 63, 70  
 Bignardi S. 82  
 Boaga J. 43  
 Böhm G. 63, 70  
 Busato L. 43

**C**

Capizzi P. 50, 98  
 Cassiani G. 43, 70  
 Castelo Branco R.M. 147  
 Ciabbari F. 11, 20  
 Civile D. 33  
 Codazzi M. 121  
 Cola S. 43  
 Colombero C. 76  
 Comina C. 76  
 Costagliola S. 126  
 Cotterle D. 63  
 Cubito A. 93

**D**

Dabove P. 76  
 Dal Moro G. 134  
 D'Alessandro A. 50, 98  
 D'Amico S. 56, 159  
 De Giorgi L. 88, 93, 112  
 De Natale G. 147  
 Dei D. 159  
 Del Ben A. 33  
 Deponte M. 63  
 Di Giuseppe M.G. 147  
 Di Massa D. 166  
 Dossi M. 106, 141

**E**

Esposito R. 147

**F**

Farrugia D. 56  
 Fedi M. 166  
 Fiorucci A. 76  
 Florio G. 166  
 Forte E. 106, 141

**G**

Galea P. 56, 159  
 Galuzzi B. 153  
 Garcea B. 20

Geletti R. 33  
 Giaccone T. 93  
 Giannotta M.T. 88  
 Gianturco E. 28  
 Gordini E. 63  
 Greco C. 93

**I**

Iannucci R. 56

**L**

Leo Imperiale M. 88  
 Leucci G. 88, 93, 112  
 Luzio D. 50, 98

**M**

Maffione S. 63  
 Martino S. 56  
 Martorana R. 50, 98  
 Masoli C.A. 63  
 Matera L. 112, 159  
 Mazzotti A. 11, 20  
 Mazzucchelli 121, 126  
 Meneghini F. 63  
 Micallef A. 159  
 Mocnik A. 33, 106  
 Moustafa S.R. 134  
 Muci G. 88

**P**

Paciello A. 56  
 Paganini P. 70  
 Pandolfi L. 28  
 Pappalardo S. 93  
 Parrini F. 159  
 Pascal I. 76  
 Patella D. 147  
 Perri M.T. 70  
 Persico R. 88, 112, 159  
 Petronio L. 63, 70  
 Peruzzo F. 11, 43  
 Pipan M. 106, 141

**R**

Rocchi S. 28  
 Romeo R. 63, 70  
 Rossi M. 70

**S**

Sambuelli L. 76  
 Santarato G. 82  
 Simonini P. 43  
 Sorgo D. 70  
 Stucchi E. 153

**T**

Tognarelli A. 28  
 Troiano A. 147  
 Troise C. 147

**V**

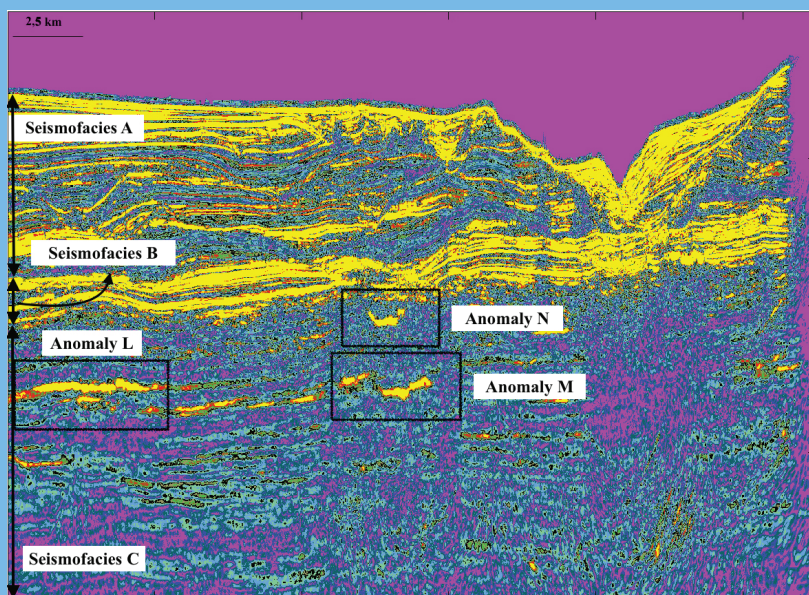
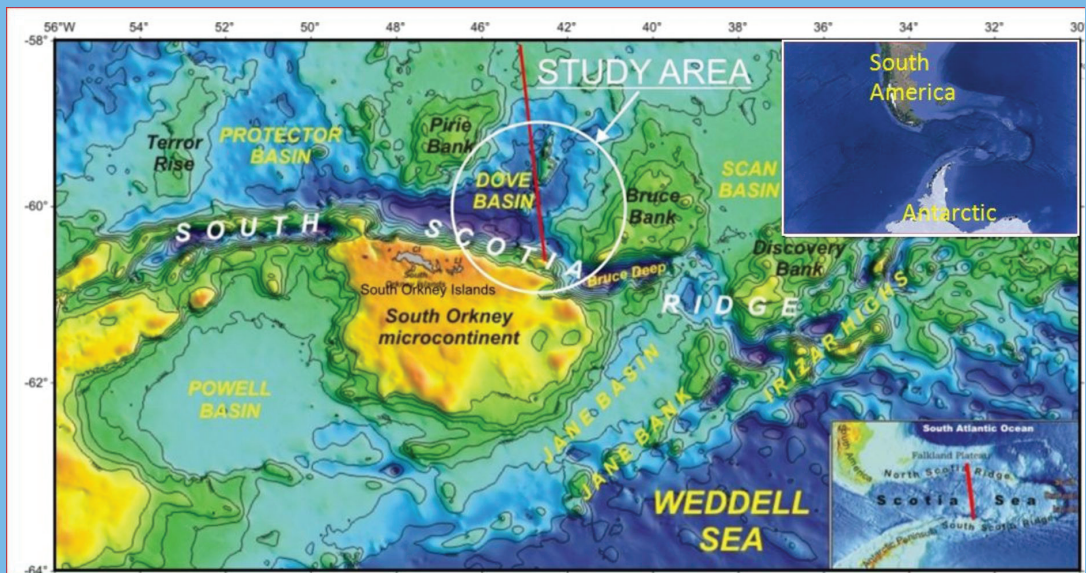
Vitale A. 166

**Z**

Zamariolo A. 106  
 Zambrini R. 106  
 Zampieri E. 153







con la sponsorizzazione di:



15° Convegno Nazionale



**CODEVINTEC**  
Tecnologie per le Scienze della Terra



misure meccaniche

volume

raccolta

ISBN 978-88-940442-7-0

ISBN 978-88-940442-4-9